



HAL
open science

Printed ceramic Piezoelectric MEMS for Energy Harvesting: towards Spark Plasma Sintering of multilayers

Maria Rua Taborda

► **To cite this version:**

Maria Rua Taborda. Printed ceramic Piezoelectric MEMS for Energy Harvesting: towards Spark Plasma Sintering of multilayers. Mechanics of materials [physics.class-ph]. Université de Bordeaux, 2019. English. NNT: 2019BORD0246 . tel-02922386

HAL Id: tel-02922386

<https://theses.hal.science/tel-02922386v1>

Submitted on 26 Aug 2020

HAL is a multi-disciplinary open access archive for the deposit and dissemination of scientific research documents, whether they are published or not. The documents may come from teaching and research institutions in France or abroad, or from public or private research centers.

L'archive ouverte pluridisciplinaire **HAL**, est destinée au dépôt et à la diffusion de documents scientifiques de niveau recherche, publiés ou non, émanant des établissements d'enseignement et de recherche français ou étrangers, des laboratoires publics ou privés.

THÈSE PRÉSENTÉE
POUR OBTENIR LE GRADE DE

**DOCTEUR DE
L'UNIVERSITÉ DE BORDEAUX**

ÉCOLE DOCTORALE:
Sciences Physiques et de l'Ingénieur

SPÉCIALITÉ:
Electronique

Par:

María Isabel RUA TABORDA

**Printed ceramic Piezoelectric MEMS for Energy Harvesting:
towards Spark Plasma Sintering of multilayers**

Sous la direction de Mme Hélène DEBEDA et Mme Catherine ELISSALDE

Soutenance prévue le 21 Novembre 2019.

Membres du jury :

Mme POULIN-VITTRANT Guylaine	Chargée de Recherche HDR, CNRS, GREMAN	Rapportrice
M. ESTOURNES Claude	Directeur de Recherche, Université de Toulouse, CIRIMAT	Rapporteur
M. DAMJANOVIC Dragan	Professeur, EPFL	Examineur
M. MAGLIONE Mario	Directeur de Recherche, ICMCB	Examineur
M. BERNARD Jérôme	Maitre de conférences, Université de Caen, LUSAC	Examineur
M. AYELA Cédric	Chargé de Recherche HDR, CNRS, IMS	Invité
M. CHUNG U-Chan	Ingénieur de Recherche, ICMCB	Invité
Mme DEBEDA Hélène	Maitre de conférences HDR, Université de Bordeaux, IMS	Directrice de thèse
Mme ELISSALDE Catherine	Directrice de Recherche, ICMCB	Codirectrice de thèse

Acknowledgements

This work would not have been possible without the help of numerous people that I would like to thank warmly. They contributed not only to the scientific aspect but also to the human aspect during these years. First of all I would like to thank my two supervisors, H  l  ne Debeda and Catherine Elissalde, for their constant support, compromise and their scientific expertise to improve and guide my work. It was a pleasure to work with them, for their expertise in their respective scientific field, but also for their very human contact. I would like especially to thank U-Chan Chung for his contribution to my knowledge on SPS technique and my general thesis work, by following my research closely, sharing his knowledge, skills and to help me overcome difficulties standing in front during the past three years.

I am very grateful to all the people from IMS and ICMCB lab, which contributed to the realization of many characterizations, especially Mario Maglione for training me on piezoelectric characterizations and Bernard Plano for SEM characterizations.

I am also very grateful to Simon Grall for its support and friendship which help me understand French culture in a wider way. I would also like to thank to MingMing and Quentin for cheer me up every time I felt I couldn't do it. A special thanks to Romain for his support and love despite everything.

Finally I thank my parents, Alberto Rua and Diana Taborda, my sisters and brother. Their constant love and support throughout my life has made me accomplished everything I've put my mind on.

MEMS céramiques piézoélectriques imprimés pour la récupération d'énergie: Vers un frittage SPS du multicouches.

Résumé

Une application émergente pour les MEMS (Micro-Electromechanical Systems) piézoélectriques concerne la récupération d'énergie mécanique vibratoire. La fabrication de ces MEMS piézoélectriques en couches épaisses sérigraphiées est une approche bas coût attractive. En effet, pour des applications MEMS de récupération d'énergie, les couches épaisses (1-100 μ m), sont une alternative intéressante aux couches minces pour maximiser le couplage électromécanique. De plus, le remplacement des substrats passifs silicium des MEMS par des substrats métalliques plus flexibles est aussi recherché pour améliorer les performances. Les couches épaisses piézoélectriques imprimées présentent cependant une porosité résiduelle néfaste pour les propriétés piézoélectriques. Ceci est dû au liant organique présent dans l'encre de sérigraphie et au traitement thermique réalisé à des températures relativement basses (<900°C) par rapport à un procédé céramique conventionnel. L'objectif de cette thèse est de développer un récupérateur d'énergie mécanique résonant (fréquence<100Hz) pour l'alimentation des systèmes autonomes. Le récupérateur d'énergie tout imprimé consiste en une structure multicouche formée de Pb(ZrTi)O₃ (PZT) comme matériau piézoélectrique actif pris en sandwich entre deux électrodes d'or. L'ensemble est sérigraphié sur un substrat en acier inoxydable (SS). L'implémentation d'une géométrie innovante a aussi conduit à une optimisation de la fréquence de résonance de la structure et de la densité de puissance. Enfin, pour améliorer la densification des couches de PZT, la technique de frittage avancé SPS (Spark Plasma Sintering) associée à la technique de sérigraphie a été explorée.

Au cours de ce travail de thèse, le récupérateur d'énergie a été réalisé par sérigraphie de toutes les couches en incorporant une étape de pressage des échantillons-avant le co-frittage conventionnel réalisé à 900°C. Le procédé de fabrication a été optimisé avec notamment une résolution des problèmes d'adhésion des couches et de déformation de la structure. Une géométrie de type zig-zag a été développée en collaboration avec l'Université de Waterloo au Canada (UW). Plus spécifiquement, ce récupérateur d'énergie MEMS dédié à des technologies de réseau électrique intelligent (Smart Grids), fonctionne sur la base d'un couplage des effets piézoélectrique et électromagnétique, avec l'intégration d'un aimant et l'interaction d'un champ électromagnétique autour d'un fil porteur de courant alternatif (AC). Avec l'aimant placé à l'extrémité de la structure et pour un courant de 7A et une distance de 6,5mm fil-aimant, une fréquence de résonance de 60Hz a été obtenue avec une puissance de sortie de 9 μ W (résistance de charge 1 M Ω). Par rapport aux autres dispositifs piézo-électromagnétiques de la littérature à base de MEMS, la densité de puissance normalisée est nettement améliorée. Une électronique associée à ce dispositif a aussi contribué à mettre en valeur les potentialités de ce microsystème (développée à UW). Bien que la performance du récupérateur d'énergie ait été prouvée, la structure présente une densification de la couche active de PZT limitée (densité \approx 82%). Ainsi, pour améliorer les performances du dispositif, la deuxième partie de cette thèse a porté sur une amélioration de la densification du PZT en utilisant le procédé SPS. Une optimisation des différents paramètres SPS (température, pression, durée et vitesse de chauffe) a d'abord été menée pour la densification des poudres de PZT. Les conditions SPS optimales ont été déterminées et des céramiques de densités proches de 98% ont été obtenues à des températures aussi basses que 850 °C. Les propriétés électromécaniques proches de celles de céramiques commerciales de PZT attestent de l'efficacité du SPS. Les poudres de PZT ont pu être densifiées sans ajout d'aide au frittage et l'utilisation originale d'une couche protectrice pour protéger le PZT de toute réduction chimique a permis d'éviter un traitement thermique post-SPS. Ces paramètres ont ensuite été transférés sur des structures simples de multicouches Au/PZT/Au/SS. Les principaux verrous identifiés sont la porosité de la couche active PZT, les problèmes d'interfaces conduisant à des interdiffusions entre les couches, les problèmes de délamination ou de courbures. Les différents essais ont conduit à la conception d'un moule SPS en graphite spécifiquement modifié et optimisé pour la densification de ce type de structures multicouches. L'efficacité du SPS en termes de réduction des températures et de rapidité du cycle de frittage s'avère une voie prometteuse pour le développement de MEMS imprimés.

Mots clés : [MEMS; Couche épaisse, Récupération d'énergie, piézoélectrique, SPS]

Title: Printed ceramic Piezoelectric MEMS for Energy Harvesting: towards Spark Plasma Sintering of multilayers

Abstract

An emerging application for piezoelectric MEMS (Micro-Electromechanical Systems) concerns the harvesting of mechanical vibratory energy. The fabrication of these piezoelectric MEMS in thick screen printed layers is an attractive low-cost approach. Indeed, for MEMS energy harvesting applications, thick layers (1-100 μm) are an interesting alternative to thin layers to maximize electromechanical coupling. In addition, the replacement of MEMS passive silicon substrates with more flexible metal substrates is also expected to improve performance. However, the printed piezoelectric thick-films have a residual porosity that is detrimental to the piezoelectric properties. This is due to the organic binder present in the screen printing ink and the heat treatment carried out at relatively low temperatures (<900°C) compared to a conventional ceramic process. The objective of this thesis is to develop a resonant mechanical energy harvester (frequency<100Hz) for the supply of autonomous systems. The printed device consists of a multilayer structure formed of $\text{Pb}(\text{ZrTi})\text{O}_3$ (PZT) as an active piezoelectric material sandwiched between two gold electrodes. The multilayer structure is screen printed on a stainless steel (SS) substrate. The implementation of an innovative geometry also led to an optimization of the resonance frequency of the structure and the power density. Finally, to improve the densification of PZT layers, the advanced SPS (Spark Plasma Sintering) sintering technique combined with the screen printing technique was explored. During this thesis work, the energy harvesting device was carried out by screen printing of all the layers. A step of pressing the samples before conventional co-sintering at 900°C was incorporated to the process. The manufacturing process was optimised, in particular by solving problems of layer adhesion and structural deformation. A zig-zag geometry was developed in collaboration with the University of Waterloo in Canada (UW). More specifically, this MEMS system dedicated to smart grid technologies, operates on the basis of a coupling of piezoelectric and electromagnetic effects, with the integration of a magnet and the interaction of an electromagnetic field around an alternating current (AC) carrier wire. With the magnet placed at the end of the structure and for a current of 7A and a distance of 6.5mm wire-magnet, a resonance frequency of 60Hz was obtained with an output power of 9 μW (load resistance 1 $\text{M}\Omega$). Compared to other piezoelectromagnetic devices in the MEMS-based literature, the normalized power density was significantly improved. Electronics associated with this device also helped to highlight the potential of this microsystem (developed at UW). Although the performance of the EH was proven, the structure has a limited densification of the active layer of PZT (density \approx 82%). Thus, to improve the performance of the device, the second part of this thesis focused on improving the densification of PZT using the SPS process. An optimization of the various SPS parameters (temperature, pressure, duration and heating rate) was first carried out for the densification of PZT powders. Optimal SPS conditions were determined and ceramics with densities close to 98% were obtained at temperatures as low as 850°C. The electromechanical properties close to those of PZT's commercial ceramics attest to the effectiveness of SPS. PZT powders could be densified without the addition of sintering aids and the original use of a protective layer to protect the PZT from chemical reduction has allowed to avoid post-SPS heat treatment. These parameters were then transferred to simple Au/PZT/Au/SS multilayer structures. The main locks identified are the porosity of the active PZT layer, interface problems leading to interdiffusion between layers, delamination or curvature problems. The various tests led to the design of a graphite SPS mould specifically modified and optimized for the densification of this complex multilayer structure. Thanks to significant advantages in reducing sintering temperatures and sintering cycle, SPS is a promising process for the development of printed MEMS.

Keywords: [MEMS, Thick-film, Energy harvesting, Piezoelectric, SPS]

Unité de recherche

[Ecole Doctorale numéro 209, Ecole Doctorale des Sciences Physiques et de l'Ingénieur (SPI),
351 cours de la Libération, 33405 TALENCE]

General content

General Introduction	8
Chapter I: State of the Art on Energy harvesting	12
Chapter II: Thick-film Technology and Sintering	49
Chapter III: Experimental methods	89
Chapter IV: Multilayer Energy harvesting fabrication	109
Chapter V: Towards SPS sintering route	163
General conclusion	213
Annexes	
Annexes Chapter II	217
Annexes Chapter III	220
Annexes Chapter IV	224
Annexes Chapter V	230
Scientific communications	233

General Introduction

Nowadays, an increasingly growing technology trend concerns an “intelligent world” where countless numbers of autonomous wireless sensing devices continuously monitor and provide information to control our environment. The concept of this intelligent world is in constant evolution. So far, this includes “wireless sensor networks (WSN),” “ambient intelligence,” and, more recently, “the Internet of Things (IoT).” It is estimated that more than a trillion of sensors are used around the world. The majority of these sensors are powered by batteries which have limited lifetime and that have to be periodically replaced or recharged. This operation can be an issue for human intervention. Therefore, the availability of energy-autonomous technologies, able to capture and store part of the energy available in the surrounding environment and to power the WSNs could speed up the wide diffusion of efficient and cost-effective WSN applications. Furthermore, these energy-autonomous technologies need to attain requirements such as small scale dimensions, low-cost, high reliability.

In this context, increasing attention has been focused in the last two decades on the recovery of energy from ambient energy sources such as light, heat and mechanical vibrations. This new field of research is referred to as Micro Energy Harvesting. An Energy Harvester can be defined as a device or system that captures (or harvests) ambient energy in the environment and converts it into electricity. Large-scale renewable power generation such as solar cell arrays and wind turbine generator can be considered as forms of energy harvesting. However, sensors networks need a smaller scale, requiring power in the range of 10–100s of microwatts. The overall dimensions of micro energy harvesters are usually in the millimeter or centimeter range but the transducers performing the electromechanical conversion are not always at the microscale.

Based on these considerations, the realization of miniaturized Energy Harvesters (EHs) taking advantage of MEMS (Micro Electro Mechanical Systems) technology is a solution full-filling both energy-autonomy and miniaturization/integration requirements. Also, aside thermoelectric and pyroelectric materials, piezoelectric compounds seem to be good candidates for the capture of small amounts of wasted energy ie. mechanical vibrations in our surroundings (human activity, machinery, car, etc.). Piezoelectric energy conversion is in fact displayed as the most interesting option for vibration energy harvesting MEMS, mainly due to its output power and compatibility with MEMS technologies.

With vibration piezoelectric EHs, the transformation from mechanical to electrical energy is obtained through the direct piezoelectric effect. The resulting energy can be stored after using a rectifier and DC-DC converter circuit. In general, one can abridge an energy harvesting system in three main steps: (1) capture the mechanical stress from vibration source, (2) converting the mechanical energy into electrical energy by direct piezoelectric transduction, and (3) processing and storing the generated electrical energy. Different approaches can be explored to optimize the extracted power, depending upon the aimed frequency (<100 Hz for ambient vibrations) and the sensor to power. These approaches cover a broad range of research field, from material science, going through mechanics, MEMS technologies until electronics.

In this context, this thesis aims to develop a MEMS EH structure capable of harvesting mechanical vibrations and converting them into electricity using piezoelectric transduction. Among inorganic compounds, PZT ($\text{PbZr}_x\text{Ti}_{1-x}\text{O}_3$) and its derivate presents larger

electromechanical properties than other piezoelectric inorganic or polymer materials. It remains preferentially used due to its outstanding properties despite its hazardous lead content. Also, for MEMS piezoelectric vibration EHs, the realization of screen-printed piezoelectric thick film layers ($10 < \text{thickness} (\mu\text{m}) < 400$) at a low cost can be automated and adapted to large volumes. Implementation of the piezoelectric MEMS achieved with a single printed technology, presents actually the following advantages: accessibility in the micro-manufacturing (stacking of layers showing various nature, geometries and dimensions) and choice flexibility of materials (piezoelectric, electrodes or substrates). However, recent works have shown that the electromechanical properties of PZT thick-films remain lower than those of the ceramic, mainly because of the too important residual porosity of the screen-printed layers. To improve the densification of both the piezoelectric material and the multilayer, we have selected the **Spark Plasma Sintering (SPS)** technique that combines the application of a uniaxial pressure and a pulsed electric current. The efficiency of SPS to densify (relative density higher than 95%) at low temperature and in short time a broad range of materials (from nanomaterials to multimaterials), is now fully recognized. Furthermore, optimization of the EH design with a complex geometry and the use of flexible substrate can be exploited to maximize power output. Such approaches are also in line with the current trend towards energy savings.

In this specific context, an interdisciplinary work has been conducted during this thesis work, for which three central and complementary axis can be defined

- (1) The first axis is focused on the thick film piezoelectric fabrication by screen-printing. The process has been carried out in a cleanroom at the IMS laboratory.
- (2) The second axis consists on the Spark Plasma Sintering based investigations targeting the densification of screen-printed structures at the ICMCB laboratory,
- (3) Finally, axis 3 includes all the characterizations of the active piezoelectric material and the EH system, carried out in between the two laboratories ICMCB and IMS. Collaborative projects with University of Waterloo and Paris-Sud University are a part of this axis. They are focused on the performance tests and electrical circuit design of complex EH structure.

A flowchart illustrating the interdisciplinary nature of the thesis work as well as the various collaborations is proposed in Figure 1.

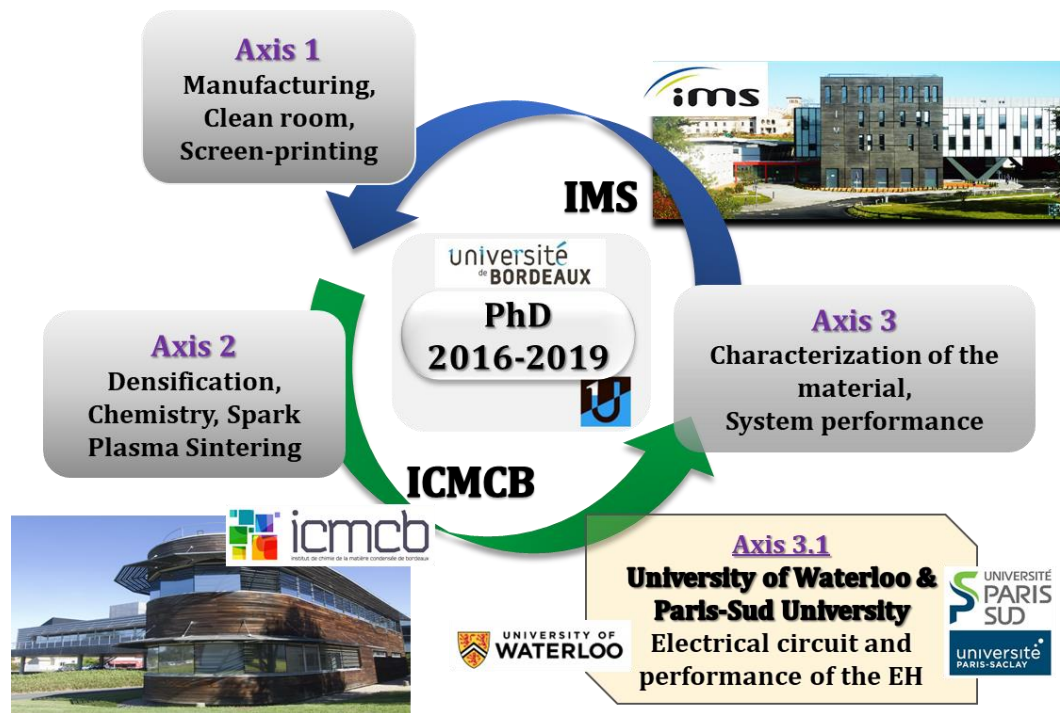


Figure 1: Thesis execution synopsis

This thesis manuscript is organized in five chapters.

Chapter one presents the state of the art on the different types of energy harvesting sources and energy conversion principles. The mechanical energy harvesting is then detailed by introducing the different types of electromechanical transducers highlighting the piezoelectric transduction. Different processes used for piezoelectric MEMS are then shown with a special focus on EH using flexible metallic substrates and PZT thick films. Qualitative comparisons of the most relevant piezoelectric EH are carried out.

Chapter two describes first the thick film technology and the different steps inherent to the process. The basics of sintering are then briefly proposed with particular emphasis on conventional technique and Spark Plasma Sintering.

Chapter three presents the different techniques and methods used to characterize the raw piezoelectric material and the fabricated piezoelectric ceramics and printed components. Characterizations are oriented on structural, microstructural and interfaces related aspects as well as dielectric and electromechanical properties.

Chapter four focuses on the EH fabrication consisting of a multilayer structure where electrodes and piezoelectric material are printed on a metallic substrate. The choice of the materials, the optimization of the fabrication of the EH with a complex geometry developed at the University of Waterloo are justified. A microstructural analysis is conducted through the comparison of different PZT based structures: a bulk ceramic, a printed disk and a cantilever (representative of the complex structure). Specific attention is paid to the effects of the passive metallic substrate on both microstructural features and functional properties. Dielectric and electromechanical characteristics and power output performance are finally investigated.

Finally, chapter five explores the SPS as a sintering route for the densification in one-step of the multilayer printed EH structure. First, the sintering conditions of the active material PZT are optimized with as a main objective to densify PZT without adding sintering aid and without additional post-sintering annealing. To do this, our approach based on the use of a carbonate protective layer is presented. Then the challenging transfer towards the sintering of the EH multilayer structure by Spark Plasma Sintering constitutes the second part of this chapter.

This manuscript ends with the general conclusions, including some perspectives for future work and experiments.

Chapter I

State of the Art on Energy Harvesting

Content

1	CONTEXT	15
2	ENERGY HARVESTING SOURCES	15
2.1	SOLAR ENERGY	16
2.2	WIND ENERGY	16
2.3	THERMAL ENERGY	17
2.4	ACOUSTIC ENERGY	18
2.5	MECHANICAL ENERGY	19
2.6	ELECTROMAGNETIC ENERGY	20
2.7	SUMMARY ON ENERGY HARVESTING SOURCES	20
3	MECHANICAL ENERGY HARVESTING	22
3.1	MECHANICAL CONVERSION PRINCIPLE	22
3.1.1	OSCILLATOR	22
3.1.2	OUTPUT POWER IN MECHANICAL ENERGY HARVESTING	24
3.2	TRANSDUCTION MECHANISMS	24
3.2.1	ELECTROMAGNETIC ENERGY CONVERSION	25
3.2.2	ELECTROSTATIC ENERGY CONVERSION	26
3.2.3	PIEZOELECTRIC ENERGY CONVERSION	27
3.2.4	COMPARISON OF THE DIFFERENT ENERGY CONVERSION MECHANISMS	27
4	PIEZOELECTRIC ENERGY HARVESTING	29
4.1	BASICS ON PIEZOELECTRICITY	29
4.1.1	HISTORIC AND APPLICATIONS	29
4.1.2	DESCRIPTION AND ORIGIN OF THE PIEZOELECTRIC EFFECT	29
4.2	CONFIGURATIONS OF PIEZOELECTRIC ENERGY HARVESTERS	32
4.3	PIEZOELECTRIC MATERIALS PROPERTIES REQUIREMENTS FOR ENERGY HARVESTING	32
4.4	ENERGY HARVESTERS BASED ON PZT AND METALLIC SUBSTRATES	34
4.4.1	OVERVIEW ON PIEZOELECTRIC MATERIALS	34
4.4.2	MICRO-FABRICATION TECHNOLOGIES FOR ENERGY HARVESTING MEMS	36
4.4.3	METALLIC SUBSTRATE BASED ENERGY HARVESTING DEVICES	38
5	CONCLUSION	42

The main objective of this first chapter is to define the background and the context related to energy harvesting. The beginning is dedicated to the available energy harvesting sources. Then the mechanical energy harvesting will be engrossed, presenting the different transductions methods with their general principle, main advantages, and drawbacks. Furthermore, piezoelectric energy harvesting (PEH) will be encompassed and carefully explained from its basics until recent advances in PEH devices, highlighting mainly the material and fabrications techniques.

1 Context

Many of nowadays applications would not be possible without progress in miniaturization and reduction of the power consumption of electronics (10's nW -100's μ W of power [1]). This is illustrated by the progress in Wireless Sensor Network (WSN) technology for smart systems. Further advances in smart sensors and WSN tend to be even more embedded and mobile in the future. However, the power supply of the sensor nodes raises some serious challenges for the widespread implementation of WSN. As the sensors need to be wireless, the power is usually provided by primary or secondary batteries¹. Nevertheless batteries have some unavoidable drawbacks. The most important one for application in WSN's is that the energy is inherently limited. As a result, the periodical replacement for long term operations can compromise the complete integration and size of the system and in some cases is not even possible, due to the difficult access of the sensor location [2]. Advances in WSN technologies have enable different solutions for battery-less autonomous sensors and network systems. Harvesting solutions using different energy sources such as heat, radio-waves, light or vibrations are promising [3]. Harvesting from environment vibrations using Micro-Electromechanical System (MEMS) energy harvesters is one of the most promising option, since it addresses both issues, autonomy and miniaturization, and allows large energy to volume ratio production by scavenging energy from external vibrations [4].

2 Energy harvesting sources

The purpose of an energy harvesting is to reuse or recover energy from different available sources that can be found in our surroundings (Figure I-1). These sources can be divided into different types: solar energy, wind energy, thermal energy, acoustic energy, mechanical energy and electromagnetic radiation. This section explains the basic principle of the main types of energy harvesting, highlighting their major advantages and drawbacks, as well as their positioning related to power performance.

¹ A primary battery is designed to be used once and discarded, and not electrically recharged and reused as secondary cells (rechargeable battery).



Figure I-2: Energy sources available in ambient environment (Photo from of <http://techon.nikkeibp.co.jp/Tech-On Japan>).

2.1 Solar energy

Solar energy generators are a well-developed technology used for large-scale energy generation (milliwatts to megawatts). Solar energy cells or photovoltaic modules generate electrical power by converting solar radiation directly into electricity using semiconductors [5]. The generated electricity can be used for many applications, such as grid systems, water heaters and outdoor lamps. There exist many other different applications mainly found in portable products, such as calculators, watches, or monitoring sensor nodes [6]. In an outdoor environment on a sunny midday, the power density of the solar radiation on the earth's surface is about 100 mW/cm^2 , making solar energy one of the most effective energy harvesting methods. Nevertheless, solar energy becomes less suitable for indoor environments due to the drop in power density to a value as low as $10 \text{ } \mu\text{W/cm}^2$. Solar cells are developed using silicon technologies, and are divided in two major categories: single-crystal silicon and polycrystalline thin-films. The efficiency of single-crystal silicon cells is between 12 to 25%. Polycrystalline thin-films and amorphous silicon solar cells are commercially available and have lower cost and efficiency than single-crystal silicon cells [7]. Most recently organic solar cells (OSC) consisting mainly in polymer materials have been studied because it is potentially cost-effective for photovoltaic applications. With polymers, molecular engineering (e.g. changing the length and functional group of polymers) can change the band gap, allowing for electronic tunability. The optical absorption coefficient of organic molecules is high, so a large amount of light can be absorbed with a small amount of materials, usually on the order of hundreds of nanometers. However low efficiency, low stability and low strength compared to inorganic photovoltaic cells remain challenging [8].

2.2 Wind energy

Wind energy uses the air flow through wind turbines to provide mechanical power to turn electric generators. It is a mature energy source used in large-scale electric power generation for grid applications. Recently, micro wind generators (micro-WGs) have been proposed as energy-

harvesting for indoor or autonomous systems (Figure I-2)[6]. Micro-WGs can generate several milliwatts of power, which is relatively large in the scope of energy harvesting. Nevertheless wind power depends on environmental conditions. In fact, wind generators depend directly on the torque generated through wind and not all locations have strong winds conditions, moreover their large dimensions are inconvenient for integration on a microelectronic scale. Reducing the size of WGs is difficult because of the wind power density and wind turbine mechanism size limitations.

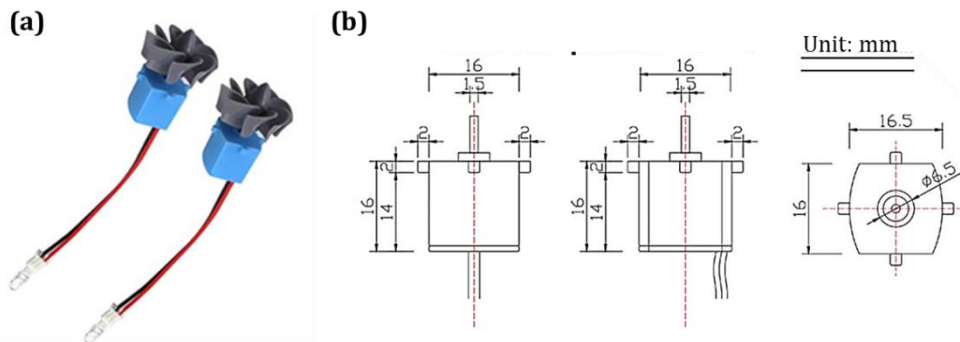


Figure I-3: (a) Picture of Micro Wind Generator (MWGs) used to power a led unit, output voltage can range from 0.01 to 15V depending on wind spin rate (maximum speed rate 300 rpm) and, (b) dimensions of MGWs structure. The structure weights 10g in total (motor + turbines paddles). (Commercialized by RMD technology, China).

2.3 Thermal energy

Thermal energy can be divided in two types: pyroelectric and thermoelectric. Concerning pyroelectric generator, a voltage is generated by heating or cooling pyroelectric materials. Pyroelectric materials possess a spontaneous polarization, a temperature variation in these materials leads to a shift in atomic positions changing the polarization and giving rise to a voltage. Thermoelectric generators (TEGs) are based on the thermoelectric effect which produces a direct conversion of temperature into electric voltage and vice versa. A thermoelectric generator basically consists of a thermocouple, which comprises p-type and n-type semiconductors and produces an electrical current proportional to the temperature difference between hot and cold junctions [6]. In metals and semiconductors, charge carriers are free to move and when a temperature gradient exists in a material, the mobile charges at the hot part diffuse to the cold one, resulting in a net charge and an electric potential (Figure I-3). The best thermoelectric materials are heavily doped semiconductors. The output voltage of TEGs is in the range of several millivolts, achieved using compacted structures with large number of thermocouples. Thermoelectric generators are mainly solid-state devices and their efficiency is often lower than 10%. TEGs are suitable for small distributed power generation in energy harvesting applications such as power plants in order to convert waste heat into additional electrical power and in automotive applications such as thermoelectric generators (ATGs) to increase fuel efficiency and for bio-WSNs [9]. The major drawback is the rejected heat that must be evacuated. It requires an additional heat dissipation mechanism and thus a larger area.

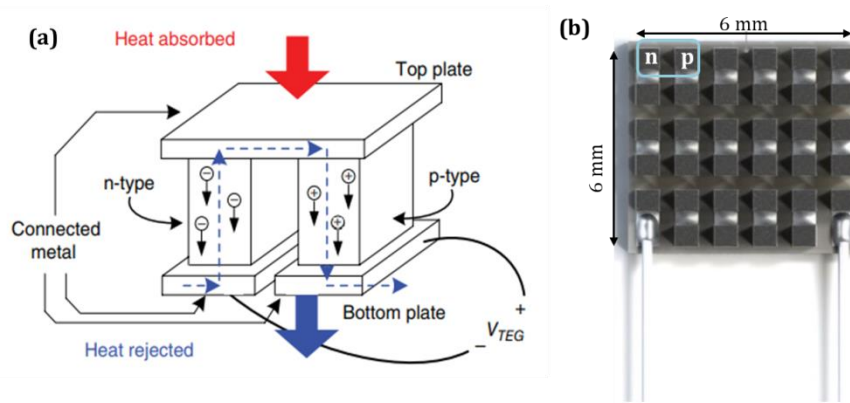


Figure I-4: (a) Scheme of a thermoelectric generator TEG elementary brick (Image from [6]), and (b) commercial TEG with a output power of $6.21 \mu\text{W}$ for a temperature increase of 73°K (1MC04-030-15_TEG from PL Engineering Ltd, Russia).

2.4 Acoustic energy

Acoustic or sound energy harvesters (AEHs) convert high and continuous acoustic waves from the environment to electrical energy using an acoustic transducer or a resonator. AEHs reported in literature can be divided in two types, electromagnetic and piezoelectric based.

The energy available in acoustic energy sources can be converted into electrical energy with a Helmholtz or quarter-wavelength resonator integrated with an energy transduction mechanism (piezoelectric transductions using a piezoelectric membrane or electromagnetic transduction using a structure integrated of a permanent magnet with a coil).

In a Helmholtz resonator, the incident acoustic pressure wave oscillates the lumped air located at the neck (Figure I-4 (a)). The downward motion of the neck's air increases the pressure of air in the cavity; however, due to the upward motion, the pressure of the cavity's air decreases. This system can be modeled as a spring-mass-damper system as shown in Figure I-4 (b). The pressure amplitude in the cavity is always higher than that of the incident acoustic wave. Hence, the fluctuating cavity's pressure triggers the energy transduction mechanism to produce the power [10]. This same principle applies for the quarter-wavelength resonator, but for a tube structure with just one open end as depicted in Figure I-4 (c). Here one-third of the tube's length near the open end acts as a neck and the remaining portion of the tube behaves like the cavity similar to the Helmholtz resonator, but the amplification factor of the quarter-wavelength resonator is relatively higher than the Helmholtz resonator for the same volume.

The power produced by the piezoelectric AEHs ranges from 0.68 pW to 30 mW , whereas for the electromagnetic AEHs the range is $1.5\text{--}1.96 \text{ mW}$. Although output power can reach the mW scale, such energy can only be recovered in very noisy environments. Acoustic resonators are still vastly used for both noise attenuation and sound augmentation [10], [11].

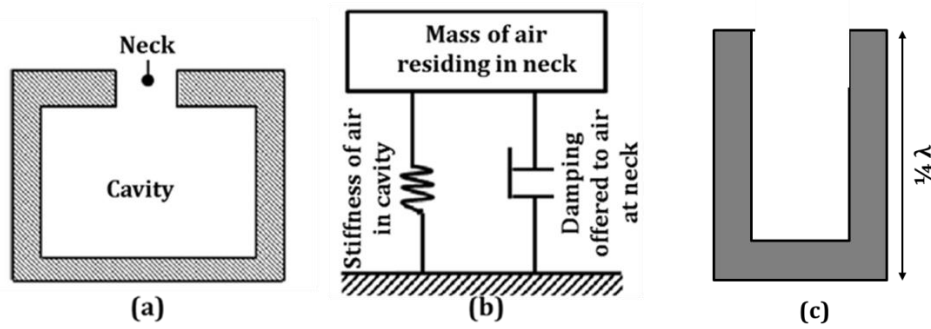


Figure I-5: (a) Cross-sectional view of the Helmholtz resonator (b) equivalent mechanical model of the Helmholtz resonator (images from [10]), and (c) scheme of a quarter-wavelength resonator.

2.5 Mechanical energy

Conversion of mechanical energy into electrical energy can be obtained from kinetic sources, such as vibrations, mechanical stresses, deformations, high-pressure motors, etc. The principle of mechanical energy harvesting is to convert the energy of the movements and mechanical oscillations of a spring-mass component mounted inside the energy harvesting, into electrical energy. This type of mechanical energy harvesting is based mainly on three principles of transduction: piezoelectric, electrostatic and electromagnetic, which will be further presented in section 3 of this chapter. The frequency of mechanical excitation depends on the source which can be generated by the human body movements or by any vibrating structure.

For human movements, it represents a few tens of Hz, while for machine vibrations, the frequency range is in the range 30-1000 Hz, with vibration amplitudes that may be low (<0.1 g). Some applications for mechanical energy harvesters, which include the energy for powering the implantable medical or wearable devices have been for instance proposed. *Shenck and Paradiso* at the MIT Media Laboratory (Massachusetts, USA) [11] proposed a pioneer vibration energy harvesting unit made of a shoe-mounted piezoelectric generator with a complete subsequent power conditioning circuit (Figure I- 5). The unit uses the human movement as vibration source. The circuit supports an active RF tag that is able to transmit a short-range, 12-bit wireless identification (ID) code, while the wearer walks.

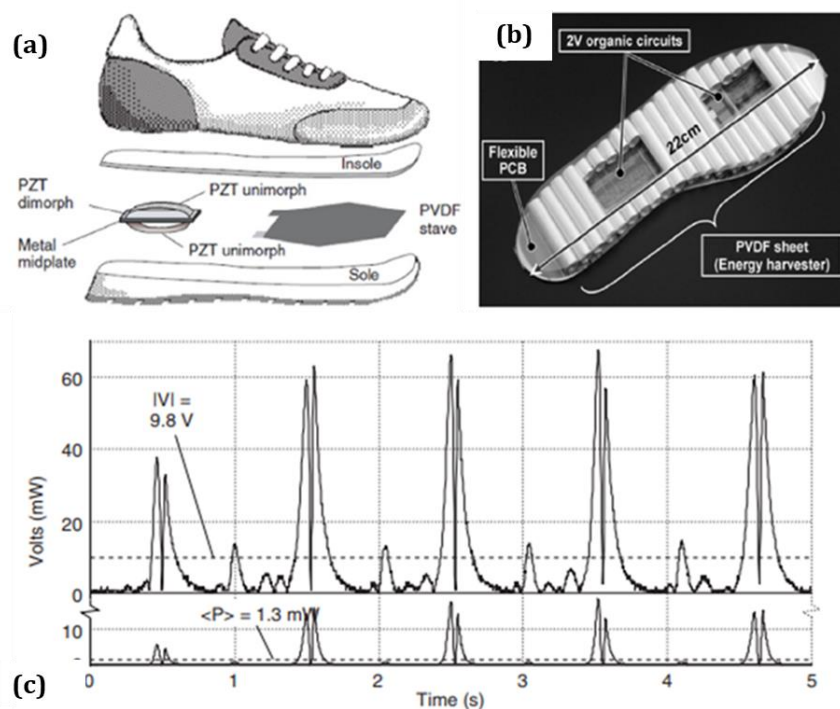


Figure I-6: (a-b) Mechanical energy harvesting, using piezoelectric transduction system mounted in shoes for scavenging human movement (c) Power and rectified voltage waveforms from brisk-walking tests. (Images from [12])

2.6 Electromagnetic energy

Electromagnetic energy can be divided in:

- Conversion of Radio Frequency (RF) electromagnetic waves into electricity based on a rectifying antenna. The energy can be recovered either from RF energy sources such as radio, television, mobile phones and WiFi communications, or from electromagnetic signals generated at a specific wavelength. For this type of energy harvesting the power generated depends on the distance between the RF transmitter and the generator.
- Resonant energy harvesting using kinetic energy to induce magnetic-field-flux variation on a fixed coil to generate energy. The principle is based on the transfer of electrical energy between two coils resonating at the same frequency. The magnitude of the magnetic field variation is proportional to the current of the power wire [1][13].

2.7 Summary on energy harvesting sources

The Table I-1 shows the power density that can be extracted with the energy sources presented in the previous paragraphs.

The harvested power is limited by the size of the energy harvesting system. In order to maintain the small dimensions requirements of microsystems, it is necessary to take into account the

maximum output power density of such energy harvesting system. Because of their limited volume, energy harvesting microstructures (volume $<1\text{cm}^3$) cannot therefore power high energy consumption devices such as smartphones or laptops (200 mW – 40 W). However, they are ideal for providing the energy needed to operate simple pressure, acceleration or temperature sensors (1-10 μW).

Table I-1: Energy sources with power density harvested [6].

Energy source	Power density ($\mu\text{W}/\text{cm}^3$)
Solar	100000 (outdoors) 10 indoors
Wind	380 for a speed of 5m/s
Thermal	1000-10000
Acoustic	0.96-100 dB
Mechanical	1-1000
Electromagnetic (RF)	0.1 for GSM 900/1800 MHz

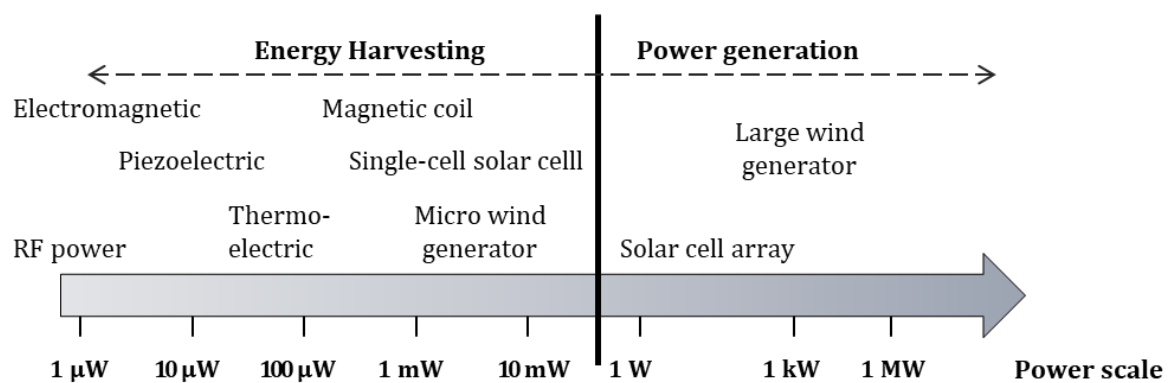


Figure I-7: Positioning of different energy sources at power scale (inspired from [6]).

Therefore converting mechanical energy from ambient vibration into electrical energy is a very interesting approach to power wireless sensor nodes, since it provides a power solution that can meet the requirements of size limitations. Moreover the source can be found almost anywhere where wireless sensor networks may potentially be deployed. In the framework of this thesis we will focus on this type of energy harvesting.

3 Mechanical energy harvesting

A mechanical energy harvesting system usually involves three elements (Figure I-7):

- The mechanical-mechanical converter that captures the energy. The best suited capture device is a mechanical oscillator with a proof (or seismic) mass [14].
- The energy converting transducer; the energy is usually transferred to the transducer with the proof mass. Note that in some systems the mechanical-mechanical converter and the transducer can be a single element.
- The electronic circuit to power the electronic load.

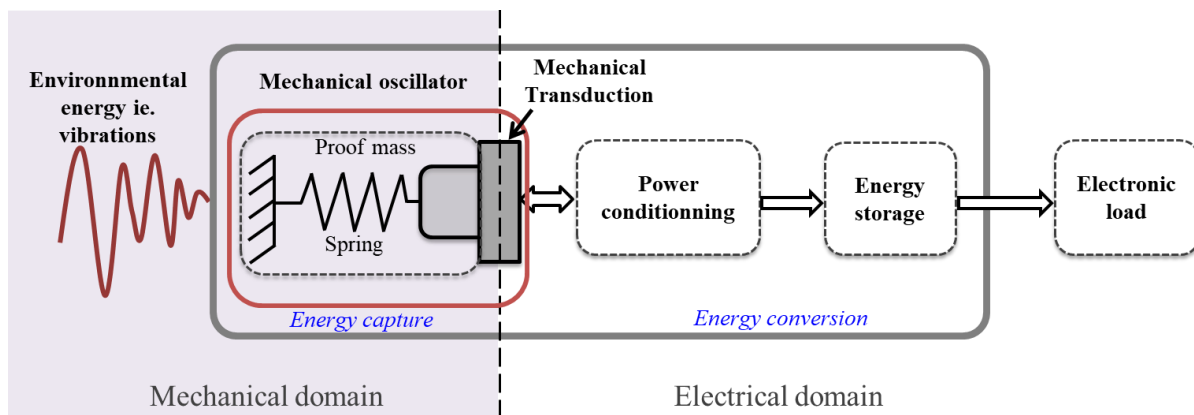


Figure I-8: Diagram block of a standard mechanical energy harvesting system.

3.1 Mechanical conversion principle

3.1.1 Oscillator

Vibration of a rigid body can be caused by several factors such as unbalanced mass in a system, tear and wear of materials and can occur in almost all dynamical systems. Most commonly, vibration energy harvester can be simply modeled as a second-order spring-mass system. The characteristics of the energy harvester can be described by a damping constant and the natural frequency of the system. This simple equivalent model based on linear system theory was proposed by Williams and Yates [15][18]. Figure I-8 shows a generic model of such a generator, where a cantilever structure with a tip mass is used (Figure I-8 (a)). The vibration source is depicted with a red point. The generic equivalent lumped spring mass system scheme is as well illustrated (Figure I-8 (b)).

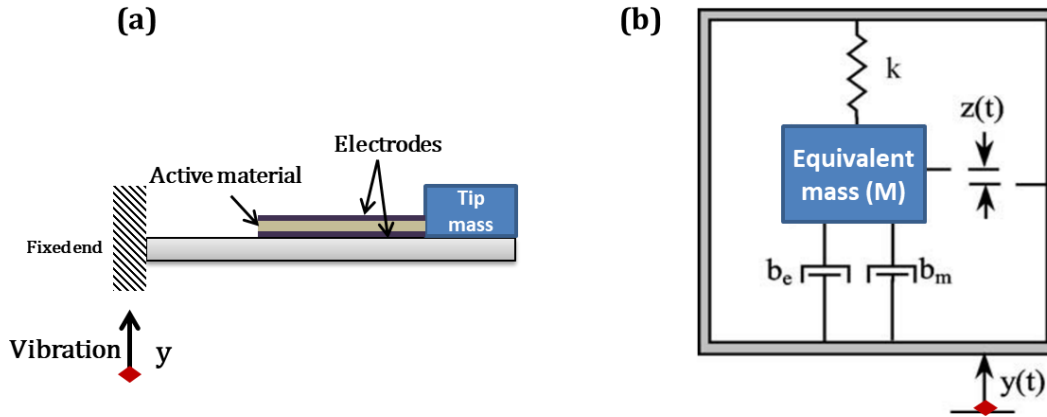


Figure I-9: (a) Cantilever beam with tip mass subjected to a vibration source excited at the base (red point) and, (b) equivalent lumped spring mass system of a vibrating rigid body. (inspired from [16])

The governing equation of motion of a lumped spring mass system can be written as:

$$M\ddot{z} + (b_E + b_M)\dot{z} + kz = -M\ddot{y} \quad (\text{Eq. 1.1})$$

where z is the spring deflection, y the input displacement, M the mass, b_E the electrically induced damping coefficient, b_M the mechanical damping coefficient, and k the spring constant. Assuming that the external base excitation is sinusoidal given as $y(t) = Y \sin \omega t$, with ω the input frequency the solution of the equation 1.1. is:

$$z(t) = \frac{\left(\frac{\omega}{\omega_n}\right)^2}{\sqrt{\left[1 - \left(\frac{\omega}{\omega_n}\right)^2\right]^2 + (2\zeta_T \frac{\omega}{\omega_n})^2}} Y \sin(\omega t - \phi) \quad (\text{Eq. 1.2})$$

where Y is the amplitude of vibration and ω_n is the natural frequency of spring mass system, ζ_T is the combined damping factor ($\zeta_T = \zeta_E + \zeta_M$) and ϕ the phase angle between output and input. From Eq. 1.2 the maximum amplitude $|z|$ is found at the resonant frequency and is inversely proportional to the resulting damping. Moreover, the lower the resonance frequency, the higher the amplitude.

The natural resonant frequency of a spring mass system is defined as:

$$\omega_n = \sqrt{k/M} \quad (\text{Eq. 1.3})$$

The phase angle can be expressed by:

$$\phi = \arctan\left(\frac{C\omega}{k - \omega^2 M}\right) \quad (\text{Eq. 1.4})$$

The quality factor can be then defined by the ratio of the amplitude of the mass z with the amplitude of the resonant excitation y at the resonant frequency ω_0 , as followed:

$$Q = \frac{z}{y} \Big|_{\omega=\omega_0} = \frac{M\omega_0}{b_E + b_M} = \frac{1}{2(\zeta_E + \zeta_M)} = \frac{1}{2\zeta_T} \quad (\text{Eq. 1.5})$$

Consequently, from Eq. 1.5, the lower total damping factor, the greater the quality factor Q .

3.1.2 Output power in mechanical energy harvesting

The power converted to the electrical system is equal to the power extract from the mechanical system by b_E , the electrically induced damping. The average harvested electrical power can be obtained from the product of velocity and force on the mass, described by:

$$P = \frac{1}{2} b_E \dot{z}^2 \quad (\text{Eq. 1.6})$$

Therefore taking into account the already described equations, the magnitude of the average power $|P|$ dissipated by the energy harvester is:

$$|P| = \frac{M \zeta_E \omega_n \omega^2 \left(\frac{\omega}{\omega_n}\right)^3 Y^2}{\left(2 \zeta_T \frac{\omega}{\omega_n}\right) + \left(1 - \left(\frac{\omega}{\omega_n}\right)^2\right)^2} \quad (\text{Eq. 1.7})$$

where Y is the displacement magnitude of input vibrations. When the generator is at resonance, $\omega = \omega_n$. The maximum dissipated power becomes:

$$|P| = \frac{M Y^2 \omega_n^3}{4 \zeta_T} \quad (\text{Eq. 1.8})$$

According to the relationship of mass, acceleration magnitude and resonant frequency previously observed, higher mass and higher acceleration result in higher output power. The maximum power delivered to the electrical domain is inversely proportional to the damping factor. Thus, when designing a vibration-based micro-generator in order to achieve maximum power output, it is important to design the generator with a high Q factor working at its resonant frequency. In addition, due to the nature of vibrations and since the output power is inversely proportional to the resonant frequency of the generator for a given acceleration, it is generally preferable to operate at the lowest available fundamental frequency, since acceleration levels associated with environmental vibrations tend to reduce with increasing frequency [17].

3.2 Transduction mechanisms

In mechanical energy harvesting, a particular transduction mechanism is used to extract electrical energy from motion. So far, existing vibration transducers are commonly based on three different conversion mechanisms: electromagnetic [18], electrostatic [19] and piezoelectric [20]. In few cases the effect of magnetostriction [21] has been investigated as well. The transduction mechanism can generate electrical energy by exploiting the relative displacement or strain based on the spring-mass system described previously.

3.2.1 Electromagnetic energy conversion

Electromagnetic energy conversion is based on Faraday's law of electromagnetic induction discovered by Michael Faraday in 1831. This law describes the interaction of a magnetic field with an electric circuit to produce an electromotive force (EMF), a phenomenon called electromagnetic induction and produced across an electrical conductor in a varying magnetic field. In an electromagnetic generator, permanent magnets are used to produce strong magnetic field and a coil is used as electric conductor [22]. Two systems can be differentiated, one with a moving magnet and permanent coil (Figure I-9 (a)), and another with a fixed magnet linked to a moving coil (Figure I-9 (b)). The EMF is described by the rate of change of the magnetic flux:

$$\varepsilon = \frac{-d\Phi}{dt} \quad (\text{Eq. 1.9})$$

Where ε is the electromotive force (EMF) and Φ is the magnetic flux. Power is extracted when the generator is loaded to a resistance allowing a current to flow in the coil. This current produces its own magnetic field, opposing the field that induces it. The interaction between the field generated by the induced current and the field from the magnets creates a force that opposes the motion [6].

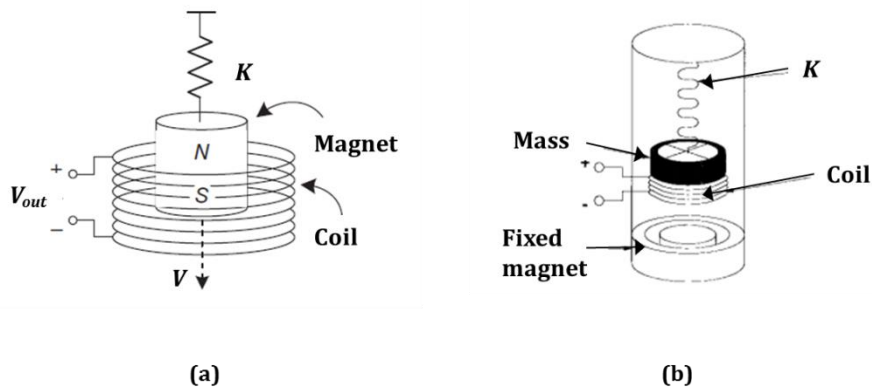


Figure I-10: Scheme of electromagnetic generators, with (a) moving and (b) fixed magnet. (Images from [6][23])

The open-circuit voltage V_{out} , which is generated by a linear electromagnetic generator, can be described as followed:

$$V_{out} = NBA_{coil}v \quad (\text{Eq. 1.10})$$

Where N is the number of turns in the coil, B is the magnetic strength of the magnet, A_{coil} is the cross-sectional area of the coil, and v is the velocity of the magnet as it goes through the coil. An electromagnetic generator is characterized by high output current level at the expense of low voltages [22]. Moreover Beeby et al., have stated that electromagnetic energy harvesters perform better in macro-scale than in micro-scale, due to the use of discrete permanent

magnets, therefore it is challenging to incorporate electromagnetic energy harvesters with the MEMS fabrication process [24].

3.2.2 Electrostatic energy conversion

Electrostatic harvesting of mechanical energy is based on varying vibration-dependent capacitance of variable capacitors (varactors) [25][26]. Electrostatic energy conversion scheme is depicted in Figure I-11. The capacitance varies between maximum and minimum values through mechanical vibrations. If the charge on the capacitor is constrained, charge moves from the capacitor to a storage device or to the load as the capacitance decreases. Thus, mechanical energy is converted into electrical energy. The voltage V across the capacitor is expressed by Eq. (1.11), where Q is the charge, d is the gap or distance between plates, A is the area of the plate, and ϵ is the dielectric constant of the free space.

$$V = \frac{Qd}{A\epsilon} \quad (\text{Eq. 1.11})$$

The energy stored in the capacitor is expressed by:

$$E = \frac{Q^2}{2C} \quad (\text{Eq. 1.12})$$

Where C is the capacitance.

Increasing the voltage or the charge increases the energy stored in the capacitor. Thus, energy transfer schemes can be classified as either charge- or voltage-constrained conversion; these two types of energy transfer schemes are adopted in various works [13].

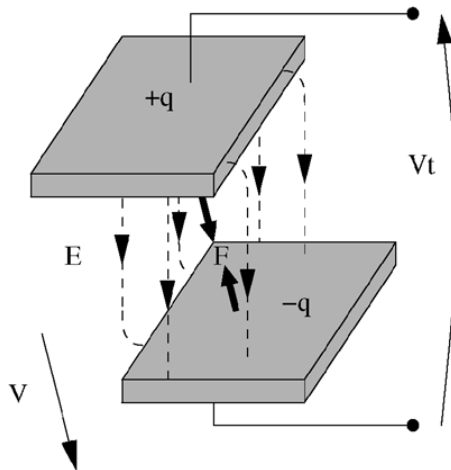


Figure I-11: Scheme of an electrostatic generator, where E represents the produced energy, q the charges and V_t the voltage across the capacitor. (Image from [27])

3.2.3 Piezoelectric energy conversion

The piezoelectric conversion is based on the piezoelectric effect characteristic of some materials. This effect can be defined in a general way as the conversion of mechanical energy into electrical energy (direct effect) or the conversion of electrical energy into mechanical energy (inverse effect). Piezoelectric coupling provides a two-way conversion between mechanical energy and electrical energy. The constitutive equations for a piezoelectric material are expressed by:

$$\delta = \frac{\sigma}{Y} + dE \quad (\text{Eq. 1.13})$$

$$D = \epsilon E + d\sigma \quad (\text{Eq. 1.14})$$

where δ is the mechanical strain, σ is the mechanical stress, Y is the Young's modulus of the material, d is the piezoelectric strain coefficient, E is the electric field, D is the electrical displacement (charge density) and ϵ is the dielectric constant of the piezoelectric material. Piezoelectric energy harvesters are typically simple structures such as unimorph or bimorph cantilevers, or double-clamped beam. Figure I-12 shows a scheme of a bimorph piezoelectric cantilever [28][29][30]. However, bimorph cantilevers are less adapted in terms of manufacturability considering existing micro-fabrication processes [3]. As a result, MEMS cantilevers mostly have a unimorph configuration. A seismic mass is usually attached at the tip of the cantilever to adjust the resonant frequency to the available environmental frequency, usually below 100Hz [16][31][32].

Piezoelectric conversion has the simplest structure among the three transducers (electromagnetic, electrostatic, piezoelectric). Moreover they can produce appropriate voltages for electronic devices. However, the mechanical properties of the piezoelectric material may limit overall performance and lifespan of the generator.

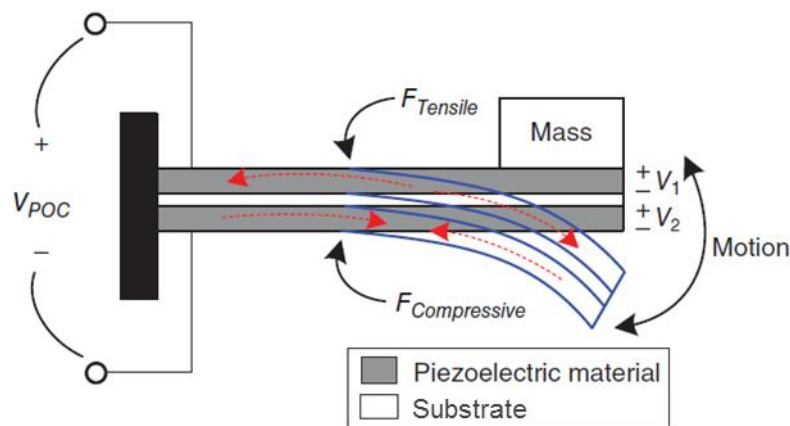


Figure I-12: Scheme of piezoelectric cantilever. (Image inspired from [6])

3.2.4 Comparison of the different energy conversion mechanisms

Advantages and disadvantages of each type of conversion mechanisms are summarized in Table I-2.

In general the main drawbacks of electromagnetic transducers are their difficulty to be integrated into MEMS fabrication process and their low energy density that limits the fields of applications. Since electrostatic and piezoelectric transducers are compatible with MEMS technologies, they are more suitable to be used in micro- or nano-scale systems while electromagnetic transducers are suitable for macro-scale systems.

The main disadvantage of electrostatic generators is the voltage source requirement to initiate the conversion process because the capacitor must be charged to an initial voltage. Moreover Roundy *et al.* [33] calculated the theoretical maximum energy density of the different transducers and it was concluded that piezoelectric and electromagnetic transducers have similar energy density which is about 10 times higher than that of electrostatic transducers.

Therefore piezoelectric energy conversion is displayed as the most interesting option for vibration energy harvesting MEMS. This is mainly due to its output power and compatibility with MEMS technologies. Nevertheless the challenge remains to guarantee good mechanical properties of the piezoelectric material since they can limit overall performance and lifespan of the generator.

Table I-2: Advantages and disadvantages of different conversion mechanisms for vibration energy harvesting.

Transduction type	Advantages	Disadvantages
Electromagnetic	<ul style="list-style-type: none"> • No external voltage source • High output current 	<ul style="list-style-type: none"> • Difficult to integrate with MEMS fabrication process • Poor performance in micro-scale systems • Low output voltages
Electrostatic	<ul style="list-style-type: none"> • Easy to integrate with MEMS fabrication process 	<ul style="list-style-type: none"> • Low output current • High output impedance • External charged or voltage source are often needed
Piezoelectric	<ul style="list-style-type: none"> • Simple structures • No external voltage source needed • Compatible with MEMS fabrication process • High output voltages 	<ul style="list-style-type: none"> • Poor coupling for thin films • Limited mechanical properties • High output impedance • Charge leakage • Low output current • Depolarization • Low coupling for polymers • Fragility of ceramic piezoelectric layers

4 Piezoelectric energy harvesting

4.1 Basics on piezoelectricity

4.1.1 Historic and applications

The root of the word piezo means pressure; hence, the original meaning of the word piezoelectricity is “pressure electricity”, the ability of some materials to develop an electric charge proportional to a mechanical stress [34]. This definition ignores the fact that the piezoelectric effect is reversible, allowing the generation of a deformation proportional to an applied voltage. Piezoelectricity was discovered by Pierre and Jacques Curie in 1880 in single crystals such as Rochelle salt and quartz. It is only in 1946 that scientists discovered that the barium titanate BaTiO_3 is piezoelectric [34]. With its increased sensitivity and higher operating temperature, PbZrTiO_3 (PZT) soon replaced BaTiO_3 in many existing devices and is still the most widely used piezoceramic today. With the apparition of Internet Of Thing (IOT) and because of the brittleness of the piezoceramics, piezoelectric composites and polymers are nowadays more and more studied for instance for wearables because of their flexibility and conformability [35]. However, their properties remain lower than those of the piezoceramics [36]. The piezoceramics can be found in a broad range of applications using either the direct or inverse piezoelectric effect. They are present in every day, for example in cleaning application for jewelry, glasses or teeth using generators of ultrasonic applications, but also in high-end technology markets such as medical technology, semiconductor technology or mechanical and automotive engineering . Some examples of applications are listed below:

- Transducers for sound and ultrasound in air (microphones, intruder alarm system, loudspeakers, etc).
- Sensors (pressure, accelerometers, chemical, ultrasonic sensors for medical applications, etc), Structural Health Monitoring (SHM),
- Actuators, motors, transformers,

Energy harvesting applications are also more and more needed with the growing of this intelligent world surrounding us. For vibration piezoelectric energy harvesters, the direct piezoelectric effect is involved. Basics on piezoelectric effect are given in the next paragraph.

4.1.2 Description and origin of the piezoelectric effect

Figure I-13 illustrates the piezoelectric effect. In the direct piezoelectric effect, also called generator or sensor effect, pressure generates charges on the surface of the piezoelectric materials. The field produced by the applied mechanical stress can be detected as an electric voltage if the piezoelectric body has electrodes. The sign of the voltage depends on the stress, either compressive or tensile. Mechanical energy is converted into electrical energy when considering the direct piezoelectric effect (Figure I-12 (a)). Conversely, the application of an electric field leads to a deformation of the piezoelectric material. This inverse effect also called actuator effect converts electrical energy into mechanical energy or motion (Figure I-12 (b)).

Expansion or contraction of the crystal depends on the polarity. When amplifications by mechanical resonance are not involved, the deformations are very small.

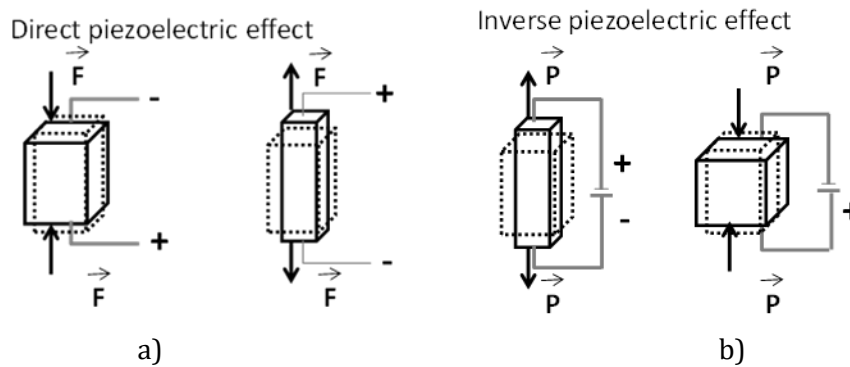


Figure I-13: Schematic of the direct and inverse piezoelectric effect.

The existence of piezoelectricity is due to the lack of a center of symmetry in the unit cell of the crystal. Consequently, as a result of the stress, a net movement of the positive and negative ions with respect to each other produces an electric dipole (polarization). This piezoelectric effect is linear and reversible, and the sign of the produced charge depends on the direction of the stress (tensile or compressive). Figure I-14 illustrates the origin of the piezoelectric effect. The link between piezoelectricity and crystal symmetry has been clearly established. Among the 32 crystallographic classes, 21 do not possess a center of symmetry and 20 of these are piezoelectric. Some piezoelectric crystals, like the quartz only develop the polarization when the force is applied, while others are already polarized without pressure applied. The well-known materials barium titanate (BaTiO_3), lead titanate (PbTiO_3) or lead zirconate titanate (PbZrTiO_3) belong to the family of piezoelectric materials which exhibit reversible polarization: they are ferroelectric materials. However, the spontaneous polarization in polycrystalline materials such as ceramics is random and a polarization process (or “poling” process) is necessary to obtain a macroscopically piezoelectric ceramic. During this process, the domains within grains can orient in the direction of the direct electric field applied at a temperature slightly below the Curie temperature (Figure I-14). A remanent polarization is thus achieved within the polycrystalline material after the removal of the field [37].

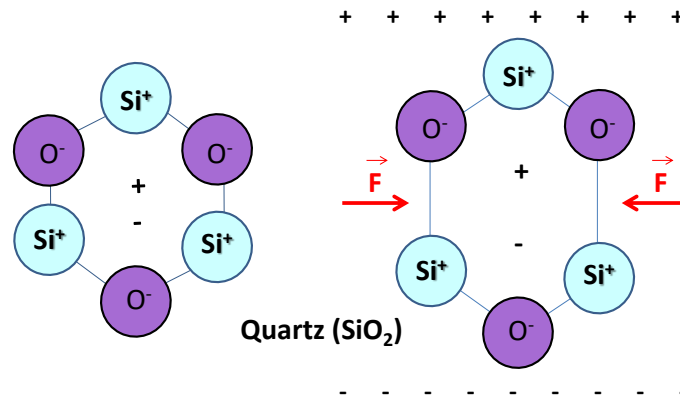


Figure I-14: Origin of the piezoelectric effect in the unit cell of a disc of quartz cut with its normal surfaces normal to the axis of non-symmetry.

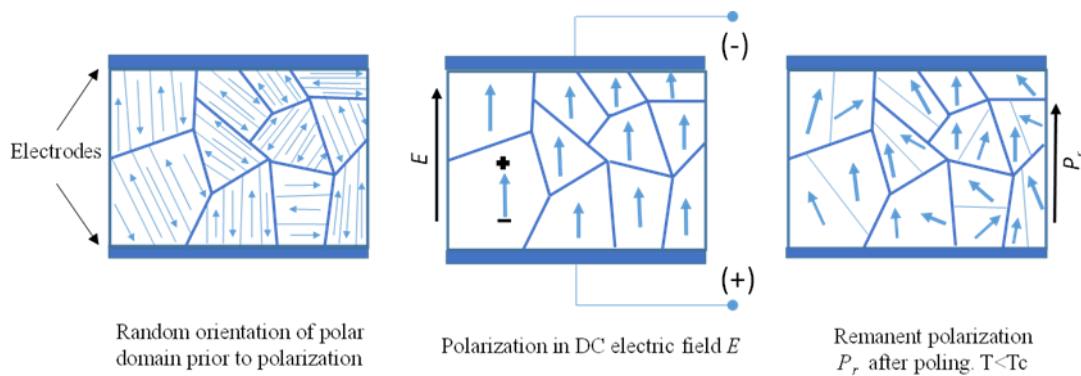


Figure I-15: Polarization principle steps in piezoelectric ceramics.

As previously discussed in section 3.2.3, mechanical characteristics are linked to electrical characteristics through basic relationships (Eq. 1.13 and Eq. 1.14) and whatever direct or inverse piezoelectric effects, the proportionality constant is the piezoelectric constant d . High d piezoelectric coefficient is preferred to develop motion or vibration. When written in tensor form, the piezoelectric coefficients transform as a third rank tensor. The matrix of the piezoelectric coefficients is hence revealing the ceramic symmetry. According to the Neumann’s principle: the symmetry elements of any physical property of a crystal must include the symmetry elements of the point group of this crystal [38]. As an illustration, the matrix of the piezoelectric coefficients in tetragonal crystals ($4mm$ symmetry) is shown in Figure I-15. The “3 direction” is determined as the polarization direction.

$$[d] = \begin{bmatrix} 0 & 0 & 0 & 0 & d_{15} & 0 \\ 0 & 0 & 0 & d_{15} & 0 & 0 \\ d_{31} & d_{31} & d_{33} & 0 & 0 & 0 \end{bmatrix}$$

Figure I-16: Matrix of the piezoelectric coefficients for crystallographic point $4mm$ (tetragonal symmetry), $6mm$ (hexagonal) and ∞m .

4.2 Configurations of piezoelectric energy harvesters

Generally, micro-scale piezoelectric energy harvesters are designed either in a unimorph or bimorph cantilever structure, where electroded piezoelectric films or ceramics are bonded onto the cantilever substrate. In some cases different electrode arrangement i.e. interdigitated electrodes can be also used (Figure I-16 (b-c)) [32]. Due to the symmetry, directions at right angles to the polar axis are equivalent and can be referred as “1” directions. The direction of the applied stress can be either along the polar axis (3-direction) or at right angles to it (1-direction), resulting in two common piezoelectric energy harvesting configurations, 33-mode and 31-mode, as illustrated in Figure I-16 (a). The 33-mode means that the compressive stress/strain is applied parallel to the 3-direction, while the voltage is generated along the same axis. In the 31-mode, the stress/strain is applied perpendicular to the polar axis and the direction of the generated voltage is at the right angle of the applied force [39][40]. The open circuit voltage of the piezoelectric is expressed by:

$$V_{oc} = \frac{d_{ij}}{\epsilon_r \epsilon_0} \sigma_{ij} t \quad (\text{Eq. 1.15})$$

Where d_{ij} is the piezoelectric coefficient, σ_{ij} the mechanical stress, t the distance between electrodes and, ϵ_r and ϵ_0 are the relative dielectric constant and the permittivity of vacuum, respectively. In general the output voltage for the 33-mode energy harvester is expected to be higher than that of the 31-mode ($d_{33} > d_{31}$) [32]. However, 33 mode is not suitable for energy harvester mainly because of limited strain due to high stiffness, and high frequency operation. The 31 mode configuration is hence usually preferred for vibration energy harvesters [30].

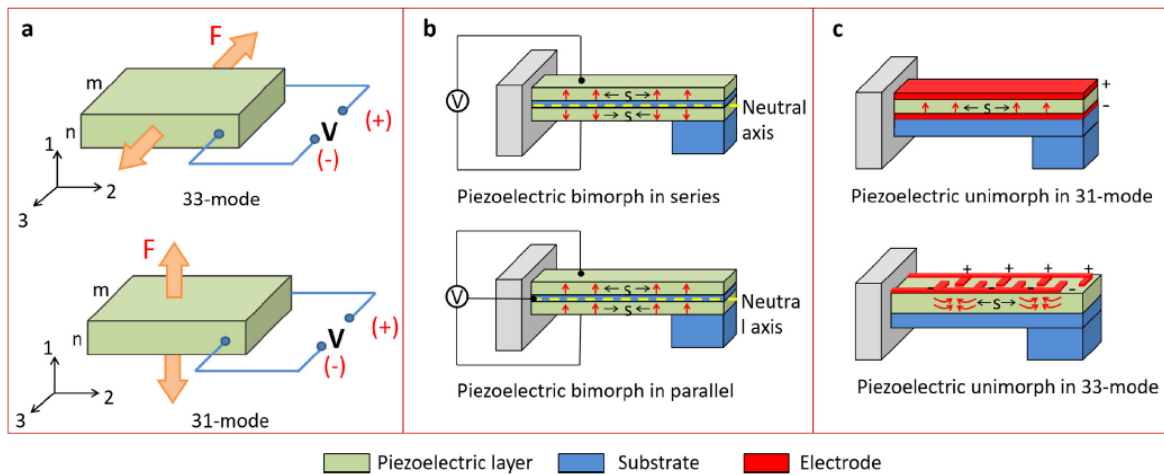


Figure I-17: (a) Piezoelectric material used in the 33-mode and the 31-mode; (b) 31-mode bimorph cantilever in series and parallel connections; and (c) 31-mode and 33-mode unimorph cantilever configuration. (Image from [39])

4.3 Piezoelectric materials properties requirements for energy harvesting

It is obvious that piezoelectric energy harvesting performance depends in a large extend on the properties of the piezoelectric material. Another important characteristic is the squared electromechanical coupling coefficient k^2 . It represents a convenient and direct evaluation of the

ability of the piezoelectric material to convert one form of energy to another. It is defined as follow:

$$k^2 = \frac{\text{mechanical energy stored}}{\text{electrical energy applied}} = \frac{\text{electrical energy stored}}{\text{mechanical energy applied}} \quad (\text{Eq. 1.16})$$

The ways to calculate this electromechanical coupling coefficient in different piezoelectric resonators will be further described in chapter 3.

Even if the electromechanical coupling coefficient indicating the energy conversion ability is a relevant criteria to choose the piezoelectric material, the Figure -of merit (FOM) should be taken into account to compare different materials for energy harvesting applications [33][41]. This FOM applicable for materials, but not for devices, is defined as the electrical energy density divided by the mechanical deformations:

$$FOM = \frac{d^2 Y^2}{\epsilon} = \frac{e^2}{\epsilon} \quad (\text{Eq. 1.17})$$

Where Y is the elastic modulus, ϵ the permittivity (or dielectric constant of the material) and e the piezoelectric stress coefficient of the material.

To get a high FOM, a compromise can be found considering both permittivity values and piezoelectric performances. As an illustration, the FOM of PZT ceramics can be tuned according to the composition and thus the properties. Undoped PZT is rarely used for applications. A range of properties can be obtained by acceptor or donor doping on A and/or B sites of the perovskite ABO_3 . Acceptor-doped PZT (K^+ , Fe^{3+} ,...) are called "hard" PZT due to compensating defects (oxygen vacancies) that stabilize the domain structure which in turn becomes difficult to be reoriented (difficult poling). Donor doped PZT (La^{3+} , Nb^{5+}), on the contrary are compensated by electrons or lead vacancies and are easy to pole. They are called "soft", exhibiting high piezoelectric coefficients, high permittivity and dielectric losses [37]. According to the targeted applications (sensors, actuators, etc...), higher or lower permittivity values may be desired. Table I-3 summarizes the main properties to consider for a piezoelectric material.

Table I-3: Main properties of a piezoelectric material.

Properties	Notation	Units	Meaning
Piezoelectric charging coefficient	d	C/N	Proportion between the generated electrical charges (in Coulomb) and the force applied to the material (in Newton).
Electromechanical coupling coefficient squared	k^2		Efficiency of the material for transduction/conversion of electrical energy into mechanical energy and vice versa.
Dielectric constant (permittivity)	ϵ	F/m	Measurement of the charge storage capacity on a material supplied at a given voltage.
Dielectric dissipation factor	$\tan\delta$	-	Measurement of the dielectric losses.
Curie temperature	T_c	$^{\circ}C$	Temperature at which the material undergoes a structural phase transition

4.4 Energy harvesters based on PZT and metallic substrates

4.4.1 Overview on piezoelectric materials

Inorganic piezoelectric materials have been extensively used in vibration energy harvesting, The most common piezoelectric inorganic materials used are $Pb[Zr_xTi_{1-x}]O_3$ (PZT), ZnO and AlN[3][39] [42]. These piezoelectric materials can be in single crystal (bulk or thin films) or polycrystalline forms (ceramics, thin or thick-films). PZT single-crystal are difficult to grow, but others lead based perovskite can be grown such as $(Pb(Mg,Nb)O_3-PbTiO_3)$ (PMN-PT). They can be sealed on a steel cantilever as shown by Badel *et al* [43]. As a result a 20-fold improvement in harvested power was displayed compared to PZT ceramic.

Ceramics used in energy harvesting application, mostly PZT, are currently thinned to get more flexibility to the energy harvester, and then bonded on the passive substrate, often metallic [3]. For MEMS devices, polycrystalline PZT thin films are currently grown by sol-gel or sputtering on the passive substrate [32][44][45].

Lead-free materials such as AlN and ZnO cannot compete with PZT and this is one of the reasons why PZT is commercialized by companies, and researches focused on PZT based applications are still very active. However lead free perovskite materials for energy harvesting is a hot topic and it is worth noting that among different options, KNN has displayed interesting results in both thin film and ceramic forms [46].

Nanomaterials can be used for the development of stretchable nanogenerators, in particular ZnO, GaN, PZT and $BaTiO_3$ nanowires [47]–[50]. Dahiya *et al.*, presented for instance stretchable piezoelectric nanogenerators for self-powered wearable electronics application, with ZnO nanowires synthesized by hydrothermal method (Figure I-17)[51].

Compared to inorganic piezoelectric materials, piezoelectric polymers, such as PVDF and its copolymer poly (vinylidene fluoride-co-tri-fluoroethylene) (PVDF-TrFE)) are easy for processing

and bio-compatible. As a result they are more suitable for flexible energy harvesting. These polymers can be processed in films or in nanofibers. Persano *et al.*, developed for example a large area, flexible, and freestanding piezoelectric textile composed of highly aligned fibers of P(VDF-TrFE) (Figure I-18) [52].

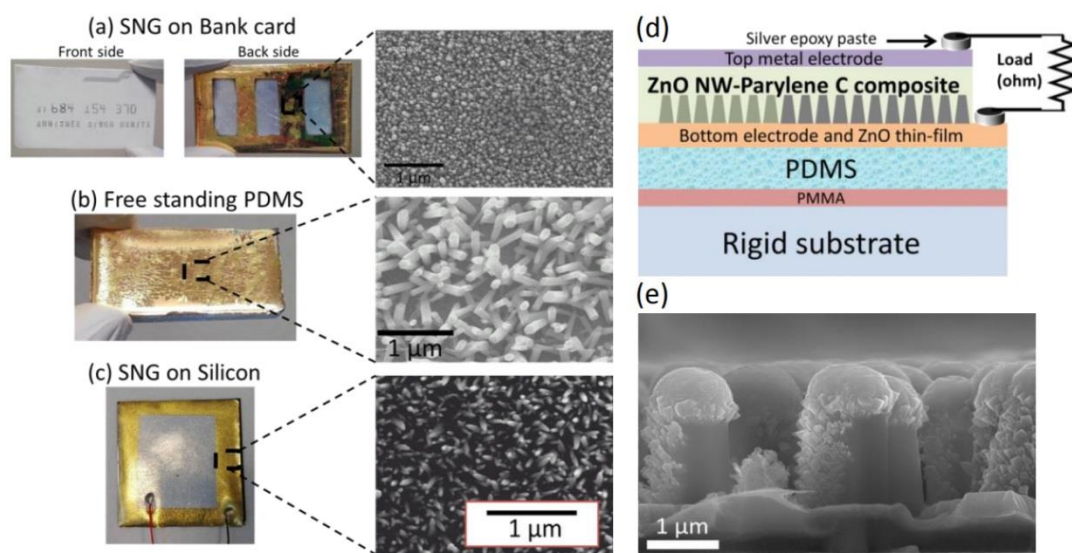


Figure I-18: Proof-of-concept for nanogenerators (SNGs = Stretchable Nano-Generators) using ZnO nanowires (NWs) fabricated on: (a) bank cards, (b) free standing PDMS and (c) silicon substrates. The magnified image in each panel shows the as-grown ZnO NWs on respective substrates. (d) The final device structure and (e) SEM image after parylene C and metal deposition on NWs grown on silicon. (Images from [51])

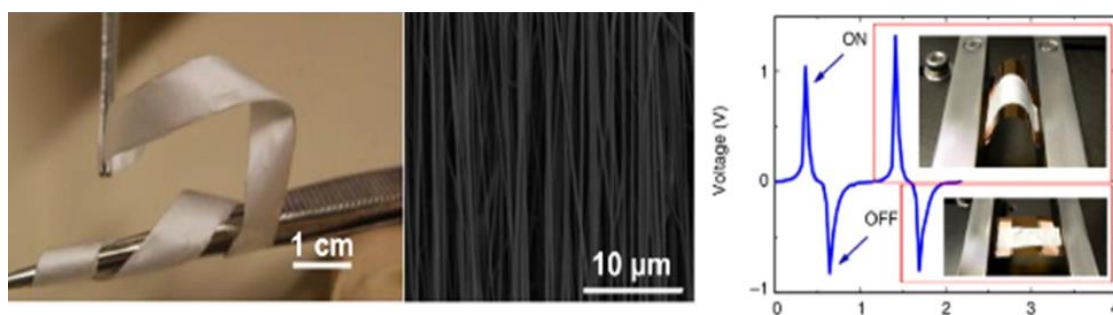


Figure I-19: (left) Photograph and SEM image of a free-standing film of highly aligned P(VDF-TrFE) fibers (right) Open-circuit voltage for the P(VDF-TrFE)-based generator under cycling bending at 1Hz. (Images from [52])

Table I-4 summarizes the properties of the main piezoelectric materials used for energy harvesting applications. Although good piezoelectric properties are required, the ultimate performance of generators devices will not depend only on the material but also on the complete material/structure assembly system and on the chosen technological processes.

Table I-4: Summary of piezoelectric materials used for energy harvesting applications.

Materials		Structure	Piezo coefficient	Reference
Inorganic	ZnO	Nanowires	$d_{33} \sim 5-10$ pC/N	[48][50]
	BaTiO ₃	Thin film	$d_{33} \sim 190$ pC/N	[53][54]
	AlN	Thin film	$d_{33} \sim 5$ pC/N	[55]
	PZT	Thin film	$d_{33} \sim 250-700$ pC/N	[56]
	KNN	Thin film	$d_{33} \sim 90$ pC/N	[57]
Polymer	PVDF	Fabric	$d_{33} \sim 20-30$ pC/N	[52]
	PET-based	Thin Film	$d_{33} \sim 630$ pC/N	[58]

4.4.2 Micro-fabrication technologies for energy harvesting MEMS

An important aspect when developing energy harvesting devices concerns the deposition and patterning of the piezoelectric materials with high crystalline quality and controlled morphology. Piezoelectric thin deposition usually refers to silicium techniques including several deposition techniques such as: sol-gel, sputtering, epitaxial growth, laser ablation processes, etc. The piezoelectric PZT is the most largely used combined with the use of silicon on insulator (SOI) wafer or bare silicon. The unimorph microcantilever design in the 31-mode with a proof mass is by far the most employed structure, due to its simplicity and very good sensitivity. Figure I-20 shows the process developed by Liu *et al.* where a silicon based microcantilever including a polycrystalline PZT sol-gel thin film is fabricated [39]. For 31-mode energy harvesting applications, the choice of the bottom electrode will influence the crystalline texture, the quality, and properties of the piezoelectric film. PZT/Pt/Ti/SiO₂/Si is the most widely applied deposition sequence, where a homogeneous (111) texture of the platinum (Pt) is commonly used to obtain a homogeneous nucleation of the same perovskite orientation [59]. The titanium (Ti) is used as an adhesion layer and additionally it plays an important role in the diffusion phenomena [60]. Also, with this sol-gel process used for PZT deposition, layer of μm thickness needs tens of monolayers deposition.

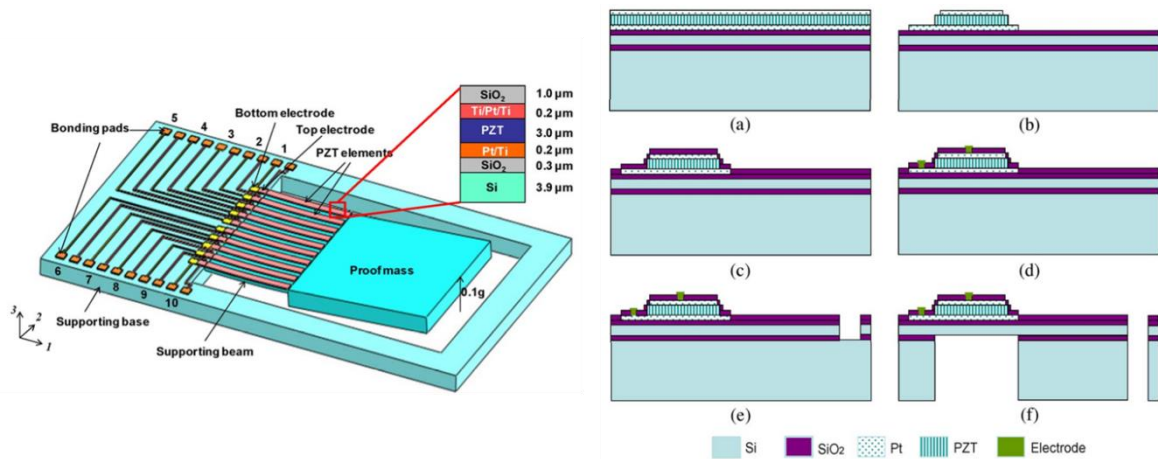


Figure I-20: In this process, the Pt/Ti top and bottom electrodes are deposited by DC magnetron sputtering on a SOI wafer and are etched with Ar ions. A $\text{Pb}(\text{Zr}_{0.52}\text{Ti}_{0.48})\text{O}_3$ film of $2.5\mu\text{m}$ -thick is deposited in between the electrodes by sol-gel method and a chemical etching is carried out to ensure its microstructuration (mixture of HF, HNO_3 , and HCl). The micro-cantilever structures are finally obtained by RIE/DRIE (Deep Reactive Ions Etching) process of Si or SiO_2 (front or backside etching). (Images from [39])

Piezoelectric thick films with high piezoelectric coefficients are advantageous to improve the output performances. Thick piezoelectric layers with thicknesses ranging from 10 to $100\mu\text{m}$ can be obtained by different deposition techniques: screen-printing, sol-gel process, electrophoretic deposition, tape-casting, or aerosol deposition [2][4][61]. Most of the piezoelectric energy harvesters with thick films are reported on a Si substrate [62]–[65]. However Si substrate can be easily broken and presents limitations such as low vibration amplitudes [3]. Flexible and compliant piezoelectric energy harvesters are more and more studied to overcome the brittleness and rigidity of the substrate and/or the piezoelectric materials. There are several feasible approaches aiming to address this requirement, such as the use of organic piezoelectric materials [66], thin films growth on flexible substrates [67], [68], nanowires growth on flexible substrates [51][69], [70], and “pattern-transfer” methods (i.e., first growing and/or patterning films on rigid substrates, and then transferring the patterns to plastic substrates) are some of the proposed options. The growth transfer process is considered to be one of the most common approach for the flexible piezoelectric energy harvesters. They can be achieved by transferring high piezoelectric perovskite thin films from rigid substrates to flexible organic ones using the soft-lithographic technique, laser lift-off process, or solution-based sacrificial layer methods. Park et al [67] presented the concept of the laser lift-off based growth-pattern-transfer process for the piezoelectric thin-film energy harvester (Figure I-21). The final PZT thin film NanoGenerator (NG) on a single thin plastic substrate converts a high-output performance of $\sim 200\text{ V}$ and $\sim 150\mu\text{A}\cdot\text{cm}^{-2}$ from the slight mechanical deformations. The short-circuit current generated from a large-area NG ($3.5\text{ cm} \times 3.5\text{ cm}$) reached up to $\sim 8\mu\text{A}$.

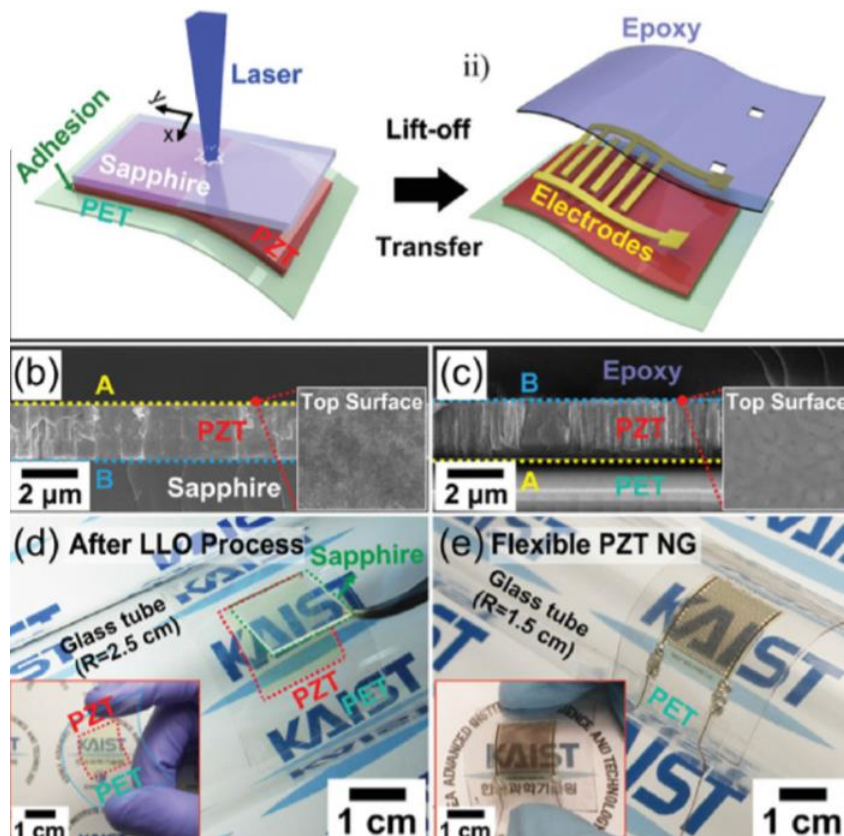


Figure I-21: (a) Scheme diagram of the fabrication process for a high-efficient, flexible, and large-area PZT thin film-based NanoGenerator (NG) using the Laser Lift Off method (LLO) on flexible PET plastic substrate. (b,c) The cross-sectional SEM images of PZT thin films on a sapphire (b) and a PET substrate (c). (d) A PZT thin film (1.5 cm \times 1.5 cm) on a PET substrate being detached from a sapphire substrate after LLO process. The inset shows the PZT thin film on a flexible substrate bent by human fingers. (e) The final flexible PZT thin film NG attached to a glass tube and bent by human fingers (the inset). (Images from [67])

The design of the devices and the chosen process depend on the required performances for a given application (frequency, acceleration, required power) and on the expected costs. Alternative processes are thus proposed. In particular thicker piezoelectric layers combined with flexible substrates (for instance metallic substrates) may be nowadays preferred to achieve higher power. Here, because of application requirements for this thesis work (flexibility, mechanical reliability, low cost, good integration), the energy harvester to develop is based on a metallic substrate with PZT thick-film. In the following section examples of EH using metallic substrates and/or PZT thick-films are hence shown.

4.4.3 Metallic substrate based energy harvesting devices

Common piezoelectric EH are millimeter size cantilevers, unimorph or bimorph with two pieces of bulk piezoelectric material sandwiching a metallic stainless substrate [30]. Thinning of the bulk bonded ceramic is moreover proposed to bridge the 1 to 100 μm gap which lies between bulk and thin film components. Once thinned, these bulk ceramics can be micro-structured on metallic supports [71], but also on silicon substrates as reported by Aktakka *et al*, 2011 [63]. With a bimorph harvester with a 50 μm PZT layer of thinned bulk ceramic reported on a stainless substrate (Figure I-22 (a)), Colin *et al* measured 3 μW at very low frequency (15Hz) and

under a 10mg acceleration, demonstrating the efficiency of such piezoelectric energy harvester[71].

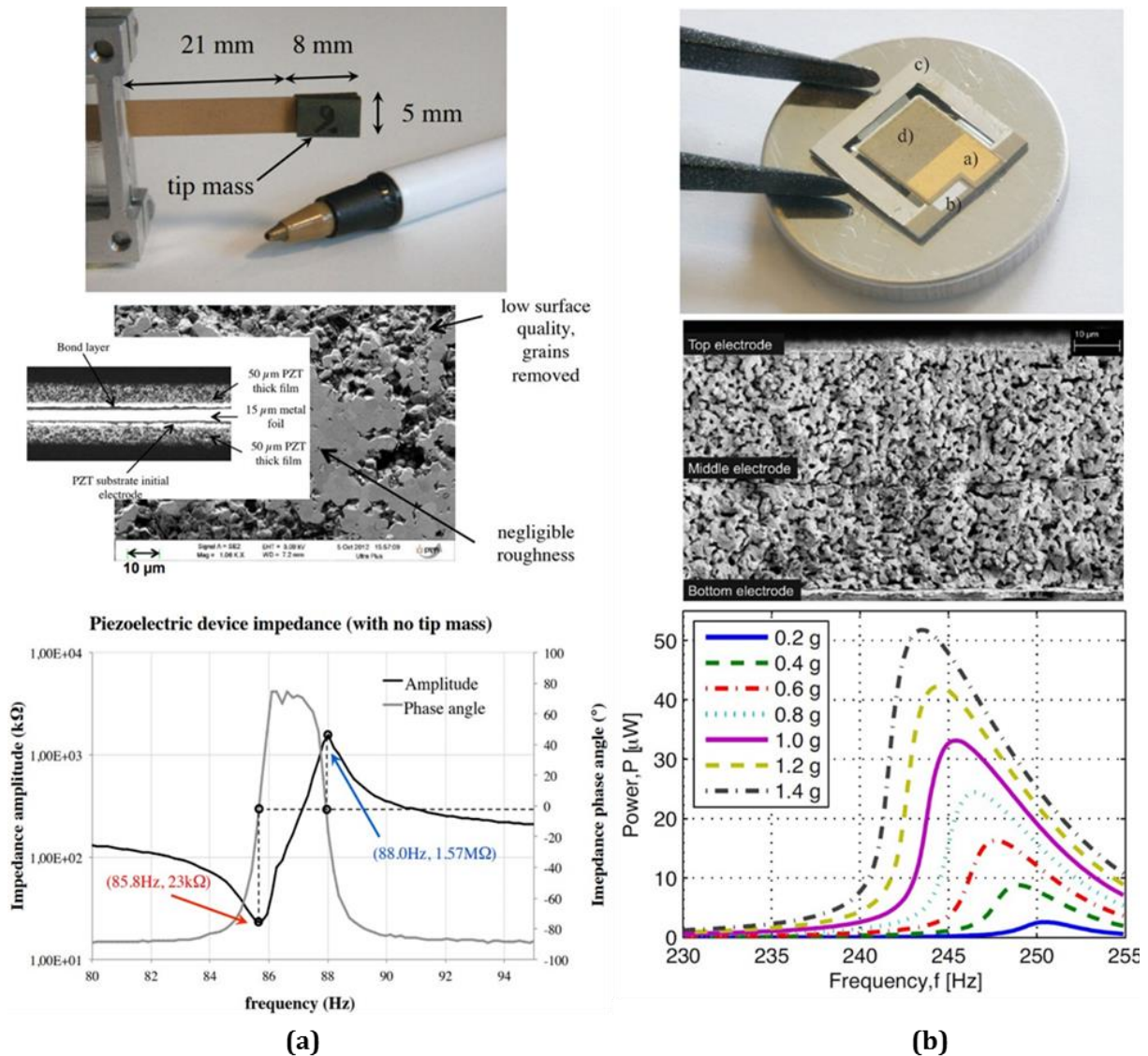


Figure I-22: Examples of bimorph piezoelectric vibration energy harvesters (EH), photograph, microstructure and electrical characterization, (a) thinned bulk PZT assembled on SS substrate [71], (b) screen-printed PZT EH [4].

These processes require additional micromachining, grinding and/or polishing of the bulk ceramics which needs finally to be manually assembled. An interesting alternative is the use of thick-film processes to fabricate the PZT transducer (screen-printing, sol-gel process, electrophoretic deposition, tape-casting or aerosol deposition). For instance, screen-printed piezoelectric thick-films implemented on stainless steel platforms have been shown to deliver power of $\sim 240 \mu\text{W}$ harvested at 66.2 Hz with an acceleration of $g = 2.8 \text{ m.s}^{-2}$ (0.3g) [72]. With the same acceleration, free-standing piezoelectric thick-films (bimorph structure) fabricated on a silicon sacrificial substrate provide $\sim 3 \mu\text{W}$ at 250 Hz though power of $\sim 50 \mu\text{W}$ is measured at 242 Hz for $g = 13.7 \text{ m.s}^{-2}$ (1.4g) [4]. Figure I-21 (b) shows the different harvested powers obtained under acceleration varying from 0.2g to 1.4g. Here, despite an additional high pressure step

(100-200MPa) before the sintering (1 hour at 850°C), the screen-printed PZT layers show average apparent porosity of 20%. Denser PZT layers can be deposited on metallic substrate through aerosol technique. For instance Lin et al deposited PZT thick-film directly on a stainless-steel substrate by aerosol deposition method at room temperature (Figure I-23 (a)) [73]. The obtained PZT thick-film showed excellent adhesion (Figure I-23(b)) and ferroelectric properties. For this EH having a volume of 13 mm³, a maximum output power of 200μW (12.658 Vp-p) could be measured with a 1.5g acceleration level and at an excitation frequency of 112.4 Hz (Figure I-22(c)).

For piezoelectric energy harvesting, stainless steel (SS) substrate is so far the most popular metallic substrate because of its relatively low Young's modulus. Other metallic substrates are also studied such as brass, copper, nickel or aluminum [61][74]. Performances of some selected vibration piezoelectric EH using metallic substrates (SS substrate mainly) can be compared in Table I-6. The different materials and technologies or processing (piezoelectric layer, substrate, proof mass) are detailed.

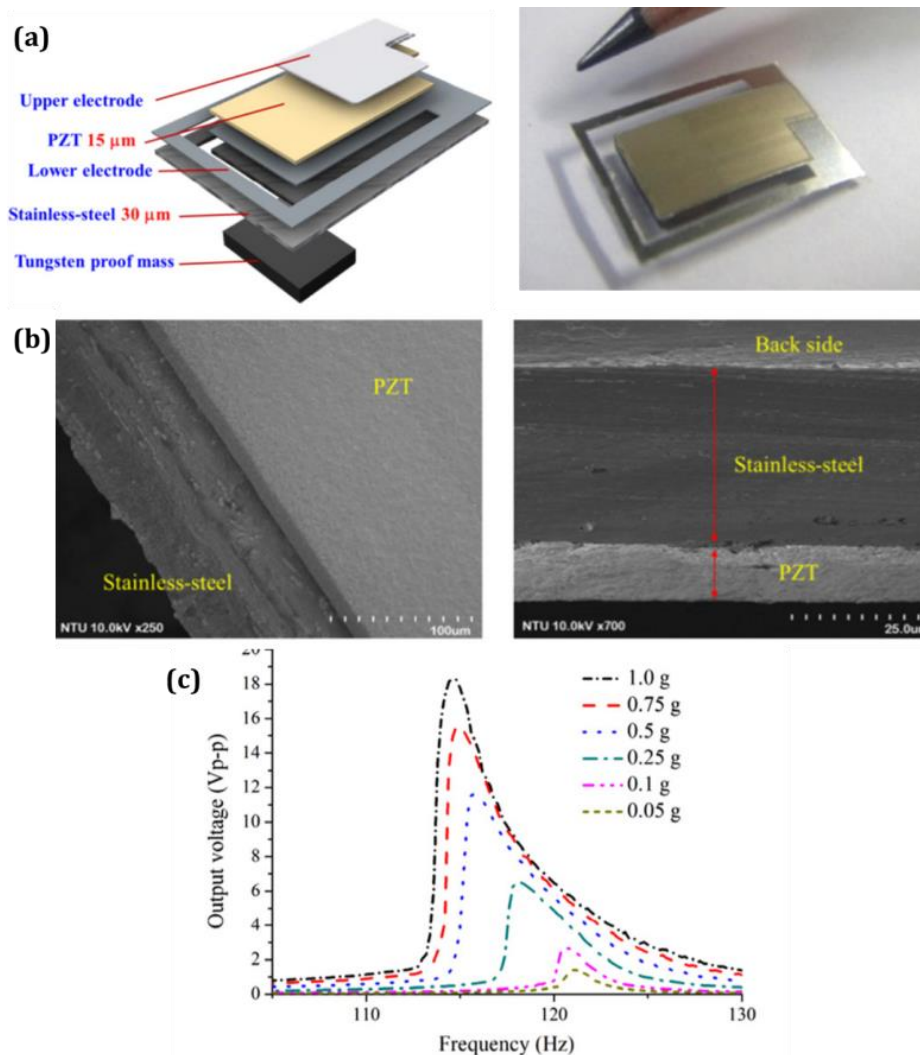


Figure I-23: (a) Micro-generators structure fabricated through aerosol, (b) SEM photograph of the PZT layer after deposition (sidewall of the PZT layer and cross-sectional view of the cantilever-beam), and (c) Experimental results of the output voltage versus excitation frequency under the open circuit conditions at different accelerations. (Images from [73])

Table I-6: Examples of performances of resonant piezoelectric cantilever type energy harvesters using different technologies

Multilayer / proof mass	Deposition piezoelectric layer technology	EH volume	Frequency/ acceleration (1g= 9.8m/s ²)	Power	References
Bimorph PZT/100µm brass/PZT// Tungsten proof mass 9.15g	PZT-5H Bulk – 280µm	1cm ³	120Hz / 0.25g	375µW	[30]
PZTAuIn/10µmSi // Tungsten proof mass 328mg	Thinned bulk PZT 20µm	7x7x0,55 mm ³	154Hz/1.5g	205µW	[63]
Bimorph Ag/PZT/Au/dielectric/110µmSS/dielectric/Au/PZT/Ag // Tungsten proof mass 3.1g	Screen-printed PZT-5H / 70µm	491mm ³	67Hz/ 0.4g	240µW	[72]
Bimorph/TiPt/PZT/TiPt/PZT/Au // Tungsten proof mass Si	Screen-printed PZT (PZ26) 20µm	0.64mm ³	242Hz /1g	33.2µW	[4]
SUS304/Pt/Ti/PZT/Al// not reported	Sol gel PZT thin film 4µm	167.6mm ³	89Hz/1g	15µW	[75]
Bimorph PZT/ Stainless steel 15µm/PZT // Tungsten proof mass 1.5 g	Thinned bulk PZT 50µm	5 x 40 mm ² x 115µm	16Hz/10mg	3µW	[71]
Pt/Ti/PZT/SS30µm// Tungsten proof mass 6x4x0,45mm ³ (0.2g)	Aerosol deposition 15µm	13 mm ³	112.4Hz / 1.5g	200µW	[73]
SS300µm/Pt/Ti/KNN/Pt// SS proof mass 25mg	KNN RF Sputtering 2.2µm PZT RF Sputtering -	7.5 x 5mm ² x 2.2µm	393Hz/1g 367Hz/ 1g	1.6µW 6.7µW	[76]
Bimorph PtTi/PZT/PtTi SS60µm/PtTi/PZT/PtTi// Tungsten proof mass 0.46g	Aerosol deposition 10µm	6x8mm ² x 80µm	120Hz/0,5g	304µW	[77]
Ni 25µm/ LaNiO ₃ /HfO ₂ /Ni//PZT /Pt // Brass proof mass 0.4g	PZT RF Sputtering 3µm	0.1155m m ³	72Hz/ 0,5g	60µW	[74]

5 Conclusion

In general, energy harvesting offers significant advantages and opportunities for the development of smart applications (smart cities, smart homes, smart health, smart agriculture, intelligent transportation, industry, security, marine, and so on). It is a promising option for creating an enhanced class of autonomous self-powered terminal nodes that can operate for much longer periods of time without the need of battery charges. It can also induce cost savings by significantly delaying battery replacement and the energy harvesting solutions can further increase the robustness in all IoTs applications.

MEMS piezoelectric energy harvesters at the $\sim\text{mm}^3$ dimensions can lead to battery-less autonomous sensors systems and networks if 10-100 μW of power can be extracted from the ambient vibration continuously, robustly and at low cost. Various types of harvester configurations, piezoelectric materials, and fabrication techniques have been explored. However, the domain of MEMs energy harvesting still faces some challenges as for instance the use of new kind of materials (organic or bio piezoelectric [78]) or processes. Also, a large number of approaches have been proposed to enhance the power output and broaden the working frequency bandwidth: These approaches concern the:

- Nature and processing of the active material to increase its properties (densification optimization for instance for PZT layers as seen in this state of art).
- Nature of the passive substrate: Tendency for flexible substrates with good mechanical reliability and wearable applications. Substrates with better thermo-mechanical compatibility with the active material for ensuring high-quality of the structure interfaces [79][80].
- Structure design: complex geometries have been explored to reduce resonant frequencies and increase strain [3][81]. Multi-frequency harvesting are also found, these one aim to achieve multiple resonant frequency in order to broaden the operating range by structure, geometries, and number of spring-mass hierarchies modifications [27]
- Hybrid mechanism: structures using more than one transduction mechanism piezoelectric- electromagnetic, piezoelectric - electrostatic [82][27], or using combined different sources, i.e. solar – vibrations [27]

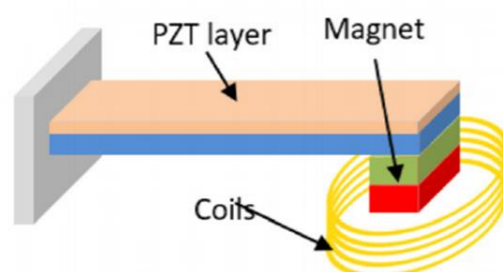


Figure I-24: A typical hybrid VEH configuration integrated with piezoelectric and electromagnetic mechanisms. (Image from [39])

- Non-linear harvesting mechanism : different dynamic response that increases the frequency bandwidth by hardening or softening the resonance characteristics of the beam structure [83]
- Electrical circuit design: used for both increasing power output and broadening the frequency bandwidth [29].

In the frame work of this thesis work, the two approaches explored for power enhancements will be the geometry design, and the active material processing. Furthermore the hybrid piezo-electromagnetic mechanism will be explored.

References

- [1] A. P. Chandrakasan and R. W. Brodersen, *Low Power Digital CMOS Design*. Springer Nature, 1995.
- [2] A. Lei et al., "MEMS-based thick-film PZT vibrational energy harvester," *Proc. IEEE Int. Conf. Micro Electro Mech. Syst.*, pp. 125–128, 2011.
- [3] S. Priya et al., "A Review on Piezoelectric Energy Harvesting: Materials, Methods, and Circuits," *Energy Harvest. Syst.*, vol. 4, no. 1, pp. 3–39, 2017.
- [4] R. Xu et al., "Screen printed PZT/PZT thick-film bimorph MEMS cantilever device for vibration energy harvesting," *Sensors Actuators, A Phys.*, vol. 188, pp. 383–388, 2012.
- [5] S. Priya and D. J. Inman, *Energy Harvesting Technologies*, 1st ed. Springer Publishing Company, Incorporated, 2008.
- [6] K.-H. Chen, *Power Management Techniques for Integrated Circuit Design*. 2016.
- [7] L. Mateu and F. Moll, "Review of energy harvesting techniques and applications for microelectronics," in *Proc.SPIE*, 2005, vol. 5837.
- [8] W. Greenbank, L. Hirsch, G. Wantz, and S. Chambon, "Interfacial thermal degradation in inverted organic solar cells," *Appl. Phys. Lett.*, vol. 107, p. 263301, Dec. 2015.
- [9] D. Patel and P. S. B. Mehta, "Review of Thermoelectricity to Improve Energy Quality," *Int. J. Emerg. Technol. Innov. Res.*, vol. 2, no. 3, p. 847, 2015.
- [10] F. U. Khan and Izhar, "State of the art in acoustic energy harvesting," *J. Micromechanics Microengineering*, vol. 25, no. 2, p. 23001, 2015.
- [11] B. Li, A. J. Laviage, J. H. You, and Y. J. Kim, "Acoustic energy harvesting using quarter-wavelength straight-tube resonator," *ASME Int. Mech. Eng. Congr. Expo. Proc.*, vol. 12, pp. 467–473, 2012.
- [12] N. S. Shenck and J. A. Paradiso, "Energy scavenging with shoe-mounted piezoelectrics," *IEEE Micro*, vol. 21, no. 3, pp. 30–42, 2001.
- [13] D. Steingart, "Power Sources for Wireless Sensor Networks BT - Energy Harvesting Technologies," S. Priya and D. J. Inman, Eds. Boston, MA: Springer US, 2009, pp. 267–286.
- [14] S. P. Beeby and T. O'Donnell, *Electromagnetic energy harvesting*. 2009.
- [15] C. B. Williams and R. B. Yates, "Analysis Of A Micro-electric Generator For Microsystems," in *Proceedings of the International Solid-State Sensors and Actuators Conference - TRANSDUCERS '95*, 1995, vol. 1, pp. 369–372.
- [16] S. Roundy, P. K. Wright, and J. Rabaey, "A study of low level vibrations as a power source for wireless sensor nodes," *Comput. Commun.*, vol. 26, no. 11, pp. 1131–1144, 2003.
- [17] M. Kurvey and A. Kunte, *RF Energy Harvesting System*. 2018.
- [18] C. Cepnik, R. Lausecker, and U. Wallrabe, "Review on electrodynamic energy harvesters-a classification approach," *Micromachines*, vol. 4, no. 2, pp. 168–196, 2013.
- [19] S. Roundy, P. K. Wright, and K. S. J. Pister, "Micro-electrostatic vibration-to-electricity converters," *ASME Int. Mech. Eng. Congr. Expo. Proc.*, no. January 2014, pp. 487–496, 2002.
- [20] H. A. Sodano, D. J. Inman, and G. Park, "A review of power harvesting from vibration using piezoelectric materials," *Shock Vib. Dig.*, vol. 36, no. 3, pp. 197–205, 2004.
- [21] L. Wang and F. G. Yuan, "Vibration energy harvesting by magnetostrictive material," *Smart Mater. Struct.*, vol. 17, no. 4, 2008.
- [22] T. J. Kamierski and S. Beeby, *Energy Harvesting Systems: Principles, Modeling and Applications*, 1st ed. Springer Publishing Company, Incorporated, 2010.
- [23] R. Amirtharajah and A. P. Chandrakasan, "Self-powered signal processing using vibration-

- based power generation," *IEEE J. Solid-State Circuits*, vol. 33, no. 5, pp. 687–695, 1998.
- [24] S. Beeby, M. Tudor, R. Torah, S. Roberts, T. O'Donnell, and S. Roy, "Experimental comparison of macro and micro scale electromagnetic vibration powered generators," *Microsyst. Technol.*, vol. 13, pp. 1647–1653, Jan. 2007.
- [25] P. Basset, D. Galayko, A. M. Paracha, F. Marty, A. Dudka, and T. Bourouina, "A batch-fabricated and electret-free silicon electrostatic vibration energy harvester," *J. Micromechanics Microengineering*, vol. 19, no. 11, p. 115025, 2009.
- [26] T. Genda, S. Tanaka, and M. Esashi, *High power electrostatic motor and generator using electrets*. 2003.
- [27] C. Lagomarsini, C. Jean-Mistral, G. Lombardi, and A. Sylvestre, "Hybrid piezoelectric-electrostatic generators for wearable energy harvesting applications," *Smart Mater. Struct.*, vol. 28, no. 3, Feb. 2019.
- [28] M. Renaud, K. Karakaya, T. Sterken, P. Fiorini, C. Van Hoof, and R. Puers, "Fabrication, modelling and characterization of MEMS piezoelectric vibration harvesters," *Sensors Actuators A Phys.*, vol. 145–146, pp. 380–386, 2008.
- [29] Z. Yang, S. Zhou, J. Zu, and D. Inman, "High-Performance Piezoelectric Energy Harvesters and Their Applications," *Joule*, vol. 2, no. 4, pp. 642–697, 2018.
- [30] S. Roundy and P. K. Wright, "A piezoelectric vibration based generator for wireless electronics," *Smart Mater. Struct.*, vol. 13, no. 5, pp. 1131–1142, 2004.
- [31] E. Reilly and L. Miller, "A study of ambient vibrations for piezoelectric energy conversion," *Proc. Power*, pp. 312–315, 2009.
- [32] B. S. Lee, S. C. Lin, W. J. Wu, X. Y. Wang, P. Z. Chang, and C. K. Lee, "Piezoelectric MEMS generators fabricated with an aerosol deposition PZT thin film," *J. Micromechanics Microengineering*, vol. 19, no. 6, p. 65014, 2009.
- [33] S. Roundy, "Energy Scavenging for Wireless Sensor Nodes with a Focus on Vibration to Electricity Conversion," Jan. 2003. Thesis report.
- [34] B. Jaffe, W. R. Cook, and H. Jaffe, "Chapter I - Historical introduction," in *Piezoelectric Ceramics*, B. Jaffe, W. R. Cook, and H. Jaffe, Eds. Academic Press, 1971, pp. 1–5.
- [35] W. Zeng, L. Shu, Q. Li, S. Chen, F. Wang, and X.-M. Tao, "Fiber-Based Wearable Electronics: A Review of Materials, Fabrication, Devices, and Applications," *Adv. Mater.*, vol. 26, no. 31, pp. 5310–5336, Aug. 2014.
- [36] S. Tadigadapa and K. Mateti, "Piezoelectric MEMS Sensors: State-of-the-Art and Perspectives," *Meas. Sci. Technol.*, vol. 20, p. 92001, Jul. 2009.
- [37] D. Damjanovic, "Ferroelectric, dielectric and piezoelectric properties of ferroelectric thin films and ceramics," *Reports Prog. Phys.*, vol. 61, no. 9, pp. 1267–1324, 1998.
- [38] R. E. Newnham and R. E. Newnham, *Properties of Materials: Anisotropy, Symmetry, Structure*. OUP Oxford, 2005.
- [39] H. Liu, J. Zhong, C. Lee, S. W. Lee, and L. Lin, "A comprehensive review on piezoelectric energy harvesting technology: Materials, mechanisms, and applications," *Appl. Phys. Rev.*, vol. 5, no. 4, 2018.
- [40] J. J. Bernstein et al., "Advanced MEMS ferroelectric ultrasound 2D arrays," in *1999 IEEE Ultrasonics Symposium. Proceedings. International Symposium (Cat. No.99CH37027)*, 1999, vol. 2, pp. 1145–1153 vol.2.
- [41] R. Elfrink et al., "Vibration energy harvesting with aluminum nitride-based piezoelectric devices," *J. Micromechanics Microengineering*, vol. 19, no. 9, 2009.
- [42] H. S. Kim, J.-H. Kim, and J. Kim, "A Review of Piezoelectric Energy Harvesting Based on Vibration," *Int. J. Precis. Eng. Manuf.*, vol. 12, Dec. 2011.

- [43] A. Badel, A. Benayad, E. Lefeuvre, L. Lebrun, C. Richard, and D. Guyomar, "Single crystals and nonlinear process for outstanding vibration-powered electrical generators," *IEEE Trans. Ultrason. Ferroelectr. Freq. Control*, vol. 53, no. 4, pp. 673–684, 2006.
- [44] P. Muralt, M. Marzencki, B. Belgacem, F. Calame, and S. Basrour, "Vibration Energy Harvesting with PZT Micro Device," *Procedia Chem.*, vol. 1, no. 1, pp. 1191–1194, 2009.
- [45] K. Morimoto, I. Kanno, K. Wasa, and H. Kotera, "High-Efficiency Piezoelectric Energy Harvesters of c-Axis-Oriented Epitaxial PZT Films Transferred Onto Stainless Steel Cantilevers," *Sensors Actuators A Phys.*, vol. 163, pp. 428–432, Sep. 2010.
- [46] M. Bah, F. Giovannelli, R. Retoux, J. Bustillo, E. Le Clezio, and I. Monot-Laffez, "Crystal Growth and Piezoelectric Properties of Lead-free Based $K_{0.5}Na_{0.5}NbO_3$ by the Floating Zone Method," *Cryst. Growth Des.*, vol. 16, no. 1, pp. 315–324, Jan. 2016.
- [47] R. Yang, Y. Qin, L. Dai, and Z. L. Wang, "Power generation with laterally packaged piezoelectric fine wires," *Nat. Nanotechnol.*, vol. 4, no. 1, pp. 34–39, 2009.
- [48] G. Zhu, A. C. Wang, Y. Liu, Y. Zhou, and Z. L. Wang, "Functional Electrical Stimulation by Nanogenerator with 58 V Output Voltage," *Nano Lett.*, vol. 12, no. 6, pp. 3086–3090, Jun. 2012.
- [49] S. N. Cha et al., "Sound-Driven Piezoelectric Nanowire-Based Nanogenerators," *Adv. Mater.*, vol. 22, no. 42, pp. 4726–4730, Nov. 2010.
- [50] Y. Qi, N. T. Jafferis, K. Lyons, C. M. Lee, H. Ahmad, and M. C. McAlpine, "Piezoelectric Ribbons Printed onto Rubber for Flexible Energy Conversion," *Nano Lett.*, vol. 10, no. 2, pp. 524–528, Feb. 2010.
- [51] A. S. Dahiya et al., "Zinc oxide nanowire-parylene nanocomposite based stretchable piezoelectric nanogenerators for self-powered wearable electronics," *J. Phys. Conf. Ser.*, vol. 1052, p. 12028, 2018.
- [52] L. Persano et al., "High performance piezoelectric devices based on aligned arrays of nanofibers of poly(vinylidene fluoride-co-trifluoroethylene)," *Nat. Commun.*, vol. 4, pp. 1610–1633, 2013.
- [53] K.-I. Park et al., "Piezoelectric $BaTiO_3$ Thin Film Nanogenerator on Plastic Substrates," *Nano Lett.*, vol. 10, no. 12, pp. 4939–4943, Dec. 2010.
- [54] Y. Qi and M. C. McAlpine, "Nanotechnology-enabled flexible and biocompatible energy harvesting," *Energy Environ. Sci.*, vol. 3, no. 9, pp. 1275–1285, 2010.
- [55] F. Stoppel, C. Schröder, F. Senger, B. Wagner, and W. Benecke, "AlN-based piezoelectric micropower generator for low ambient vibration energy harvesting," *Procedia Eng.*, vol. 25, pp. 721–724, 2011.
- [56] G.-T. Hwang et al., "Self-Powered Wireless Sensor Node Enabled by an Aerosol-Deposited PZT Flexible Energy Harvester," *Adv. Energy Mater.*, vol. 6, no. 13, p. 1600237, Jul. 2016.
- [57] S. S. Won et al., "Lead-free Mn-doped $(K_{0.5},Na_{0.5})NbO_3$ piezoelectric thin films for MEMS-based vibrational energy harvester applications," *Appl. Phys. Lett.*, vol. 108, no. 23, p. 232908, Jun. 2016.
- [58] J. Zhong et al., "Flexible PET/EVA-based piezoelectret generator for energy harvesting in harsh environments," *Nano Energy*, vol. 37, pp. 268–274, 2017.
- [59] D. Vijay and S. Desu, "Electrodes for $PbZr_xTi_{1-x}O_3$ Ferroelectric Thin Films," *J. Electrochem. Soc. - J Electrochem SOC*, vol. 140, pp. 2640–2645, Sep. 1993.
- [60] T. Maeder, L. Sagalowicz, and P. Muralt, "Stabilized Platinum Electrodes for Ferroelectric Film Deposition Using Ti, Ta and Zr Adhesion Layers," *Jpn. J. Appl. Phys.*, vol. 37, Apr. 1998.
- [61] T. Monin et al., "First experimental demonstration of a Self-Oscillating Fluidic Heat Engine

- (SOFHE) with piezoelectric power generation,” *J. Phys. Conf. Ser.*, vol. 773, p. 12039, Nov. 2016.
- [62] E. E. Aktakka, R. L. Peterson, and K. Najafi, “A self-supplied inertial piezoelectric energy harvester with power-management IC,” in *2011 IEEE International Solid-State Circuits Conference*, 2011, pp. 120–121.
- [63] E. E. Aktakka, R. L. Peterson, and K. Najafi, “Thinned-PZT on SOI process and design optimization for piezoelectric inertial energy harvesting,” *16th Int. Solid-State Sensors, Actuators Microsystems Conf. Beijing*, pp. 1649–1652, 2011.
- [64] E. E. Aktakka, R. L. Peterson, and K. Najafi, “Wafer-Level Integration of High-Quality Bulk Piezoelectric Ceramics on Silicon,” *IEEE Trans. Electron Devices*, vol. 60, no. 6, pp. 2022–2030, 2013.
- [65] K. Tanaka, T. Konishi, M. Ide, and S. Sugiyama, “Wafer bonding of lead zirconate titanate to Si using an intermediate gold layer for microdevice application,” *J. Micromechanics Microengineering*, vol. 16, no. 4, pp. 815–820, 2006.
- [66] S. Guerin, S. A. M. Tofail, and D. Thompson, “Organic piezoelectric materials: milestones and potential,” *NPG Asia Mater.*, vol. 11, no. 1, p. 10, 2019.
- [67] K.-I. Park et al., “Highly-Efficient, Flexible Piezoelectric PZT Thin Film Nanogenerator on Plastic Substrates,” *Adv. Mater.*, vol. 26, no. 16, pp. 2514–2520, Apr. 2014.
- [68] C. K. Jeong et al., “Self-powered fully-flexible light-emitting system enabled by flexible energy harvester,” *Energy Environ. Sci.*, vol. 7, no. 12, pp. 4035–4043, 2014.
- [69] K. Y. Lee et al., “P-Type Polymer-Hybridized High-Performance Piezoelectric Nanogenerators,” *Nano Lett.*, vol. 12, no. 4, pp. 1959–1964, Apr. 2012.
- [70] Z. L. Wang, “Towards Self-Powered Nanosystems: From Nanogenerators to Nanopiezotronics,” *Adv. Funct. Mater.*, vol. 18, no. 22, pp. 3553–3567, Nov. 2008.
- [71] M. Colin, S. Basrour, L. Rufer, C. Bantignies, and A. Nguyen-Dinh, “Highly efficient low-frequency energy harvester using bulk piezoelectric ceramics,” *J. Phys. Conf. Ser.*, vol. 476, no. 1, 2013.
- [72] D. Zhu, S. P. Beeby, M. J. Tudor, and N. R. Harris, “A credit card sized self powered smart sensor node,” *Sensors Actuators A Phys.*, vol. 169, no. 2, pp. 317–325, 2011.
- [73] S.-C. Lin and W.-J. Wu, “Piezoelectric micro energy harvesters based on stainless-steel substrates,” *Smart Mater. Struct.*, vol. 22, no. 4, p. 45016, 2013.
- [74] H. G. Yeo and S. Trolier-McKinstry, “Effect of piezoelectric layer thickness and poling conditions on the performance of cantilever piezoelectric energy harvesters on Ni foils,” *Sensors Actuators A Phys.*, vol. 273, pp. 90–97, 2018.
- [75] Q. Wang, H. Kuwano, and Z. P. Cao, “Metal-based piezoelectric energy harvesters by direct deposition of PZT thick-films on stainless steel,” *Micro Nano Lett.*, vol. 7, no. 12, pp. 1158–1161, 2012.
- [76] Y. Tsujiura, E. Suwa, H. Hida, K. Suenaga, K. Shibata, and I. Kanno, “Lead-free piezoelectric MEMS energy harvesters of stainless steel cantilevers,” *2013 Transducers Eurosensors XXVII 17th Int. Conf. Solid-State Sensors, Actuators Microsystems, Transducers Eurosensors 2013*, no. June, pp. 474–477, 2013.
- [77] W. H. Tang, T. K. Lin, C. T. Chen, Y. H. Fu, S. C. Lin, and W. J. Wu, “A High Performance Piezoelectric Micro Energy Harvester Based on Stainless Steel Substrates,” *J. Phys. Conf. Ser.*, vol. 1052, no. 1, 2018.
- [78] A. Gaur, S. Tiwari, C. Kumar, and P. Maiti, “A bio-based piezoelectric nanogenerator for mechanical energy harvesting using nanohybrid of poly(vinylidene fluoride),” *Nanoscale Adv.*, vol. 1, no. 8, pp. 3200–3211, 2019.

- [79] S. R. Oh, T. C. Wong, C. Y. Tan, K. Yao, and F. E. H. Tay, "Fabrication of piezoelectric polymer multilayers on flexible substrates for energy harvesting," *Smart Mater. Struct.*, vol. 23, no. 1, Jan. 2014.
- [80] F. R. Fan, W. Tang, and Z. L. Wang, "Flexible Nanogenerators for Energy Harvesting and Self-Powered Electronics," *Advanced Materials*, vol. 28, no. 22. Wiley-VCH Verlag, pp. 4283–4305, 08-Jun-2016.
- [81] D. F. Berdy, P. Srisungsitthisunti, B. Jung, X. Xu, J. F. Rhoads, and D. Peroulis, "Low-frequency meandering piezoelectric vibration energy harvester," *IEEE Trans. Ultrason. Ferroelectr. Freq. Control*, vol. 59, no. 5, pp. 846–858, 2012.
- [82] I. Paprotny, Q. Xu, W. W. Chan, R. M. White, and P. K. Wright, "Electromechanical energy scavenging from current-carrying conductors," *IEEE Sens. J.*, vol. 13, no. 1, pp. 190–201, 2013.
- [83] A. Hajati and S. G. Kim, "Ultra-wide bandwidth piezoelectric energy harvesting," *Appl. Phys. Lett.*, vol. 99, no. 8, Aug. 2011.

Chapter II

Thick-film technology and Sintering

Content

1 THICK-FILM TECHNOLOGY	52
1.1 INTRODUCTION	52
1.1.1 Hybrid thick-film circuit	52
1.1.2 Basics of the process	52
1.1.3 Evolutions of the screen-printing process	54
1.2 SCREENS	54
1.2.1 Screen characteristics	54
1.2.2 Screen manufacture	55
1.3 SUBSTRATES	57
1.3.1 Ceramic	57
1.3.2 Silicon	57
1.3.3 Organic	58
1.3.4 Metallic	58
1.4 PASTES	58
1.4.1 Basics on rheology	58
1.4.2 Rheology of a screen-printing paste	60
1.4.3 Paste composition	60
1.4.4 Paste preparation	63
1.5 DEPOSITION	65
1.5.1 Squeegee	65
1.5.2 Screen-printing machine and critical parameters	66
1.6 DRYING	70
1.7 PARTIAL CONCLUSION	70
2 SINTERING	71
2.1 DEFINITION OF SINTERING	71
2.1.1 Types of sintering	71
2.2 PRINCIPLE	72
2.2.1 Stages of sintering	72
2.2.2 Constrained sintering under pressure	73
2.3 CONVENTIONAL SINTERING METHOD	74
2.3.1 Shaping (case of ceramics)	74
2.3.2 Pressing	75
2.3.3 Sintering of screen-printed thickfilms by conventional method	75
2.3.4 Furnace set-up for conventional sintering	78
2.4 SPARK PLASMA SINTERING (SPS)	79
2.4.1 SPS Machine	81
2.4.2 Partial conclusion	82

One of the central aspects of this thesis work is the use of thick-film technology for the fabrication of the energy harvester structure. In this chapter, the thick-film technology is presented, detailing the standard different stages and features of the technique. As part of this process, the conventional sintering process is described and the Spark Plasma Sintering technique (SPS), is lastly emphasized. The understanding of each step of the different techniques plays an essential role in the selection of several characteristics of the EH structures (materials, geometries, sintering cycles...). This chapter aims to give a general description of the thick-film technology while highlighting the characteristics considered and selected for this thesis work.

1 Thick-film technology

1.1 Introduction

1.1.1 Hybrid thick-film circuit

Thick-film technology was introduced in the 1950s for the fabrication of the hybrid thick-film circuit when the replacement of the printed circuit board process was envisaged. A hybrid thick-film circuit comprises integrated circuits, discrete passive components and thick-films (conductors, resistors or dielectrics) reported on a substrate, being a ceramic substrate in most of the cases [1]. The use of thick-film technology was nevertheless overshadowed in the 1960s by the development of silicon technology. It found again popularity in the 1980s with the arrival of Surface Mounted Technology (SMT), SMT devices being reported on circuit boards using screen-printed solder paste. Nowadays, thick films are not only used in hybrid circuits but also in sensors, actuators and MEMS [1]. Figure II-1 shows an example of a hybrid circuit.

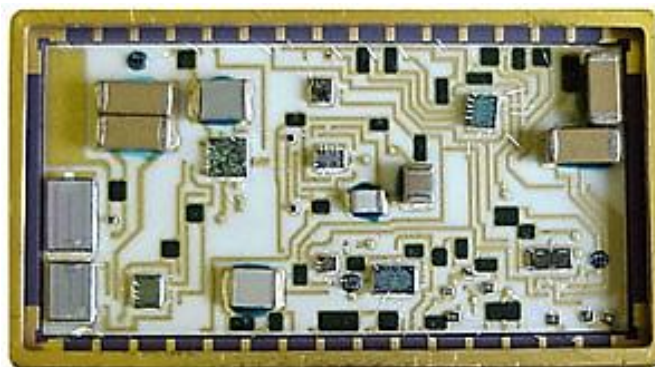


Figure II-1: Hybrid circuit containing conductor tracks, 8 integrated circuits, 2 thick and thin film resistors, and 8 capacitors. The substrate is housed in a 32 pin ceramic package. (Image from [2])

1.1.2 Basics of the process

One of the characteristics of the thick-film technology is the film deposition method, also called screen-printing. This additive process, classically recognized as a kind of art, was updated and modernized in order to be used as a scientific tool for microelectronic technology. The main evolutions are the screen materials and the more sophisticated screen-printer equipment. With this technique, conductive, resistive and dielectric layers of a controlled thickness (from 1 μm to

a few tens of microns per deposit) with line definition until 100 μm can be printed. Figure II-2 illustrates the principle of the screen-printing process.

The screen is typically made with a specific mesh fabric attached with tension to a metallic frame. The mesh is coated with an ultra-violet (UV) sensitive emulsion, and the desired pattern is produced by photolithography on this emulsion. During printing, the screen is held at a constant distance from the substrate, typically 0.5 mm. The ink (or paste) is applied to the upper surface of the screen. Then, the squeegee traverses the screen under pressure (Figure II-2). The screen is hence in contact with the substrate, and the ink is forced through the open areas of the screen mesh. At this step, due to the surface tension between the ink and the substrate, a deposit of the paste in the desired pattern on the substrate is obtained, and the screen is moved away from the substrate. It is important to notice that the rheological properties of the paste are critical to achieve a good definition of the final deposited layer. This will be further detailed in the section devoted to pastes.

The next stage of the process is to dry the deposited layer to remove the organic solvents from the paste. Finally, as the paste contains fine powders, it must be exposed to a high temperature in order to form a solid layer; this is referred to sintering. Figure II-3 summarizes the different steps of the standard thick-film process. For a complete thick-film hybrid circuit, further steps are necessary to report the active or passive components (chips or SMT components) and for the final packaging.

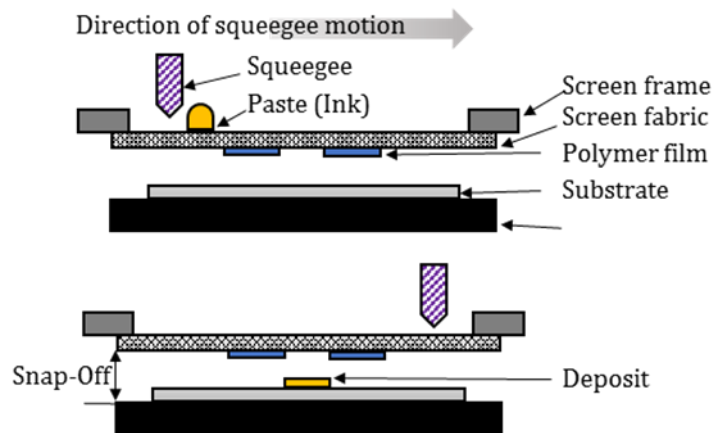


Figure II-2: Scheme of the screen-printing process principle.

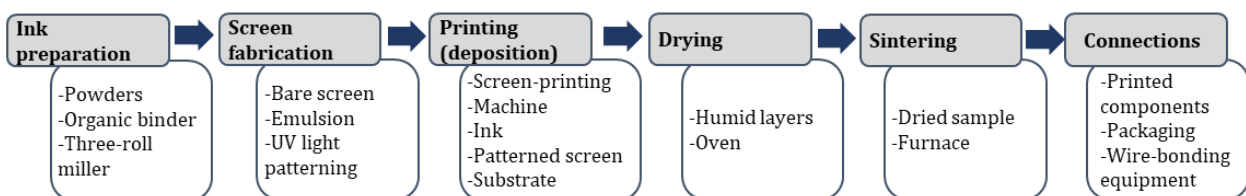


Figure II-3: Fabrication steps of the standard thick-film technology.

1.1.3 Evolutions of the screen-printing process

Among numerous technologies nowadays available for printing films in microelectronics, screen-printing is the simplest, most flexible and cheapest process. The most valuable advantages of screen-printing are the low investment required in equipment and the large choice of materials, including substrates and pastes. It allows valorization of the properties of materials and development of applications in the field of passive components, sensors and actuators. Nevertheless, standard screen-printing technology presents a line width limited to 100 μm . Modifications of standard screen-printing have been therefore proposed for integration purpose or performance improvement. Polymer thick-films represent, for instance, important achievements leading to various applications on flexible substrates [3]. The screen-printing has also been recently considered for MEMS by using a sacrificial layer [4].

1.2 Screens

1.2.1 Screen characteristics

The function of the screen is to define the pattern of the printed film and to control its thickness. The screens are made of mesh fabric attached to a metallic frame and characterized (Figure II-4) by:

- The wire diameter d that depends on the type of fabric.
- The number of wires per inch (mesh count M). This mesh count and the filament diameter determine the resolution of the deposit. In general, a typical mesh count might be 200 wires per inch i.e. 200 meshes.
- The ink passage zone which is the opening of mesh O . It depends on the mesh count and on the filament diameter. In general, the opening of the mesh must be 3 to 5 times greater than the maximum diameter of solid particles in the paste.
- The thickness of the mesh fabric is a function of the tension of the mesh fabric on the frame. The tension varies from 8 to 30 N/cm.
- The emulsion covering part of the fabric, of thickness E_f , chosen according to the final desired thickness (see deposition section 1.5).

Common materials for screens mesh are polyester, nylon, or stainless steel. The standard screen is in polyester, which has the highest resilience and excellent elastic properties (higher than stainless steel), and thus is interesting for printing on uneven surfaces. Definition properties of the layers are generally high, and such screen has a long lifetime with low squeegee wear.

Nylon has the highest flexibility. The open areas are hence deformed during the print leading to elongated images. Conductor tracks for the highest layer level in a multilayer circuit are printed with such screen. High viscosity pastes should also not be used because of their low resilience. Stainless steel screens are more expensive but produce excellent line definition and durability, and are particularly well suited to flat substrates. They provide the highest percentage of open area for a given mesh count because the wire diameter can be very narrow. *Typical characteristics of stainless steel screens used in this work are reported in Table II-1.*

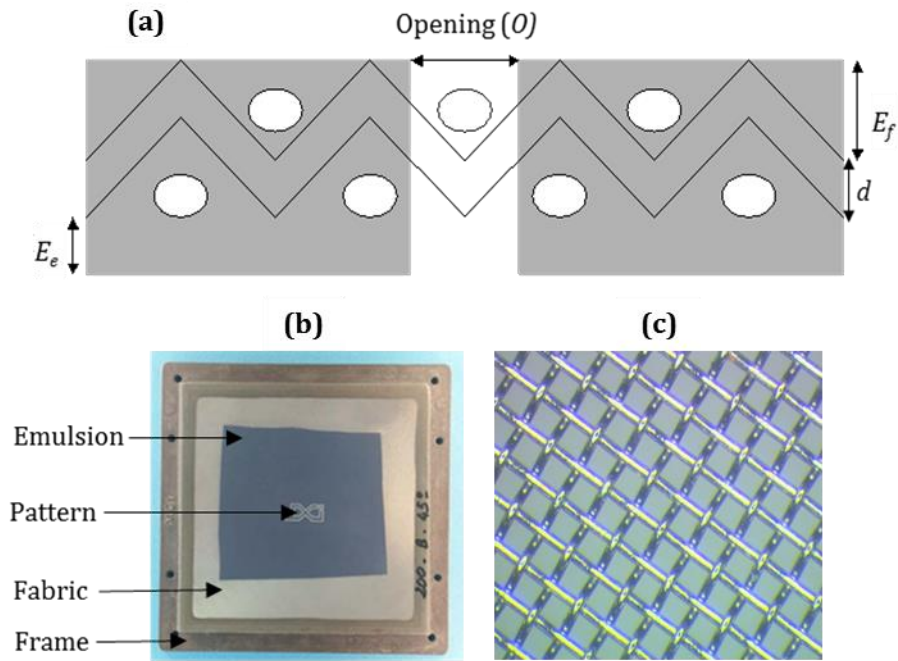


Figure II-4: (a) Typical mesh scheme of thick-film screens with characteristic parameters (thicknesses of fabric (E_f) and emulsion (E_e), wire diameter (d) and opening of mesh (O)). (b) Picture of a screen after UV patterning with the different constituents, and (c) zoom on the fabric mesh.

Table II- 1: Characteristics of stainless steel screens.

Screen type (mesh count M)	Wire diameter d (μm)	Opening of mesh O (μm)	Fabric thickness (μm)	Tension 0.5% \ddagger (N/m)	Humid deposit thickness (μm)
70	65	300	140 ± 3	21-23	185-230
200	36	90	80 ± 2	20-22	81-97
325	24	53	52 ± 1.5	13-15	58-71
400	18	45	40 ± 1	8-10	50-61

*Data from DEK society. Thickness of final humid deposit depends on the emulsion thickness and tension.

Note that, for specific applications (e.g. solder paste deposition, or any application where important thickness is required and the definition of deposit is not a limitation) metallic stencil can replace the mesh screen. The stencil is made of a stainless steel foil micro-machined by laser, and its thickness is typically between 100 and 250 μm .

1.2.2 Screen manufacture

The design of the printed circuit can be completed with the different available commercial software packages. CleWins4 has been selected in the framework of this thesis. Design guidelines such as track width (minimum 100 μm), track spacing (minimum 150 μm), fiducials shape (circular or cross) (Figure II-6 (left)), and size must be taken into account depending on the selected screen. When the UV photolithography step is led, an accurate photo-plotter has to be used to print the design on a plastic sheet (Clicherie, Pessac France). Another option is to

send the generated files (extension .cif) to fabricate the screen directly (Marabu Bondy France or DB Products, Savigny, France).

Once the screen fabric is attached to the metallic frame, the light-sensitive emulsion must be deposited on it before the UV photolithography exposure. Direct emulsion process and direct film method are the typical methods [5].

Direct film method is used here, where an UV sensitized film (negative film from MS Capillary Film - Murakami, Tokyo, Japan) is attached to a transparent sheet of polyester backing. The emulsion supported on the backing film is first placed on the screen (Figure II-5). After heating 1 h at 40 °C, the backing film is removed, and the emulsion can be UV exposed with the pattern mask before its development in water. The UV exposure time varies according to the mesh size and thickness of the polymer film (between 5 μm and 100 μm). For a 325 meshes screen with a 50 μm thick emulsion, the exposure time is for instance 40 s. The complete assembly for the screens fabrication is described on Figure II-6 (right).

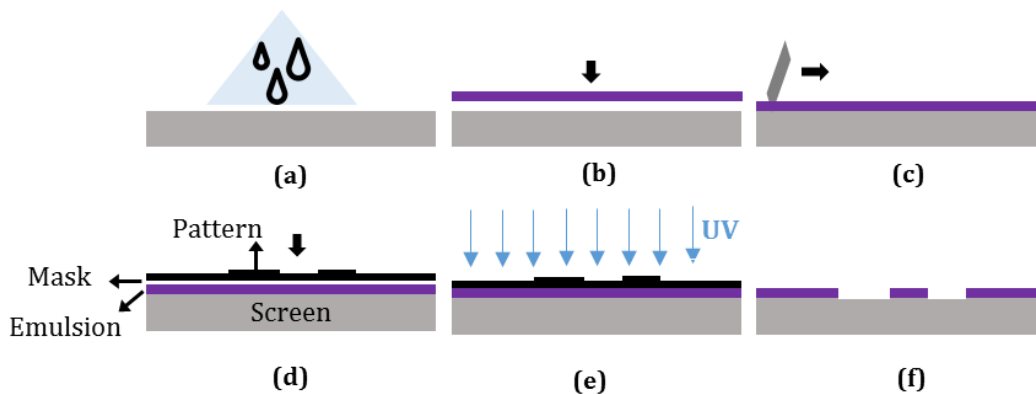


Figure II-5: Photolithographic screen manufacture. (a-c) direct emulsion deposition process (d) screen with deposited negative emulsion film and plastic pattern mask, (e) UV light exposure of the negative emulsion: the UV exposed parts reticle, (f) screen after development: the non-exposed UV parts corresponding to the desired pattern have been dissolved in water.

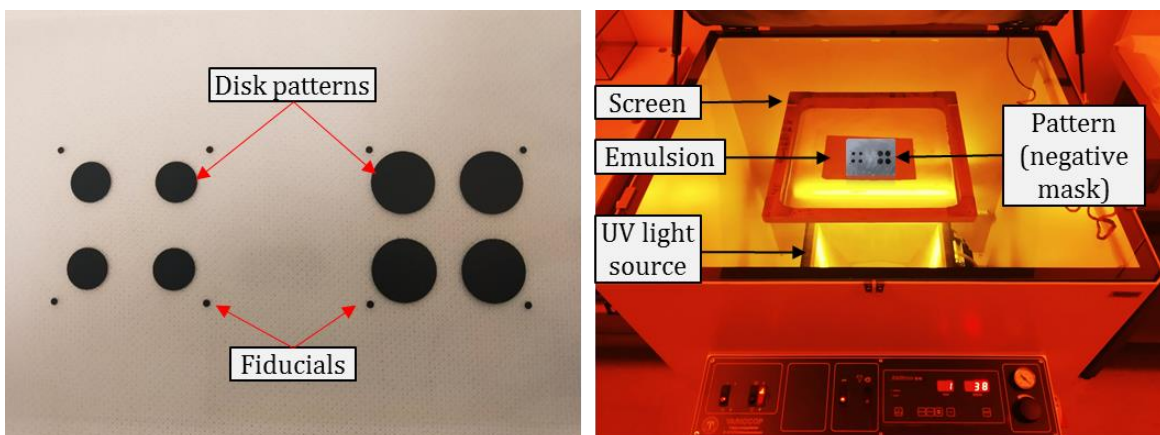


Figure II-6: Patterns design with respected circular-shape fiducials (left). Complete assembly for screen fabrication with UV exposure machine Technigrapp - Variocop S used at the IMS laboratory (right).

1.3 Substrates

In classical thick-film technology, the substrate is the mechanical support for the printed layers, which must provide electrical insulation. Other properties should be considered, depending on the final aimed applications: dielectric properties (permittivity and dielectric strength), thermal properties (thermal conductivity, thermal coefficient of expansion, melting point, etc.), mechanical properties (Young's modulus, strength, etc.), density, and cost [6]. The well-known substrate materials used in classical thick-film technology are ceramic substrates, but for sensors, actuators or MEMS applications, other substrates can be preferred such as organic, silicon or metallic substrates. Table II-2 summarizes the most important properties of the substrates that can be used in thick-film technology. The next paragraphs give some details on the most relevant substrates.

Table II- 2: Main substrates and properties to be considered when choosing substrates for thick-film technology [1][6].

Properties /Material	Silicon	Alumina (96%)	AlN	Polymers	Stainless steel (SS)
Dielectric constant (at 1kHz)	11	9.5	8.7	2.6-3.1	--
Dielectric strength (kV/mm)	10	12	14	9-16	--
Thermal conductivity (W/m-K)	148	26	160-190	0.2 -0.29	10-34.3
Thermal coefficient of expansion (CTE) ($10^{-7}/^{\circ}\text{C}$)	2.6	6.3	4.6	10-69	7-21.1
Young's modulus (GPa)	112-186	300	322	3-5	5-310
Melting point ($^{\circ}\text{C}$)	1414	2000	2227	200-270	1230-1700
Density (g/cm^3)	2.3	3.8	3.3	1.4	8.1
Cost	Low	Low	High	Average	Average

1.3.1 Ceramic

Some well-known substrate materials used in thick-film technology are the alumina (Al_2O_3), beryllium monoxide (BeO) and aluminium nitride (AlN) ceramics. However alumina is the most common substrate used in the vast majority of worldwide commercial hybrid circuits. Purity of alumina substrate can be found from 96 to 99%. The remaining percent corresponds to magnesia and silica, which improve the densification. A good compromise is obtained in terms of electrical, thermo-mechanical and chemical properties. Moreover, it provides a low-cost solution. Beryllium monoxide has a high thermal conductivity and is used in applications where rapid heat removal is required. It is, however, a very toxic material and is therefore only used in limited applications. Aluminium nitride is mainly an alternative for BeO , with a high thermal conductivity and also improved mechanical properties such as higher flexural strength [6].

1.3.2 Silicon

Silicon, standard in microelectronics for integrated circuits (IC) can be also used in thick-film technology to integrate thick-films having specific properties for sensors or actuators, while keeping the integration of electronic circuits. Silicon or silicon on insulator wafers (SOI) can be

simply used as a support during the thick-film process prior to the release of the thick-film [7][8]. Also, as for silicon MEMS, silicon membranes can be prepared by either volume or surface micromachining before the screen-printing step [9]. Koch et al. screen-printed for instance PZT and electrodes on a 70 μm silicon membrane for micropump application [10].

1.3.3 Organic

Organic and flexible printed electronics are becoming more and more popular [11]. Polymer (PET polyethylene, PEN Polyethylene naphtalate or PI polyimide) and even paper substrates can support printed based pastes [12]. Cermet thick-film pastes are not compatible with these organic substrates and special polymer thick-film pastes should hence be selected. Whereas the temperature of operation of these substrates is typically in the range 120-150 $^{\circ}\text{C}$, the maximum processing temperature (curing of the polymer pastes) is usually limited to ≈ 200 $^{\circ}\text{C}$, except for PI for which 400 $^{\circ}\text{C}$ can be reached.

1.3.4 Metallic

Insulated metals have been successfully used in hostile environment because of their mechanical strength, good thermal properties, shielding character and low cost potential. Porcelain enamel which are steel substrates coated with a glassy layer of thickness ($\approx 100\mu\text{m}$) is an example of such substrate. Nevertheless, it presents drawbacks such as temperature limitation, and complex fabrication process [13]. Stainless steel substrates covered by a screen printed dielectric layer or a tape can be an option and have been successfully used for heating or energy harvesting [14] [15].

In this work, stainless steel substrate will be used to support the printed piezoelectric layers. It has a lower Young's modulus than alumina or than silicon and is hence more attractive for energy harvesting application. It can be found at different thicknesses (<250 μm).

1.4 Pastes

The study of the rheology of screen printing inks is of great interest since the quality of the obtained deposits depends on the viscosity of the inks.

1.4.1 Basics on rheology

Isaac Newton established the fundamental law of rheology, introducing the notion of viscosity [16]. Let us consider a liquid situated between two flat and parallel surfaces, one of which is in motion in relation to the other (Figure II-7). The speed of a fluid point differs from adjacent planes to a dv quantity when moving vertically from a dy quantity. This defines the speed gradient (D), also called as the shear speed, which is expressed by:

$$D = dv/dy \text{ (s}^{-1}\text{)} \quad \text{(Eq. 2.1)}$$

The shear stress is defined by:

$$\tau = \frac{F}{S} \text{ (Dyne. } cm^{-2} \text{ in CGS, or Pa in S.I.)} \quad (\text{Eq. 2.2})$$

Where F is the force necessary to overcome the sum of friction forces existing between two neighboring planes (called viscosity forces), and S the surface.

The viscosity is then defined as the ratio between these two quantities:

$$\eta = \frac{\tau}{D} \text{ (Pa. s in S.I. or Poise in CGS, } 10 \text{ poi} = 1 \text{ Pa. s)} \quad (\text{Eq. 2.3})$$

Therefore, the viscosity depends on the nature of the liquid itself (viscosity forces) and the shear stress. Different rheological behaviors can be found:

- The Newtonian behavior: the viscosity is independent of the speed gradient. Pure liquids often exhibit this type of behavior (water, mineral oil, molasses, etc.).
- The pseudo-plastic or rheo-fluidifying behavior: the viscosity decreases when the speed gradient increases. This is the common behavior of liquids with several phases, at least one of which is solid.
- The dilatant behavior (or rheo-thickening): the viscosity increases when the speed gradient increases, conversely to the pseudo-plastic behavior. This behavior is rare but occurs for highly concentrated suspensions.

All these behaviors are reversible. However, for a constant gradient speed, if the viscosity varies, i.e. it decreases as a function of time, the behavior is said to be thixotropic. The opposite effect is called anti-thixotropic.

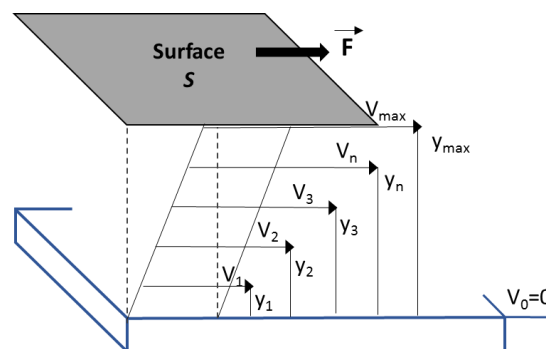


Figure II-7: Scheme of Newtonian behavior: fluid between two flat and parallel surfaces, one of which is in motion in relation to the other.

1.4.2 Rheology of a screen-printing paste

For an excellent printing quality, an ideal screen printing paste (or ink) must have a pseudo-plastic and moderate thixotropic behavior, in order to ensure:

- An adapted fluidity when passing through the screen (i.e., fast printing under squeegee pressure),
- Fast settling of the film in the desired geometry after removal of the squeegee and good ink smoothing.

The viscosity of the paste will hence be modified during each step of the printing process, as described in Figure II-8. The main stages, where the speed gradient strongly varies, are the following:

- Before agitation, the viscosity of the ink must be high to keep the particles in suspension before use. The paste is homogenized with a spatula ($10^{-2} \text{ s}^{-1} < D < 1 \text{ s}^{-1}$).
- During screen printing, the ink is subjected to shearing stresses due to the passage of the squeegee. The viscosity must decrease with the applied shearing stresses so that the ink passes through the screen ($10 < D < 1000 \text{ s}^{-1}$ and $\eta < 50 \text{ Pa}\cdot\text{s}$ for $D \sim 100 \text{ s}^{-1}$).
- Once the deposit has been made, the ink must be "coated" or "smoothed" in order to remove the trace from the screen. The viscosity should slowly return to its original value to allow the ink to smooth in time ($10^{-1} < D < 1 \text{ s}^{-1}$); this is the thixotropic behavior.

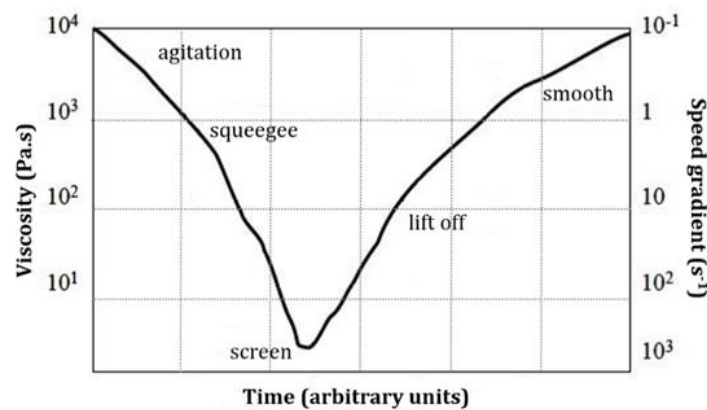


Figure II-8: Variation of the viscosity η of the paste and the speed gradient D during screen-printed deposition.

1.4.3 Paste composition

Two types of pastes (or inks) can be considered: the so-called "mineral" inks with generally firing temperatures between 500 and 1100 °C, and the so-called "polymer" inks, developed for low temperature applications, whose consolidation by polymerization is carried out below 200 °C. Polymer inks will not be detailed, but rather that of mineral inks consisting of a mineral and an organic phase.

1.4.3.1 Mineral phase

The mineral phase differentiates each ink as it defines the final function of the screen-printed layer. It contains:

- The active material in the form of a powder generally calibrated from 0.1 to 10 microns. It provides to the printed layer its final properties (conductor, resistive, insulator, magnetic, piezoelectric, etc.). Commercial conductive inks are manufactured from silver, gold, platinum powders, or from metals alloys from these metals (Ag-Pt, Ag-Pd, Ag-Pd-Pt, Au-Pt, etc.). The films characteristics (sinterability, conductivity and solderability) are strongly affected by size and shape of metal particles. Finally, resistive inks usually consist of ruthenium dioxide (RuO_2) or ruthenate ($\text{Bi}_2\text{Ru}_2\text{O}_7$ or PbRu_2O_6), with different proportions of glasses. For other applications as sensors, a myriad of metal oxides can be used (SnO_2 , WO_3 , ZnO , ZrO_2 , etc.) [17].
- Additives or dopants are introduced in small quantities and may be used to adjust physico-chemical and electrical properties, or to reduce the sintering temperature, promoting adhesion, etc.
- The mineral binder: it is generally a glass frit which has a softening point in the range 400-600 °C. Hence, during the firing temperature, the viscosity of the glass is low enough to assist the sintering of the mineral part. This glass being liquid will wet both the substrate and the grains. During cooling, this phase solidifies and ensures the cohesion of the layer and its adhesion to the substrate. Its coefficient of thermal expansion should be as close as possible to that of the substrate. Silica glasses with a large amount of Pb are often present in thick-film resistors and often in conductors. New pastes are nevertheless developed to follow the RoHS directives (Restriction of the use of certain Hazardous Substances as Pb, Bi, Cd, etc).

1.4.3.2 Organic phase

It is a mixture of volatile solvents and polymers or resins. It provides a homogenous suspension of the particles in the paste and the suitable rheological properties for the printing stage. It should also temporarily ensure the cohesion of the mineral part after the printing process and be removed entirely in the following steps of the process (drying and sintering).

The most straightforward formulation of organic vehicle used in previous work [18] for feasibility studies is based on terpeneol-type solvents and cellulose type resins. A well-known formulation of paste is ethylcellulose dissolved by terpeneol and butyl carbitol solvents.

Most of the solvents are removed during drying (120 °C-150 °C) while organic binders are only removed by firing in air atmosphere at temperature ranging from 150 °C to 550 °C. Acrylic resins are alternative to ethylcellulose for paste compositions requiring nitrogen firing, as they depolymerize when heated. The relative fractions of these ingredients depend on both the shape and nature of the inorganic part.

When using polymer pastes, the thick films are not fired at high temperature, unlike conventional inorganic pastes. The glassy binder is indeed substituted by a thermosetting resin which purpose is to ensure the cohesion of the layer. A drying or drying and curing step at a temperature in the range from 150 °C to 300 °C will then give to the printed layer its final structure. Several types of resins can be found:

- Phenolic resins: they have very good dielectric properties, but they can also be used as conductive inks when loaded with metallic powders.
- Epoxy resins: they have similar properties to those of phenolic resins.
- Polyimide resins: they have a higher curing temperature; they resist at higher temperatures providing hence a more reliable and stable system because of a higher temperature resistance.

For polymer-based conductors, silver powder is the most common additive, for polymer-based resistors, a mixture of carbon black, graphite and silver powders is used; finally polymer-based dielectrics include a pigment and inorganic filler.

Figure II-9 summarizes the composition of inks for thick-film technology.

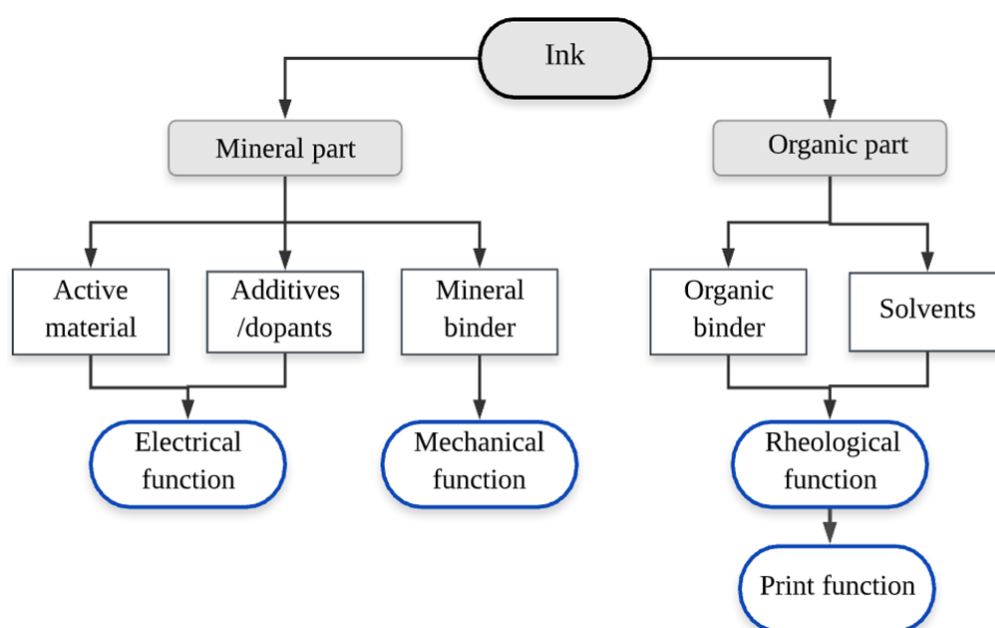


Figure II-9: Constituents of a mineral ink for screen-printing.

In this thesis, for the EH layer, mineral pastes will be used: PZT based paste will be home-made, whereas electrodes based on Au will be provided by ESL (Electro Science laboratory www.electroscience.com, further information in chapter 4). The specific preparation of the PZT ink used in this work will be later explained in chapter 4.

Also, a low temperature paste based on epoxy and carbonate will be prepared to be used as sacrificial or protective layer. The preparation of this paste will be given in chapter 5.

1.4.4 Paste preparation

1.4.4.1 Milling

Before incorporating the active powder into the organic phase, a milling step is necessary if the grain diameter is not adapted ($> 10 \mu\text{m}$) or if large agglomerates are present. A uniform distribution of precursors is hence obtained.

Planetary milling machine (Retsch PM4 at IMS (Figure II-10 (a)) is used for this process stage. The powder is wet in ethanol vehicle and placed in an agate jar (7.5 mm \varnothing) with agate spheres (10 mm \varnothing) (Figure II-10 (b)). At each rotation of the platform, the jar rotates around its axis of rotation, but in the opposite direction. The centrifugal and Coriolis forces lead to a rapid acceleration of the milling balls, leading to grinding by friction [19] (Figure II-10(c)).

This process is carried out during 12 h using 30 g of powder with 40 g of ethanol and 13 agate spheres per jar. A speed of 400RPM is used during milling. The grain size is checked out before and after milling by a laser diffraction spectrometry analysis. Afterwards the powder is dried at 40 °C in an oven.

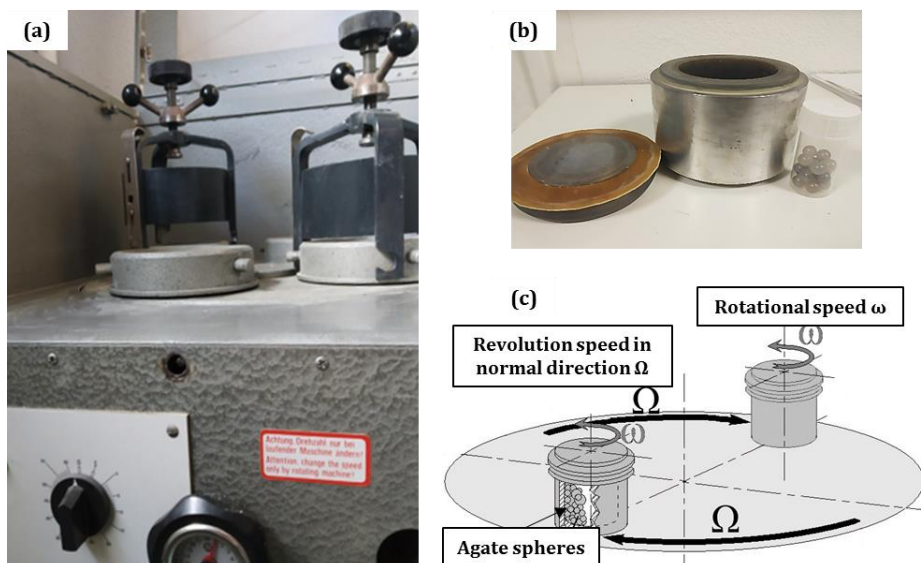


Figure II-10: (a) Planetary milling machine used at IMS laboratory (Retsch PM4), (b) agate jar and spheres (b), and (c) principle scheme of planetary milling (Image inspired from [20]).

1.4.4.2 Powder mixing

If the mineral phase powder is based on two or more powders (active material and/or additives and/or mineral binder), the powders must be mixed before adding the organic phase. They are first weighted with a precision Sartorius balance. A minimum of 10 g is required for the further organic incorporation step.

The mixture is then placed in a plastic container with agate spheres (10 mm \varnothing) and ethanol solvent. The containers are then introduced in a Turbula shaker mixer (Turbula System Schatz

T2F at IMS) (Figure II-11). The efficiency in the homogenization comes from rotation, translation, and inversion according to the Schatz geometric theory [21].

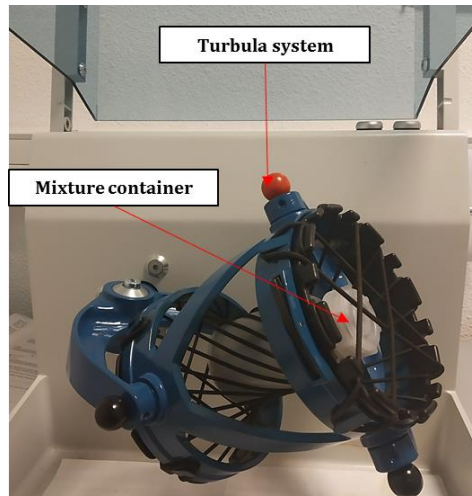


Figure II-11: Turbula shaker-mixer T2F system used at IMS laboratory.

Mixing is carried out during 7 h at a frequency of 101 min^{-1} . The homogenized solution is then dried at $40 \text{ }^\circ\text{C}$ in an oven.

1.4.4.3 Organic phase incorporation

Finally, the organic binder is added to the powder mixture in order to provide a desired viscosity for the thick-film paste. A three-roll mill is used (Figure II-12). This equipment is composed of three in lines SiC rolls separated by an adjustable gap. The rolls rotate in opposite directions at different speeds by a factor of 3 relative to each other (Figure II-12 (b)). After each cycle, the ink is scraped off the front roll and the paste is collected and introduced again in the first roll, led for mix, refine, disperse, and homogenize materials fed into it. The roll gaps have to be adjusted, i.e. gradually decreased until the desired dispersion has been obtained. Care should be taken if too much stresses are applied to ductile metal powders present in conductive pastes.

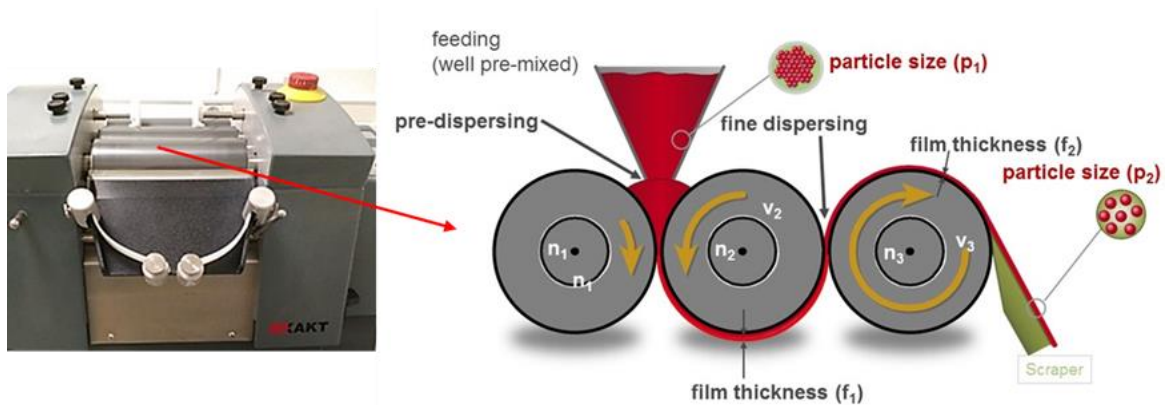


Figure II-12: Three-roll mill picture (EXAKT 80) used at IMS laboratory (left), and dispersing principle scheme (right) with $v_3=3v_2$; $v_2=9v_1$ [22].

The mixture (organic and mineral phases) is first blended manually in a mortar with the suitable proportions which vary typically between 10 to 20% vol. Then it is transferred in a three roll mill (EXAKT 80 at IMS) (Figure II-12 (left)). The used gap is typically of 2 mm. The dispersion control of the ink is carried out during 5 cycles with a speed of the three roll mill between 18-58 RPM.

1.4.4.4 Control of the viscosity

If the viscosity is not well adapted, the rheological properties of the ink will not be suitable, for example high η doesn't let the ink smooth after printing (section 1.4.2). Hence, the viscosity needs to be controlled after the paste preparation, by printing tests and measurements with a rheometer. The rheometer used is a parallel plate cone-type measurement system which consists on a cone structure with an angle α (lower than 1°) respecting the horizontal plane of its position (Figure II-13 (a)). It allows to measure the shear speed depending on the stress applied. The appropriate quantity of ink is placed between the cone and the parallel plan. Then, thanks to the progressive rotation of the cone a shear stress is produced.

The shear speed D is related to angular velocity ω and cone angle α by equation $D = \omega / \alpha$. Viscosity measurements are carried out by increasing and decreasing the shear speed and deducing the shear stress τ . The curves $\eta = f(D)$ can then be obtained (Figure II-13 (b)).

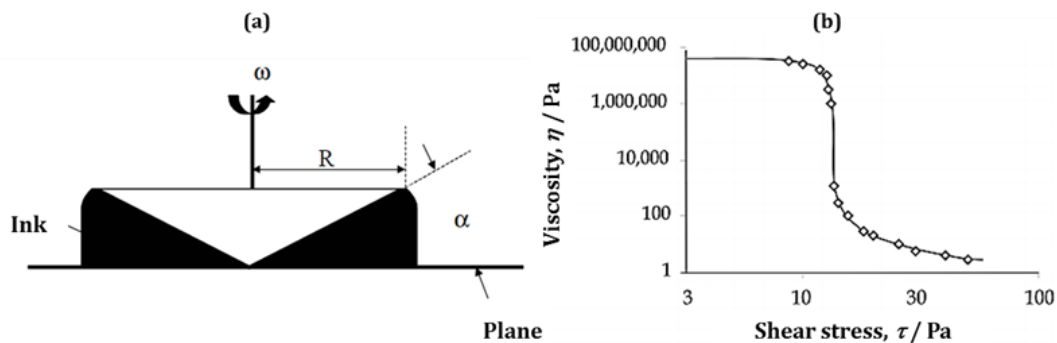


Figure II-13: (a) Scheme of rheometer cone-type system used for viscosity measurements, and (b) characteristic curves $\eta = f(D)$ that can be obtained (melted chocolate). (Image from [19])

The rheometer used is a CARRIMED parallel plate cone-type measurement system present at ELORPrinTec-Université de Bordeaux. The shear speed D varies between 10^{-1} and 10^4 s^{-1} . The viscosity measurement range for this system is between $\eta = 0.1$ and $\eta = 5.10^3$ Pa. s.

1.5 Deposition

1.5.1 Squeegee

The squeegee is a flexible blade. Its function is to transfer the paste through the screen and onto the screen. Lifetime of the squeegee and screen are linked to squeegee's material, shape and pressure applied during the printing. Squeegees must be also resistant to the solvents and pastes used in thick-film processing. Common squeegees are in polyurethane or neoprene, with hardness in the range 50-90 durometers [5]. For stencil screens, metallic squeegees are

recommended. Photographs of a typical squeegee and the corresponding blade are shown in Figure II-14.

The squeegee construction used in this work is shown in Figure II-14 (a), with an angle of attack of 45°.

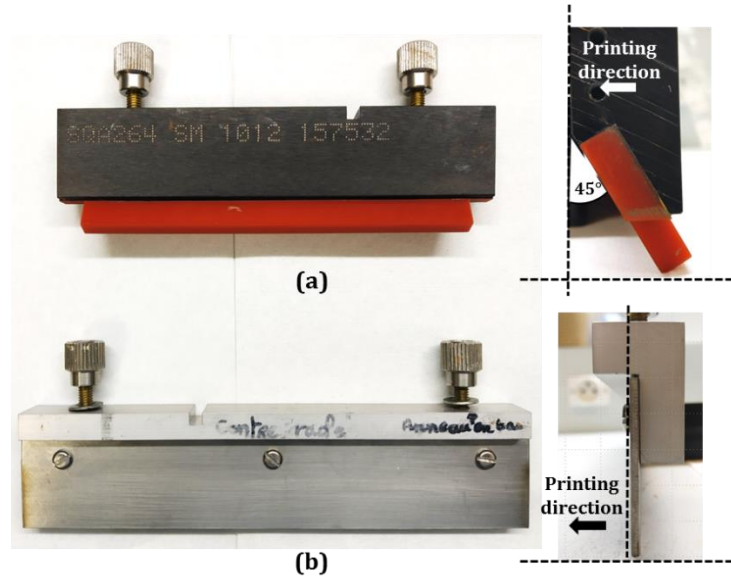


Figure II-14: (a) Photographs of the polyurethane squeegee used in this work, (b) and the metallic squeegee for stencil screens.

1.5.2 Screen-printing machine and critical parameters

The screen-printing equipment used at IMS laboratory is a DEK Horizon 03IX, which includes an automated sight-reading and alignment system. A photo of the DEK is shown in Figure II-15.

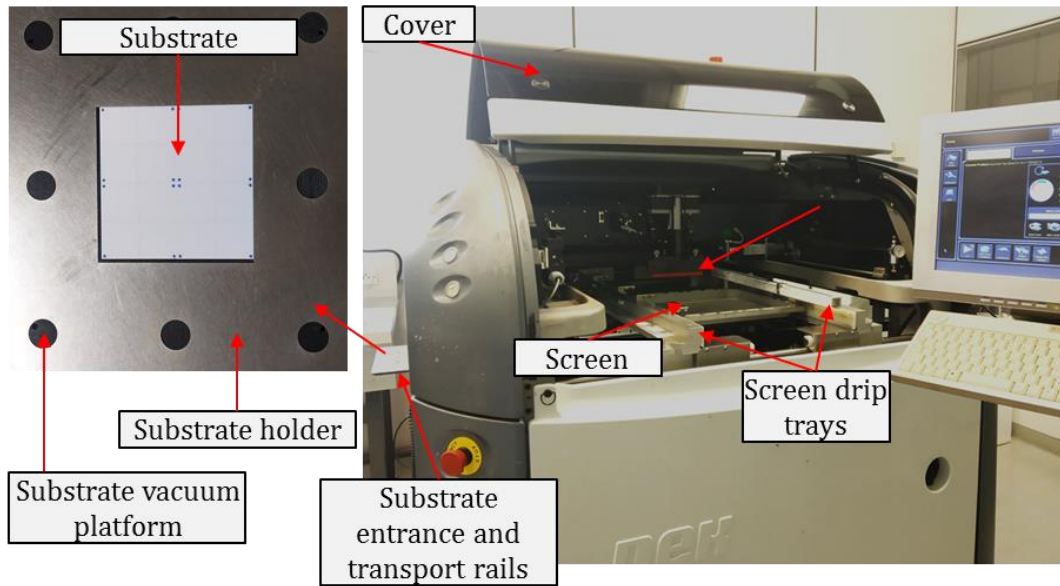


Figure II-15: DEK Horizon screen-printing machine used at IMS laboratory.

Different parameters need to be carefully optimized in order to obtain a good deposition:

- Alignment and fiducials:** The alignment of the screen and substrate is crucial so that the paste can be printed at the desired position. This is ensured via the video recognition of circular fiducials of 1 mm diameter. These fiducials are incorporated into the screen patterns and filled up with silver epoxy resin (ESL1901, Annex 1) to facilitate their recognition. The fiducials are also printed on the stainless steel substrate holder. A blue dielectric ink (ESL4924, Annex 2) sintered at 850 °C is used for this purpose. The contrast with the substrate must be strong for a good alignment. However, slight inaccuracies in the automatic alignment have been noted so a constantly manual verification of the alignment is required.
- Off-contact distance:** Screen printing requires the screen to be slightly separated from the substrate. The “off-contact distance” also known as “snap-off distance” should be kept to a minimum to prevent image distortion. This off-contact distance is required to prevent the screen from adhering to the substrate which would cause separation problems and damage print quality. Off-contact distance allows the mesh to come in contact with the substrate only at the printing edge during the printing. Off contact distances of 0.5 mm - 3.0 mm are common and values of 0.1 mm - 0.2 mm is possible with stainless steel masks. Excessive off-contact distance generates print quality and alignment problems. In most situations, the best off-contact distance is the lowest one. Off-contact distance is controlled by the distance between the platform substrate and the screen.
- Squeegee pressure:** Optimization of the squeegee pressure is necessary, since this one can limit the amount of paste transferred, and thus the thickness. It also affects the definition and uniformity of the print. The optimal pressure depends on the paste viscosity, screen tension, and off-contact distance (distance between squeegee and

substrate). Squeegee pressure is also very critical when superposition of layers is made, high pressures can damage the previous printed layers. Pressure load values ranged from 1 to 20 kg.

- **Squeegee speed:** This parameter affects directly the thickness of deposit and depends on the rheological properties of the paste. At higher speed, a smaller amount of paste is transferred and as a result the layer thickness is lower. Squeegee print speed values range from 10 to 200 mm/s.
- **Printing direction:** Printing should be carried out in the direction of the longest possible length of the patterns in order to have a more homogenous deposit. If two layers are printed next to each other, the printing order has to be taken into account since this affects the shape of the junction.
- **Emulsion thickness and screen mesh:** The setting of the screen-printer associated with the screen mesh and its emulsion thickness determines the final deposited thickness and its precision. Examples of screens are given in Table II-3. For a film deposited with a given screen, the thickness of the deposit (T) can be approximated by the relation (2.4):

$$T = 0.5E_t + E_f \quad (\text{Eq. 2.4})$$

Where E_t and E_f correspond to thicknesses of the fabric and the emulsion, respectively [5].













Table II- 3: Examples of screen characteristics and emulsion thickness for different kinds of pastes.

Paste	Screen characteristics (mesh)	Emulsion thickness (μm)
Conductor	235 - 325	15 - 25
Resistor	165 - 200	25 - 40
	200 - 325	5 - 20
Dielectric and overglaze	200 - 325	20 - 30
Solder paste	100 - 165	30 - 120

- **Separation speed:** This is the speed at which the substrate is separated from contact of the screen after printing. This is rather a consequence of the off-contact distance for mesh screens, but may be a problem in the case of the stencil screen where too low speed can generate some uniformities of the deposit. The speed usually used is 1 mm/s.

Table II-4 reports some characteristic parameters impacting both the printed thickness and the resolution [5].

Table II- 4: Impact of the different screen-printing parameters on the printed thickness and resolution. The arrows symbols indicate the increasing (blue arrow) or decreasing of the parameter (black arrow). (Inspired from [5])

Parameter	Action	Results	
		Thickness	Resolution
Off-contact distance			
Squeegee pressure			
Squeegee speed			
Emulsion thickness			

In this thesis work, the screen and its emulsion and each of the parameters (off contact-distance, separation speed, squeegee pressure, and speed) have been optimized experimentally to reach the desired thickness and resolution (Table II-5). It is worth noting that the values for the squeegee pressure and speed are an approximation from the different deposition processes carried out since these parameters depend on the ink viscosity, which was observed to be very sensitive to slight temperature changes and lifespan. Even under controlled conditions (clean room), these two parameters need to be readapted beforehand to each deposition.

Table II- 5: Parameters of screen-printing process used in this thesis work.

Parameter	Value
Off-contact distance	1 mm for all substrates
Squeegee pressure	8 kg for bottom electrode 4 kg for active layer 6 kg for top electrode
Squeegee speed	80 mm/s for bottom electrode 65 mm/s for active layer 80 mm/s for top electrode
Emulsion thickness	Electrodes: 15 μm Active layer: 50 μm (x 2 for aim thickness < 90 μm)
Separation Speed	1 mm/s

1.6 Drying

After the screen-printing and the paste smoothing, the film has to be dried at temperatures between 120 °C and 150 °C in a conventional oven. During this stage, the most volatile organic solvents are removed. The thickness of the layer can be decreased of approximately 50%, this value depends on the proportion of organic vehicle. If the component is a multilayer, after each drying of the layers, the next layer is printed and dried again.

Other types of drying (or curing) can be led depending on the nature and thickness of the layer. When considering thick layers (>100 μm) the drying has to be progressive in order to avoid cracks and bubbles within the layers. During this progressive drying a ramp of 1.2 °C/min is chosen and controlled by a Heratherm (Thermo Scientific) oven.

Control of the thickness should be done either after the drying step, or after firing.

1.7 Partial conclusion

From the above sections, thick-film technology appears to be cheap and straightforward. The flexibility and accessibility of this technology result from the possibility to print different shapes and thicknesses, with a stack of layers of different nature. The prototyping of this technology with the integration of the conditioning electronics on the same substrate offers a major advantage.

However, several issues can appear due to the multicomponent nature of the pastes and the fired films, and the presence of the substrate on which the layers are bounded (except for free-standing layers for MEMS applications). A deep understanding of the physico-chemical reactions occurring during the transformation of the deposited layers into the functional component is necessary to optimize the properties of the final component.

2 Sintering

The densification step is one of the key steps in the process. In a first stage, the densification of the screen-printed deposited materials has been carried out by a conventional sintering approach, in order to validate the screen-printing fabrication process as a route to MEMS production for energy harvesting applications. Then, we have implemented the Spark Plasma Sintering (SPS) technique into the fabrication process for further improvement of densification, and therefore optimization of overall properties.

Conventional sintering method and its application into the screen-printing fabrication process will be first described. The Spark plasma sintering (SPS) technique will be then introduced.

2.1 Definition of sintering

Sintering is defined as a thermal treatment for bonding particles into a coherent, predominantly solid structure via mass transport events that often occur at atomic scale [23]. This consolidation leads to higher strength and lowers the surface energy by reducing surface area through the formation of interparticles bonds.

2.1.1 Types of sintering

From a technical point of view, free sintering (conventional sintering) which is carried out without any mechanical stress (heating under air or controlled atmosphere) can be distinguished from constrained sintering performed in the vast majority of cases with the simultaneous action of heat and external pressure, and more often used for materials hard to densify. Different types of sintering can be mentioned:

- **Solid state diffusion sintering:** Consolidation is made in the absence of any liquid phase and includes single phase, mixed powders and mixed phases sintering in the solid state.
- **Liquid Phase sintering:** Consolidation is favored by a low amount of liquid phase that accelerates mass transport rates and densification. The liquid can result from melting of one component or formation of an eutectic and allows an efficient rearrangement of particles. The capillary force allows rapid compaction without the need of pressure.
- **Constrained sintering:** Consolidation with the help of pressure (Hot Pressing (HP), Hot Isostatic Pressing (HIP)), or assisted by microwave (microwave sintering) or Electric Current Activated/Assisted Sintering (ECAS)

We will focus in the next section on solid state sintering that represents the main concern of this study: free sintering by conventional method and then Spark Plasma Sintering (SPS).

2.2 Principle

2.2.1 Stages of sintering

Solid state sintering occurs in three different stages: the initial stage, the intermediate stage and the final stage (Figure II-16). The description of these different stages is based on a model of two spherical particles of the same diameter and of the same nature. Starting from an assembly of particles, the different parameters observed during the different stages are presented in Table II-6. The main parameters that need to be monitored are the neck size ratio (contacts between adjacent particles) defined as X/D , the relative density, the linear shrinkage and the reduction of the surface area S/S_0 (X = neck size, D = particle diameter, ΔL = length variation, L_0 = initial length, S = specific area, S_0 = initial specific area).

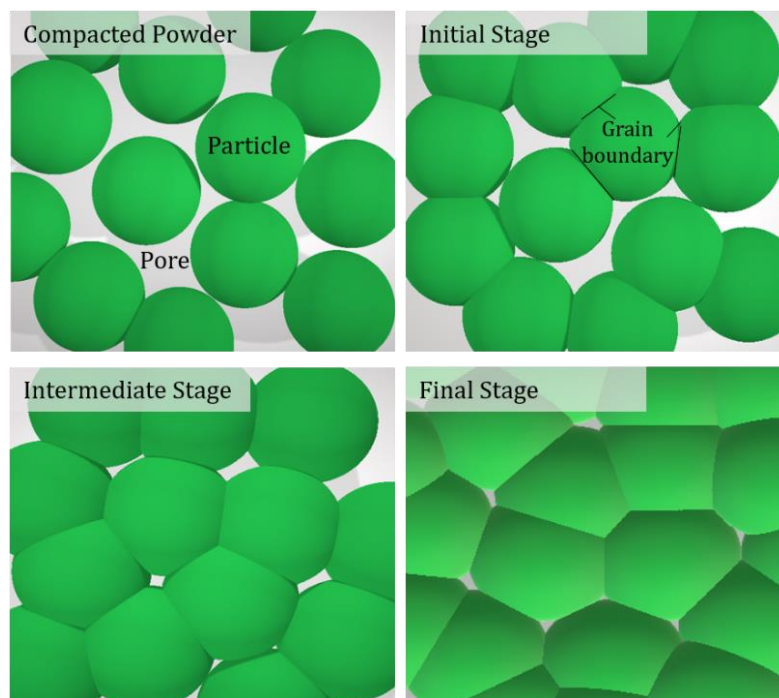


Figure II-16: Graphical representation of the different stages of solid state sintering from a powder compacted with spherical particles of the same size.

Table II- 6: Changes observed during the three stages of solid state sintering (X = neck size, D = particle diameter, ΔL = length variation, L_0 = initial length, S = specific area, S_0 = initial specific area) [25].

Parameter	Initial stage	Intermediate stage	Final stage
Neck size ratio, X/D	<0.33	0.33 - 0.5	> 0.5
Relative density, %	60 - 66	66 - 92	> 92
Linear shrinkage, $\Delta L/l_0$ %	<3	3 - 13	> 13
Surface area, S/S_0 %	100 - 50	50 - 10	<10

2.2.1.1 Initial Stage

This stage is initiated at particle contact points by weak Van der Waals cohesive forces. Contact pressure is often estimated at 1 MPa [25]. The particle rearrangement takes place and the geometry of the contacts evolves with sintering. The neck growth is accompanied by interparticle shrinkage. At the end of the initial stage, the initial surface energy is reduced by almost 50 %, the ratio X/D is less than 0.33, the relative density of the material varies between 60 and 66 % and the reduction of the specific surface area less than 50 %.

2.2.1.2 Intermediate Stage

It is the main part of the densification process during which different phenomena govern the evolution of the microstructure. Important geometric changes in the pore shape occur, leading to an interconnected pore structure made of cylindrical pores along three grains edges (Figure II-16). The densification often observed towards the end of the intermediate stage, is due to the mobility of the grain boundaries in the compact densifying and consisting of an essential area of solid-solid interfaces. At the end of this stage, the system is described as a stack of polyhedral grains linked by their faces and the relative density reached is about 92%.

2.2.1.3 Final Stage

Final stage occurs when most of the pores shrink. The porous network left in the previous stage becomes geometrically unstable, as the density increases the pores spheroidize and are no longer connected. At this stage, the closed porosity is difficult to remove, densification is slowed down and accompanied by grain growth.

2.2.2 Constrained sintering under pressure

The application of pressure during the sintering of a compact allows improving the rate of densification at the same temperature, compared to free sintering (without pressure application). The applied pressure also influences the rearrangement stage (particles sliding) and allows to eliminate agglomerates, particularly for nanometric powders.

The applied pressure increases the contact between particles providing additional energy W that is quantitatively estimated with Eq. (2.5).

$$W = P\beta \quad (\text{Eq. 2.5})$$

Where W is the energy supplied by the pressure, P is the applied pressure and β the volume of a mole of particle.

The use of pressure during sintering is an efficient approach to improve densification while minimizing grain growth [26][27].

2.3 Conventional sintering method

Conventional sintering is most commonly used for its simplicity of implementation. Heat treatment is carried out at temperature below the melting temperature of the main components of the material, allowing the formation of bonds between particles through diffusion of matter [28]. In addition to its simple implementation, this technology is the least limited in terms of shape and size of materials that can be sintered. However, it is a high energy consumption process since densification relies on the diffusion mechanisms activated at high temperatures.

Conventional sintering is carried out in electric furnaces, some with the potential to reach 3000 °C while controlling the sintering atmosphere. Heat is transmitted to the sample by convection and radiation mechanisms, so temperature gradients may exist between the surface and the sample volume [29][30].

2.3.1 Shaping (case of ceramics)

2.3.1.1 Powder blending

Ceramic powders usually incorporate additives as sintering aids to decrease high sintering temperatures and to inhibit grain growth. The mixing also includes a lubricant/binder (e.g. stearic acid, zinc stearate, organic) which have several functions:

- Powder flows more easily.
- Die friction is reduced, so more uniform product density is achieved, part is ejected without cracking and die life is increased.

This process is carried out in the same way as described in section 1.4.4 "Powder milling", of this chapter.

2.3.1.2 Compaction

The powder is pressed into a shaped mold/die at high pressure: e.g. 350-800 MPa for steels, 70-275 MPa for aluminum and 100-150 MPa for alumina molds. Presses need capacities (maximum force) up to hundreds of tons force (several MN) to achieve these pressures. The press capacity usually limits the size of the part that can be formed. The compact, called the 'green compact', remains fragile and must be handled carefully.

For ceramic materials, the linear dimensions of the green compact will be 15-20 % greater than those of the sintered body due to the porosity (up to 50 %). For metals, the powder particles themselves deform during compaction and the green compact has a similar density to the final product (up to 95 % of bulk metal); there is little or no shrinkage during sintering [31]. This compaction step can be carried out using different methods (uniaxial or isostatic pressure). For the screen-printed samples isostatic pressing beforehand conventional sintering step is necessary in order to improve densification and adhesion between layers [32].

2.3.2 Pressing

2.3.2.1 Uniaxial pressing (case of ceramics)

Uniaxial pressing involves the compaction of powder into a rigid die by applying pressure in a single axial direction through a rigid punch or piston. The presses are usually mechanical or hydraulic.

In the framework of this thesis, the ceramic discs are shaped using a manual hydraulic press (Specac press KBR) located at IMS laboratory, with a gradual application of a load of 2.5 tons for a 13 mm diameter steel die.

2.3.2.3 Isostatic pressing (case of printed thick films)

Isostatic pressing is used to compact the printed samples placed in a flexible plastic bag. This sealed container (sealed after vacuum) is the mold for the sample, fluid pressure is exerted over the entire outside surface of the container.

The pressure exerted by the fluid during isostatic pressing manufacture, provides uniform compaction of the sample. Isostatic pressing is commonly used over conventional metallurgical techniques to produce large quantities, have high thickness to diameter ratios, or for superior material properties. Isostatic pressing tends to have long cycle times and is preferred for short production runs. This manufacturing process consists of two main categories, cold isostatic pressing and hot isostatic pressing.

In the framework of this thesis, the pressing of the different layers of the printed structures, are carried out at the EXXELIA TEMEX society (Pessac, France) using an isostatic pressure of 40 MPa at 65 °C during 4 min.

2.3.3 Sintering of screen-printed thickfilms by conventional method

The dried and pressed screen-printed layers are then sintered. The duration of a classical conventional sintering cycle in an oxidizing (air) or neutral (nitrogen) atmosphere is approximately 60 minutes with a 10-15 minutes step at temperature between 850 °C and 950 °C depending on the inks. Different events occur during the heat treatment (Figure II-17):

- From ambient temperature to 500 °C: decomposition of binders of high molecular weight (debinding). Oxygen supply is required at this stage, as well as elimination of combustion or decomposition products.
- From 500 °C to 800 °C, softening of the particles of the vitreous binder is carried out and sintering process begins.
- From 750 °C up to the sintering temperature, the vitreous binder becomes liquid and wets the particles. The grains are getting closer, the sintering becomes faster and the contact between the glass and the substrate starts to reach adhesion.

- At the sintering temperature, densification continues as the chemical and mechanical interactions between the substrate and the layer are favored by the presence of vitreous binders or oxides.
- During cooling, the glass phase gradually solidifies and seals the layers on the substrate. The layer generally brings mechanical constraints to the substrate. These are applied to the layer-substrate interface.

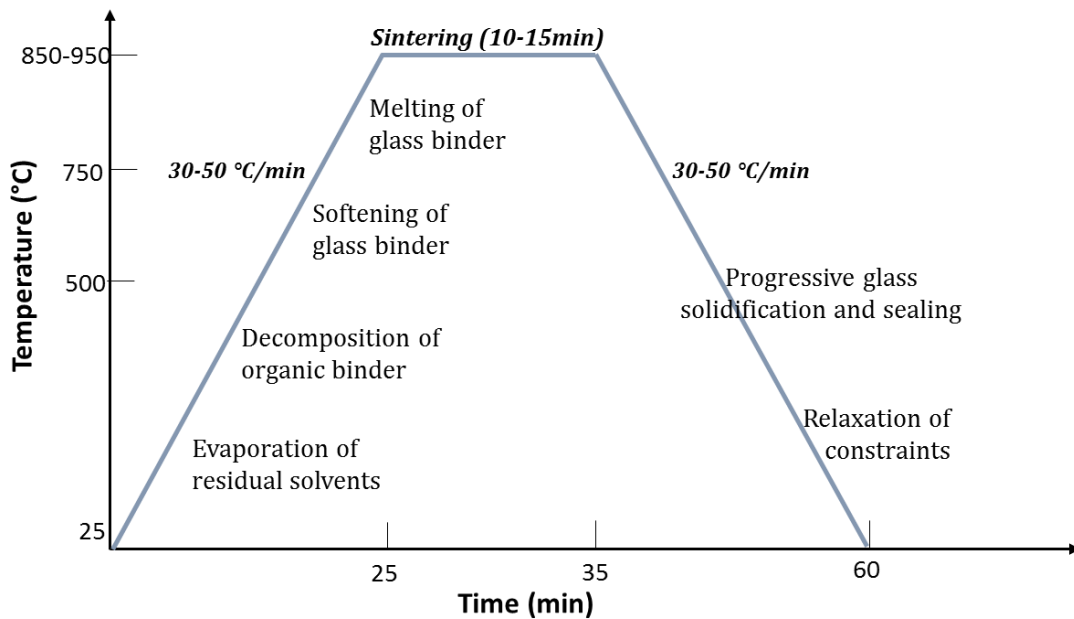


Figure II-17: Different events occurring during conventional sintering cycle of screen-printed layers.

After the heat treatment, the thick layers show residual porosity due in part to the voids left after the removal of the organic binder (Figure II-18)[6]. In some specific cases, a significant level of porosity can be desired, for example in the case of some ferroelectric layers when vibrations in the thickness mode (k_{33} , d_{33} ...) are targeted [33][34] or gas sensors [35], but it is often inadequate for several applications [36][37], in particular when good mechanical properties are required. For example, in the case of conductive inks (Figure II-19), the lack of compactness contributes to the increase in the resistivity of thick layers compared to that of bulk materials.

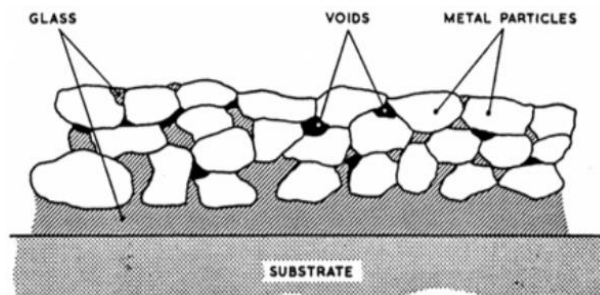


Figure II-18: Microstructure of a thick-film layer after firing. (Image from [38])

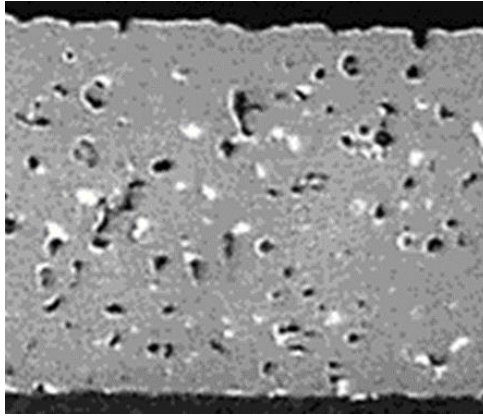


Figure II-19: Cross-section view of a screen-printed copper layer sintered at 900 °C (M=300). (Image from [39])

In general depending on the ink nature, several solutions can be considered to control the compactness of the screen-printed deposits.

- The most common solution is the introduction of a glass phase in more or less high concentration. It softens at the sintering temperature, wets the grains, brings them closer together, and fills the intergranular zones. As a result, the deposit is obtained with low porosity.

In the case of dielectric inks, the glass phase must be added in limited quantities, otherwise the dielectric constant will drop significantly. This glass phase can be for example a lead borosilicate with a low melting point (ternary system $\text{Bi}_2\text{O}_3\text{-SiO}_2\text{-PbO}$ melting at 500 °C) or a glass that recrystallizes on cooling (ternary system $\text{Al}_2\text{O}_3\text{-SiO}_2\text{-BaO}$). In the case of resistive inks, the glass phase allows to limit the porosity but also to modify the electrical resistance of the layer. In this case, the most commonly used glass phase is lead borosilicate.

In addition to reduce the porosity of the layer, the glass phase also promotes adhesion of the deposit onto the substrate. For example, placed on ceramic substrates, the glass phase is present at the interface between the ceramic and the deposit. On cooling, the glass phase solidifies and ensures adhesion of the deposit to the substrate. Good compatibility between the coefficients of thermal expansion of the glass and the substrate is necessary.

- When the presence of a glass phase is problematic (for example, in the case of conductive inks), a low level of porosity can be achieved by increasing sintering temperature ($850 < T$ (°C) < 950) close to the melting temperature of the metals ($T_m(\text{Ag})=961$ °C, $T_m(\text{Au})=1063$ °C, $T_m(\text{Cu})=1083$ °C, ...). However, a small quantity of glass phase (2 to 10 % in volume of lead borosilicate) or of reactive binder (3 % in volume of CdO , CuO or Al_2O_3) does not significantly affect the properties of the layer.
- When the active components of the ink have a very high melting temperature (1250 °C-1400 °C), which is the case for most oxides, the limitation of the sintering temperature below 1000 °C is not enough to ensure proper sintering of the thick layers. In this case, it is possible to add a mineral phase compatible with the active material whose role is to cause intergranular melting via an eutectic composition. This phenomenon of dissolution-precipitation by formation of a transient liquid phase at a temperature close to the

sintering temperature accelerates and improves the densification of the material and consequently reduces the porosity.

2.3.4 Furnace set-up for conventional sintering

Figure II-20 shows the furnace used in the framework of this thesis (AET technologies vertical furnace). The furnace consists of a 16 cm inner diameter ceramic quartz tube vertically positioned, at the top of which a high temperature resistance heating to 1100 °C is located. This system creates a temperature gradient in the tube. A quartz rod and a quartz support (sample holder) allow to move the samples into the tube. An engine attached to the base of the quartz rod and a worm gear allows to control the position and speed of movement of the samples. A type K thermocouple allows to supervise the temperature of the samples. Speed variations and the position of the samples in the tube correspond respectively to variations of temperature gradients and temperature values. This system allows to reach heating and cooling ramps of maximum 100 °C/min while maintaining the possibility of long holding time at a fixed temperature. The oven also allows to perform sintering in controlled atmosphere (air or nitrogen).

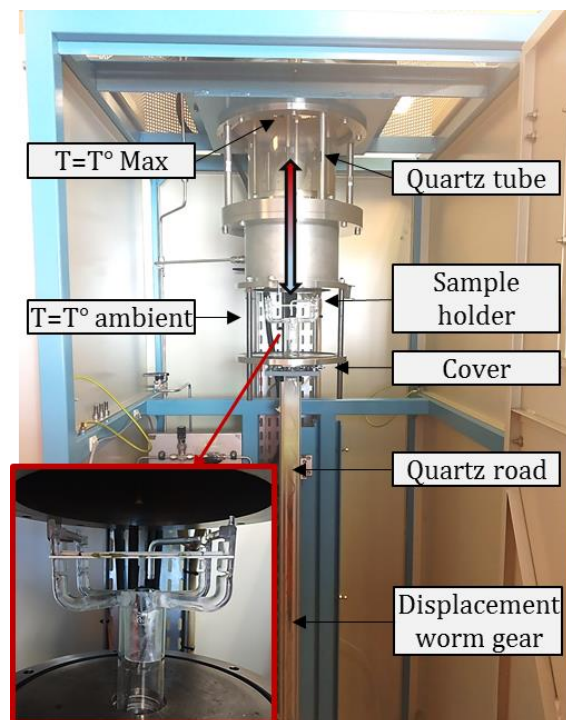


Figure II-20: Furnace used for conventional sintering (AET technologies vertical furnace) used at IMS laboratory.

2.4 Spark Plasma Sintering (SPS)

ECAS (Electric Current Activated/Assisted Sintering) technology has many variants such as the Pulsed Electric Current Sintering (PECS), the Plasma Assisted Sintering (PAS), the Pulse Discharge Sintering (PDS), and the Flash Sintering (FS). Spark Plasma Sintering (SPS) is a non-conventional sintering technique that belongs to this ECAS group and to the techniques called FAST (Field Assisted Sintering Technique). It consists on the simultaneous application of a uniaxial pressure and an electrical current. This technique differs from others in its specific method of heating the sample. Heating is carried out by passing a pulsed electric current of high intensity and low voltage through the electrodes of the press, the punches, the matrix (in graphite or WC-Co) and sometimes through the sample if conductive. When the sample is an insulator, the current only passes through the mold [40], this current allows the temperature to rise by Joule effect heating.

The most appealing features of SPS lies on the high heating rates, allowing to achieve high densification in fast thermal cycles. As a consequence, this technique has been the most widely used technology among ECAS technologies in recent years.

For this process, the powder is loaded in a die (typically graphite) whose inner wall has been previously covered with a graphite foil (papyex) (Figure II-21) used to prevent possible reactions between the matrix and the material, but also to facilitate the release of the sample from the mold. A graphite foil disc is also placed between the powder and the pistons. The matrix is placed between the graphite spacers that will be used to drive and concentrate the current from the electrodes, as well as to transmit the pressure applied to the sample. The current flow allows the temperature to rise by Joule effect. This current gets through punches, and can also pass totally or partially through the powder according to the electric conductivity of the material to sinter [40]. The matrix transfers the heat produced by conduction towards the core of the sample. For conventional sintering methods, such as natural sintering and resistive hot pressing, the heating of the furnace resistances allows the temperature rise, the heat created is transferred by convection/radiation leading to longer heating times in contrast with SPS.

In the majority of cases, this assembly (matrix + punches) is in graphite so that sintering temperatures can reach more than 2000 °C, but the pressure is limited to 100 MPa. However, it is possible to use other materials such as steel or ultra-hard carbide systems. In this case, the temperature is limited to 900 °C (100MPa), and the applied pressure can reach 900 MPa (100°C) for a tungsten carbide system. SPS sintering process is usually done with primary vacuum, using controlled atmospheres (neutral, nitrogen, argon).

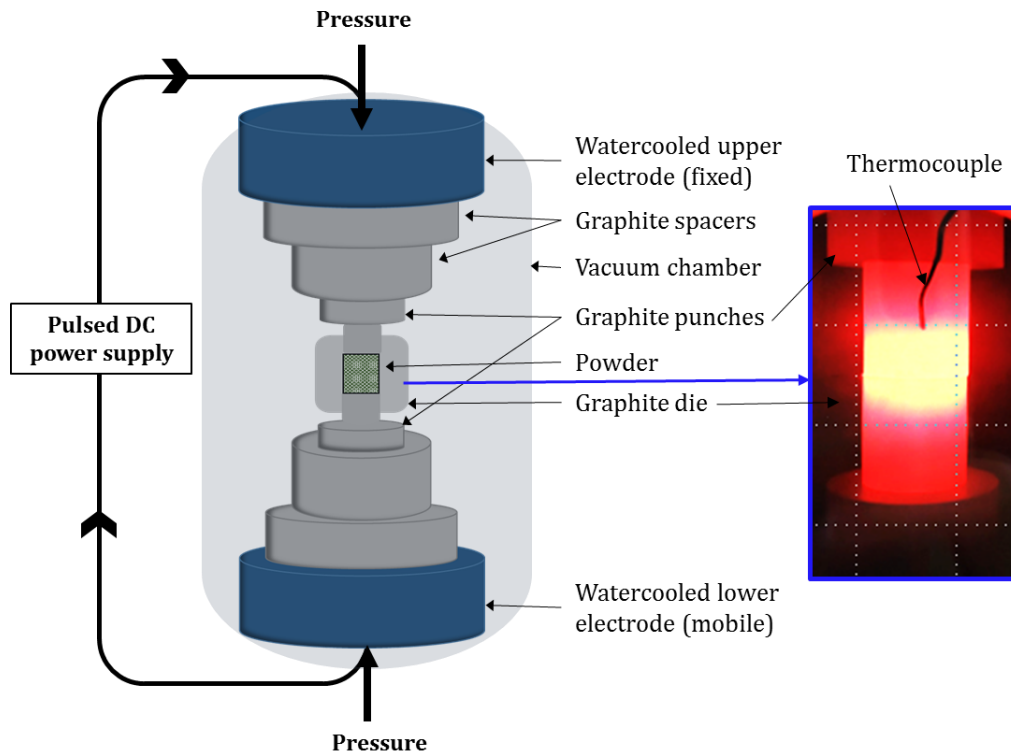


Figure II-21: Schematic of the SPS sintering process.

The experimental parameters that have a strong influence on the densification in SPS are mainly the temperature, the applied pressure, and the heating and cooling rates. During a SPS cycle, the temperature can be measured by an optical pyrometer (at the surface of the die, or the top piston from above) and by a thermocouple placed at the closest to the sample. The comparison of these two methods of measurement can lead to a difference of several tens of degrees [41].

The applied force is in between 3 kN and 50 kN (considering SYNTEX SPS-515S) and is converted to a pressure considering the diameter of the mold. Throughout the SPS cycle, a sensor records the displacement of the set-up between the electrodes along the compaction axis, allowing to observe the dilatation/contraction effects which can be useful for reproducibility process behavior when considering samples of same nature.

The heating rates can reach several hundred degrees per minute which represents a significant advantage of SPS technology compared to more conventional methods, where the heating speed is limited to a maximum of a few tens of degrees per minute. Cooling is done by natural or controlled ramp.

The SPS is recognized as a very efficient technology to sinter a wide range of materials, whether they are electrical/thermal conductors or insulators [42]–[44]. It can be used to consolidate functional, new or unusual materials, nanomaterials, and multi-materials [45]–[47]. SPS allows to sinter materials at lower temperature and shorter time than conventional or hot pressing techniques. This represents a significant advantage for materials hard to sinter by conventional techniques, for nanostructured materials as well as for controlling interfaces in multi-materials.

This technique is generally used without the use of sintering aids. Some examples of materials sintered by SPS are:

- Metals: nanocrystalline iron [48], aluminum powder [41], iron molybdenum alloy [49], Mo-Si-Mo Multi-Layer Metal Assembly [50], formation of a new phase ($\text{Cu}_x\text{V}_2\text{O}_5$) by direct interaction of metallic copper with vanadium oxide V_2O_5 [51].
- Ceramics: oxides (Al_2O_3 - γ [52], Al_2O_3 - α [53], Y_2O_3 [54], YAG [54], MgO [54], ZrO_2 [55], ZnO [56]), superconducting YBaCuO [57], non-oxides (sintering of translucent AlN [58] , SiC [59], cubic BN [60]), cermets ($\text{TiB}_2 + \text{Cu}$, $\text{ZrB}_2 + \text{Cu}$ [61])
- Composites: several ceramic-metal, ceramic-intermetallic, ceramic-ceramic composites have been sintered by SPS, such as WC-Co [62], alumina-TiC-Ni [63], TiB_2 -SiC [64], $\text{Si}_3\text{N}_4/\text{SiC}$ [65], $\text{Si}_3\text{N}_4/\text{BN}$ [66], CuTiZrNiSnSi alloy from a mixture of amorphous powders and copper powder. Cu particles provide ductility to the final product [67].
- Polymers: polyethylene, polypropylene and polyimide [68].

2.4.1 SPS Machine

The SPS equipment used during this thesis work is a SYNTEX Dr. Sinter lab. 515- S (Figure II-22). This equipment located in the ICMCB laboratory allows to reach a temperature of ~ 2500 °C with a maximum heating rate of 500 °C/min. It provides the option to monitor the temperature by a thermocouple (25 °C - 900 °C) and optical pyrometer (600 °C – 3000 °C) control. The uniaxial press has a maximum load of 50 kN.

In the framework of this thesis, only the thermocouple is used, under a vacuum atmosphere with a primary vacuum (6-10 Pa)) with a pulsed direct current (12-2 On/Off). For ceramic pellets and multilayer structures, graphite molds of 10 mm and 30 mm have been respectively used.

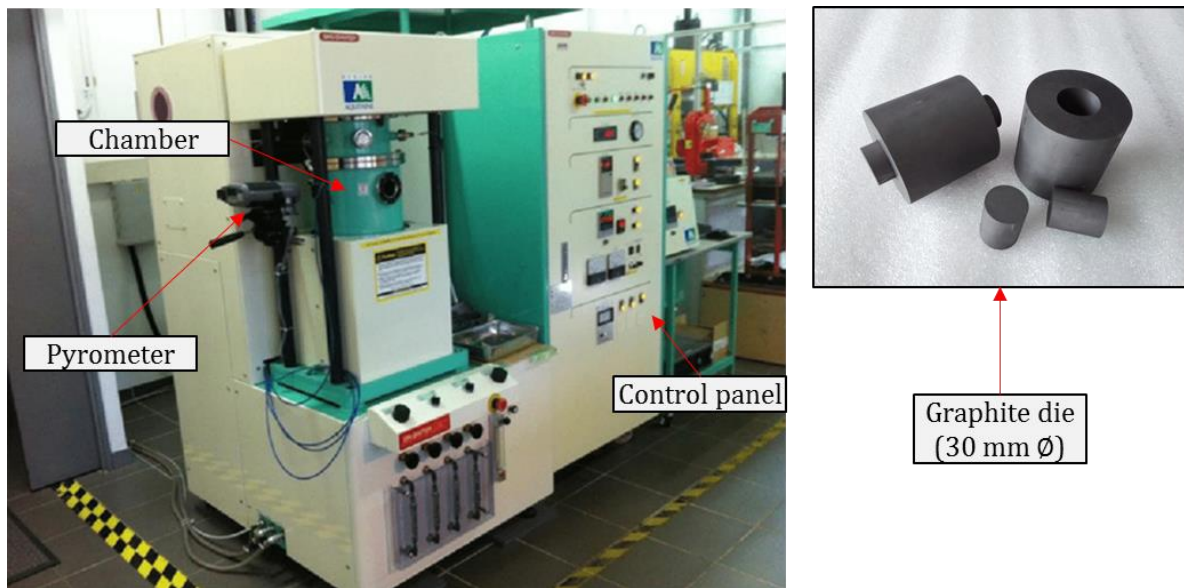


Figure II-22: SPS Doctor Sinter lab. 515- S used at ICMCB Laboratory.

2.4.2 Partial conclusion

Some advantages and limitations of SPS can be underlined:

Benefits:

- Rapid sintering process
- Higher densification rates
- Lower sintering temperatures
- Controlled/limited/supressed grain growth (nanomaterials)
- Compaction and sintering steps are combined in one step
- Efficient process suitable for all kinds of materials
- Easy to use
- Versatility of the process

Limitations:

- Thermal gradients can be expected in large sample (scale up)
- Simple geometric shapes are mostly performed but complex shape are under development (French Patent FR1560654 (2015) [69][70][71])
- Pulsed Current Generator Cost
- Contamination with carbon (additional post sintering heat treatment performed at 800-100 °C)
- Mass production still limited
- Reducing environment

The trend towards lower energy consumption while keeping optimum reliability requires an optimization of the sintering stage decreasing the sintering temperature, limiting the number of

thermal treatments and controlling the chemistry according to the sintering environment. Such an optimization is mandatory in particular when processing complex devices such as integrated printed thick-films, for which the co-sintering/assembly with metals remains challenging. In this context, the use of advanced sintering process such as Spark Plasma Sintering appears as a relevant approach given its specificities: fast kinetics, lower sintering temperatures and short sintering cycles.

References

- [1] S. Schmitt, *La microélectronique hybride : la couche épaisse*. Hermès, 1990.
- [2] I. Sanchez Associates, "Servo Loop hybrid circuit," Massachusetts.
- [3] A. Malik and B. Kandasubramanian, "Flexible Polymeric Substrates for Electronic Applications," *Polym. Rev.*, vol. 58, no. 4, pp. 630–667, Oct. 2018.
- [4] C. Lucat, P. Ginet, C. Castille, H. Debéda, and F. Ménil, "Microsystems elements based on free-standing thick-films made with a new sacrificial layer process," *Microelectron. Reliab.*, vol. 48, no. 6, pp. 872–875, 2008.
- [5] M. L. Topfer, "Thick-film microelectronics; fabrication, design, and applications." Van Nostrand Reinhold Co., New York, pp. x, 210 p., 1971.
- [6] N. White, "Thick Films," in *Springer Handbook of Electronic and Photonic Materials*, Springer International Publishing, 2017, pp. 1–1.
- [7] B. Ziaie, A. Baldi, and M. Atashbar, "Introduction to Micro/Nanofabrication," in *Springer Handbook of Nanotechnology*, Berlin, Heidelberg: Springer Berlin Heidelberg, 2007, pp. 197–238.
- [8] G. Hu, H. Edwards, and M. Lee, "Silicon integrated circuit thermoelectric generators with a high specific power generation capacity," *Nat. Electron.*, vol. 2, no. 7, pp. 300–306, Jul. 2019.
- [9] D. Briand and J. Courbat, "Micromachined semiconductor gas sensors," in *Semiconductor Gas Sensors*, Elsevier, 2020, pp. 413–464.
- [10] M. Koch, N. Harris, and R. Maas, "The dynamic micropump driven with a screen printed PZT actuator related content A novel micropump design with thick-film piezoelectric actuation," 1998.
- [11] S. M. F. Cruz, L. A. Rocha, and J. C. Viana, "Printing Technologies on Flexible Substrates for Printed Electronics," in *Flexible Electronics*, InTech, 2018.
- [12] V. Thenot, "Impression et recuits sélectifs d'encre métalliques sur papier – Optimisation des propriétés électriques de boucles RFID-HF en vue d'une production industrielle," 2017.
- [13] G. Radosavljevic and W. Smetana, *Printed films - 15*. Woodhead Publishing Limited, 2012.
- [14] S. J. Stein, R. Wahlers, M. Heinz, M. A. Stein, R. Tait, and R. Humphries, "Thick Film Heaters Made From Dielectric Tape Bonded Stainless Steel Substrates," in *Microelectronics 1995*, 1995, vol. 2649, p. 125.
- [15] S. C. Lin and W. J. Wu, "Piezoelectric micro energy harvesters based on stainless-steel substrates," *Smart Mater. Struct.*, vol. 22, no. 4, 2013.
- [16] J. D. Goddard, "Mechanics of Non-Newtonian Fluids. By W. R. S CHOWALTER . Pergamon Press," *J. Fluid Mech.*, vol. 100, no. 03, p. 671, Oct. 1980.
- [17] M. Prudenziati and B. Morten, "Thick-film sensors: an overview," *Sensors and Actuators*, vol. 10, no. 1, pp. 65–82, 1986.
- [18] M.-P. Martin, "Réalisation de varistances sérigraphiées à base de ZnO pour des applications en électronique de puissance : influence des électrodes sur les propriétés électriques du composant de protection," Université de Bordeaux, 2003.
- [19] H. A. Barnes and D. Bell, "Controlled-stress rotational rheometry : An historical review," 2003.
- [20] E. Roblot, P. Grosseau, B. Guillhot, B. Classen, C. Haehnel, and E. Gaffet, *A study on the action mechanisms of grinding aids used for clinker comminution*. 2005.
- [21] I. Bauman, D. Curic, and M. Boban, "Mixing of solids in different mixing devices," *Sadhana*,

- vol. 33, pp. 721–731, Dec. 2008.
- [22] “Exakt Technologies.” [Online]. Available: <https://exaktusa.com/>. [Accessed: 01-Oct-2019].
- [23] E. Olevsky, “Sintering Theory,” Darmstadt Int. Spring Sch. F. Assist. Sinter. Tech., 2011.
- [24] R. M. German, “Sintering theory and practice,” *Solar-Terrestrial Phys.*, p. 568, 1996.
- [25] R. M. German, “Sintering,” in *Encyclopedia of Materials: Science and Technology*, Elsevier, 2001, pp. 8641–8643.
- [26] D. Bernache-Assollant, *Chimie-physique du frittage*. Hermes Science Publications, 1993.
- [27] Z. A. Munir, U. Anselmi-Tamburini, and M. Ohyanagi, “The effect of electric field and pressure on the synthesis and consolidation of materials: A review of the spark plasma sintering method,” *Journal of Materials Science*, vol. 41, no. 3, pp. 763–777, Feb-2006.
- [28] R. H. R. Castro, “Overview of Conventional Sintering,” 2012, pp. 1–16.
- [29] F. Paul, W. Meneskloou, G. Link, X. Zhou, J. Haußelt, and J. Binder, “Impact of microwave sintering on dielectric properties of screen printed Ba_{0.6}Sr_{0.4}TiO₃ thick films,” *J. Eur. Ceram. Soc.*, vol. 34, pp. 687–694, Mar. 2014.
- [30] P. Yadoji, R. Peelamedu, D. Agrawal, and R. Roy, “Microwave sintering of Ni-Zn ferrites: Comparison with conventional sintering,” *Mater. Sci. Eng. B Solid-State Mater. Adv. Technol.*, vol. 98, no. 3, pp. 269–278, Apr. 2003.
- [31] I. Hutchings, “Powder Processing,” 2012.
- [32] S. Gouverneur, “Mise au point d’un nouveau procédé de densification de couches épaisses sérigraphiées : application à la fabrication de composants passifs,” <http://www.theses.fr>, Jan. 1994.
- [33] C. R. Bowen, V. Y. Topolov, and H. A. Kim, “Piezoelectric mechanical energy harvesters and related materials,” *Springer Ser. Mater. Sci.*, vol. 238, pp. 113–138, May 2016.
- [34] G. Martínez-Ayuso et al., “Model Validation of a Porous Piezoelectric Energy Harvester Using Vibration Test Data,” *Vibration*, vol. 1, no. 1, pp. 123–137, 2018.
- [35] Y. A. Perera-Mercado, G. C. Leon, and G. P. Piñerez, “Porous Ceramic Sensors: Hydrocarbon Gas Leaks Detection,” in *Recent Advances in Porous Ceramics*, InTech, 2018.
- [36] H. Debeda, “Dispositifs multi-capteurs sélectifs au méthane, réalisés en technologie microélectronique hybride couches épaisses,” 1996.
- [37] M. Kosec, J. Holc, B. Malič, and V. Bobnar, “Processing of high performance lead lanthanum zirconate titanate thick films,” *J. Eur. Ceram. Soc.*, vol. 19, no. 6–7, pp. 949–954, Jun. 1999.
- [38] IDC Technologies - Technology Training that Works, “Thick film technology.”
- [39] H. Debeda, M. . Rachidi, F. Menil, and C. Lucat, “New metallized alumina substrates for powder hybrids,” *Ind. Ceram.*, vol. 21, no. 1, April, p. 34-36, 2001.
- [40] S. Grasso, Y. Sakka, and G. Maizza, “Electric current activated/assisted sintering (ECAS): A review of patents 1906-2008,” *Science and Technology of Advanced Materials*, vol. 10, no. 5, 20-Nov-2009.
- [41] U. Anselmi-tamburini, S. Gennari, J. Garay, and Z. A. Munir, “Fundamental investigations on the spark plasma sintering/synthesis process: II. Modeling of current and temperature distributions,” *Mater. Sci. Eng. A*, vol. 394, pp. 139–148, Mar. 2005.
- [42] C. Elissalde et al., “Single-step sintering of zirconia ceramics using hydroxide precursors and Spark Plasma Sintering below 400 °C,” *Scr. Mater.*, vol. 168, pp. 134–138, Jul. 2019.
- [43] G. Motsi, S. Guillemet-Fritsch, G. Chevallier, M. Shongwe, P. Olubambi, and C. Estournès, “Microstructural evolution and mechanical properties of pure titanium powders processed by spark plasma sintering,” *Powder Technol.*, vol. 345, Mar. 2019.
- [44] A. Fregeac, F. Ansart, S. Selezneff, and C. Estournès, “Relationship between mechanical

- properties and microstructure of yttria stabilized zirconia ceramics densified by spark plasma sintering,” *Ceram. Int.*, Aug. 2019.
- [45] C. Guiderdoni et al., “The preparation of carbon nanotube (CNT)/copper composites and the effect of the number of CNT walls on their hardness, friction and wear properties,” *Carbon N. Y.*, vol. 58, pp. 185–197, 2013.
- [46] R. Chaim, R. Marder, C. Estournès, and Z. Shen, “Densification and preservation of ceramic nanocrystalline character by spark plasma sintering,” *Adv. Appl. Ceram.*, vol. 111, no. 5–6, pp. 280–285, Aug. 2012.
- [47] A. Kasperski, A. Weibel, C. Estournès, C. Laurent, and A. Peigney, “Multi-walled carbon nanotube–Al₂O₃ composites: Covalent or non-covalent functionalization for mechanical reinforcement,” *Scr. Mater.*, vol. 75, pp. 46–49, 2014.
- [48] B. Srinivasarao, K. Oh-ishi, T. Ohkubo, T. Mukai, and K. Hono, “Synthesis of high-strength bimodally grained iron by mechanical alloying and spark plasma sintering,” *Scr. Mater.*, vol. 58, no. 9, pp. 759–762, May 2008.
- [49] S. Libardi, M. Zadra, F. Casari, and A. Molinari, “Mechanical properties of nanostructured and ultrafine-grained iron alloys produced by spark plasma sintering of ball milled powders,” *Mater. Sci. Eng. A-structural Mater. Prop. Microstruct. Process.*, vol. 478, pp. 243–250, Apr. 2008.
- [50] W. Chen, U. Anselmi-Tamburini, J. E. Garay, J. R. Groza, and Z. A. Munir, “Fundamental investigations on the spark plasma sintering/synthesis process: I. Effect of dc pulsing on reactivity,” *Mater. Sci. Eng. A*, vol. 394, no. 1–2, pp. 132–138, Mar. 2005.
- [51] J. Galy, M. Dolle, T. Hungria, P. Rozier, and J. P. Monchoux, “A new way to make solid state chemistry: Spark plasma synthesis of copper or silver vanadium oxide bronzes,” *Solid State Sci.*, vol. 10, no. 8, pp. 976–981, Aug. 2008.
- [52] R. S. Mishra, J. A. Schneider, J. F. Shackelford, and A. K. Mukherjee, “Plasma activated sintering of nanocrystalline γ -Al₂O₃,” *Nanostructured Mater.*, vol. 5, no. 5, pp. 525–544, 1995.
- [53] G. Bernard-Granger and C. Guizard, “Densification mechanism involved during spark plasma sintering of a codoped α -alumina material: Part I. Formal sintering analysis,” *J. Mater. Res.*, vol. 24, no. 1, pp. 179–186, Jan. 2009.
- [54] R. Chaim, A. Shlayer, and C. Estournes, “Densification of nanocrystalline Y₂O₃ ceramic powder by spark plasma sintering,” *J. Eur. Ceram. Soc.*, vol. 29, no. 1, pp. 91–98, Jan. 2009.
- [55] G. Bernard-Granger and C. Guizard, “Spark Plasma Sintering of a Commercially Available Granulated Zirconia Powder: I. Sintering Path and Hypotheses About the Mechanism(S) Controlling Densification,” *Acta Mater.*, vol. 55, pp. 3493–3504, Jun. 2007.
- [56] B. Dargatz et al., “FAST/SPS sintering of nanocrystalline zinc oxide-Part I: Enhanced densification and formation of hydrogen-related defects in presence of adsorbed water,” *J. Eur. Ceram. Soc.*, vol. 36, no. 5, pp. 1207–1220, Apr. 2016.
- [57] J. R. Groza and A. Zavaliangos, “Sintering Activation by External Electrical Field,” *Mater. Sci. Eng. A*, vol. 287, pp. 171–177, Aug. 2000.
- [58] Y. Xiong, Z. Y. Fu, and H. Wang, “Microstructural effects on the transmittance of translucent AlN ceramics by SPS,” *Mater. Sci. Eng. B Solid-State Mater. Adv. Technol.*, vol. 128, no. 1–3, pp. 7–10, Mar. 2006.
- [59] F. Guillard, A. Allemand, J. D. Lulewicz, and J. Galy, “Densification of SiC by SPS-effects of time, temperature and pressure,” *J. Eur. Ceram. Soc.*, vol. 27, no. 7, pp. 2725–2728, 2007.
- [60] Y. Zhao and M. Wang, “Effect of sintering temperature on the structure and properties of polycrystalline cubic boron nitride prepared by SPS,” *J. Mater. Process. Technol.*, vol. 209,

- no. 1, pp. 355–359, Jan. 2009.
- [61] T. Venkateswaran, B. Basu, G. B. Raju, and D. Y. Kim, “Densification and properties of transition metal borides-based cermets via spark plasma sintering,” *J. Eur. Ceram. Soc.*, vol. 26, no. 13, pp. 2431–2440, 2006.
- [62] B. Yaman and H. Mandal, “Spark plasma sintering of Co-WC cubic boron nitride composites,” *Mater. Lett.*, vol. 63, no. 12, pp. 1041–1043, May 2009.
- [63] T. Rodriguez-Suarez et al., “Electroconductive Alumina-TiC-Ni nanocomposites obtained by Spark Plasma Sintering,” *Ceram. Int.*, vol. 37, no. 5, pp. 1631–1636, 2011.
- [64] M. Singlard et al., “Spark plasma sintering and mechanical properties of compounds in TiB₂-SiC pseudo-diagram,” *Ceram. Int.*, vol. 44, no. 18, pp. 22357–22364, 2018.
- [65] D. S. Perera, M. Tokita, and S. Moricca, “Comparative Study of Fabrication of Si₃N₄/SiC Composites by Spark Plasma Sintering and Hot Isostatic Pressing,” *J. Eur. Ceram. Soc.*, vol. 18, no. 4, pp. 401–404, 1998.
- [66] Y. L. Li, R. X. Li, and J. X. Zhang, “Enhanced mechanical properties of machinable Si₃N₄/BN composites by spark plasma sintering,” *Mater. Sci. Eng. A*, vol. 483–484, no. 1-2 C, pp. 207–210, Jun. 2008.
- [67] C. K. Kim, S. Lee, S. Y. Shin, and D. H. Kim, “Microstructure and mechanical properties of Cu-base amorphous alloy matrix composites consolidated by spark plasma sintering,” *Mater. Sci. Eng. A*, vol. 449–451, pp. 924–928, Mar. 2007.
- [68] M. Omori, “Sintering, consolidation, reaction and crystal growth by the spark plasma system (SPS),” *Mater. Sci. Eng. A*, vol. 287, no. 2, pp. 183–188, Aug. 2000.
- [69] C. Estournès, C. Manière, and L. Durand, “French Patent number FR1560654 .deposited the 04/11/2015.”
- [70] C. Manière, E. Nigito, L. Durand, A. Weibel, Y. Beynet, and C. Estournès, “Spark plasma sintering and complex shapes: The deformed interfaces approach,” *Powder Technol.*, vol. 320, pp. 340–345, 2017.
- [71] C. Manière et al., “Chapter 3 - How to overcome the main challenges of SPS technology: Reproducibility, multi-samples and elaboration of complex shapes,” G. Cao, C. Estournès, J. Garay, and R. B. T.-S. P. S. Orrù, Eds. Elsevier, 2019, pp. 77–108.

Chapter III

Experimental Methods

Content

1	PHYSICO-CHEMICAL CHARACTERIZATIONS	92
1.1	PARTICLE SIZE DISTRIBUTIONS	92
1.2	DENSITY MEASUREMENT	92
1.3	LAYER THICKNESS MEASUREMENT	93
1.4	X-RAY DIFFRACTION	94
1.5	SCANNING ELECTRON MICROSCOPY (SEM)	95
1.5.1	Principle and equipment	95
1.5.2	Samples preparation	95
1.5.3	Images analysis	96
2	THERMAL ANALYSES	96
2.1	THERMOGRAVIMETRIC ANALYSIS (TGA)	96
2.2	DILATOMETRY	96
3	DIELECTRIC AND ELECTROMECHANICAL CHARACTERIZATIONS	97
3.1	SAMPLE PREPARATION	97
3.2	DIELECTRIC MEASUREMENTS	97
3.2.1	Basics	97
3.2.2	Set-up	98
3.3	ELECTROMECHANICAL CHARACTERIZATIONS	99
3.3.1	Polarization	99
3.3.2	Vibration modes	100
3.3.3	Equivalent electrical circuit	102
3.3.4	Electromechanical properties calculations	103

This chapter focuses on the characterization techniques used to control each step of the fabrication process and to probe the performances of the obtained materials.

1 Physico-chemical characterizations

1.1 Particle size distributions

The measurement of the size and statistical size distribution of the particles is carried out using laser diffraction spectroscopy. This method is used to estimate the particle size of wet or dry particles. Wet process is carried out using the powder dispersed in a medium (water, alcohol, etc.). Ultrasound can be used for better dispersion. For dry process, the powder is fed directly into the empty vessel. The principle of measurement involves the diffraction of laser radiation by suspended particles (Mie theory) [1]. The particles are approximated as spheres, homogeneous and isotropic and of a given refractive index. Laser granulometry is therefore precise in the case of spherical powders.

For this study, particle size distributions of the raw powders are evaluated at ICMCB using laser diffraction spectroscopy Malvern Mastersizer 2000 from wet dispersions after ultrasound (1 minute in water). According to the supplier, this device can analyze the particle size distribution over a wide range of particle sizes: from 0.02 μm to 2000 μm with an accuracy of 0.1 % for a monomodal powder.

1.2 Density measurement

The experimental density $\rho_{\text{experimental}}$ of the disk shaped ceramic samples is determined by geometric method measuring dimensions and volume. From the evaluation of the mass m , thickness l , and radius r of the sample, the following expression is used (Figure III-1):

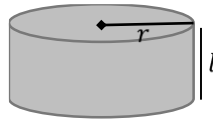


Figure III-1: Dimensions of the ceramic sample for experimental density evaluation

$$\rho_{\text{experimental}} = \frac{m}{\pi r^2 l} \quad (\text{Eq. 3.1})$$

The relative density (d_r) of the sample is deduced subsequently from the ratio of the experimental and the theoretical densities.

$$d_r = \frac{\rho_{\text{experimental}}}{\rho_{\text{theoretical}}} * 100 \% \quad (\text{Eq. 3.2})$$

With the measurement errors $\Delta l = \pm 0.15 \text{ mm}$, $\Delta r = \pm 0.13 \text{ mm}$, and $\Delta m = \pm 0.01 \text{ mg}$ an uncertainty of $\Delta d_r = 0.141 \text{ g/cm}^3$ for d_r is found out. In order to have a more precise determination of the

relative density, complementary methods can be used: helium pycnometry, Archimede's method or mercury porosimetry.

In this work, analysis of SEM images is used to estimate the level of porosity (paragraph 1.1.5) and then to confront the results with the experimental density ($\rho_{experimental}$) obtained by geometric method.

1.3 Layer thickness measurement

A tencor profilometer (Model KLA-Tencor alpha step IQ available at IMS) is used to evaluate thicknesses of the dried or fired printed layers. This operation is necessary during the screen-printer settings, or to characterize the final energy harvester volume. Thanks to a scan of a diamond stylus, this equipment is able to measure step height, roughness and waviness on sample surfaces. Figure III-2 shows an example of the thickness profile that can be obtained.



Figure III-2: Example of thickness profile (left), and Tencor contact profilometer used at IMS (right) laboratory.

For the roughness determination (Figure III-3), different parameters can be provided:

- R_{max} the largest difference between peaks and valleys in an individual sampling length within the overall evaluation length.
- R_a the average roughness over the sampling length.
- R_t the distance between the highest peak and lowest valley over the evaluated length.

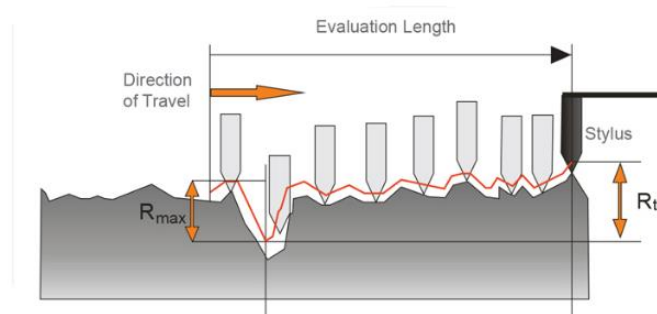


Figure III-3: Profilometer principle for roughness measurement (Image from [2])

In this work, measurements are carried out on printed samples using a minimum contact force of 0.03 mg, a scan speed of 20 $\mu\text{m/s}$, a sampling rate of 100 Hz and a maximum scan length of 2 mm.

1.4 X-ray diffraction

X-ray diffraction analysis (XRD) is used to qualitatively characterize the phase(s) present in the sample (powder or ceramic). XRD can also give other structural features such as lattice parameters, crystallite size, etc. An X-ray beam of defined wavelength irradiates the sample to be analyzed. If this one is crystallized, the atoms arranged periodically cause the incident X-rays to diffract (Figure III-4). This phenomenon occurs at certain angles, characteristic of the observed crystalline phase. The directions in which interference is constructive, called diffraction peaks, can be determined by Eq. 3.3, known as Bragg's law [3].

$$2d \sin \theta = n \cdot \lambda \quad (\text{Eq. 3.3})$$

Where d is the interreticular distance, θ the deviation of the half angle between the incident beam and the direction of the detector, n the reflection order and λ the wavelength of the incident X-rays.

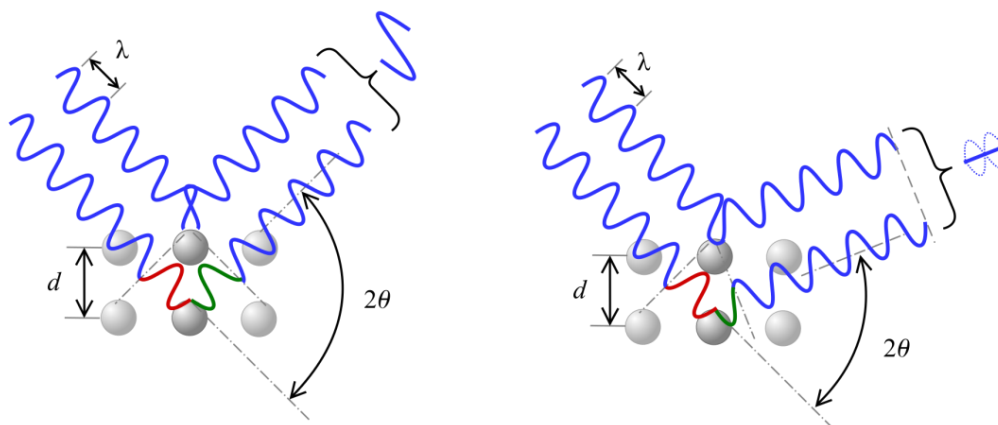


Figure III-4: Scheme of Bragg's law. According to the 2θ deviation, the phase shift causes constructive (left -) or destructive (right -) interferences. (Image from [4])

X-ray diffraction analysis of the powders and ceramics are performed at ICMCB using a PANalytical X'Pert MPD Bragg-Brentano θ - θ geometry diffractometer equipped with a secondary monochromator. The Cu $K\alpha_1$, α_2 ($\lambda_1 = 1.54060 \text{ \AA}$, $\lambda_2 = 1.54441 \text{ \AA}$) radiations are generated at 40 kV and 40 mA. The XRD patterns are recorded at room temperature in the angular range $2\theta = 8$ - 80° , and are further analyzed using DIFFRAC.EVA software (developed by BRUKER corporation, Massachusetts, US).

1.5 Scanning electron microscopy (SEM)

1.5.1 Principle and equipment

Scanning electron microscopy (SEM) is used to observe sample microstructure (grain size and their morphology, porosity) and local chemical analysis using an EDS detector (Energy Dispersive Spectroscopy). The principle is based on the interaction between an electron beam and the sample irradiated. This interaction produces secondary and backscattered electrons. Electrons are used for imaging; the secondary electrons give topological (surface) information while backscattered electrons provide information on chemical composition. Backscattered electron images in the SEM display compositional contrast that results from different atomic number elements and their distribution [5]. Energy Dispersive Spectroscopy (EDS) allows to identify particular elements and their relative proportions (atomic percentage).

A scanning electron microscope consists essentially of an electron gun fitted with a tungsten filament cathode, whose function is to produce a fine electron beam on the sample, a sample stage to control sample position, and detectors to capture and analyze the radiation emitted by the sample. In addition, the apparatus needs to be equipped with a vacuum pump system (Figure III-5) [6].

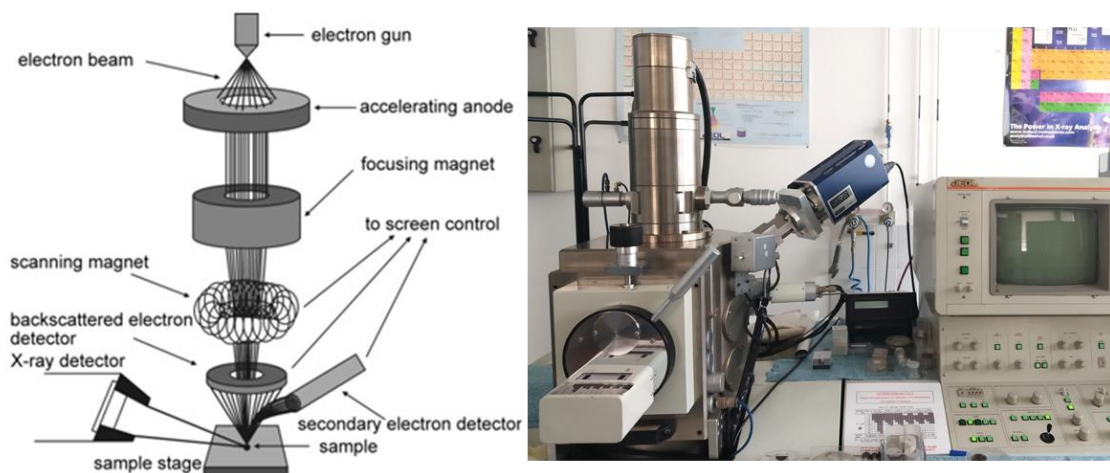


Figure III-5: Schematic of SEM (left) (Image from [6]), and SEM JEOL, JSM-6100 used for observation of ceramics at IMS Laboratory.

The scanning electron microscopes used in this work are the JEOL, JSM-6100 for ceramic samples (IMS Laboratory) and ZEISS EVO50 for specific observation of the interfaces of the printed structures (Placamat – UMS 3626, Université Bordeaux). Both SEM are equipped with an EDS (Energy Dispersive Spectroscopy) detector that enables qualitative/quantitative analyses and element mapping.

1.5.2 Samples preparation

Prior to SEM observations, ceramic samples are coated with ultrathin layer gold deposited on the sample by low-vacuum sputter deposition.

SEM observations are performed on fractured sections for ceramic samples. For printed multilayer structures, sections are prepared using cross polished (Ilion+ II 697) technique at a low energy (5keV), in order to obtain a proper cross-section surface. Samples are prepared at PLACAMAT Platform at ICMCB laboratory.

1.5.3 Images analysis

Evaluation of the porosity from SEM images is carried out by counting observable holes of the microsection plane image and then by calculating their cumulative area. The process is done using the program ImageJ. The ratio of the surface of holes on the total observed surface allows an estimation of the percentage of porosity in the solid [7].

Average grain size is directly measured during images acquisitions using different tools provided by the SEM interface program considering approximately a hundred grains.

2 Thermal analyses

2.1 Thermogravimetric analysis (TGA)

Thermogravimetric analysis or thermal gravimetric analysis (TGA) determines the mass of a sample over time as the temperature changes. This measurement provides information on phase transitions, adsorption, desorption, as well as thermal decomposition, and solid-gas reactions (e.g. oxidation or reduction) [8].

The used equipment is a Thermobalance SDT Q 600 TA Instrument available at ICMCB. TGA analysis of samples is carried out on a small amount of powder (~ 500 µg) under argon atmosphere. The temperature range is 25-680°C and the ramp is 2°C/min.

2.2 Dilatometry

Measurements of thermal coefficient of expansion (TCE) allows to better understand thermo-mechanical interactions between the material's constituents of the multilayer thick films structure occurring during sintering. This analysis accurately measures the dimensional changes of a sample as a function of temperature without applying force. This allows to characterize the linear coefficient of expansion α_L (°C⁻¹) by the following expression:

$$\alpha_L = \frac{\Delta L}{L_0} \frac{1}{\Delta T} = f(T) \quad (\text{Eq. 3.4})$$

With ΔL the length increase, L_0 the initial length and, T the sample temperature.

Measurements are carried out with a dilatometry analyzer (DIL Netzsch 402 ED available at ICMCB) using disc samples of 3mm thickness and 6mm diameter with an accuracy of $\Delta L/L_0$ of 0.002%.

3 Dielectric and electromechanical characterizations

3.1 Sample preparation

In order to access the dielectric and electromechanical properties of the ceramic materials, conductive electrodes have to be deposited on the two parallel faces of the ceramic. For printed multilayer structures, gold electrodes are printed within the thick film process (see chapter 4).

For bulk ceramics, after sintering, both sides are polished using abrasive paper or a fine-grained diamond grinding wheel. Gold electrodes of around 100 nm are then deposited by sputtering onto the ceramic surfaces (tape scotch is placed at the side borders of the pellets in order to avoid short circuit between surfaces). Two silver wires (diameter 0.1mm) are finally attached to the center of each electrode using silver epoxy ink (ESL1901S (see Annex 1 chapter 2)) further dried at 120°C during 1h.

3.2 Dielectric measurements

3.2.1 Basics

The response of a material subjected to alternative field with variable frequency generally depends on the frequency of the field. The permittivity, deduced from capacitance measurements, is a complex function of the (angular) pulsation ω of the applied field that decomposes into real and imaginary parts as follow:

$$\varepsilon(\omega) = \varepsilon_0(\varepsilon_r'(\omega) - i\varepsilon_r''(\omega)) \quad (\text{Eq. 3.5})$$

With $\varepsilon_0 \sim 8.85 \times 10^{-12}$ F/m the permittivity of free space (vacuum).

ε_r' characterizes the ability to store charges in the dielectric and the imaginary part ε_r'' , is the contribution of energy dissipation. Dielectric losses are usually expressed by the loss angle δ :

$$\tan \delta = \frac{\varepsilon_r''}{\varepsilon_r'} \quad (\text{Eq. 3.7})$$

An ideal capacitor would have high relative permittivity ε_r' and negligible dielectric losses.

In a parallel plate capacitor, the dielectric material separates two conductive metal electrode plates. The capacitance is a function of the distance between plates, the surface of electrodes, and the relative permittivity.

$$C = \epsilon_0 \epsilon_r' \left(\frac{S}{t} \right) \quad (\text{Eq. 3.8})$$

With S the electrodes surface of the capacitor and t its thickness.

Considering ferroelectric materials, the thermal evolution of the relative permittivity ϵ_r' (or dielectric constant) presents a divergence inferred by a maximum of the dielectric constant at the Curie Temperature (T_c) which corresponds to the transition temperature between the ferroelectric ($T < T_c$) and paraelectric (non-ferroelectric) phases ($T > T_c$) [9]. An illustration is given for BaTiO_3 in Figure III-6.

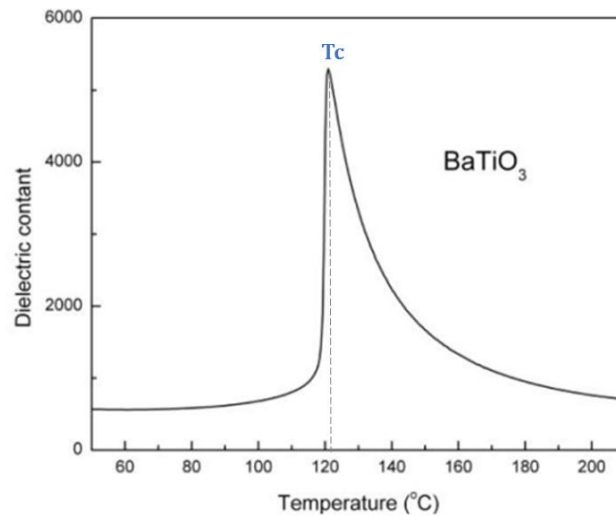


Figure III-6: Evolution of the dielectric permittivity of BaTiO_3 as a function of temperature (Image from [8]).

3.2.2 Set-up

Dielectric measurements are carried out at ICMCB on disc samples. The sample is placed inside a tubular furnace, suspended near a thermocouple for temperature regulation, and between two electrically insulated cylindrical copper electrodes. These are connected to an impedance bridge LCR meter HP4194A, which allows to measure the capacitance and dielectric loss of the sample as a function of temperature and frequency (Figure III-7). Measurements are performed under vacuum with a frequency sweep from 100 Hz to 1 MHz, a number of points between 200-1000, under low excitation level of 1V. Thanks to a resistor located within the furnace, heating is carried out from room temperature until 350 °C (623 °K).

The HP4194A analyzer and the Eurotherm temperature control are driven with a LabVIEW program developed at ICMCB laboratory.

Relative permittivity constant and dielectric loss values can be obtained at room temperature and at 1kHz (as usually reported in literature[10]) or as a function of temperature (25°C – 350°C) and frequency (100Hz-1MHz)

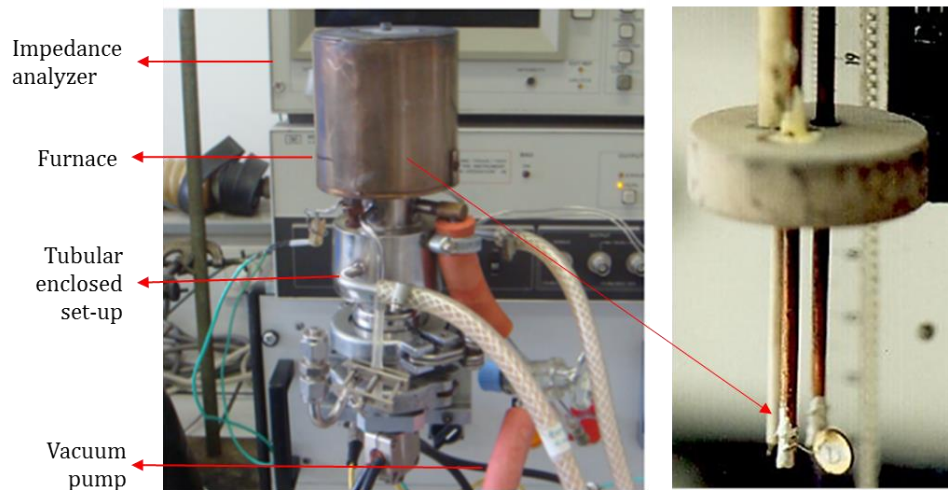


Figure III-7: Dielectric measurements set-up at ICMCB (left) complete set-up (right) connected sample within the furnace.

3.3 Electromechanical characterizations

3.3.1 Polarization

The polarization step is necessary for piezoelectric ceramics to exhibit piezoelectric properties. It consists of submitting the sample to a continuous high voltage. The spontaneous polarization in ferroelectric polycrystalline ceramics is random and a polarization process (also called “poling process”) is necessary to obtain a macroscopically piezoelectric ceramic. During this process, the domains within the grains reorient in the direction of the applied electric field. A remanent polarization is thus achieved within the material after the removal of the electric field. The polarization of the samples is made in an AET Technologies chamber furnace available at IMS (Figure III-8). The samples are placed inside an isolated platform. Electric contacts are provided by two conductive silver wires (diameter 0.1mm) glued on one side to the center of each electrodes. On the other side, they are connected to two metal rods that deliver the connection with the power supply.

After vacuuming, introduce of nitrogen into the chamber is carry out for ensuring a controlled dried polarization atmosphere, the system is brought to a temperature slightly below the Curie temperature T_C . Then, the voltage is applied across the sample (power supply AET Technologies 1.6kV-1.5mA) and held during 10 minutes. Throughout this period, the current should not exceed $10\mu\text{A}$ in order to avoid breakdown of the dielectric material. The sample is subsequently cooled ($\approx 10\text{ }^\circ\text{C}/\text{min}$) while maintaining the electric field. Finally, the electric field is cut off, and the sample is short-circuited for evacuating residual charges located at the surface.

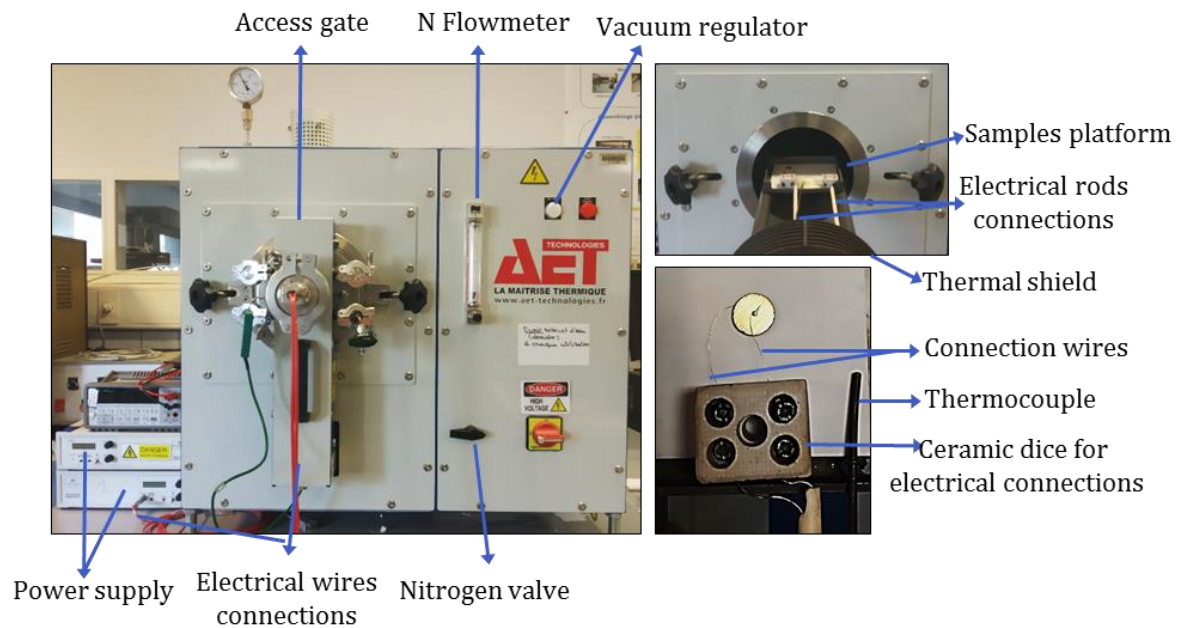


Figure III-8: Pictures of the polarization furnace used at the IMS laboratory.

3.3.2 Vibration modes

When excited by an alternating electric field the piezoelectric sample deforms at the field's frequency. When the frequency becomes close to a specific vibration mode of the sample, impedance (or admittance) submits high variations and minimum and maximum of the impedance can be respectively identified to the resonance and anti-resonance frequencies (Figure III-9). For complex shapes of sample, resonant modes are interfering and are hence difficult to identify. Therefore particular sample shapes are usually chosen to favor a well-defined resonance mode and to ease the understanding of the acoustic wave propagation (Table III-1).

As already mentioned in the state of the art chapter, 33 or 31 modes are usually promoted for energy harvesting piezoelectric applications.

In the framework of this thesis, the 31 mode will be chosen for energy harvesting application using resonant cantilevers. Also, for disks sintered by SPS, the planar mode will be considered.

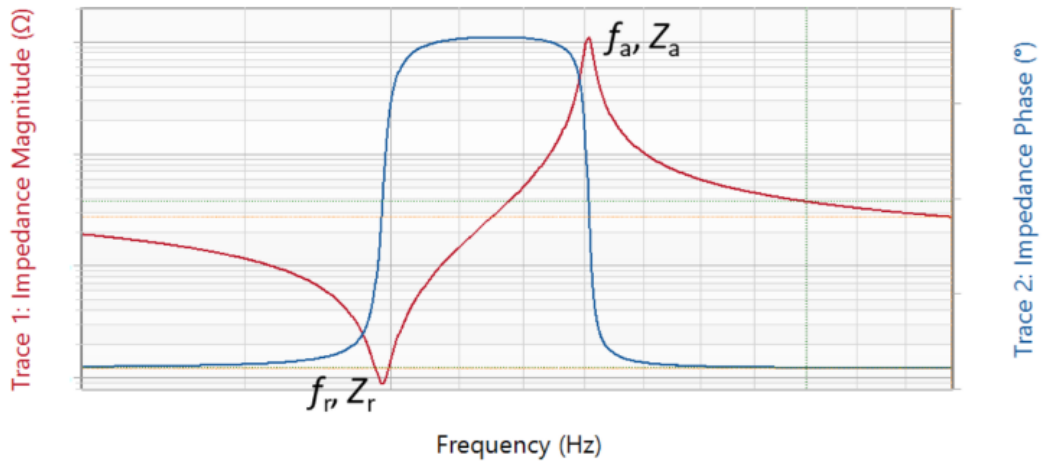


Figure III-9: Typical impedance curve (in red) with a minimum $|Z_r|$ at the resonance frequency f_r and a maximum $|Z_a|$ at the anti-resonance frequency f_a . (Image from [11])

Table III-1: Vibration modes favored in different geometries. The electric field is applied parallel to the polarization P (white arrow) and the direction of displacement is shown with black arrows. (Inspired from [12])

Vibration mode	Mode subscript M: constant	Sample geometry	Dimension required L : Length; W : Width; T : Thickness; D : Diameter
Transverse length mode	M_{31}		$T, W < L/5$
Radial mode or planar mode (Fundamental)	M_p, M_{31}, M_{33}		$D > 10T$
Thickness extension mode	M_{33}, M_t		$D > 10T$
Longitudinal length mode	M_{33}		$D < L/2.5$
Thickness shear mode	M_{15}, M_{11}		$L > 3.5(T, W)$

3.3.3 Equivalent electrical circuit

For each resonance mode, an equivalent electrical circuit exists, which has to be distinguished to the dielectric ($R_0//C_0$) equivalent circuit. Due to the resonance, the new equivalent circuit shows a motional branch ($R_m L_m C_m$) in parallel with the dielectric ($R_0//C_0$) circuit (Figure III-10).

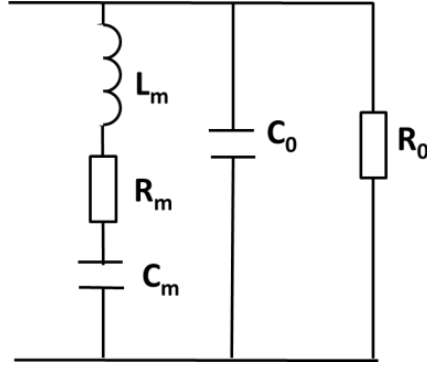


Figure III-10: Electrical equivalent circuit diagram of a piezoelectric resonator near the resonance. C_0 and R_0 are respectively the capacity and leakage resistance representing the dielectric losses of the sample out of resonance. The branch with subscript m describes the behavior nearby resonance and is defined as the motional branch.

Based on the proposed equivalent circuit for a piezoelectric resonator, for a sinusoidal excitation of angular frequency ω , the behavior of the conductance G and the susceptance B can be determined as a function of ω . Indeed, the complex admittance Y (inverse of the impedance Z) can be described as follow:

$$\begin{aligned}
 Y = G + jB &= \frac{1}{R_0} + jC_0\omega + \frac{1}{R_m + jL_m\omega + \frac{1}{jC_m\omega}} \\
 &= \frac{1}{R_0} + jC_0\omega + \frac{R_m - j\left(L_m\omega - \frac{1}{C_m\omega}\right)}{R_m^2 + \left(L_m\omega - \frac{1}{C_m\omega}\right)^2}
 \end{aligned} \tag{Eq. 3.9}$$

If $a = L_m\omega - \frac{1}{C_m\omega}$, then:

$$Y = \frac{1}{R_0} + \frac{R_m}{R_m^2 + a^2} + j\left(C_0\omega - \frac{a}{R_m^2 + a^2}\right) \tag{Eq. 3.10}$$

The conductance G and the susceptance B are respectively real and imaginary parts of the admittance Y . As a result, they can be identified from Eq. 3.10:

$$G = \frac{1}{R_0} + \frac{R_m}{R_m^2 + a^2} \tag{Eq. 3.11}$$

$$B = C_0\omega - \frac{a}{R_m^2 + a^2} \quad (\text{Eq. 3.12})$$

Figure III-11 illustrates an example of G and B curves as a function of frequency for a resonance mode of a piezoelectric material, from which the R_m , C_m and L_m can be extracted. These two curves can be in depth studied (maximum, minimum, limits when ω tends to zero or infinity (Annex 1). By assuming R_0 to be infinite and by using $G(\omega)$ and $B(\omega)$ curves, the component values of the motional branch of the equivalent circuit can be then deduced with the following relationships:

$$R_m = \frac{1}{G_{max}}, \quad L_m = \frac{R_m}{2\pi(f_n - f_u)} \quad \text{and} \quad C_m = \frac{1}{4\pi^2 L_m f_r^2} \quad (\text{Eq. 3.13})$$

Where f_u and f_n are measured at $G = \frac{G_{max}}{2}$ and f_r the resonance frequency at $G = G_{max}$.

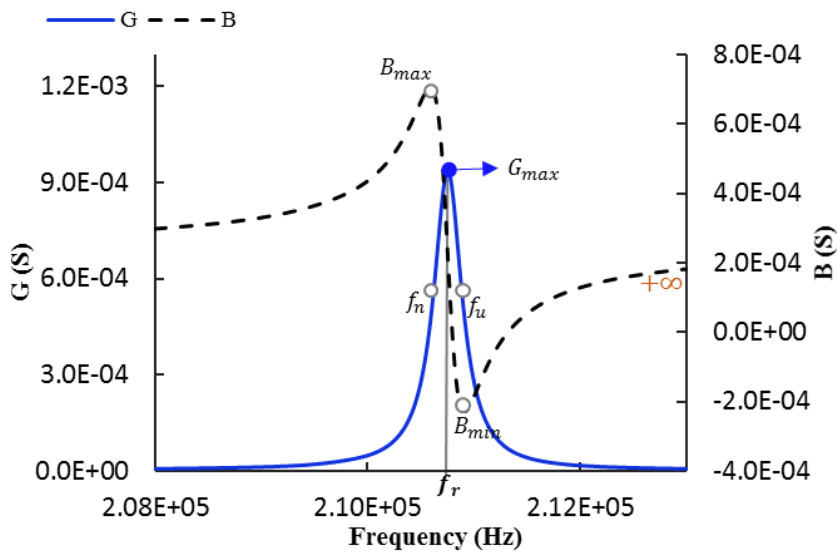


Figure III-11: Conductance G and susceptance B as a function of the frequency. Special points (G_{max} , B_{max} , B_{min} , f_n and f_u) are represented, allowing extraction of R_m , C_m and L_m . The frequencies f_n and f_u are defined at $G = G_{max}/2$ and correspond to the bandwidth at -3dB or $|Y| = |Y|_{max}/\sqrt{2}$.

3.3.4 Electromechanical properties calculations

Calculations of electromechanical coefficients such as electromechanical coupling coefficients factors (k) and piezoelectric coefficients (d) are done in accordance to the IEEE standard model [13]. In practice, resonant modes have to be identified and characteristic frequencies have to be measured.

3.3.4.1 Characteristic frequencies

The highlighting of the admittance circle $B(G)$ is sufficient to prove that the material is piezoelectric and characteristic frequencies can be identified in this circle for a particular resonance (Figure III-12).

- f_u and f_n defined at $G = \frac{G_{max}}{2}$ or $|Y| = \frac{|Y|_{max}}{\sqrt{2}}$
- f_r and f_a , the resonance and anti-resonance frequencies defined respectively at maximum and minimum impedance Y
- f_p and f_s , the parallel and series resonance frequencies defined at the maximum resistance and maximum conductance respectively.

IEEE Standard [13] identifies these six frequencies which are often merged, when the quality factor Q_m is higher than 50: $f_u \approx f_s \approx f_r$ and $f_a \approx f_p \approx f_n$.

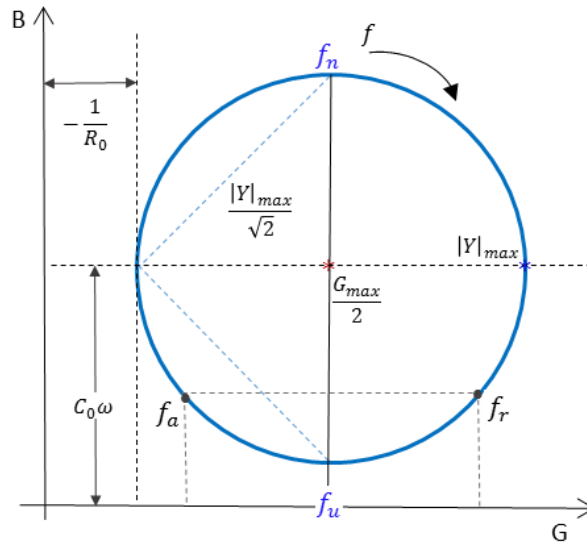


Figure III-12: Characteristic frequencies that can be identified in the admittance circle for a particular resonance. The deviation between circle and axes represents R_0 and the capacitance C_0 of the dielectric part of the equivalent circuit.

3.3.4.2 Mechanical Quality factor Q_m

The mechanical quality factor Q_m represents the mechanical losses of a piezoelectric material. It is expressed as a function of the characteristic frequencies of the resonance peak of G and can be hence deduced from the elements of the equivalent circuit R_m , C_m and L_m . For a given f_r , high quality factor Q_m will clearly be related to the curve shape (high and narrow peak) (Figure III-11).

$$Q_m = \frac{f_r}{f_n - f_u} = \frac{1}{R_m} \sqrt{\frac{L_m}{C_m}} \quad (\text{Eq. 3.14})$$

3.3.4.3 Electromechanical coupling coefficient k

The electromechanical coupling squared coefficient k^2 is defined as the ratio of the mechanical energy accumulated in response to an electrical input or vice versa. For a disk where the planar vibration mode is promoted, electromechanical coefficients k_p and k_{31} can be calculated thanks to the measured frequencies f_r and f_a according to the equations:

$$k_{31}^2 = \frac{\pi f_a}{2 f_r} \frac{1}{\frac{\pi f_a}{2 f_r} - \tan\left(\frac{\pi f_a}{2 f_r}\right)} \quad (\text{Eq. 3.15})$$

$$k_p^2 \cong 2.51 \frac{f_a - f_r}{f_a} - \left(\frac{f_a - f_r}{f_a}\right)^2 \quad (\text{Eq. 3.16})$$

The value of 2.51 comes from the Bessel function [14]. Another parameter, k_{eff} , is frequently used to express the effective electromechanical coupling coefficient of an arbitrary resonator, either at fundamental resonance or at any overtone. It is expressed as follows:

$$k_{eff}^2 = \frac{f_a^2 - f_r^2}{f_r^2} \quad (\text{Eq. 3.17})$$

In this work, k_p , k_{31} and k_{eff} will be the coefficients taken into account.

3.3.4.4 Elastic compliance s

The elastic matrix for a cylindrical poled ceramic is:

$$\begin{array}{cccccc} S_{11} & S_{12} & S_{13} & 0 & 0 & 0 \\ S_{12} & S_{11} & S_{13} & 0 & 0 & 0 \\ S_{13} & S_{13} & S_{33} & 0 & 0 & 0 \\ 0 & 0 & 0 & S_{44} & 0 & 0 \\ 0 & 0 & 0 & 0 & S_{44} & 0 \\ 0 & 0 & 0 & 0 & 0 & 2(S_{11}-S_{12}) \end{array}$$

Elastic compliance is the ratio of a material's change in dimensions (strain) in relation to an externally applied load (stress). For a piezoelectric material, the compliance depends on whether the strain is parallel or perpendicular to the poling axis and on the electrical boundary

conditions. For instance, for 31 mode of a disk, s_{11}^E elastic constant is calculated at a constant electric field E from the following equation:

$$s_{11}^E = \frac{1}{4\rho f_r^2 D^2} \quad (\text{Eq. 3.18})$$

Where ρ is the density of the material and D is the diameter of the disk ceramic; Young's modulus can be also deduced using the inverse of the s_{11}^E expression (Eq. 3.18).

3.3.4.5 Piezoelectric constants d

The piezoelectric charge coefficient d describes the ratio of electric charge generated per unit area to an applied force (C/N or m/V). Taking into account the dielectric matrix presented in chapter 1, and using the planar vibration mode of a disk, from which k_{31} is calculated (previous paragraph), the piezoelectric constant is calculated with the following expression:

$$d_{31} = k_{31} \sqrt{\varepsilon' s_{11}^E} \quad (\text{Eq. 3.19})$$

Where ε' represents the dielectric permittivity measured far from the resonance frequency, usually measured at 1kHz or $2f_r$. It should be noted that the piezoelectric coefficient calculated above is only valid at frequencies far from resonance and doesn't consider any non-linear behavior of the ceramic. It may also vary with the degree of polarization of the ceramic.

3.3.4.6 Figure of merit FoM

Even if the electromechanical coupling coefficient indicating the energy conversion ability is a good criteria to choose the piezoelectric material, the Figure of Merit (FoM) [14]–[17] should be taken into account to further compare different materials for energy harvesting applications. This FOM applicable for piezoelectric materials, but not for devices, is defined as the electrical energy density divided by the mechanical deformations in dielectric materials.

$$FoM = \frac{d^2 E^2}{\varepsilon'} \quad (\text{Eq. 3.20})$$

Where E the Young's modulus, d the piezoelectric constant, and ε' the dielectric constant.

Figure III-13 summarizes the procedure used for the determination of the piezoelectric material properties. Capacitance measurements are carried out at 1kHz at room temperature.

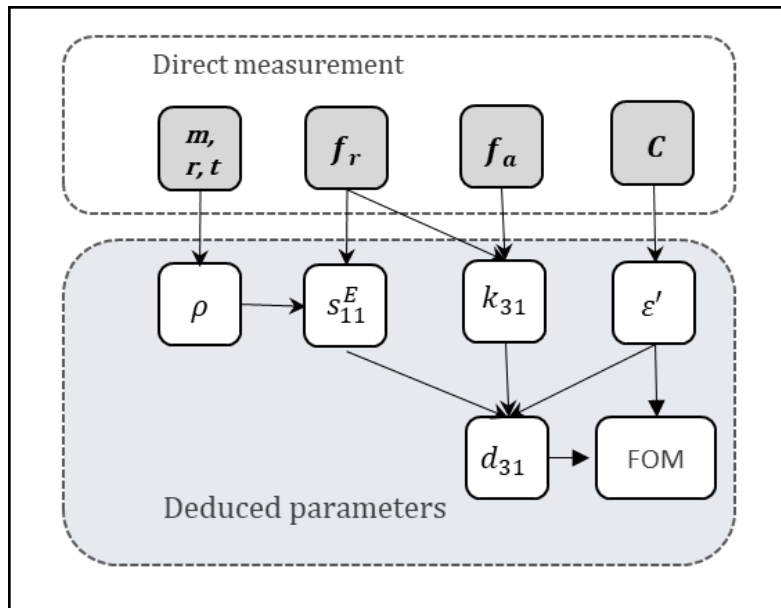


Figure III-13: Scheme of coefficient determination method using IEEE standard (planar vibration mode for a disk) (Inspired from [18]).

References

- [1] D. Hahn, "Light Scattering Theory," Jan. 2004.
- [2] "Elcometer 7062 MarSurf PS10 Surface Roughness Tester." [Online]. Available: <https://www.elcometer.com/en/coating-inspection/surface-cleanliness-surface-profile/surface-roughness/elcometer-7062-marsurf-ps10-surface-roughness-tester.html>. [Accessed: 27-Sep-2019].
- [3] W. H. Bragg and W. L. Bragg, "The Reflection of X-rays by Crystals Article cited in :," Proc. R. Soc. Lond., vol. 88, no. A, pp. 428–438, 1913.
- [4] "Loi de bragg principle." [Online]. Available: https://upload.wikimedia.org/wikipedia/commons/7/74/Loi_de_bragg.png. [Accessed: 27-Sep-2019].
- [5] L. Reimer, Scanning Electron Microscopy: Physics of Imaging Formation and Microanalysis, vol. 45. 2003.
- [6] "Components in a SEM - Nanoscience Instruments." [Online]. Available: <https://www.nanoscience.com/techniques/scanning-electron-microscopy/components/>. [Accessed: 27-Sep-2019].
- [7] C. Chilev, Y. Stoycheva, M. Dicko, F. Lamari, P. Langlois, and I. Pentchev, "A New Procedure for Porous Material Characterization," Int. J. Sci., vol. 5, no. 4, pp. 131–140, 2017.
- [8] A. W. Coats and J. P. Redfern, "Thermogravimetric Analysis A Review. Analysts Journal, vol 88.
- [9] D. Damjanovic, "Ferroelectric, dielectric and piezoelectric properties of ferroelectric thin films and ceramics," Reports Prog. Phys., vol. 61, no. 9, pp. 1267–1324, 1998.
- [10] T. Jordan and N. Langley, "Piezoelectric Ceramics Characterization," NASA/CR-2001-211225 ICASE Rep. No. 2001-28, p. 23, 2001.
- [11] "A practical guide to characterization of piezoceramic components and materials." [Online]. Available: <https://www.omicron-lab.com/applications/detail/news/a-practical-guide-to-characterization-of-piezoceramic-components-and-materials/>. [Accessed: 27-Sep-2019].
- [12] Ferroperm Piezoceramics, "High Quality Components and Materials," 2003.
- [13] A. Box, "Standard on Piezoelectric Crystals," IEEE Int. Symp. Appl. Ferroelectr., 1961.
- [14] S. Roundy and P. K. Wright, "A piezoelectric vibration based generator for wireless electronics," Smart Mater. Struct., vol. 13, no. 5, pp. 1131–1142, 2004.
- [15] R. Elfrink et al., "Vibration energy harvesting with aluminum nitride-based piezoelectric devices," J. Micromechanics Microengineering, vol. 19, no. 9, 2009.
- [16] S. Priya et al., "A Review on Piezoelectric Energy Harvesting: Materials, Methods, and Circuits," Energy Harvest. Syst., vol. 4, no. 1, pp. 3–39, 2017.
- [17] R. Xu and S.-G. Kim, "Figures of Merits of Piezoelectric Materials in Energy," PowerMEMS, pp. 464–467, 2012.
- [18] T. Hoang et al., "Characterization of a thin piezoelectric material before integration into a cantilever-based mechanical energy harvester," in 2016 IEEE International Ultrasonics Symposium (IUS), 2016, pp. 1–4.

Chapter IV

Multilayer EH fabrication

Content

INTRODUCTION	113
1 EH DESIGN CONSIDERATIONS	113
1.1 RESONANT FREQUENCY AND STRAIN OF A RECTANGULAR MICRO-CANTILEVER	113
1.2 COMPLEX GEOMETRY	114
1.3 MATERIALS FOR THE PASSIVE SUBSTRATE	116
1.4 SUMMARY OF ENERGY HARVESTING SPECIFICATIONS	118
2 MATERIALS AND DESIGN	119
2.1 METHODOLOGY	119
2.2 MATERIALS CONSTITUTING THE EH STRUCTURE	121
2.2.1 Active material PZT	121
2.2.2 Electrodes	124
2.2.3 Substrate	124
2.3 DESIGN OF THE COMPLEX GEOMETRY	125
3 FABRICATION PROCESS: CANTILEVER AND COMPLEX EH STRUCTURE	127
3.1 SCREEN FABRICATION	127
3.1.1 Screen characteristics	127
3.1.2 Layer mask and photolithography patterning	127
3.2 PZT PASTE	129
3.2.1 Paste Formulation	129
3.2.2 Paste preparation	129
3.3 PRINTING	131
3.3.1 Substrate holder	131
3.3.2 Layers deposition	131
3.4 SINTERING	132
3.5 POLARIZATION	134
3.5.1 Simple cantilever	134
3.5.2 Strain matched polarization technique (SME) for the zig-zag geometry	134
4 FABRICATION OF PRINTED DISKS AND CERAMICS	136
4.1 PRINTED DISKS	136
4.2 CERAMICS	137
5 CHARACTERIZATIONS	137
5.1 MICROSTRUCTURAL ANALYSIS	137
5.2 STUDY OF INTERFACES WITHIN THE MULTILAYER CANTILEVER	138
5.3 DIELECTRIC CHARACTERIZATIONS	144
5.4 ELECTROMECHANICAL CHARACTERIZATIONS	144

6	ENERGY HARVESTING APPLICATION	147
6.1	CHARACTERIZATION UNDER MECHANICAL VIBRATIONS	147
6.1.1	Model for piezoelectric vibration energy harvester	147
6.2	PIEZOELECTROMAGNETIC ENERGY HARVESTER (HYBRID APPLICATION)	153
6.2.1	Principle and experimental set-up	153
6.2.2	Results	154
7	CONCLUSION	158

The first phase of this work consists in the development of an EH device for autonomous small systems. The different steps of the EH structure fabrication are presented in this chapter, as well as the characterizations and performances.

Introduction

The objective we are seeking is to fabricate and characterize a screen-printed low-frequency piezoelectric energy harvester that can be used in autonomous systems. In this case, the MEMS structure must vibrate with a target resonance frequency value below 100 Hz.

For this purpose, in this chapter, after general considerations on EH design, the selection of the EH structure including the choice of materials and geometry is justified. Then, fabrication process is optimized. In a second step, in-depth investigation of the PZT based EH is carried out, focusing on interfaces, microstructure and electromechanical properties relationships. For this purpose, ceramic samples (printed or bulk disks) are also prepared in order to better understand the phenomena occurring at the interfaces, or to ease the dielectric and electromechanical characterizations. Finally, a simple cantilever EH is tested under mechanical vibrations whereas the selected EH with a complex geometry is tested as a piezo-electromagnetic energy harvester, by integrating a magnet on its extremity.

1 EH design considerations

1.1 Resonance frequency and strain of a rectangular micro-cantilever

The piezoelectric energy harvester converts mechanical into electric energy more efficiently when the applied vibration frequency is closer to the resonance frequency of the device. A few percent of mismatched frequency with resonance results in a dramatic decrease of output power. Therefore, adjusting the resonant frequency of the device to the external vibration source is essential in order to ensure a good energy conversion efficiency [1].

Also, for a mechanical structure integrating a piezoelectric material and a seismic at its end, harvesting the maximum of ambient energy implies maximizing the strain on the top surface of the structure. In the case of a simple shaped rectangle micro-beam, analytical expressions of the resonance frequency f_r and of the strain ε along the length x of the micro-beam can be expressed as following [2][3]:

$$f_r = \frac{1}{2\pi} \sqrt{\frac{k}{m_{eff} + M_{eff}}} \quad (\text{Eq. 4.1})$$

$$\varepsilon_{\text{Rectangle}}(x) = \frac{6F}{Eb^3} (L-x) \quad (\text{Eq. 4.2})$$

With $k = 3EI/L^3$ and $I = \frac{bh^3}{12}$

And where k is the stiffness of the micro-beam, I the micro-beam's second moment of area, m_{eff} its effective mass for the first flexural resonant mode, M_{eff} the effective mass of the seismic mass (punctual mass at the free-end of the micro-beam equivalent to the effect of the seismic mass). F is the equivalent inertial force at the free-end of the micro-beam due to the vibration of the support, E is the Young's modulus of the micro-beam with L its length, h its thickness and b the width.

Finally, the resonance frequency can be simplified, by assuming that the seismic mass is much heavier than the micro-beam:

$$f_r = \frac{1}{2\pi} \sqrt{\frac{k}{m_{eff} + M_{eff}}} \sim \frac{1}{2\pi} \sqrt{\frac{k}{M_{eff}}} \quad (\text{Eq. 4.3})$$

For a simple shaped rectangular micro-beam, according to equations 4.1 and 4.3, different solutions can be proposed in order to match the ambient vibration frequencies (< 100 Hz) with the resonance frequency of the EH structure.

The natural frequency of energy harvester is usually adjusted by increasing the weight of the seismic mass. However, the use of big seismic masses severely affects the structural integrity and durability of the harvesters.

Another option is to decrease the stiffness of the resonator. This can be done by optimizing the cantilever's geometry (ie. increase of length and decrease of width and thickness) or by decreasing the Young's Modulus (ie. using flexible materials). However, in MEMS applications the area of the harvester has to be under 10cm². This area restriction would typically result in a resonance frequency much higher than 100 Hz. Therefore, the method for reducing the spring constant of the energy harvester through the use of specific geometries requires to fit the maximum allowed area, and as result the use of flexible materials is an interesting alternative solution. Also, according to equation 4.2, the reduction of the micro-beam resonator stiffness will be beneficial to increase the generated strain during vibration and hence the harvested power. The two next paragraphs detail solutions found in the literature to reduce the resonant frequency with complex geometry, and to improve generated strain with adapted materials.

1.2 Complex geometry

To overcome the MEMS size limitations and maintain a low resonant frequency, a long cantilever can be for instance folded into a spiral one, as seen in Figure IV-1 (a-left). Here, researches showed that the length of the spiral needs to be at least half a turn to obtain a low frequency. But the fundamental vibration of these long spirals is dominantly torsional, what is therefore not ideal for energy harvesting.

A sandwich of two spirals beams (Figure IV-1 (a-right)) is a better option showing a resonance (first mode) vertically and where horizontal and twisting modes are suppressed [4].

A zig-zag geometry (Figure IV-1 (b)) is another solution that again reduces the natural frequency by increasing the effective length, while maintaining high power [5]. This zig-zag can be modeled as a few straight beams, with rectangular cross sections, placed next to each other on the main plane. Each beam is connected to its neighbor beams at its ends. If the beam comprises a piezoelectric layer, strain occurs in the piezoelectric layer when the beams deflect out of the plane, which generates electrical energy. This zig-zag geometry can outperform 1D cantilever

beams in terms of power density and low resonance frequency for a given surface area. However, the fundamental bending mode shape of the zig-zag still includes torsion as in the spiral geometry. As the number of beam elements increases, the torsion related to natural frequencies decreases faster than the bending modes.

Other solutions are found in the literature to reduce the effect of torsion in spiral or zig-zag configurations. Berdy *et al.* addressed this problem by using a fixed-fixed configuration instead of a free-fixed one. Two zig-zag beams are connecting at their free end in this meandered geometry (Figure IV-1 (c)) [6].

Another cantilever-like configuration without free-ends, called the “elephant”, is proposed by Sharpes *et al.* to reduce torsional effects and enhance pure bending for the fundamental mod (Figure IV-1 (d)) [7]. This design is a closed circuit meandering configuration where the two free-ends of the meanders are joined and it produces greater bending in the clamped beam, part showing the highest amount of strain. In this work, higher power is measured compared to the zig-zag configuration, with the piezoelectric layer located on the clamped beam.

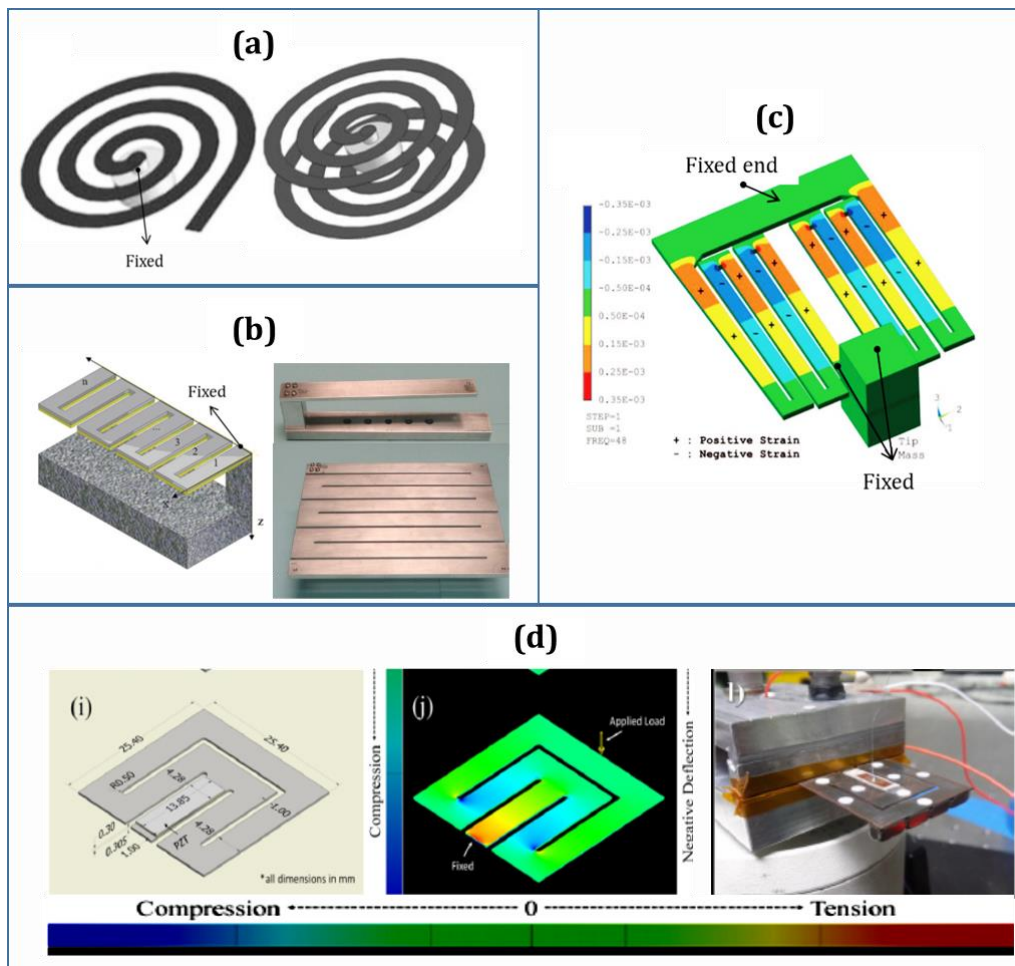


Figure IV-1: Proposed 2D geometries of energy harvester to reduce resonance frequency of the structure and to improve generated strain, (a) spiral and double spiral connected, (b) zig-zag design with experimental structures in aluminum (length of the beam= 171.4mm), (c) meandering configuration with simulated strain, and (d) elephant drawing, stress analysis and picture of the fabricated EH (steel substrate and PZT). (reproduced from [4], [5], [7], [8])

1.3 Materials for the passive substrate

Because of their lower Young modulus, flexible substrates enable considerable reduction of the resonance frequency and offer enhanced toughness compared with brittle Si-based cantilevers. Moreover, the piezoelectric response on flexible substrates is higher because of increased strain (equation 1.2). Therefore, researchers try nowadays to exploit the piezoelectric effect with various flexible substrates, such as metal based (aluminum, copper, brass, stainless steel foils), textile fabric, common paper and flexible plastic [9]–[11]. Flexible electronics have advantages such as low-cost synthesis of material, and easy manufacture of thin film devices by printing technologies or vacuum evaporation/sublimation, or large surfaces can be obtained [12]. Furthermore, for printing process, it can be extended to "smart materials and systems" with new ink-based functional materials such as electroactive polymers for example.

Among flexible substrates, thin polymeric foils are extremely attractive because they are lightweight and inexpensive making it possible to target high-volume and low-cost commercial products. Nevertheless, the processing of these materials being usually carried out at temperatures below 180–190 °C makes them attractive for organic technology based on low-temperature printing or evaporation techniques [12], but not for inorganic materials. Polyethylene terephthalate (PET) and polyethylene naphthalate (PEN) constitute the two main flexible substrates used today in the development of flexible electronics. They provide good resistance to solvents and a discrete tolerance to temperature. Also their intrinsic transparency makes them suitable as substrates for transparent electronics [13][14].

In contrast, metal-based substrates are attractive for piezoelectric vibration energy harvesting MEMS, especially metallic foils, due to their low stiffness and high fracture strength, both necessary to withstand mechanical deformations and to increase the reliability. Moreover, the large Thermal Expansion Coefficient (TEC) of metals such as copper, nickel, or stainless steel (as compared with that of PZT) produces compressive stress in plane during cooling down from the crystallization temperature to the Curie temperature, which can be used to reduce the permittivity and enhance the FoM for energy harvesting. Indeed, the total stress of a thin film material mechanically constrained to a substrate includes three contributions : intrinsic stress (deposition parameters), extrinsic stress (dimensional changes occurring during crystallization or phase transition), and thermal stress [15][16]. The contribution of thermal stress, in particular during cooling, is significant in thick films. It arises from the thermal expansion mismatch between the substrate and the material. The direct correlation between the thermal stress/strain and the volume fractions of c- and a-domains in a tetragonal film is well documented [15]. According to the type of stress (tensile or compressive), specific domain states (a- or c-) are favored (Figure IV-2). As a result, tuning the difference of TEC between the film and the substrate allows to control the domain state at T_c . The resulting domain structure affects film properties such as dielectric constant and remanent polarization [16]–[19].

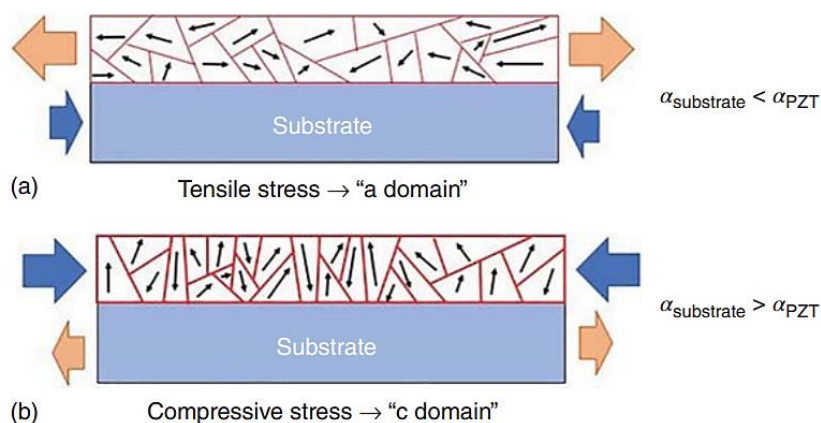


Figure IV-2: Illustration of domain structure in the film under (a) tensile stress and (b) compressive stress, in the cases where the stresses are controlled by thermal expansion mismatch (reproduced from [15]).

In the literature, for EH applications, piezoelectric ceramics (already polarized) can be bonded on the metallic substrates or thin/thick films can be deposited on the metallic substrate prior to their polarization. For instance, Berdy *et al.* developed the meandering EH. The meandering piezoelectric energy harvester is a commercial bimorph type with thick ceramic (270 μm) on brass (0.13-mm) and thin nickel electrodes. The shaping is done using a femtosecond pulsed laser (Figure IV-3). In case of piezoelectric ceramics, when complex geometries are chosen, laser micromachining can be done. Polishing can also be led to reduce the ceramic thickness and hence improve the flexibility.

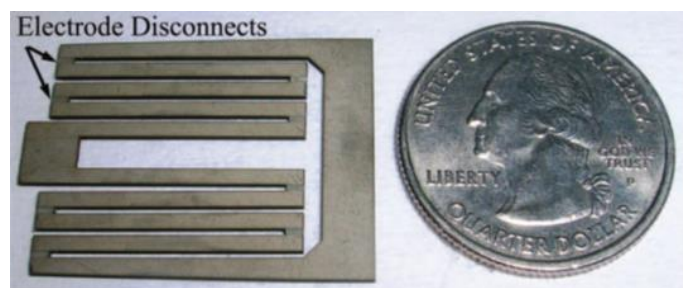


Figure IV-3: Photograph of a laser-machined meandering piezoelectric energy harvester (reproduced from [6])

Monin *et al.* also worked with piezoelectric spirals realized from commercially available piezoelectric buzzers (PUI Audio Inc., AB4113B) [20]. They were micromachined using LPKF Protolaser U3 laser machining tool, they consist of a 100 μm thick brass shim (41mm diameter) carrying two 150 μm layers of PZT (29mm diameter) (Figure IV-4). The obtained resonant frequencies range from 8Hz to 650 Hz, with a maximum generated power up to 0.5 μW . Additionally, electrode surfaces can be further optimized to fit with the stress field so that the coupling coefficient of the transducer is maximized.

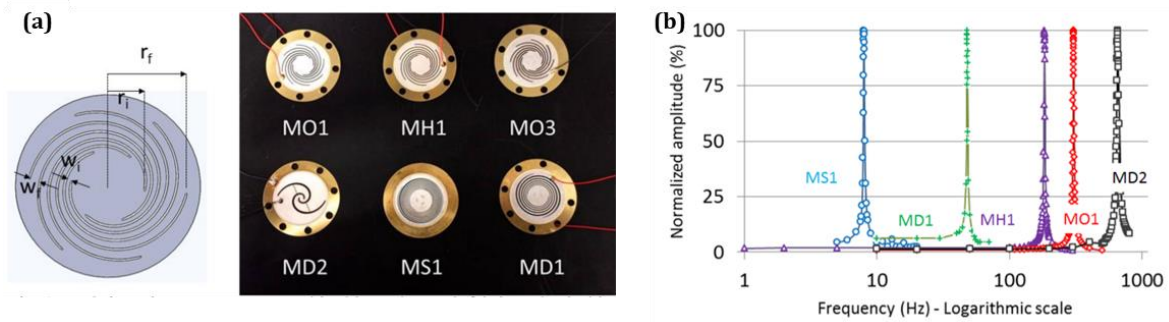


Figure IV-4: (a) Spiral fabricated from a laser micromachined buzzer (PZT/brass). Each spiral is named with different acronyms: M stands for Membrane, S for Simple (1 spire), D for Double (2 spires), H for Hexa (6 spires) and O for Octo (8 spires)), and (b) Normalized amplitude versus frequency (Hz). The resonance frequencies range from 8 Hz to 650 Hz. For each curve, the amplitude is normalized with respect to its maximum value.(reproduced from [20])

Furthermore, metal foils can maximize their flexibility with small thicknesses or mesh-type structure for wearable applications (Figure IV-5) [21]. However, one challenge in the growth/crystallization of oxide films such as PZT on metal foils is the thermomechanical incompatibility between the metal substrate and the oxide film. Many solutions are based on manufacturing processing using passivation layers or pretreatment of substrates.

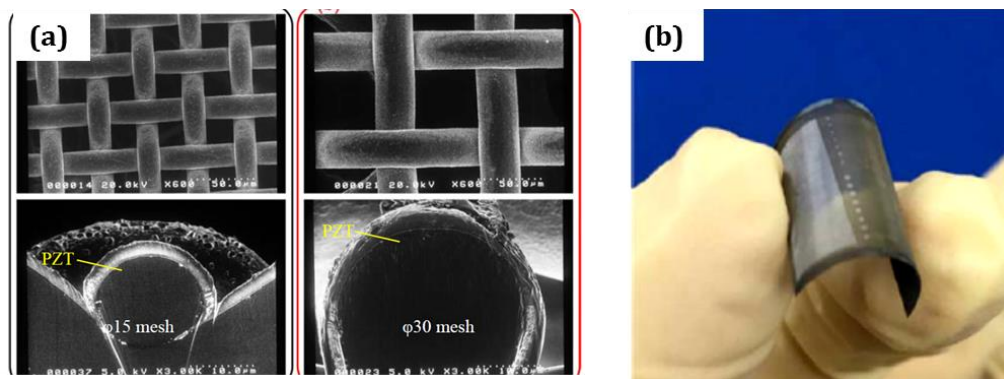


Figure IV-5: (a) SEM images of PZT layers deposited on Pt/Ti-coated SS mesh substrates ((a) $\phi 15$ mesh and (b) $\phi 30$ mesh) and (b) image of PZT thin films on stainless mesh substrates. (reproduced from [21])

1.4 Summary of energy harvesting specifications

The summary of the energy harvester specifications is depicted in Figure IV-6. The use of screen-printing thick film technology to deposit the active piezoelectric film on a metallic substrate (already shaped) followed by a post-polarization step is attractive. Indeed, it represents a low cost and easy shaping process, piezoelectric films are thick enough and passive substrate is flexible (provided it is thin enough). Finally, when using bulk ceramics bonded on the metallic substrate, there is no need of additional mechanical steps usually required to achieve the expected geometry (laser micromachining or mechanical polishing). This mechanical step could induce stresses in the piezoelectric material and lead to a modification of the piezoelectric properties.

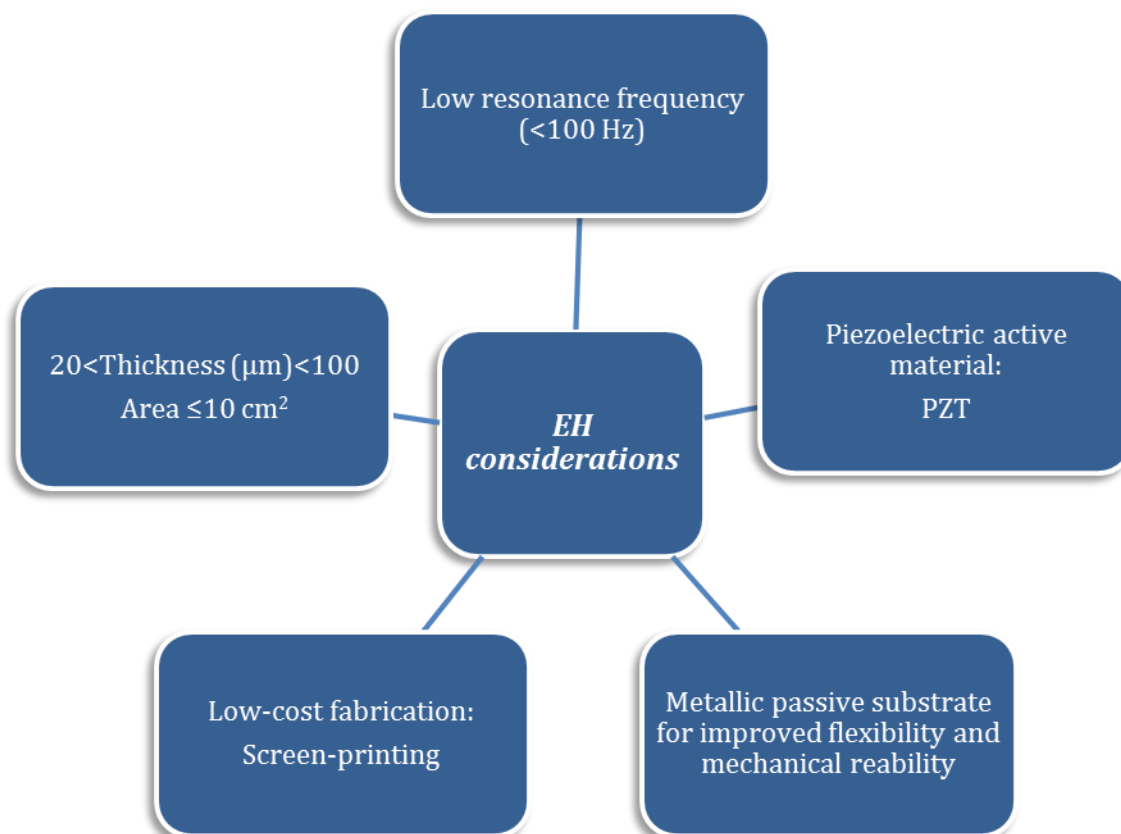


Figure IV-6: Summary diagram of EH requirements

2 Materials and design

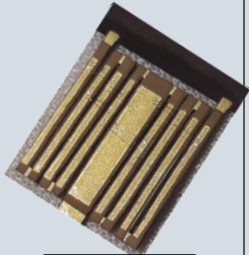



2.1 Methodology

Figure IV-7 shows the basic scheme of the multilayer structure considered as the “elementary brick” of the study. It consists of a piezoelectric layer screen-printed on the top of a metallic substrate and sandwiched between two electrodes. Nevertheless, keeping in mind the final goal to optimize the process and the properties of the EH with a complex geometry, our approach is also to consider three types of PZT based samples: a bulk ceramic, a screen-printed disk, and a simple multilayer cantilever (Table IV-1). Indeed, according to the sample shape and constituting elements, microstructural, dielectric, electromechanical characterizations and energy harvesting tests are more or less suitable and will be performed accordingly. Through such complementary investigations, we aim a better understanding of the impact of PZT microstructure and interfaces (electrodes/active layer/substrate) on the electromechanical performances of the multilayer energy harvester. The next paragraphs give details on the nature of each constituent of the multilayer.



Figure IV-7: Scheme of the multilayer considered as the “elementary brick” of the EH structure.

Table IV-1: Description of the different materials and corresponding characterizations used in a complementary approach.

SAMPLE	 Zig-zag	 Cantilever	 Printed disk	 Ceramic
Layer materials	SS/Au/PZT/Au	SS/Au/PZT/Au	Au/PZT/Au	Au/PZT/Au
Technology	All layers are screen-printed on SS substrate and co-fired	All layers are screen-printed on SS substrate and co-fired	Multi-layer Au/PZT/Au screen-printed on a sacrificial layer and co-fired	Bulk ceramic (conventional sintering), Sputtered Au after sintering
Area dimensions Au thickness PZT thickness	11.5mmx12.7 mm ≈10μm ≈50μm	30mmx2mm ≈10μm ≈50μm	Diameter ≈8mm ≈10μm ≈100μm	Diameter ≈1.4mm ≈100nm ≈2mm
Structure (XRD)	No	No	Phase composition	Phase composition
Microstructure analysis (SEM, EDS)	No	Interfaces, PZT grain size, porosity, Chemical analysis	PZT grain size, porosity, Chemical analysis	PZT grain size, porosity, Chemical analysis
Dielectric and electro-mechanical characterizations (impedance analyzer + IEEE calculations)	No	Basic electrical model of the EH.	Permittivity Piezoelectric and electromechanical coefficients	Permittivity Piezoelectric and electromechanical coefficients
Energy harvesting test (extracted power)	Piezoelectric-magnetic principle	Shaker vibration	No	No

2.2 Materials constituting the EH structure

2.2.1 Active material PZT

Piezoelectric Lead Zirconate Titanate printed (PZT) material is selected for the EH application because of its outstanding electromechanical properties compared to other materials chosen for this application (see chapter 1, Tables I-4 and I-6). A hard PZT type powder, PZ26 from Ferroperm, already studied in the Laboratory for other MEMS fabricated by thick film technology [22] is selected. This powder is used for all the 4 structures studied (Table IV-1). The characteristics and properties of this PZT type are given Table IV-2.

Table IV-2: Pz26 (Navy I) Hard type PZT properties (From *meggitferroperm.com*)

Material property	Symbol	Value
Density (g/cm ³)	ρ	7.70
Mechanical Quality Factor	Q_m	>1000
Relative dielectric permittivity at 1 kHz	ϵ	1300
Dielectric dissipation factor at 1 kHz (%)	$Tan \delta$	0.3
Curie temperature (°C)	T_c	>330
Electromechanical factor (planar mode)	k_p	0.56
Piezoelectric charge coefficient (pC/N)	d_{33}	300

The exact composition of the commercial PZ26 powder is not provided. The XRD pattern of the powder at room temperature displays a perovskite phase without pyrochlore phase. The XRD pattern shows that $PbZr_xTi_{1-x}O_3$ powder has a composition $0.44 < x < 0.53$ near the morphotropic phase boundary (MPB) with predominant tetragonal and rhombohedral crystalline structures (Figure IV-8). The width of the MPB region depends on the compositional homogeneity and on the sample processing conditions (Figure IV-9). A composition belonging in this range is suitable to achieve enhanced piezoelectric properties [23]. Concerning the PZT particle size, SEM pictures show that the PZT powder is formed of agglomerates ($\approx 10 \mu m$) made of micrometer and mainly sub-micrometer particles (Figure IV-10). This is in good agreement with the results provided by granulometry analysis (Annex 1)

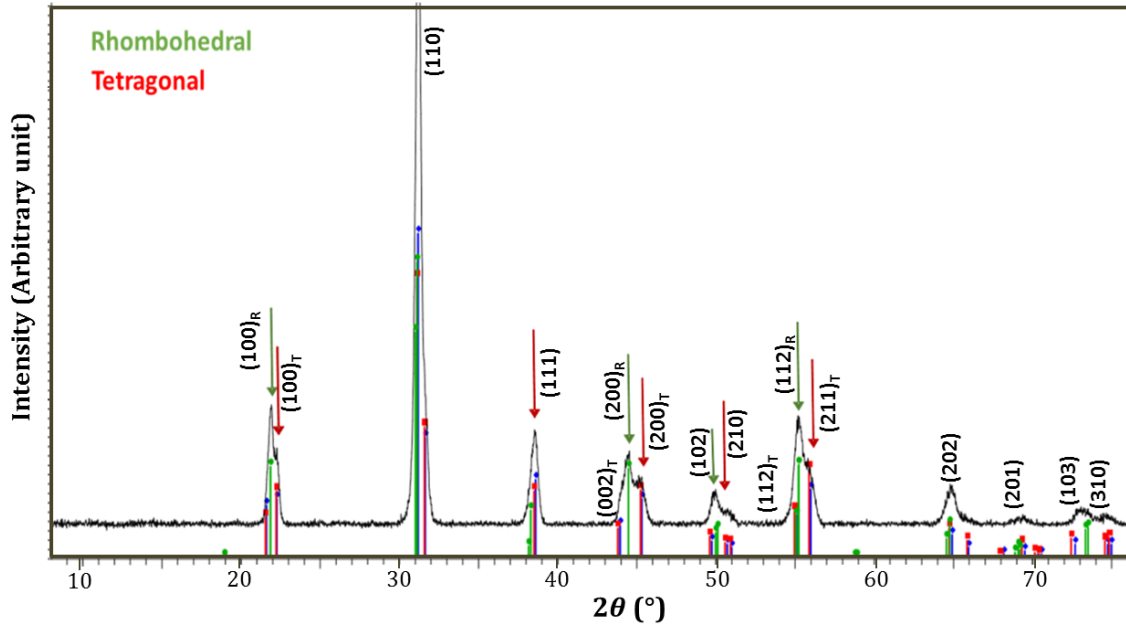


Figure IV-8: XDR pattern of PZT PZ26 initial powder with diffraction peaks indexed in the rhombohedral and tetragonal symmetries.

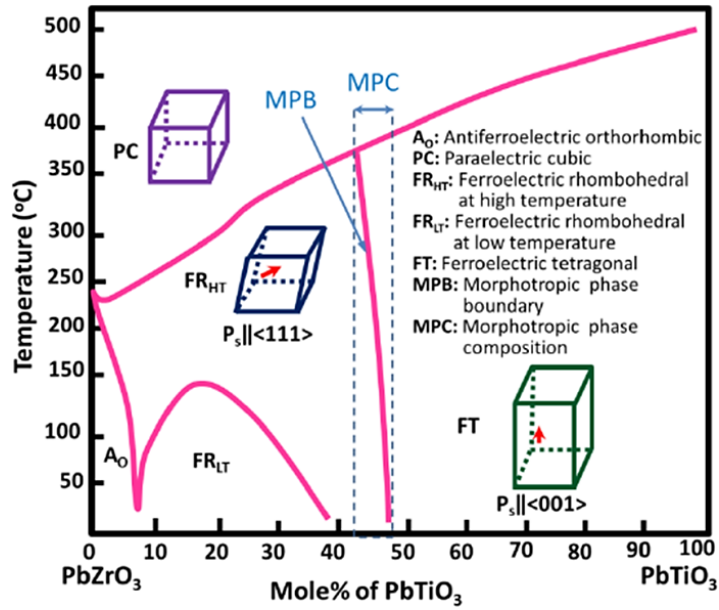


Figure IV-9: Phase diagram for PZT, with relevant regions labeled (reproduced from [23])

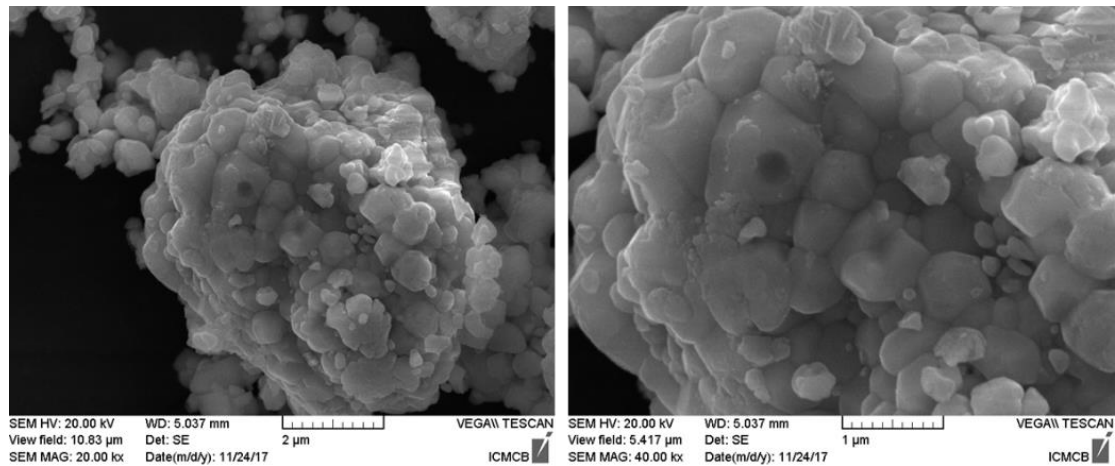


Figure IV-10: SEM pictures of PZT powder obtained at different magnifications.

2.2.2 Electrodes

A gold and terpeneol-based ink ESL8836 from ESL (ElectroScience, www.electroscience.com, Annex 2) is used for the modified zig-zag structure, the cantilever and the printed disk. Electrodes should be very thin compared to the PZT layer. This kind of conductive film is specially designed to achieve thin and dense films on ceramic substrates ($<9\mu\text{m}$). Moreover, the fact that it is well suited for automatic thermosonic wire-bonding is interesting for the electrodes connections needed for the next steps of polarization and electromechanical tests. Note that, as in most of the thick film pastes, a glass frit is present in the composition to promote densification and adhesion on the substrate (Table IV-3). Previous thesis work showed good compatibility between gold paste and PZT pastes after sintering. This is the reason why once again we selected this type of conductor.

Table IV-3: Concentration of the different elements in the commercial ESL8836 gold ink [24].

Compounds	Au	PbO	SiO ₂	CdO	Al ₂ O ₃	Bi ₂ O ₃	CaO
%mol	84	4.8	4.6	2.7	1.7	1.2	0.9

2.2.3 Substrate

Since the target resonance frequency is relatively low, a substrate material with a low Young's modulus has to be selected to reduce the stiffness of the EH. The substrate should also be compatible with all the fabrication steps of the process, especially the firing of the printed layers, typically between 850°C-950°C. As mentioned in chapter 3, silicon wafers, or alumina substrates classically used in thick film technology have too high Young's modulus. Therefore, metallic substrates are preferred. Different metallic substrates used as passive substrates for EH can be found in the literature [15][25]–[28]. Among them, stainless steel (SS) is selected because of its high melting temperature (Table IV-4). Preliminary tests with SS301 and SS316 showing lower CET have been first performed to check the compatibility with the future Au ESL8836 electrode. After the firing at 850°C (temperature recommended by ESL provider), better adhesion and less oxidation are observed with the SS301. SS301 substrate is hence kept as the substrate material of the EH structure (see Table IV-5 for SS301 chemical composition).

Table IV-4: Properties of metallic substrate materials employed in EH applications (properties generally found in industrial providers) [www.matweb.com and manufactures]

Material	Density (g/cm ³)	E (GPa)	Melting temperature (°C)	Expansion coefficient (at <650°C) (μm/m-°C)
Brass	8.50	97	900-940	19.0
Copper	8.96	110-128	1084	16.5
301 Stainless steel	7.88	193	1400 - 1420	18.0
304 Stainless steel	8.00	193	1400-1455	18.7
316 Stainless steel	8.00	193	1370-1400	17.5

Table IV-5: Typical concentration of the different elements constituting the SS301 stainless steel

Compounds	Fe	Cr	Ni	Mn	Si	C	N	P	S
%mol	70.7-78	16-18	6-8	≤2	≤1	≤0.15	≤0.10	≤0.045	≤0.030

2.3 Design of the complex geometry

This section shows how modeling has allowed to select the specific zig-zag geometry briefly introduced in Table IV-1. This specific geometry has been designed and optimized for piezo-electromagnetic application. The objective is to maximize the power density while maintaining a fundamental frequency in the range of 60 Hz to match the resonance frequency of the North American power grid. A permanent magnet is used in the design as a tip mass to harvest energy from the electromagnetic field of the current-carrying wire and to help tune the natural frequency of the system to the desired frequency.

For the optimization of the geometry, the energy harvester is modelled using the 3D FEA software COMSOL Multiphysics and its associated MEMS module. The material properties (stainless steel and PZT) used for these simulations are presented in Tables IV-6 and IV-7. Note that the properties of the Au electrode are not taken into account, considering that its thickness is lower than that of the PZT and will not affect the overall performances.

Table IV-6: 301 Stainless steel properties (collaboration Waterloo, Canada, [29]).

Young's modulus	193 GPa
Density	7.88 g/cm ³
Poisson's ratio	0.24
Thickness	0.254 mm

Table IV-7: Screen-printed PZT parameters determined experimentally at IMS. (collaboration Waterloo, Canada, [29]).

Young's modulus	43 GPa
Density	5.5 g/cm ³
Piezoelectric coefficient d₃₁	-40 pC/N
Thickness	0.075 mm

The EH selected geometry is described in Figure IV-11 (a). It is a centrally-supported meandering geometry with an overall footprint of 14.7 mm x 12.7 mm (187 mm²) which excludes the extra space near the clamp that is used for fine-tuning the resonant frequency. The 0.254 mm thick stainless steel substrate supports the 75 μ m thick strips of PZT on each beam. A fixed-end boundary condition is imposed by clamping one end of the central beam. The remainder of the structure is unrestricted and a neodymium magnetic proof mass is attached to the opposite end. This kind of magnet is selected due to its strong magnetic flux density and availability in a variety of sizes. The properties of this magnetic tip mass used for the simulation are given in Table IV-8.

This proposed geometry results in higher energy harvesting efficiency: bending modes are dominant during harvesting and torsional mode effects in the clamped beam are reduced. The proposed geometry also minimizes the area of strain nodes, which subsequently results in a greater harvestable area.

Table IV-8: Neodymium magnet (NdFeB, N42) properties. (collaboration Waterloo, Canada, [29]).

Young's modulus	160 GPa
Density	7500 kg/m ³
Poisson's ratio	0.24
Dimensions	3.175 mm x 3.175 mm x 12.7 mm
Weight	0.96 g
Magnetic remanence	1.32 T

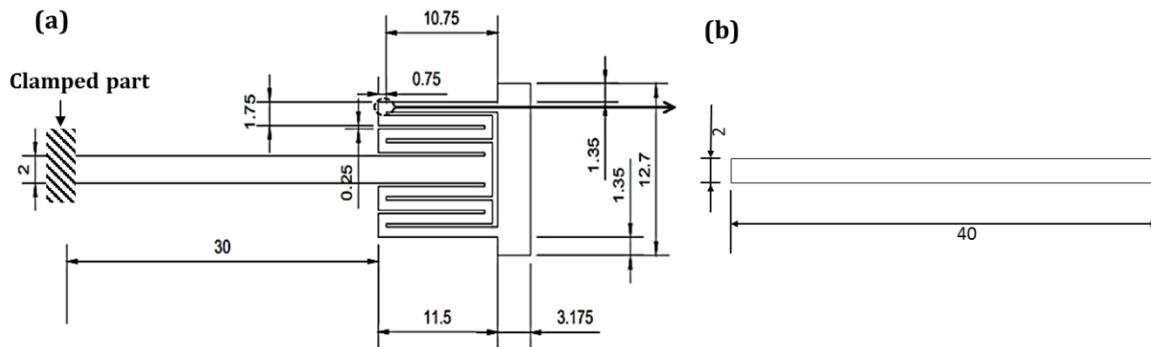


Figure IV-11: Dimensioned (mm) schematic of energy harvester substrate (a) optimized geometry (modified zig-zag) and, (b) simple structure corresponding to the middle branch of the modified zig-zag structure used for preliminary experiments and characterizations.

With an eigenfrequency analysis performed using the Solid Mechanics physics in COMSOL, the natural frequency and mode shapes can be obtained. The obtained strain contour and the corresponding displacements are shown in Figure IV-12. Each beam experiences either tension (red color) or compression (blue color) along its entire length during cyclic motion. This is a critical but interesting characteristic, as any strain node within the length of the beam would require segmented electrodes to avoid charge cancellation. Additionally, an alternating strain pattern across adjacent beams is observed, and as output voltage depends on it, continuous

electrode across the entire structure cannot be used before polarization. Consequently, the PZT need to be placed along the length of each beam with discontinuities at each beam end to avoid strain nodes. The particular configuration of the electrodes developed to avoid voltage cancellation will be detailed in the next paragraph (screens and polarization).

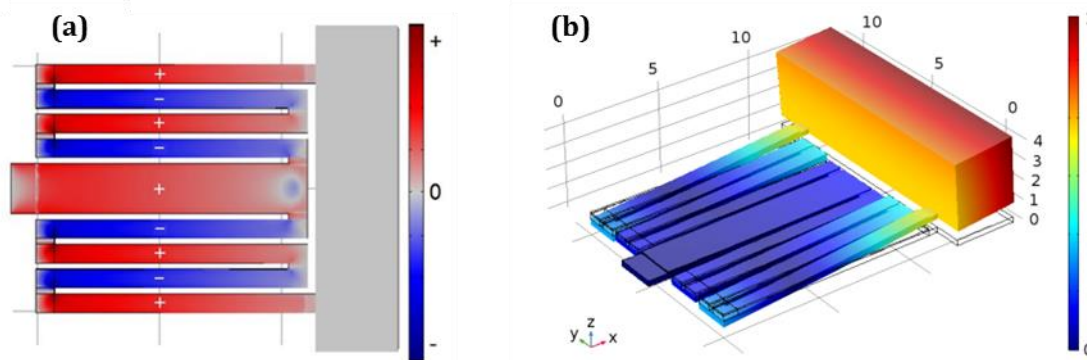


Figure IV-12: 3D FEA COMSOL analysis of fundamental mode shape showing (a) Strain. (b) Total displacement (in mm) (isometric view).

3 Fabrication process: cantilever and complex EH structure

3.1 Screen fabrication

3.1.1 Screen characteristics

The determination of the screen's characteristics (mesh count and emulsion thickness) is guided by the search of a compromise between definition and layer thickness. The electrodes must be thin (few microns after firing) and well defined while the PZT must be thicker (40-80 μm after firing) to ensure good properties, but not too much to avoid high thermal stresses. The selected screens and their characteristics are described in Table IV-9.

Table IV-9: Selected screens for the printing of the layers on the SS substrate

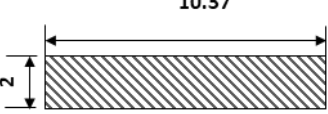
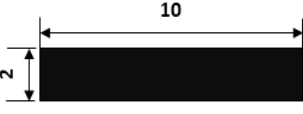
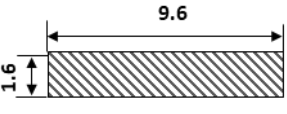
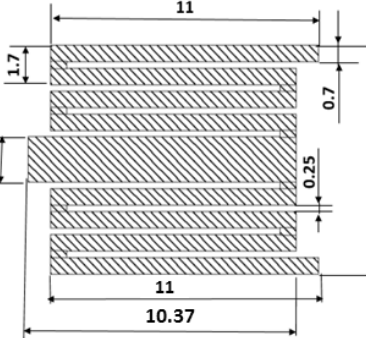
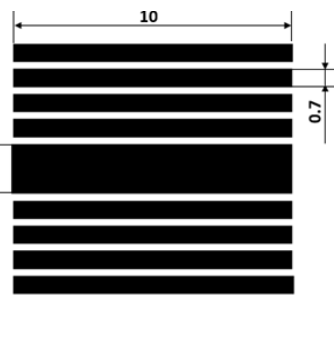
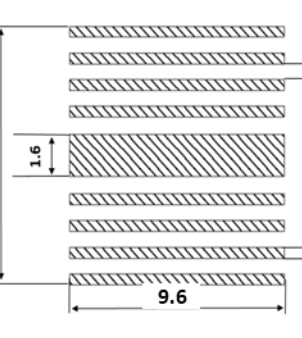
Layer	Screen type (mesh count M) (μm)	Light-sensitive emulsion thickness (μm)	Layer thickness after firing (μm)
Au electrodes	325	15	8-12
PZT active layer	200	50 (x2 for thicker layers)	40-80

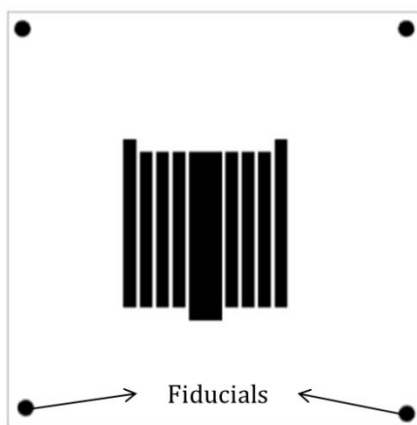
3.1.2 Layer mask and photolithography patterning

The software CleWin5 is used to design the electrodes and the piezoelectric layer in accordance with the substrate geometry defined in section 2.3. Short-circuits are avoided using a gap of 200 μm between the electrodes layers. The layers design (Table IV-10) is converted separately

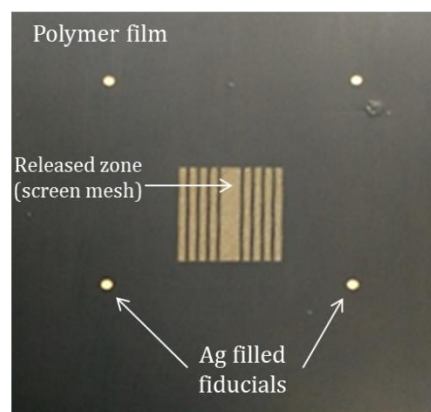
into a suitable photo-plotter format, and then translated into a patterned thick-film screen using a UV photo sensitive polymer film (chapter 3, section 1.2.2). Figure IV-13 shows a resulting screen for the PZT layer after UV patterning. The mask design (as the others) contains four circular guidelines (fiducials) in four corners necessary for the alignment of the PZT layer on the bottom gold layer

Table IV-10: Geometries of the different layers of the EH structure (dimensions are in mm).

Structure	Bottom Au electrode	PZT	Top Au electrode
Simple			
Modified Zig-Zag			



(a)



(b)

Figure IV-13: (a) Mask with circular guidelines (fiducials) for alignment purpose, (b) photograph of a fabricated screen.

3.2 PZT paste

3.2.1 Paste Formulation

PZT paste is fabricated at the IMS laboratory. It is based on the mineral part and a commercial organic vehicle ESLV400 (alcohol-ester type solvent with an ethylcellulose binder (see Annex 3)). The mineral part is a mixture of $\text{PbZr}_x\text{Ti}_{1-x}\text{O}_3$ powder (PZ26 Ferroperm) with the ternary system LBCu consisting of a mixture of the powders Li_2CO_3 , Bi_2O_3 , CuO (from Sigma Aldrich). The LBCu is an additive used as sintering aid to lower the sintering temperature of PZT. Previous work has already shown a better densification and reproducibility of the PZT based screen-printed thick films when using the PZ26 powder mixed with LBCu [30][31][32]. The complex system LBCu cannot be rigorously considered as a liquid phase sintering. There is an eutectic with a melting point at 690°C for the system $\text{Bi}_2\text{O}_3\text{-Li}_2\text{CO}_3$, ensuring a liquid phase sintering. The efficiency of LBCu to lower sintering temperature of PZ26 has been fully demonstrated in comparison with other sintering aids such as borosilicate glasses [30][33]. In particular, if only LiBiO_2 is used, the sintering temperature is decreased down to 1000°C but the addition of CuO allows a further decrease down to 800°C [31]. The composition used in this work is given in Table IV-11.

Table IV-11: Composition of the mineral part of the PZT ink formulation.

Powder	%wt
PZT (PZ26)	97.00
Li_2CO_3	0.80
Bi_2O_3	1.20
CuO	1.00

3.2.2 Paste preparation

To improve the efficiency of the sintering aid, the size of the powders constituting the sintering aid are first homogenized. A milling step is hence carried out and afterwards, the grain sizes of CuO , Li_2CO_3 and Bi_2O_3 powders are $5\mu\text{m} \pm 0.03$, $19\mu\text{m} \pm 0.11$ and $6\mu\text{m} \pm 0.03$ respectively (results presented in Annex 4). In previous works [22], the described mixture PZT +3%wt LBCu paste is used to print the PZT layers. PZT, Li_2CO_3 , Bi_2O_3 and CuO are weighed and mixed with the turbula in a container with 8 agate balls and 40 ml of ethanol for 12 hours. After drying at 120°C , during 7h, the organic binder ESLV400 and the powder are mixed in a mortar. The paste is then processed in the three-cylinder mixer for 20 minutes to homogenize the mixture (see chapter 3). The proportion of the organic binder is critical to achieve the good rheological properties of the paste and as a result a good definition of the layer. On one hand, a fluid ink (higher quantity of organic binder) lead to a better smoothing after printing ie. marks left by the screen meshes disappear. On the other hand, a more viscous ink allows a better hold and definition of the pattern, but mesh traces can still be visible. Of course, in both cases, pseudo-plastic and thixotropic behaviors should be kept (see chapter 2). Moreover, if the paste has too high organic phase content, it can lead to the apparition of cracks and bubbles due to a rapid evaporation of the solvent during the drying step. Therefore, three different proportions have been tested (Table IV-12) to determine an optimal proportion mineral/organic phase. The viscosity

measurements of the different inks display values less than 50 Pa.s for a shear rate of 100 s⁻¹ (Figure IV-14). As expected, pastes 1 and 2 have lower viscosity than paste 3 because of the lower content of organic binder. Although paste 3 viscosity has similar rheological behavior as the two commercial pastes, the quality of the deposited layers is not satisfactory as seen in Figure IV-15, where meshes traces are observed. The probable reason is that the two commercial pastes have been optimized for other applications requiring different rheological behaviors. In contrast, pastes 1 and 2 give both a good quality of deposit. Paste 2 with the ratio PZT powder/organic vehicle ratio (85.7/14.3 %wt.) is then selected, to benefit from its lower vehicle proportion in comparison with paste 1.

Table IV-12: Composition of the three tested pastes. The deviations are due to possible errors induced by the weighing procedure.

Paste	PZT + 3% LBCu (%wt)	ESLV400 (%wt)
1	85.0 ±0.2	15.0 ±0.2
2	85.7 ±0.3	14.3 ±0.1
3	89.9 ±0.2	10.1 ±0.2

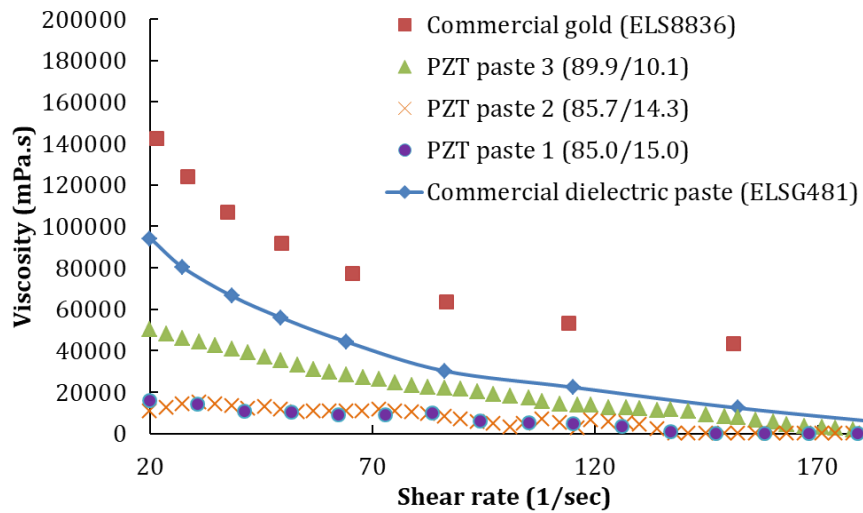


Figure IV-14: Viscosity of the ink tested for PZT formulation. Measurements made at 25°C with the Brookfield rheometer (Elorprintec, Pessac).

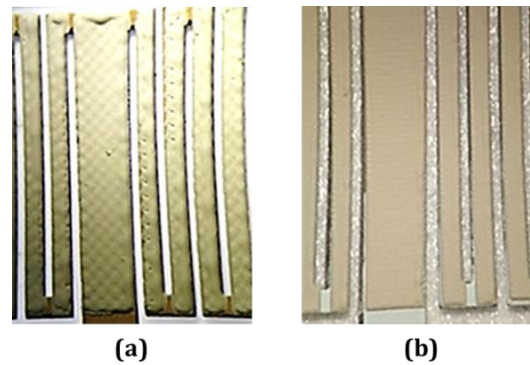


Figure IV-15: Printing tests for two prepared pastes, (a) paste 3 and (b) paste 2. (See Figure IV-14 for the corresponding viscosities. Paste 1 picture is equivalent in deposit quality aspect)

3.3 Printing

3.3.1 Substrate holder

For the deposition of the layers, because the expected device has a complex geometry, commercial substrate holders cannot be used. Special holders are fabricated. They are made of stainless steel micromachined by laser cut with thicknesses of 200, 250 and 300 μm for different PZT thicknesses. Four circular fiducials are then printed (dielectric paste ESL 4924, see Annex 2 chapter 2) on the substrate holder and then fired at 850 $^{\circ}\text{C}$. They are the references for the future alignment of the screens (Figure IV-16). This substrate holder is also used for the simple cantilever fabrication, since it has the same dimension than that of the central beam of the zig-zag geometry. The printed parameters (off-contact distance, squeegee speed and pressure) are also first optimized for the simple cantilever before the transfer towards the zig-zag geometry.

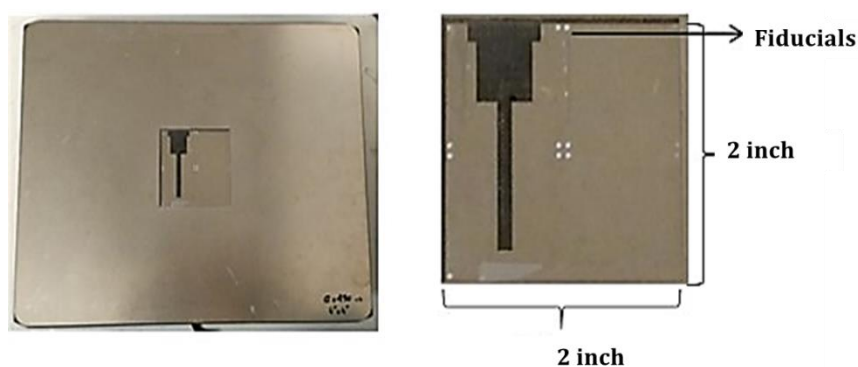


Figure IV-16: Stainless steel substrate holder fabricated for the layers deposition on the zig-zag shaped SS substrate.

3.3.2 Layers deposition

Once the alignment settings between the screen and the substrate are performed, the bottom gold electrode is first printed and dried for 20 minutes at 120 $^{\circ}\text{C}$. Next, the PZT layer and top gold

electrode are printed successively, with a drying step during 20 min at 120°C between each deposition. A slow drying rate of 1°C/min until 120°C is preferred for PZT layer to avoid bubbles or cracks. A description of these successive steps is illustrated in Figure IV-17. Multiple layers deposition for Au and/or PZT (printing and drying between each deposition) can be done depending if a thicker layer is expected.

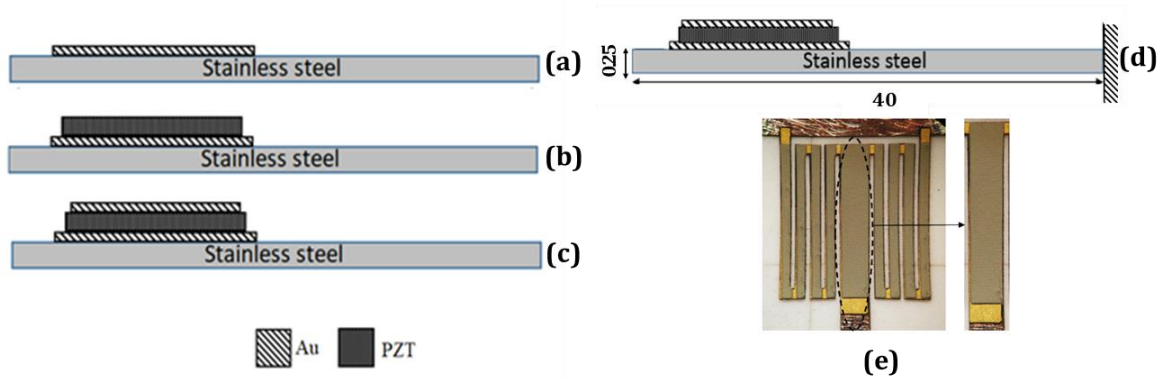


Figure IV-17: Fabrication steps of the screen-printed EH multi-layer (modified zig-zag and simple cantilever): (a) bottom Au electrode, (b) active PZT layer (c) top Au electrode, (d) cross section of the cantilever (dimensions in mm), (e) modified zig-zag EH with dried PZT layer after printing.

3.4 Sintering

After printing, the stack of the printed layers is first isostatically pressed 5 min at 40 MPa and fired at 65°C in order to improve the PZT densification [30]. The thermal profile used has already been optimized in previous work at IMS Laboratory [22], leading to efficient densification of the PZT +3wt% LBCu at 900°C. Higher sintering temperature than 900°C results in composition inhomogeneity reflecting significant loss of PbO. The corresponding density and electromechanical properties are altered as shown in many studies reported in literature for non-stoichiometric PZT [34][35].

The temperature profile shown in Figure IV. 18 comprises the following steps:

- Heating at 40°C/min until 250°C
- Heating at 1°C/min between 250°C and 450°C, in order to allow the progressive decomposition of organic binders
- Heating at 40°C/min from 450°C until 900°C. Contribution of sintering aid to promote densification (especially melting of the $\text{Li}_2\text{CO}_3\text{-Bi}_2\text{O}_3$ eutectic at around 690°C)
- Sintering time: 2 hours at 900°C
- Cooling at 40°C/min to about 150°C
- Samples are finally let to cool down naturally till room temperature.

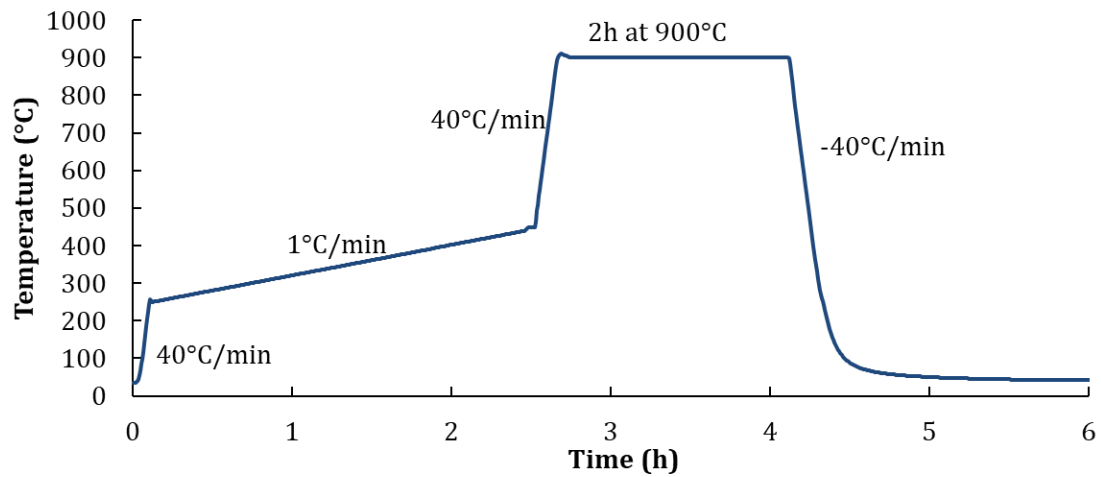


Figure IV-18: Sintering cycle used for densification of PZT+3%wtLBCu ceramics.

A stylus profilometer is used to measure the thickness of the samples after firing. Two measurements are made along line A-A and B-B as shown in Figure IV-19 (a). The A-A scan shows the variation of the thickness along the length of the center beam whereas the B-B scan shows the variation of the thickness in between the beams. The obtained thicknesses after firing are summarized in Table IV-13.

Table IV-13: Thickness values of the printed layers after firing

Layer	Thickness (μm)
Bottom Au electrode	8 ± 2
PZT	55 ± 3
Top Au electrode	10 ± 2

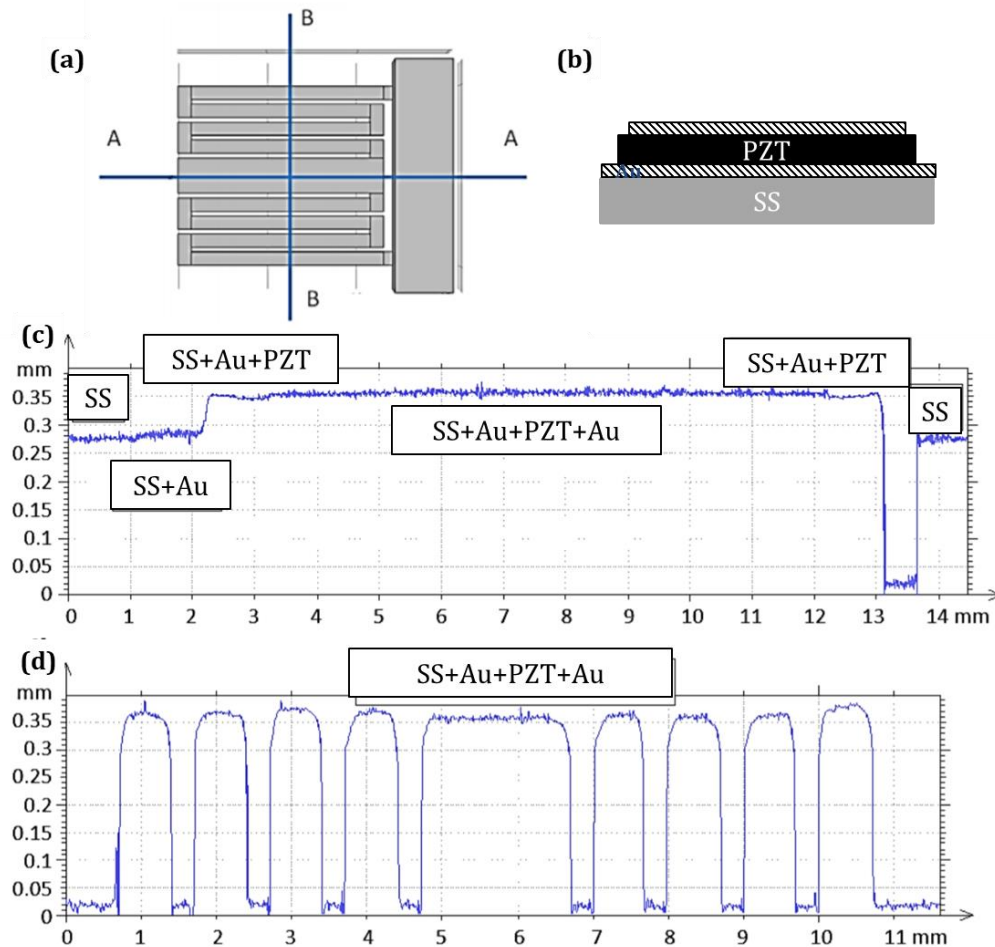


Figure IV-19: (a) Thickness measurement lines across the sample for stylus profiling (b) profile along line A-A, (d) profile along line B-B. The SS substrate has a thickness of $254\mu\text{m}$.

3.5 Polarization

Once fired, electrical connections for polarization and electrical characterizations are performed.

3.5.1 Simple cantilever

For the simple cantilever structure, Ag wires of diameter $100\mu\text{m}$ are glued on the top and bottom Au electrodes with Ag epoxy paste as detailed in chapter 3. For the modified zig-zag structure, the strain-matched polarization technique is used as Berdy *et al.* [6]. This implies more complicated electrodes connections as detailed in the next paragraph.

3.5.2 Strain matched polarization technique (SME) for the zig-zag geometry

During vibration, each adjacent beam has opposite strain as shown by COMSOL simulation of the strain (paragraph 2.3, Figure IV-12), and positive strain produces negative charges and vice versa. Thus, to match the strain plots and to avoid voltage cancellation across the harvester, a strain matched-electrode polarization is done where each beam of the EH is polarized such that

the adjacent beam has the opposite polarization direction (Figure IV-20). By using this approach, after the polarization, the top electrodes of all the beams are connected together for the EH test, and all the beams have the same voltage polarity .

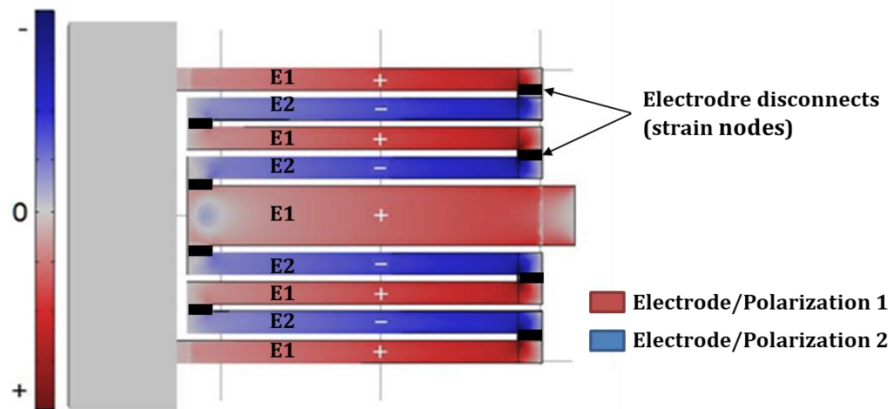


Figure IV-20: Left Strain contour plot showing tension (red) and compression (blue) (right) strain matched electrodes.

For the electrical connection of the thin beams showing the same strain (beams positive and negative beams groups named b_{i+} or b_{i-} in Figure IV-22, with $i = 1, 2, 3$ or 4) micro-wire bonding of Au wires ($100 \mu\text{m} \phi$) has been done at IMS, using the ball-bonding technique. Thanks to alumina tool, the Au wire is positioned to the top of the Au printed electrode of the PZT beam. A static pressure combined with ultrasonic vibrations creates a local welding and the connection is achieved (Figure IV-21 (b)). Heating effect is added to improve the bonding ($T = 80^\circ\text{C}$). After this wire bonding (two wires are connected in parallel to improve the reliability), each beam is polarized in opposite directions (as in bimorph configurations according to their tension or compression under vibration). This polarization step is carried out using two independent power suppliers according to the protocol described chapter 3, section 3.3.1. An electric field of $50\text{kV}/\text{cm}$ is applied for negative and positive beams during 10 min at 280°C .

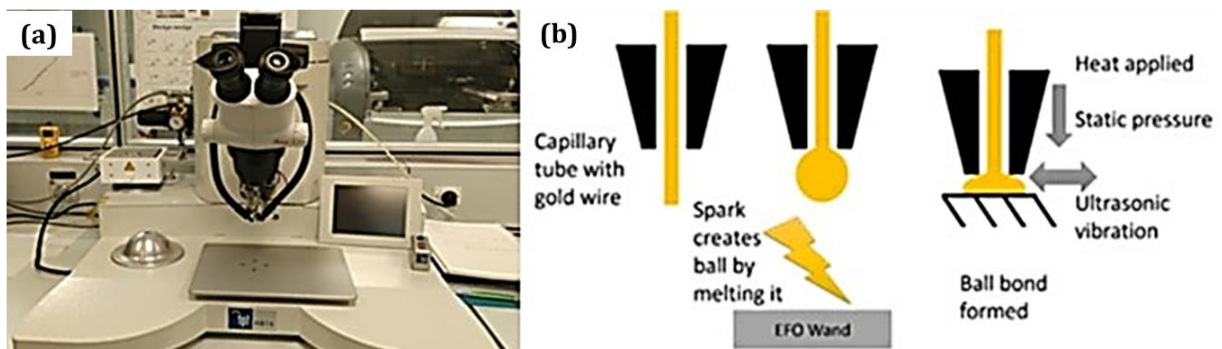


Figure IV-21: (a) Ball-bonding equipment K&S 4524 used at the IMS laboratory and (b) principle.

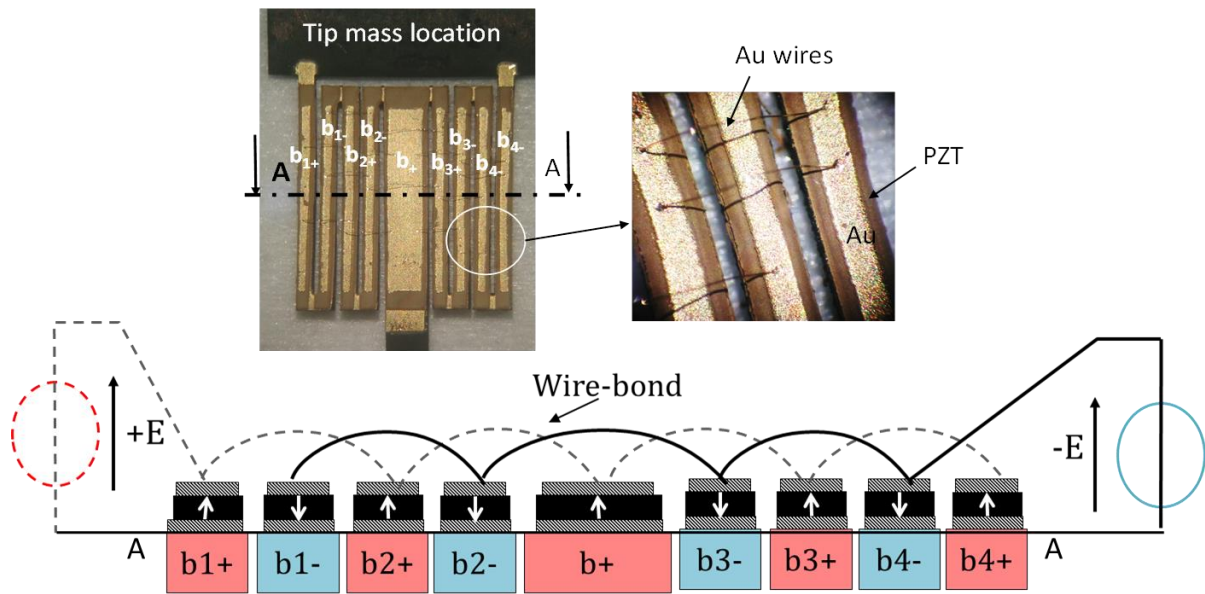


Figure IV-22: Photograph of the fabricated EH with the wire-bonding and scheme of the bonded wires.

4 Fabrication of printed disks and ceramics

To better understand the different key parameters of the fabrication process that could impact the performances of the EH structure, ceramics and free-standing printed PZT disks are also studied. The study of ceramics allows to investigate the influence of the LBCu sintering aid on the densification of the active PZT material, while the free-standing PZT printed disks with the same PZT formulation (PZT + 3%wt LBCu, + organic binder), allow to analyze the active SS substrate effect.

4.1 Printed disks

Screen-printed disks are made using the same Au and PZT+LBCu inks described in section 3.2.1. Once printed, the electroded PZT layers must be completely released from the substrate. This is achieved thanks to a sacrificial layer process classically used in MEMS process. The role of this sacrificial layer is to support the active layers during the densification process, without affecting the sintering process and with the minimum interactions with the active layers. The sacrificial layer needs to be first deposited on a ceramic substrate prior to the Au, PZT and Au layers stacking (Figure IV-23). This sacrificial polyester based layer ESL 244T (further information in Annex 5) is removed during the sintering process leading to free-standing piezoelectric disks ready for polarization process and for electromechanical characterizations [36]. Here, the circular shape of electroded printed PZT layers is aimed to further conduct piezoelectric characterizations on a simple disk, according to IEEE standards [34]. The screen selected for the deposition of gold electrodes is the same as the one used for the cantilevers fabrication (325 meshes, 15 μm emulsion). A 150 μm thick metallic stencil is used to achieve thick printed PZT layers in one step. The screen for the sacrificial layer is a 70 μm screen mesh with 50 μm thick photosensitive film.

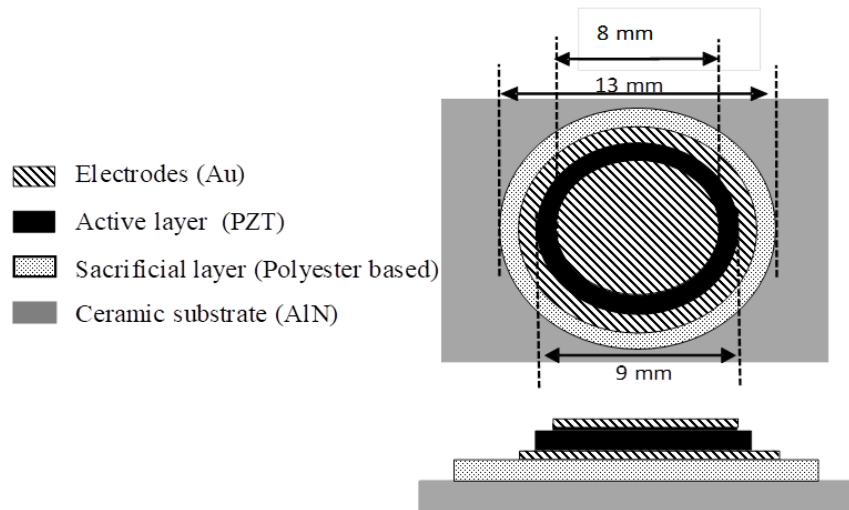


Figure IV-23: Schematic view of the screen-printed layers for the disks fabrication.

The firing cycle and the polarization step are carried out using respectively the sintering profile described paragraph 3.4. and the polarization protocol detailed in chapter 3. With a maximum applied voltage of 0.35kV.

4.2 Ceramics

The PZT powder is prepared using the same paste formula as for the screen-printing process (PZT + 3%wt LBCu) adding 15 wt % ESLV400 organic binder to the powder mix, followed by a drying step at 120°C during 8h. The green pellets (13mm diameter) are uniaxially pressed with a pressure of 18.5 ± 2 MPa, and then sintered following the firing cycle detailed in the section 3.4. Afterwards, Au electrodes (≈ 100 nm) are sputtered on the ceramic disk surfaces for polarization and electromechanical characterizations (following the protocol explained in chapter 3). A maximum electric field of 8 kV/cm is applied.

5 Characterizations

5.1 Microstructural analysis

The microstructures of PZT corresponding to the ceramic, the printed disk and the simple cantilever are compared (Figure IV-24). As previously mentioned, the PZT is mixed with similar content and nature of organic binder and sintering aid (3%wt LBCu) whatever the design. The firing profile remains the same for all the three structures. Highly densified ceramic is obtained at 900°C (relative density ≈ 97 %) confirming efficient densification at such low temperature thanks to the use of the LBCu sintering aid. SEM images of the fracture surface confirm a low level of apparent porosity and reveal a mean grain size of about $3\mu\text{m}$ with a narrow grain size distribution (Figure IV-24 (a)). The relative density is lower for printed structures (Figure IV-24 (b, c)). An estimated apparent porosity of 8% and 20% is evaluated, for printed disks and cantilevers respectively. The grain size distribution is broader and it is difficult to estimate precisely the average grain size considering the melted aspect of the grains or agglomerates. In

the co-fired structures, the sintering shrinkage mismatch between the electrodes and the active PZT layer must be considered. Differences in shrinkage behavior can generate stresses and defects and lead to constrained sintering compared to free sintering [35][37]. Retardation of PZT sintering kinetics can thus be expected. In cantilevers, mechanical clamping from the substrate is an additional parameter to consider. Furthermore, the specific preparation for SEM observation of cantilevers can explain the melted aspect of PZT grains (Figure IV-24 (b)). In comparison, free surfaces in ceramics allow both more efficient debinding and densification providing a faster kinetic pathway for mass transport and leading to enhanced PZT grain growth.

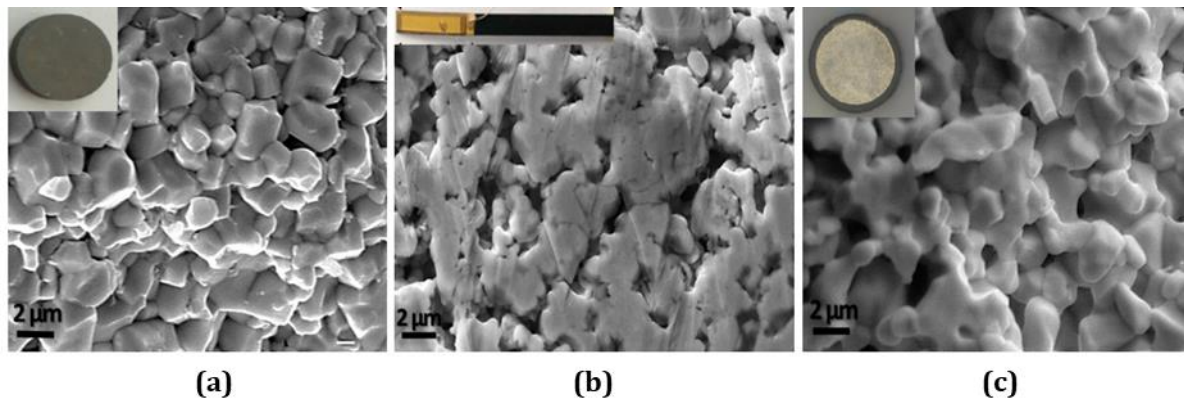


Figure IV-24: SEM images of PZT + 3%wt LBCu for (a) fracture section of ceramic, (b) printed cantilever cross polished section and, (c) fracture section of free standing printed disk.

5.2 Study of interfaces within the multilayer cantilever

When considering EH cantilevers structures, thermal stresses take place during firing cycle due to the difference of thermal expansion coefficients (CET) between the different materials constituting the structure. Figure IV-25 shows the complete energy harvester after firing with two different PZT layer thicknesses (55 and 100 μm). Bending of the structure is observed for the $\approx 100\mu\text{m}$ final thickness (Figure IV-25 (b)) and peeling off of the layer can arise (Figure IV-25 (d)). Indeed, thermal stresses during the firing lead to significant deformation of the structure. This is confirmed by the high difference between the CTE of SS and PZT ceramic highlighted through dilatometry analysis (Figure IV-26). In the high temperature range (500-600 $^{\circ}\text{C}$), an average of CET values of 16.7 and 4.7 $\text{ppm}/^{\circ}\text{C}$ are obtained for SS and PZT, respectively.

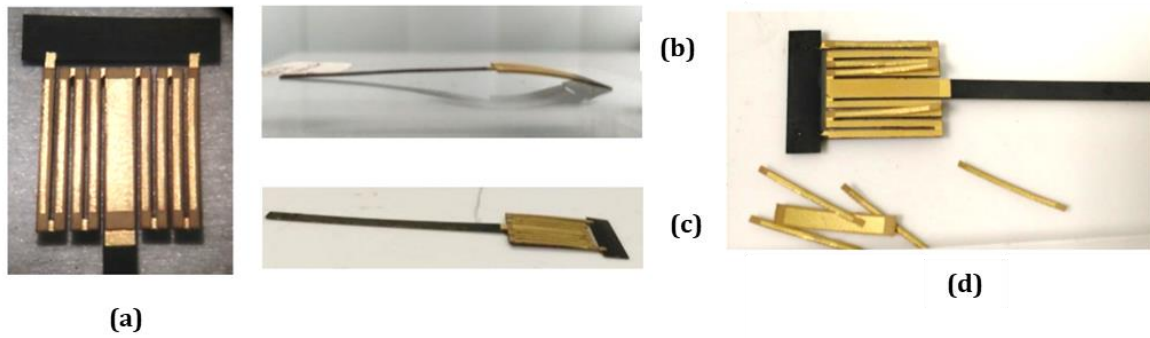


Figure IV-25: (a) Modified zig-zag cantilever EH structure after firing, (b) with a 100µm thick PZT layer, (c) with a 55 µm thick PZT, (d) peeling off of the layers for 100µm thick layers.

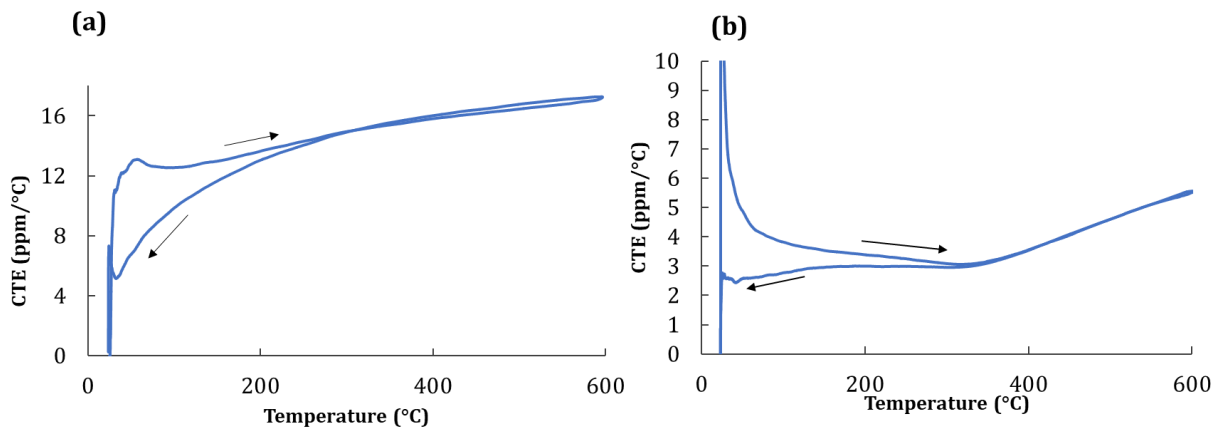


Figure IV-26: Thermal expansion coefficient as a function of temperature for SS substrate (a), and PZT ceramic (b).

Hsuen *et al.* have proposed a mathematical solution to evaluate the thermal stress in multilayered films on substrates. For this purpose, the system's total strain is decomposed into a uniform bending component [38]. The cross-section of our multilayered system is shown in Figure IV-27, where the film layers of individual thicknesses (t_{1Au} , t_{PZT} , t_{2Au}) are bonded sequentially to the stainless steel (SS) substrate (thickness t_s). The coordinate system is defined in such a way that the interface between the bottom Au layer (noted $1Au$) and the SS substrate is located at $z = 0$, with $z = h_n$ layer. Given the conditions: **(1)** The multilayer structure is subjected to a temperature change (ΔT), with residual thermal stresses (σ) (eq. 4.4 and eq. 4.5), **(2)** the substrate's thickness is much more higher than the one of the active layer ($t_s \gg t_{PZT}$), **(3)** the layers arrangement is asymmetrical and, **(4)** only the PZT and SS CET mismatch is considered to contribute to final bending (Au layer effect is overlooked). The curvature $1/r$ of the structure can be then evaluated using Eq. 4.6.

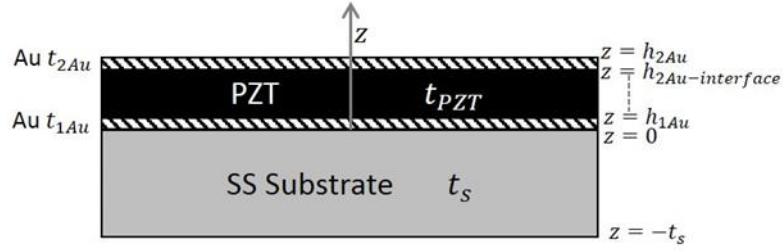


Figure IV-27: Cross section of multilayer structure with coordinate system used in the analysis [38].

$$\sigma_s = \frac{E'_s(3z + 2t_s)}{3r} \quad (\text{for } -t_s \leq z \leq 0) \quad (\text{Eq. 4.4})$$

$$\sigma_{PZT} = \frac{E'_s t_s^2}{6t_{PZT} r} \quad (\text{for } t_s \gg t_{PZT}) \quad (\text{Eq. 4.5})$$

$$\frac{1}{r} = \frac{6E'_{PZT} t_{PZT} (\alpha_{PZT} - \alpha_s) \Delta T}{E'_s t_s^2} = \sum \frac{1}{r_i} \quad (\text{with } r_i = \text{PZT or S}) \quad (\text{Eq. 4.6})$$

Where σ_s and σ_{PZT} are the thermal stresses in the substrate and PZT layer, respectively. $E' = E/(1 - \nu)$ is the biaxial modulus with E the Young's Modulus and ν is the Poisson's ratio of SS substrate or PZT layer individually. α_{PZT} and α_s are the thermal expansion coefficients of the substrate and PZT layer, respectively. $1/r$ is the physical representation of the component curvature upcoming from the mismatch between the substrate and the active layer. Using the properties reported in Table IV-14, the estimated curvature of the multilayer structure is calculated for different PZT thicknesses, considering a $\Delta T = 100^\circ\text{C}$.

Table IV-14: Elastic properties, average thermal expansion coefficient (500°C-600°C) and thicknesses of PZT and SS.

SS Young's Modulus (GPa)	193*
PZT Young's Modulus (GPa)	40*
SS Poisson's ratio	0.24*
PZT Poisson's ratio	0.33**
α_{SS} (ppm/°C)	16.7
α_{PZT} (ppm/°C)	4.7
t_{SS} (μm)	250
t_{PZT} (μm)	10-100

*[29]

**[39]

For a PZT thickness of $\approx 100\mu\text{m}$, an absolute value of 2.69 mm for the theoretical maximum curvature is obtained with a concave facing up structure whereas the experimental curvature is 3.5 mm (Figure IV-28). Experimental curvature is evaluated at the highest curvature point containing the PZT active layer of the structure. To validate the trend predicted by the analysis, several cantilevers with different PZT thicknesses have been fabricated (35, 55, 60, 70, 80, 100 μm). The maximum deviation between the experimental and calculated values reaches 29% for

a PZT thickness of 100 μm (Figure IV-28), this high percentage of error can be explained considering that at higher t_{PZT} (80-100 μm) the condition of the analytical solution $t_s \gg t_{\text{PZT}}$ is no longer valid. Decreasing PZT thickness leads indeed to both lower curvature values and a better agreement between experimental and calculated data. Thermal stresses can thus be significantly reduced by adjusting the PZT thickness.

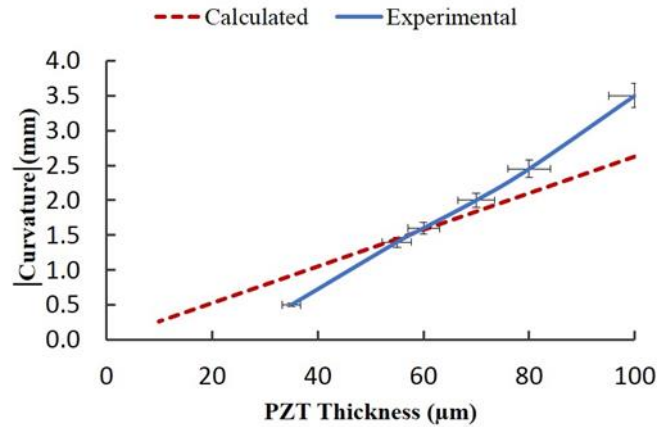


Figure IV-28: Comparison between calculated absolute values using Eq.4.6 and the measured experimental values for the curvature of multilayer structure analysis.

Cantilevers made with PZT thickness lower than 60 μm do not show significant bending (around 1 mm only) (Figure IV-25 (c)). The selected PZT thickness is thus 55 μm .

SEM observations of the cross-section of a non-deformed cantilever ($t_{\text{PZT}} \approx 55 \mu\text{m}$) allow to probe the good quality of the interfaces in terms of cohesion and composition (Figure IV-29 (a)). Good adhesion of the printed layers is observed between the top gold electrode and the PZT layer without delamination (Figure IV-29 (b)). The thickness of the top and bottom Au electrodes are 10 and 8 $\mu\text{m} \pm 2 \mu\text{m}$, respectively. The top Au electrode roughness ($\approx 300 \text{ nm}$) allows smoothing the PZT layer roughness.

The porosity within the active layer is homogeneously distributed without any significant evidence of densification gradients. Tensile stress due to the substrate effect does not seem to hinder densification close to the interface. However, the formation of an interfacial layer of about 20 μm between the bottom gold electrode and the SS substrate can be evidenced in Figure IV-29 (c). This interfacial layer results from interdiffusion between the substrate and the bottom electrode during the sintering process. Bulk diffusion or diffusion across defect paths (dislocations in the metal, the porosity of gold due to thermal decomposition of organics) can explain the cross-diffusion between the two layers.

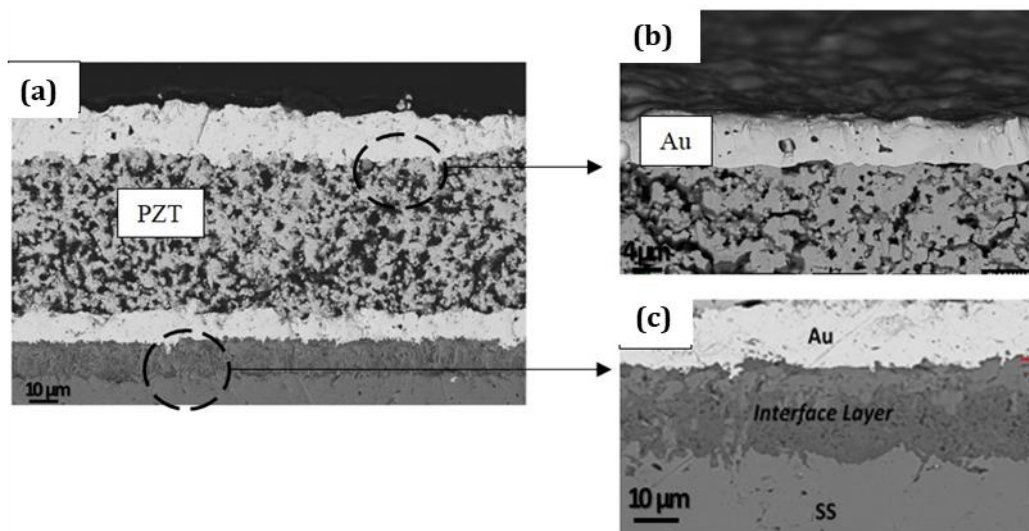


Figure IV-29: SEM analysis of (a) Au/PZT/Au/SS, (b) top Au electrode/PZT interface and, (c) interface layer between bottom Au electrode and SS substrate

EDX analysis of the different layers (Figure IV-30) reveals that the interface layer between bottom Au electrode and SS substrate contains 45% of the elements constituting the gold ink (Si, Pb, Cu) and 55% of elements of the SS substrate (Fe, Cr). The high level of oxygen confirms the partial oxidation of the substrate in the vicinity of the interface.

The interface layer still ensures cohesion between the electrode and the substrate without the presence of Kirkendall porosity that could be more detrimental [16]. However, such diffusion process at the electrode/substrate interface creates a passive layer whose mechanical properties would impact more globally the properties of the device and has to be accurately controlled.

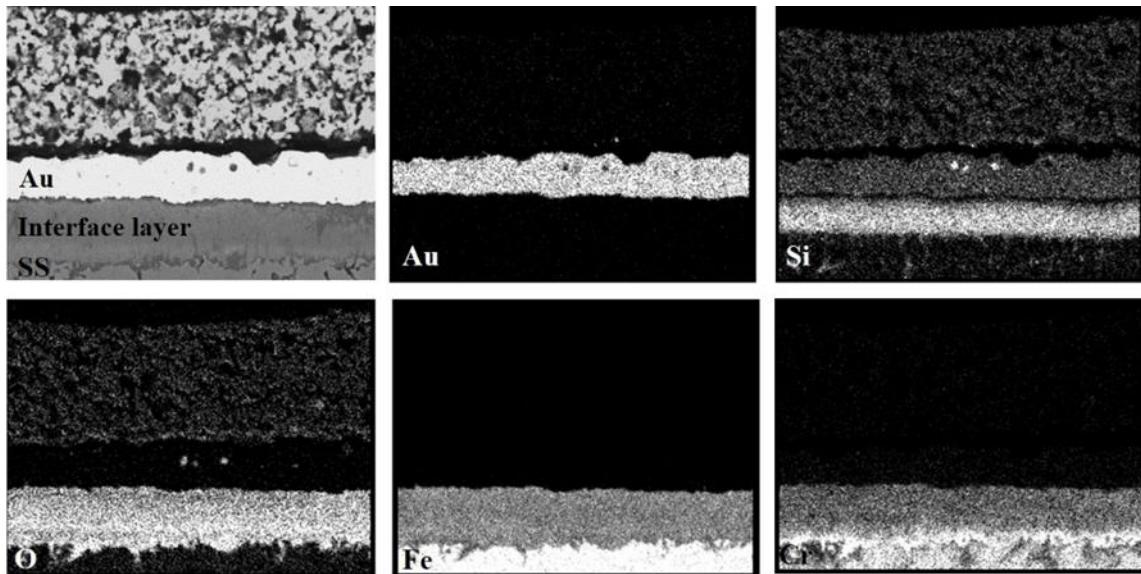


Figure IV-30: Figure 1: Energy Dispersive X-ray (EDS) analysis of SS/Au/PZT multilayer structure: chemical cartography of Au/SS interface layer after sintering.

5.3 Dielectric characterizations

Dielectric measurements at different temperatures and frequencies are first carried out on PZT ceramics in order to determine the Curie temperature (T_c) (Figure IV-31). The Curie temperature, determined at the maximum of capacitance, occurs at 330°C as expected for the PZ26 [39]. Considering measurements performed 24 hours after poling at 0.5kV/mm, a relative permittivity of 1200 and dielectric losses lower than 0.14% are measured at room temperature for 1 kHz. The permittivity value is slightly lower than the one reported for commercial PZT (Pz26 from ferroperm) ceramic ($\epsilon' \approx 1300$ – sintering at 1200°C). Nevertheless, the differences between the two ceramics in terms of grain size and poling conditions (2-8kV/mm for the commercial ceramic) can explain this difference in permittivity values. Dispersion of the permittivity at low frequencies near T_c is observed but there is no signature of conduction mechanisms activated at high temperature ($T > 400^\circ\text{C}$). However, the increase of $\tan \delta$ from 380°C reflects the existence of residual space charges.

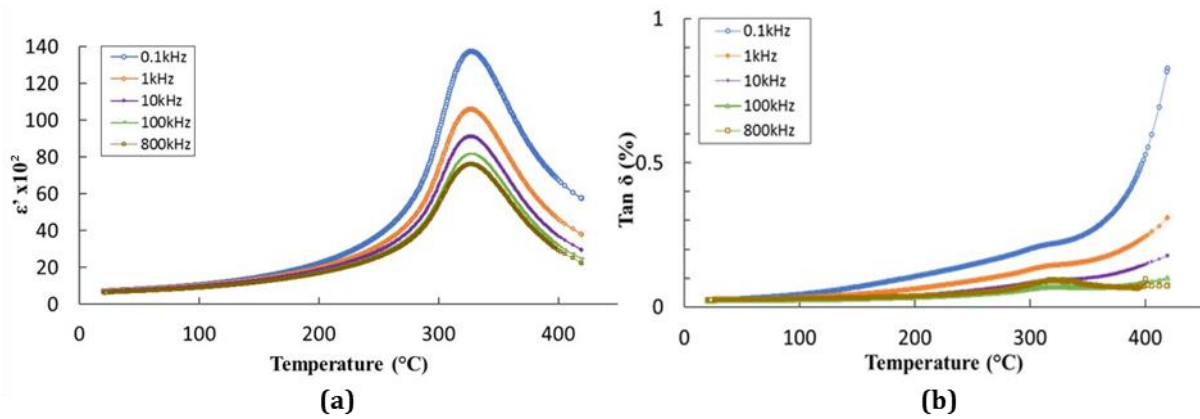


Figure IV-31: Permittivity (a) and $\tan \delta$ (b) for PZT ceramic at different frequencies and as a function of temperature ($23 < T(^{\circ}\text{C}) < 450$).

Capacitance measurements are also carried out for the printed disk. Relative permittivity close to 600 and dielectric losses $\sim 2.5\%$ at room temperature and 1 kHz are obtained. Such lower permittivity values compared to PZT ceramics can be partly explained by the lower relative density in the printed disk but cannot be rigorously compared because the applied poling electric field is not the same. However, the level of porosity is also a parameter that determines the maximum value of the field applied during poling.

5.4 Electromechanical characterizations

Admittance measurements are performed for ceramics, printed disk and simple cantilever structures. Results for simple cantilever EH harvesting are showed in Figure IV-32. By using the resonant frequency f_r and anti-resonant frequency f_a , effective electromechanical coupling factor $k_{eff} = 11\%$ is found, as well as a mechanical quality factor of $Q_m = 301$.

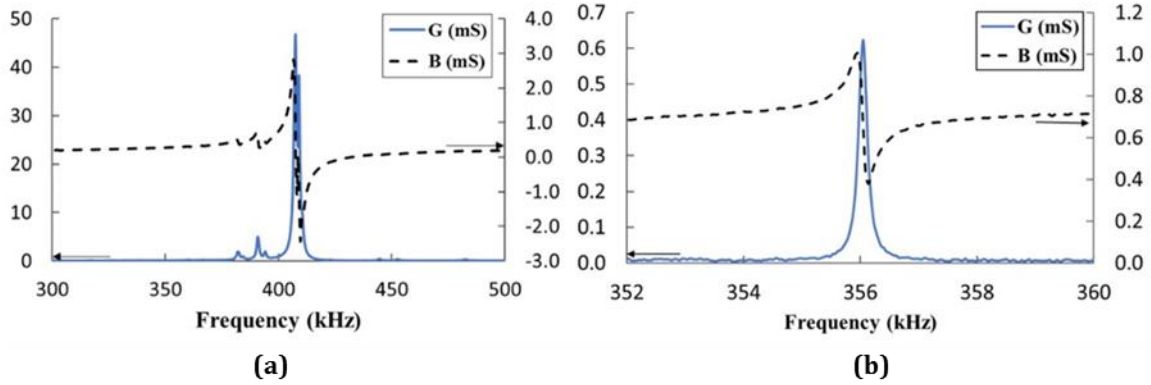


Figure IV-32: Impedance measurements: Conductance (G) and Susceptance (B) of (a) printed disk (b) and printed simple cantilever.

Values of k_{eff} of 26% and 28% approximatively are obtained for printed disk and ceramic pellets, respectively (Graphics in Annex 6). In general, better properties for ceramic pellets are expected due to higher densification. Nevertheless k_{eff} of printed disk is found to be similar demonstrating the efficiency of the process with the sacrificial layer and LBCu sintering aid. Furthermore the polarization conditions of the ceramic pellets with an applied field depending on the thickness of the sample are probably not optimized, which could disrupt the complete exploitation of the ceramic pellet performance [41].

Correlating the printing structures, the lower k_{eff} value obtained for the cantilever clearly shows the effect of the passive metallic substrate. Furthermore, a good value of piezoelectric coefficient d_{31} of 95 pC/N is estimated for printed disks (values are calculated as explained in chapter 3 section 3.3.4). Cantilever piezoelectric coefficients have a contribution from d_{31} depending on substrate properties, which cannot be equivalent with the standard IEEE model [34]. It is worth to know that these measurements have been carried out without any clamping of the PZT layer on the substrate. Nevertheless, the simple conductance measurement is relevant as it is directly related to the piezoelectric response of the structure.

Table IV-15 reports the material characteristics and summarizes the dielectric and piezoelectric properties of the PZT based EH structures compared with ceramics and printed free structures (printed disk). A systematic comparison with the commercial ceramic from Ferroperm is also included as well as two examples of PZT layers deposited on metallic substrate found in literature. As expected, the bulk ceramics present the highest dielectric permittivity due to higher density. Compared to the commercial one (sintering at 1200-1300°C), the ceramic sintered in the present work at 900°C presents slightly lower permittivity values but they remain in the same range of the commercial ones despite a significantly lower sintering temperature. Lower dielectric properties are also obtained for printed PZT in comparison with ceramics due to lower densification as discussed in section 5.1. Dielectric losses are also increased in printed layers (by a factor 10).

Electromechanical coupling and piezoelectric coefficients k_{31} , k_{eff} , and d_{31} , are deduced using the standard IEEE model [40]. Ceramics samples show the highest values approaching those of the commercial sample, comforting the role of LBCu to enhance densification at low temperature [22].

Free-standing printed disks with printed electrodes exhibit also very good piezoelectric and electromechanical coefficients. For these printed disks, the lower level of densification (compared to ceramic pellets) combined with higher thickness of printed electrodes, and poorer interface quality (compared to sputtered electrodes) [42] impact the global dielectric and piezoelectric performances. Nevertheless, similar piezoelectric properties are observed as those of the ceramic pellets also sintered with LBCu. Again, as already mentioned, the polarization conditions probably affect the piezoelectric properties.

For EH cantilever structures, lower electromechanical coupling and piezoelectric coefficients are obtained, as confirmed by finite element simulation analysis for the modified zig-zag cantilever [29]. Overall lower properties are expected for cantilever multilayer structure due to the presence of the passive metallic substrate supporting the active PZT layers. The substrate induces mechanical clamping stresses that limit the active material densification. Lou-Moeller *et al.* [29] also confirmed the limitations of the properties of printed PZT (PZ26) thick film when bounded on silicon and alumina substrates. They showed that sintering aids, inherent porosity and mechanical clamping from the substrate, are the three main contributions leading to lower properties values. Furthermore, referring to literature where very dense thin films are also deposited by aerosol on a cantilever SS substrate [43], electromechanical coupling factor k_{eff} of around 10 are also obtained (Table IV-15). In our case, even if our printed PZT layers present more porosity than the aerosol PZT layers, their higher thickness help to improve the electromechanical coefficient of the multilayer cantilever. More dense and thicker PZT layers clearly improve the performances of the EH as shown in Table IV-15 through the results reported by Colin *et al* on thinned bulk PZT glued on both sides of a SS cantilever [26]. With such a bimorph configuration and even with a glue interface between the SS substrate and the PZT, an increase of coupling coefficient is obtained thanks to the optimized properties of the thinned bulk ceramic. It is necessary to take into account that electrical properties will also depends on polarization step, therefore a rigorous comparison can only be made under same pooling conditions.

Table IV-15: Summary of properties for the different PZT equivalent structures.

Structure/ Properties	Ceramic PZT+ 3%wt LBCu	Printed disk PZT+ 3%wt LBCu	Simple cantilever (PZT+ 3%wt LBCu printed on SS	Zig-zag EH structure Simulated values [27]	PZ26 Ferroperm (ceramic pellets fired at 1200- 1300°C)	Simple cantilever with thinned bulk ceramic PZT/ SS 15µm/ PZT [26]	Simple cantilever with aerosol PZT / SS [43]
Density g/cm ³	7.6	7.4	6	5.5	7.8	--	--
Dimensions (mm): Diameter or footprint	∅:11.45	∅:7.74	9.80 x 2	14.70 × 12.70	--	5 x 40	6 x 4
PZT Thickness	1.92	0.10	0.55	0.55	--	0.10	0.01
ϵ' (at 1kHz, 25°C)	1200	600	--	630*	1300	--	--
$\tan \delta$ (at 1kHz)(%)	~0.2	~2.5	--	1.5 *	0.3	--	--
k_{31} (%)	28	26	--	--	33	--	--
k_{eff} (%)	28†	26†	11†	15•*	--	23•	10•
d_{31} (pC/N)	110†	95†	--	40•*	130	--	17•

-- Not Reported.

* Value used in simulation

• Impedance measurements carried out on clamped structure

† Impedance measurements carried out on non-clamped structure

6 Energy harvesting application

6.1 Characterization under mechanical vibrations

These experiments have been led by Associate Pr. Alexis Bremen (ISEP, LISITE Paris) and Pr Elie Lefeuvre (Université Paris-Saclay, C2N –Palaiseau). Before detailing the experiments, it appears to us useful to give basics on the electromechanical model of the piezoelectric resonator used as EH.

Here, the tested cantilever is a simple cantilever (dimensions 10x2x0.250mm) with a $\approx 50 \mu\text{m}$ PZT screen-printed on it. It is worth noting that these dimensions have not been optimized for the application (middle branch of the modified zig-zag geometry).

6.1.1 Model for piezoelectric vibration energy harvester

Thanks to the coupling between vibrations and electrical energy through the piezoelectric element, most of piezoelectric vibration energy harvesters (PVEH) based on a linear mechanical oscillator excited around one of its resonance frequencies can be modeled by the simple PVEH model presented Figure IV-33 [44].

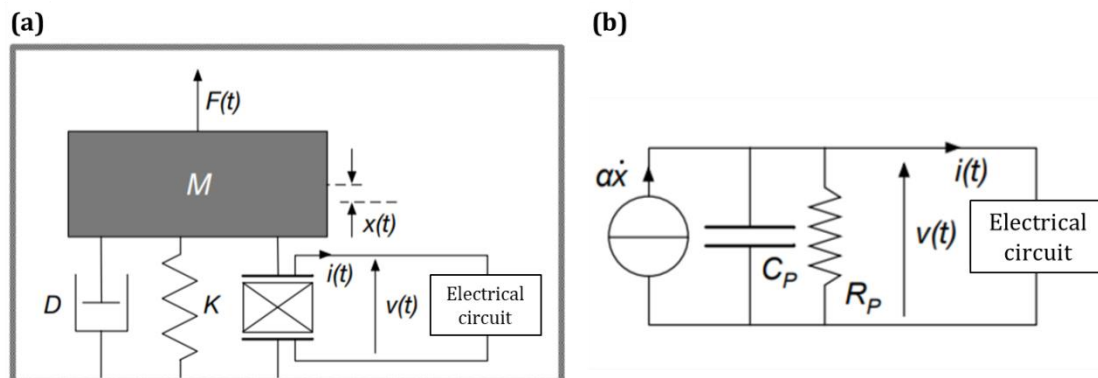


Figure IV-33: Scheme of a piezoelectric vibration EH, (a) mechanical model, and (b) electrical model. [44]

This basic linear model is based on electromechanical transduction. The electrical and mechanical equations of equilibrium provide an accurate and reliable representation of the PVEH behavior around its resonance frequency. Even if it does not describe all types of configurations, its study is a prerequisite for more complex modelling (multiple resonance modes, non-linearity due to ferroelectric hysteresis, mechanical non linearities).

In this model, the piezoelectric element is characterized by its electromechanical force coefficient α [NV^{-1}], its clamped capacity (at no strain) C_p [μF] as well as its leak resistance R_p [Ω] (or conductance $A_p=1/R_p$ [S]). M [kg] is the equivalent dynamic mass, D [Nm^{-1}s] is the damping coefficient due to mechanical losses, and K [Nm^{-1}] represents the stiffness of the system (if the piezoelectric element is short-circuited). An external force applied to the system F [N] (due to external vibration for instance) induces x [m] the relative displacement between the mass and the housing. V [V] and I [A] are respectively the voltage at the ends of the piezoelectric element

and the generated electrical current, if an electric load is connected. The equilibrium equations of this electromechanical system are therefore:

$$I = \alpha \dot{x} - C_p \dot{V} - A_p V \quad (\text{Eq. 4.7})$$

$$M \ddot{x} + Kx + D \dot{x} + \alpha V = F \quad (\text{Eq. 4.8})$$

Then, for the characterization of the PVEH, four parameters are usually used. They are the natural pulsation ω_0 [rad. s⁻¹] when the piezoelectric element is short-circuited, as well as three dimensionless parameters: the squared electromechanical coupling coefficient k^2 , the mechanical quality factor Q_M and the resistive loss coefficient ξ_E . These parameters have the followed expressions:

$$\omega_0 = \sqrt{\frac{K}{M}} \quad (\text{Eq. 4.9})$$

$$k^2 = \frac{\alpha^2}{KC_p + \alpha^2} \quad (\text{Eq. 4.10})$$

$$Q_M = \frac{\sqrt{KM}}{D} \quad (\text{Eq. 4.11})$$

$$\xi_E = \frac{1}{2R_p C_p \omega_0} \quad (\text{Eq. 4.12})$$

In the majority of applications, R_p is very large compared to $(C_p \omega_0)^{-1}$ and ξ_E can be neglected. Q_M corresponds to mechanical losses. k^2 corresponds, in quasi-static mode, to the efficiency of the electromechanical conversion between electrical and mechanical energy. For an open circuit system submitted to a static force it represents the ratio between the generated electrostatic energy and the total energy in the system.

If the PVEH is excited by a sinusoidal ambient acceleration, and if it is connected to an electrical load modeled by the complex admittance $\underline{Y}_L = A_L + jB$, the electrical network is shown Figure IV-34. In the frequency domain, the corresponding piezoelectric voltage V is then given (Eq. 4.13), where $A_p = 1/R_p$:

$$\underline{V} = \frac{\alpha j \omega X}{A_p + A_L + j(C_p \omega + B)} \quad (\text{Eq. 4.13})$$

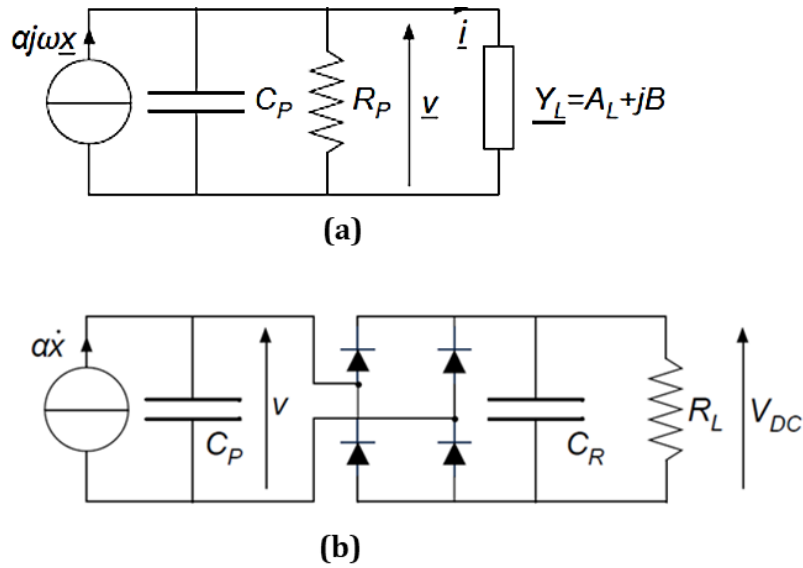


Figure IV-34: (a) Electrical networks showing the PEVH connect to (a) to an electrical load \underline{Y}_L (b) to a classical rectifier followed by a resistive load (b) [reproduced from [44]]

Then, even if a realistic energy harvesting circuit should include a rectifier (Figure IV-34 (b)), the harvested energy being the energy dissipated in the real component of the electrical load can be expressed as:

$$P = V^2 A_L \quad (\text{Eq. 4.14})$$

V being the RMS value of the piezoelectric voltage

5.1.2. Results

5.1.2.1 Linear electromechanical model

Before the measurement of the harvested power, the electromechanical parameters of the linear model presented in the previous paragraph are determined using the equivalent circuit shown Figure IV-35. For this electrical network, the governing equations must be the same as for Eq. 4.7 and Eq. 4.8. This is achieved for the values of the electrical resonator $\{R_m = D, C_m = K^{-1} \text{ and } L_m = M\}$. Here, to get the model, the cantilever is clamped on the shaker ($\approx 2\text{mm}$ is clamped, see Figure IV-36), and the amplitude and the phase of the admittance Y of the piezoelectric resonator are measured around the resonance frequency (Figure IV-37). Using a Matlab fit, the parameters of the model are extracted (Table IV-16).

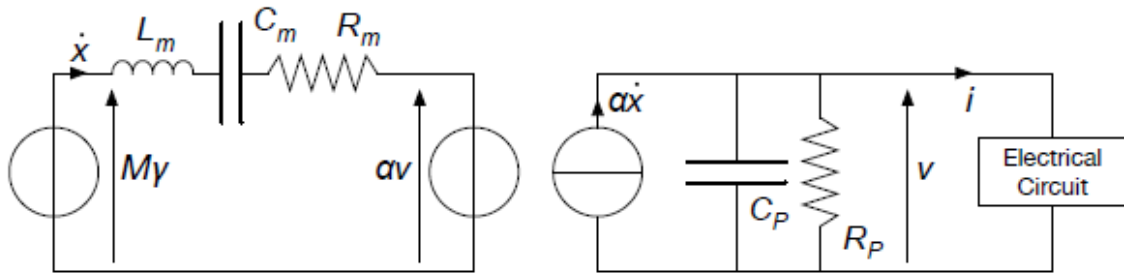


Figure IV-35: PVEH's equivalent electrical network. Electromechanical transduction is modeled by the αv voltage source and $\alpha\dot{x}$ current source (see Eq. 4.7 and 4.8, Figure IV-33). The mechanical resonance is represented by the electrical resonator $\{R_m C_m L_m\}$ [44]

Table IV-16: Some identified parameters of the PEVH (collaboration ISEP/C2N)

Resonant pulsation ω_0 (rad/s) (frequency(Hz))	816.85 rad.s ⁻¹ (129.9 Hz)
squared electromechanical coupling coefficient k^2,	0.0443
Mechanical quality factor Q_M	301
Clamped capacity C_p	464pF

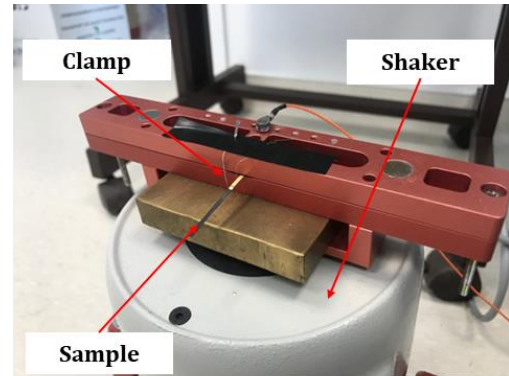
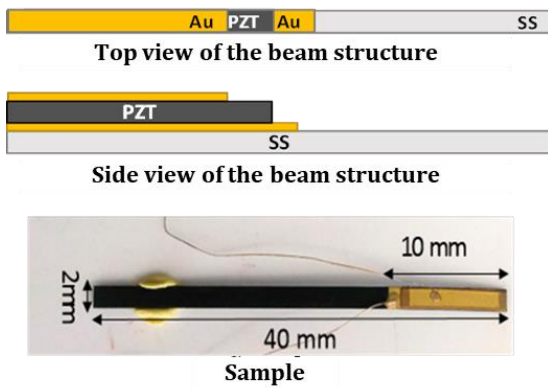


Figure IV-36: Photographs (left) of the tested sample and (right) of the cantilever clamped above the shaker ($\approx 2\text{mm}$ is clamped) (collaboration ISEP/C2N)

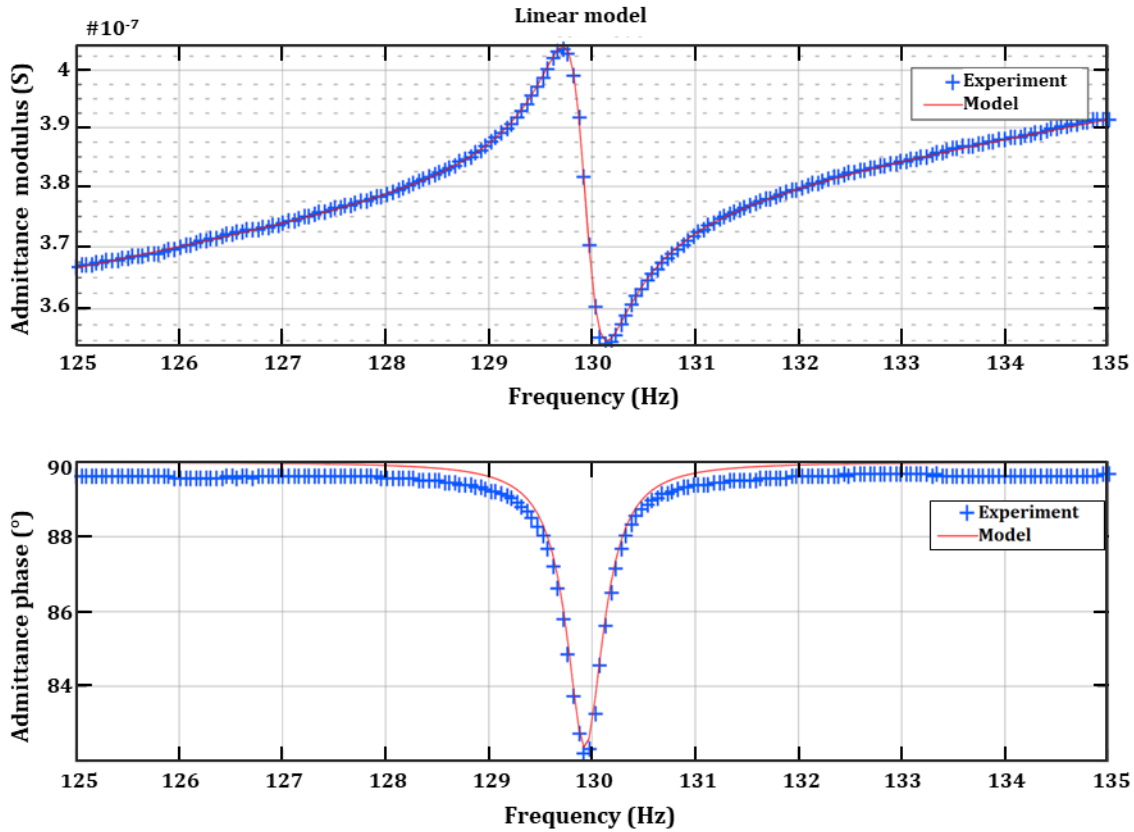


Figure IV-37: Results of admittance measurements for simple cantilever EH structure, (Top) module, and (bottom) phase. (collaboration ISEP/C2N)

Without tip mass, the resonant frequency is shown to be $\approx 130\text{Hz}$ and so, further tests under vibrations are led without any tip mass glued on the tip. The rather weak electromechanical squared k^2 can be related to huge difference between the PZT and the stainless steel substrate volumes. The calculated merit factor $k^2 Q_m = 0.133$ is here too low to achieve maximum harvested power, as shown in [45] (20 times lower than the reference value of π).

5.1.2.2 Tests under vibrations

The cantilever is driven under vibration on the shaker with accelerations varying from 0.2g to 0.5g. The voltage is then measured across a resistive load of $2.7\text{M}\Omega$, value close to the optimal theoretical value ($R_{opt} = \frac{1}{C_0 \cdot 2\pi \cdot f_0} = 2.64\text{M}\Omega$ which corresponds to the value of the impedance modulus at resonance frequency). A voltmeter with an internal resistance of $100\text{M}\Omega$ is used. With this resistive load, a maximum power of $1.3\mu\text{W}$ is produced by the harvester at 0.5 g amplitude with a natural frequency of 129.3Hz (Figure IV-38).

A decrease in resonance frequency is noticed with increasing acceleration and the shape of the peak becomes asymmetric. This classic behavior is attributed to the nonlinear response of PZT under stress due to Young's Modulus and quality factor decreases [46][47]. Indeed, reduction of quality factor is due to increase in mechanical losses with the amplitude of vibration (mainly air

friction). On the other hand, the resonance frequency decreases because the Young's Modulus reduces the spring constant (so-called "softening effect").

The harvested power is lower than those reported in the literature (Table IV-17). However, the substrate thickness and properties, the mass tip, the type of cantilever (i.e. unimorph or bimorph) and better piezoelectric properties represent several degrees of freedom to improve the performances.

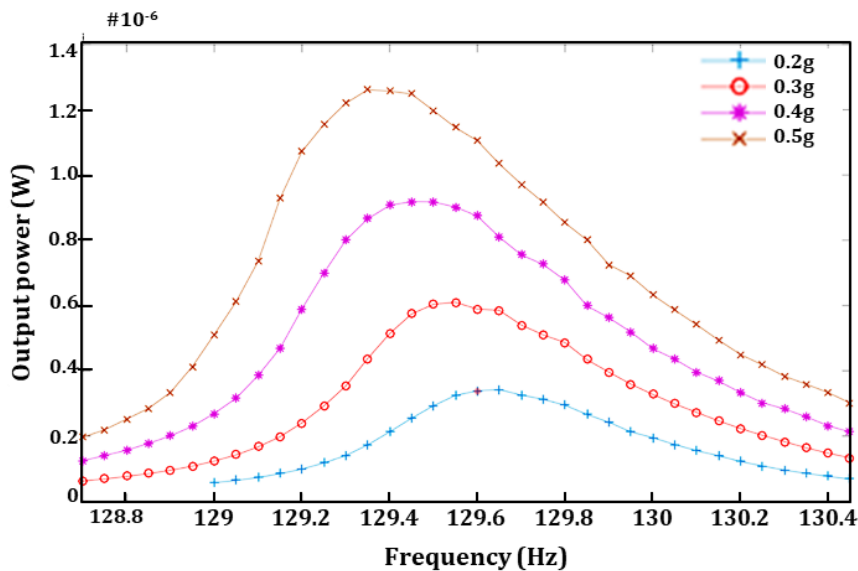


Figure IV-38: Output power as a function of frequency for different accelerations, with a resistive load of 2.7 M Ω . (collaboration ISEP/C2N)

Table IV-17: Comparison with literature results.

Ref.	SS dimension / PZT thickness / Proof mass	Power/ frequency/ acceleration	Effective volume (without tip mass) (mm ³)	Normalized Power density $\mu\text{W}/(\text{mm}^3\text{g}^2)$
Zhu, 2011 [48]	110 μm / Screen-printed PZT-5H 70 μm (bimorph)/ Tungsten 3.1g	240 μW / 67Hz/ 0.4g	162.00	9.2592
Tsujiura, 2013 [49]	300 μm / PZT RF Sputtering -2.2 μm / Proof mass 25mg	6 μW / 367Hz/ 1g	12.18	0.4930
Tang, 2018 [28]	30 μm / PZT Aerosol 10 μm (bimorph)/ Tungsten 0.46g. Unimorph	304 μW / 126Hz/ 0.5g	38.40	31.6667
		122 μW /111 Hz/ 0.5g	33.60	14.5238
This work	250 μm / Screen printed PZT + LBCu 50 μm / No proof mass	1.3 μW / 129.3Hz/ 0.5g	6.00	0.8666

6.2 Piezoelectromagnetic energy harvester (hybrid application)

These experiments have been led at University of Waterloo, Canada, Department of Mechanical and Mechatronics Engineering (Egon Fernandes supervised by Pr Armaghan Sahelian). This collaborative project has been conducted thanks to the UW-UB fund (2015-2017).

6.2.1 Principle and experimental set-up

The working principle of the piezoelectromagnetic screen-printed energy harvester is shown Figure IV-39. A permanent magnet is attached to its tip. If the harvester is mounted above an AC-carrying electrical wire, the coupling between the magnet and the alternating magnetic field produced by the wire creates a sinusoidal electromagnetic force. This force excites the cantilever and as a result the piezoelectric material is deformed. Charges are generated across the electrodes due to the direct piezoelectric effect, and, if the harvester is connected to an electrical load, a voltage is generated. The amplitude of the output power is maximized if the frequency of the AC current (ie. the frequency of the electromagnetic force) matches the harvester's resonance frequency.

Before the tests, a neodymium magnet (3.175 mm x 3.175 mm x 12.7 mm) is glued on the tip using a thin layer of epoxy adhesive cured for two days (Figure IV-39). The piezoelectromagnetic energy harvester is then experimentally tested to validate the results of the FEA model. The experimental test setup is shown Figure IV-40. The unit is mounted above a current carrying wire (10 AWG) using an acrylic base and 1.5 mm thick spacers to control the distance between the magnet and the wire. An LMS SCADAS mobile data acquisition system is used to control the current amplitude and frequency in the wire to perform a frequency sweep analysis using the Sine Control module. A Fluke i400s AC clamp is used to provide the feedback control for the system. The sinusoidal input is amplified through a Modal Shop 2050E09 power amplifier. During excitation, a Polytec OFV-505 laser vibrometer and OFV-5000 controller can measure the tip displacement of the harvester. The output voltage produced by the system is given by the LMS system with input impedance of 10 M Ω using a 10:1 probe. Different resistive loads values are obtained with an Elenco resistor substitution box. The frequency resolution of the data acquisition is 0.01 Hz.

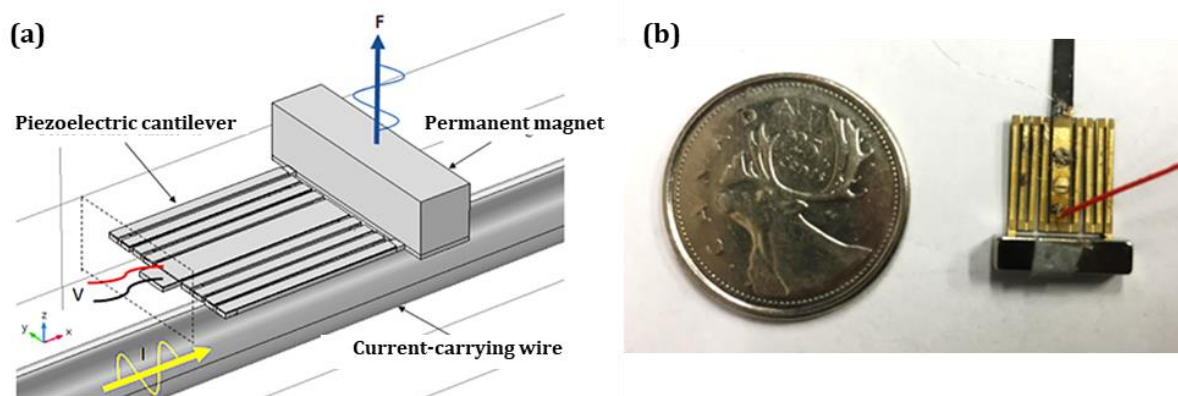


Figure IV-39: (a) Working principle of the piezo-electromagnetic harvester, (b) photograph of the fabricated energy harvester. (Collaboration Waterloo, Canada, reproduced from [29])

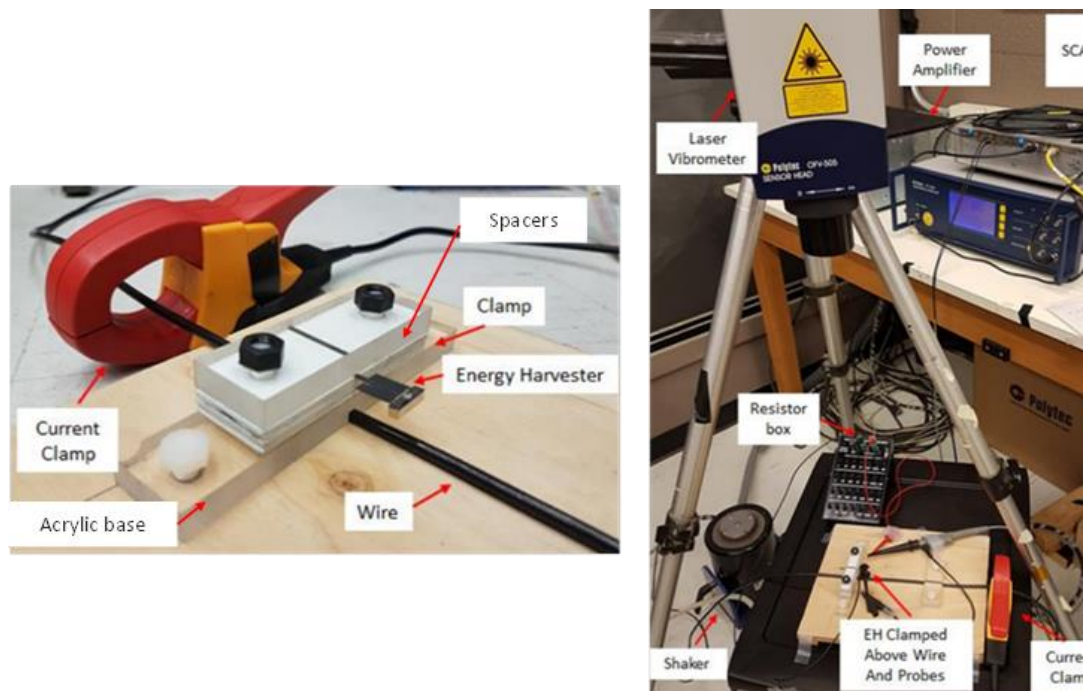


Figure IV-40: Experimental test setup of the piezo-electromagnetic energy harvester (left) EH clamped and placed on a current-conducting wire. (right) laser vibrometer set-up. (Collaboration Waterloo, Canada, reproduced from [29])

6.2.2 Results

First experiments measuring tip displacement and open-circuit for the EH show a good agreement between COMSOL model and measurement (Figure IV-41). Also, with magnet tip mass and fine tuning of the harvester clamping, the experimental resonant frequency is 60.3Hz (only 0.1Hz error with the modeled value), value compatible with the North American power grid.

Then, the energy harvester is tested with increasing resistive loads from 10 k Ω to 1 M Ω and the generated power is calculated from the square of the measured root mean square (RMS) voltage V_{RMS} across the load resistance R using:

$$P = \frac{(V_{RMS})^2}{R} \quad (\text{Eq. 4.15})$$

The measured and simulated power are shown in Figure IV-42 and are again in excellent agreement. No noticeable shift in resonant frequency is seen across the load sweeps. Further tests show that the optimal load range is between 1 M Ω and 2 M Ω , with small variation (less than 5%) in power production. The 1M Ω value is then selected for the following tests.

Finally, with the 1M Ω load resistor, the power outputs are measured using different distances to the wires (6.5, 9.5 and 12.5mm), and various electric current values (from 1 to 7 A). Too small

distance or high current values are avoided for possible detrimental effect on the structure during vibration. The obtained curves (Figure IV-43) show that, as expected, the overall power output grows significantly as the distance between the magnet and wire are minimized. This is due to the fact that the force on the magnet is inversely proportional to the square of the distance and the power output is proportional to the square of the force [29]. Again, because of changes in both Young's Modulus and quality factor for higher current (ie. larger force) nonlinear effects appear and result in a lower experimental power than expected [50].

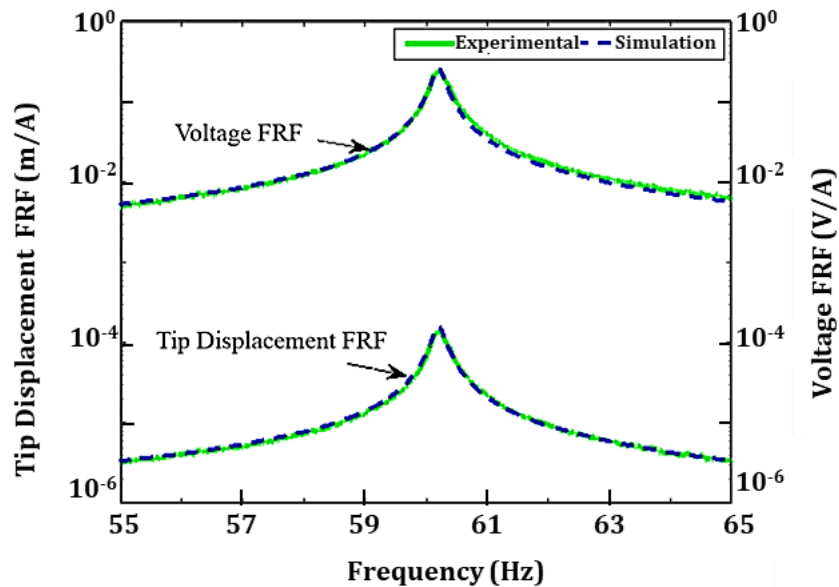


Figure IV-41: Tip displacement and voltage Frequency Response Function –FRF) ; the wire is at a distance of approximately 12.5mm and carries a 1A current (Collaboration Waterloo, Canada, reproduced from [29])

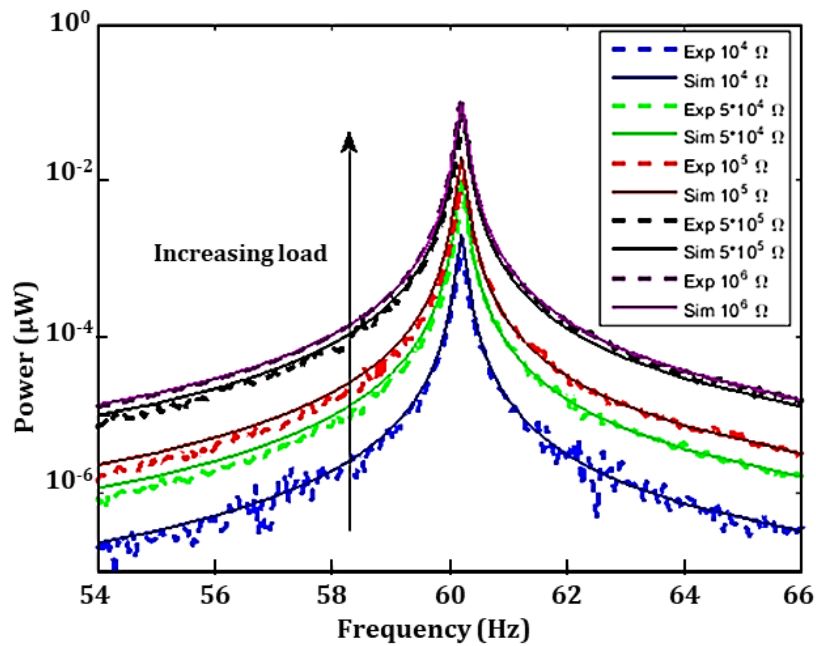


Figure IV-42. Calculated and simulated power curves across 10 k Ω to 1 M Ω resistive loads (wire current = 1 A at a distance of 12.5 mm). (Collaboration Waterloo, Canada, reproduced from [29])

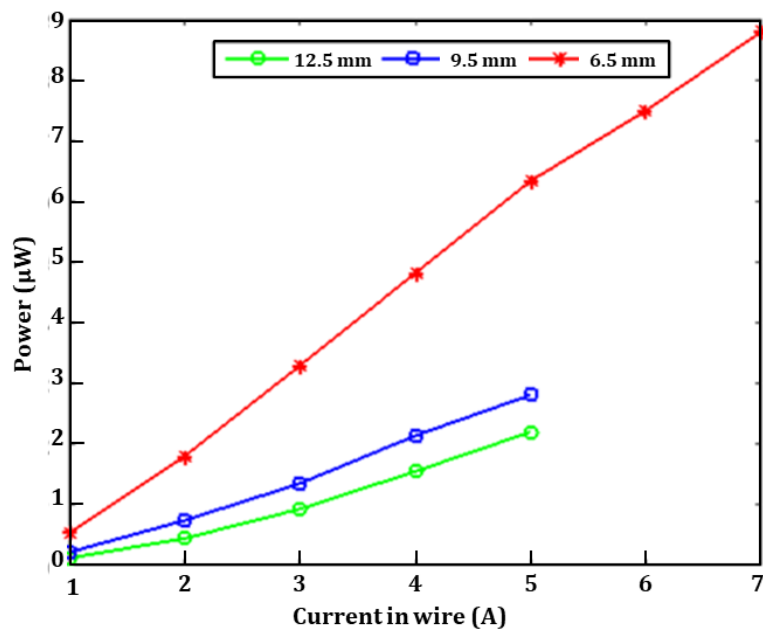


Figure IV-43: Power output as a function of electric current and distance from wire for the optimal 1M Ω load. (Collaboration Waterloo, Canada, reproduced from [29])

The results have been compared to previous works found in the literature. For this purpose, the normalized power density of the piezoelectromagnetic energy (in $\mu\text{W}/(\text{T} \cdot \text{A} \cdot \text{mm}^3)$) is calculated for a fair comparison. The overall power output is indeed dependent of the distance magnet-wire, the remanence of the magnet and the current in the wire. This normalized harvested power density is calculated by considering the effective volume as the sum of the volume of all beams and the magnet. The results gathered in Table IV-18 show that the printed EH developed during this work gives a normalized power density more than 2 times higher compared to

Paprony *et al.* [51] and Olzevsky *et al.* [52] works (2.9 and 2.2 times increase respectively). This validates the proposed modified zig-zag geometry combined with the advantages of the screen-printing thick film technology. The results are even comparable to the bulk PZT units [50], [53] whereas it is known that bulk PZT has a higher electromechanical coupling. Finally, the energy harvester has a good potential compared to larger scale units [50][53].

Table IV-18: Normalized power density for previous piezoelectromagnetic harvesters and the present work. (Collaboration Waterloo, Canada). (reproduced from [29])

Ref.	Deposition method	Magnet distance (mm)	Magnetic remanence (T)	Wire current (A)	Power output (μ W)	Frequency (Hz)	Normalized Power density μ W/ (T*A*mm ³)
Paprotny, 2010 [51]	Sputtered AlN	2.5*	1.32	1	2 (simulated)	57*	0.084695
Olszewsk, 2016 [52]	Sputtered AlN	2*	1.3	2	1.5	42.3	0.111537
Paprotny, 2013 [53]	Bulk PZT	2.5	1.48	20	2700	60	0.329337
Chen, 2015 [50]	Bulk PZT	2	1.4*	2.5	295.3	50	0.263098
He, 2013 [54]	Bulk PMgN-51	4	1.45	10	566	50	2.348645
This work	Screen-printed PZT	6.5	1.32	7	9	60	0.242502

*Values interpolated from data in the referenced literature.

7 Conclusion

In this chapter, screen-printing and co-firing of PZT layers in sandwich between Au electrodes all deposited on stainless steel substrate (301 SS) have been successfully fabricated, with simple cantilever shape or complex modified zig-zag geometry. Their microstructural characteristics and functional properties have been investigated and compared to those of PZT based ceramics and printed disk. The densification has been achieved at 900°C with the use of the LBCu sintering aid. Lower densification is shown for the cantilever structures with the SS passive substrate and can be due to the mechanical clamping from the SS substrate that generates constrained sintering. Even if the overall piezoelectric properties are reduced, properties are comparable to those of the literature, confirming the good potentiality of such devices for EH MEMS applications. Compared to bulk ceramics, the main limiting features are the interfaces and the bending issues. The microstructural analysis of the interfaces in the cantilever has highlighted the formation of an interphase layer between the substrate and the bottom gold electrode after sintering. This interface is considered as a passive layer that ensures cohesion between the electrode and the substrate but that could limit the dynamics of the structure under performance. Bending arising from TEC differences between the different materials constituting the cantilever structures has been shown to be dependent on the thickness of the active piezoelectric material. Both modeling and experimental approaches have confirmed the possibility to reduce thermal stresses by decreasing the PZT layer thickness. This insight will be further exploited in chapter 5.

Both simple and modified zig-zag cantilevers have been finally tested for EH application. For the simple cantilever, the maximum power of 1.3 μ W measured with a shaker is too low for the implementation of the EH in a MPPT circuit (MPPT : Maximum Power Point Tracking) whose own consumption is at least 10 μ W[55]. It is worth noting that this simple cantilever has not been optimized for this application, being simply the central part of the modified zig-zag structure. In addition to material properties (active or passive layers), thicknesses optimization, tip mass use and bimorph cantilever structure type are some possible routes for performances improvement.

Additionally, in the case of the piezo-electromagnetic modified zig-zag energy harvester, within the collaboration with the University of Waterloo, Department of Electrical Engineering (Zongxian Yang and Sid Zarabi supervised by Associate Professor Lan Wei and Pr David Wairn) a dynamic power conditioning module circuit has been developed. This circuit is adapted to the tens of microwatts provided by the modified zig-zag EH. Again, as for the MPPT circuit, the system is completely powered by the EH. Even with a low input power, encouraging results were displayed with this dynamic power management, which was able to work with the electrical characteristics of the fabricated printed modified zig-zag energy harvester. This flexible system could achieve a read-transmit duty cycle depending on the characteristics of different EHs and intensity of current passing through the wire being monitored (Figure IV-44).

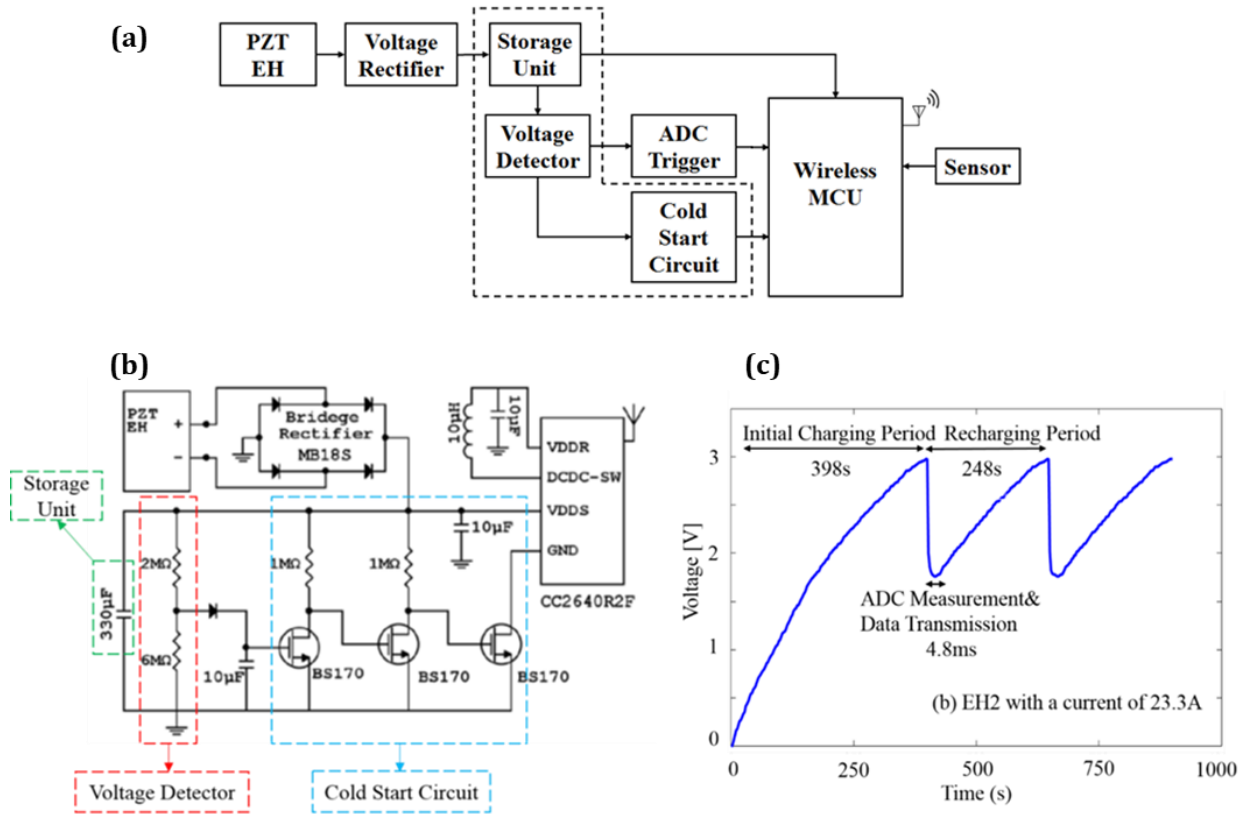


Figure IV-44: Dynamic power conditioning module circuit (a) design architecture, (b) power conditioning module circuit schematic, and (c) Charging/Discharging behavior of the Storage. Here the unit is capable of reading a 60 Hz Alternating Current (AC) sensor signal with a peak voltage in the range of 100 mV to 900 mV with accuracy no less than 91.4%. For carrying currents in the range of 8.4A to 30A, a read-transmit duty cycle from <4min to 18min has been achieved. (Collaboration Waterloo, Canada) (reproduced from [56])

References

- [1] S. Priya et al., "A Review on Piezoelectric Energy Harvesting: Materials, Methods, and Circuits," *Energy Harvest. Syst.*, vol. 4, no. 1, pp. 3–39, 2017.
- [2] H. NESSER, "Fabrication et caractérisation des MEMS composites pour la récupération d'énergie mécanique" Thesis Manuscrit, 2016.
- [3] S. M. Heinrich and I. Dufour, "Toward higher-order mass detection: Influence of an adsorbate's rotational inertia and eccentricity on the resonant response of a bernoulli-euler cantilever beam," *Sensors (Switzerland)*, vol. 15, no. 11, pp. 29209–29232, Nov. 2015.
- [4] W. J. Choi, Y. Jeon, J. H. Jeong, R. Sood, and S. G. Kim, "Energy harvesting MEMS device based on thin film piezoelectric cantilevers," *J. Electroceramics*, vol. 17, no. 2–4, pp. 543–548, 2006.
- [5] M. A. Karami and D. J. Inman, "Analytical modeling and experimental verification of the vibrations of the zigzag microstructure for energy harvesting," *J. Vib. Acoust. Trans. ASME*, vol. 133, no. 1, pp. 1–10, 2011.
- [6] D. F. Berdy, P. Srisungsitthisunti, B. Jung, X. Xu, J. F. Rhoads, and D. Peroulis, "Low-frequency meandering piezoelectric vibration energy harvester," *IEEE Trans. Ultrason. Ferroelectr. Freq. Control*, vol. 59, no. 5, pp. 846–858, 2012.
- [7] N. Sharpes, A. Abdelkefi, and S. Priya, "Two-dimensional concentrated-stress low-frequency piezoelectric vibration energy harvesters," *Appl. Phys. Lett.*, vol. 107, no. 9, 2015.
- [8] D. F. Berdy, P. Srisungsitthisunti, B. Jung, X. Xu, J. F. Rhoads, and D. Peroulis, "Low-frequency meandering piezoelectric vibration energy harvester," *IEEE Trans. Ultrason. Ferroelectr. Freq. Control*, vol. 59, no. 5, pp. 846–858, 2012.
- [9] Z. Gao, C. Bumgardner, N. Song, Y. Zhang, J. Li, and X. Li, "Cotton-textile-enabled flexible self-sustaining power packs via roll-to-roll fabrication," *Nat. Commun.*, vol. 7, May 2016.
- [10] Z. Qiu, X. Zhang, and C. Ye, "Vibration suppression of a flexible piezoelectric beam using BP neural network controller," *Acta Mech. Solida Sin.*, vol. 25, no. 4, pp. 417–428, Aug. 2012.
- [11] S. Khan, L. Lorenzelli, and R. S. Dahiya, "Technologies for Printing Sensors and Electronics Over Large Flexible Substrates: A Review," *IEEE Sens. J.*, vol. 15, no. 6, 2015.
- [12] V. Zardetto, T. Brown, A. Reale, and A. Di Carlo, "Substrates for Flexible Electronics: A Practical Investigation on the Electrical, Film Flexibility, Optical, Temperature, and Solvent Resistance Properties," *J. Polym. Sci. Part B Polym. Phys.*, vol. 49, pp. 638–648, May 2011.
- [13] E. Gusarova, "Flexible devices for energy harvesting based on printed organic piezoelectric P(VDF-TrFE) materials," Université Grenoble Alpes, 2015.
- [14] S. Mishra, L. Unnikrishnan, S. K. Nayak, and S. Mohanty, "Advances in Piezoelectric Polymer Composites for Energy Harvesting Applications: A Systematic Review," *Macromolecular Materials and Engineering*, vol. 304, no. 1. Wiley-VCH Verlag, 01-Jan-2019.
- [15] H. Haitao and J. F. Scott, *Ferroelectric Materials for Energy Applications*. Wiley-VCH Verlag GmbH & Co. KGaA, 2018.
- [16] H. G. Yeo and S. Trolier-McKinstry, "Piezoelectric Energy Generation," in *Ferroelectric Materials for Energy Applications*, Wiley-VCH Verlag GmbH & Co. KGaA, 2018, pp. 33–59.
- [17] C. Yeager and S. Trolier-McKinstry, "Epitaxial $\text{Pb}(\text{Zrx,Ti1-x})\text{O}_3$ ($0.30 \leq x \leq 0.63$) films on

- (100)MgO substrates for energy harvesting applications," *J. Appl. Phys.*, vol. 112, Oct. 2012.
- [18] G. Han et al., "Stress-controlled Pb(Zr 0.52Ti 0.48)O₃ thick films by thermal expansion mismatch between substrate and Pb(Zr 0.52Ti 0.48)O₃ film," *J. Appl. Phys.*, vol. 110, no. 12, Dec. 2011.
- [19] G. L. Brennecka, W. Huebner, B. A. Tuttle, and P. G. Clem, "Use of stress to produce highly oriented tetragonal lead zirconate titanate (PZT 40/60) thin films and resulting electrical properties," *J. Am. Ceram. Soc.*, vol. 87, no. 8, pp. 1459–1465, 2004.
- [20] T. Monin et al., "First experimental demonstration of a Self-Oscillating Fluidic Heat Engine (SOFHE) with piezoelectric power generation," *J. Phys. Conf. Ser.*, vol. 773, p. 12039, Nov. 2016.
- [21] T. Nishi, T. Ito, T. Umegaki, and I. Kanno, "High flexible piezoelectric PZT thin films deposited on stainless steel mesh," *IOP Publ. IOP Conf. Ser. J. Phys. Conf. Ser.*, vol. 1052, p. 12037, 2017.
- [22] R. Lakhmi, H. Debeda, I. Dufour, C. Lucat, and M. Maglione, "Study of screen-printed PZT cantilevers both self-actuated and self-read-out," *Int. J. Appl. Ceram. Technol.*, vol. 11, no. 2, pp. 311–320, 2014.
- [23] S. Pramanik, B. Pinguan-Murphy, and N. A. Abu Osman, "Developments of Immobilized Surface Modified Piezoelectric Crystal Biosensors for Advanced Applications," *Int. J. Electrochem. Sci.*, vol. 8, pp. 8863–8892, Jan. 2013.
- [24] L. Simon, S. Le Dren, and P. Gonnard, "PZT and PT screen-printed thick films," *J. Eur. Ceram. Soc.*, vol. 21, no. 10–11, pp. 1441–1444, 2001.
- [25] Q. Wang, H. Kuwano, and Z. P. Cao, "Metal-based piezoelectric energy harvesters by direct deposition of PZT thick films on stainless steel," *Micro Nano Lett.*, vol. 7, no. 12, pp. 1158–1161, 2012.
- [26] M. Colin, S. Basrour, L. Rufer, C. Bantignies, and A. Nguyen-Dinh, "Highly efficient low-frequency energy harvester using bulk piezoelectric ceramics," *J. Phys. Conf. Ser.*, vol. 476, no. 1, 2013.
- [27] S.-C. Lin and W.-J. Wu, "Piezoelectric micro energy harvesters based on stainless-steel substrates," *Smart Mater. Struct.*, vol. 22, no. 4, p. 45016, 2013.
- [28] W. H. Tang, T. K. Lin, C. T. Chen, Y. H. Fu, S. C. Lin, and W. J. Wu, "A High Performance Piezoelectric Micro Energy Harvester Based on Stainless Steel Substrates," *J. Phys. Conf. Ser.*, vol. 1052, p. 12038, 2018.
- [29] E. Fernandes et al., "Design, fabrication, and testing of a low frequency MEMS piezoelectromagnetic energy harvester," *Smart Mater. Struct.*, vol. 27, no. 3, 2018.
- [30] H. Debéda, P. Clément, E. Llobet, and C. Lucat, "One-step firing for electroded PZT thick films applied to MEMS," *Smart Mater. Struct.*, vol. 24, no. 2, 2015.
- [31] X. X. Wang, K. Murakami, O. Sugiyama, and S. Kaneko, "Piezoelectric properties, densification behavior and microstructural evolution of low temperature sintered PZT ceramics with sintering aids," *J. Eur. Ceram. Soc.*, vol. 21, no. 10–11, pp. 1367–1370, 2001.
- [32] A. J. Medesi, H. Meier, C. Megnin, and T. Hanemann, "A novel Co-casting process for piezoelectric multilayer ceramics with silver inner electrodes," in *Procedia Engineering*, 2015, vol. 120, pp. 124–129.
- [33] A. Medesi et al., "Low Temperature Sintering of PZT," *Artic. J. Phys. Conf. Ser.*, 2014.
- [34] A. Box, "Standard on Piezoelectric Crystals," *IEEE Int. Symp. Appl. Ferroelectr.*, 1961.
- [35] D. Ravi and D. J. Green, "Sintering stresses and distortion produced by density differences in bi-layer structures," *J. Eur. Ceram. Soc.*, vol. 26, no. 1–2, pp. 17–25, 2006.

- [36] H. Debéda, C. Lucat, and V. Pommier-Budinger, "Printed Piezoelectric Materials for Vibration-based Damage Detection," *Procedia Eng.*, vol. 168, pp. 708–712, 2016.
- [37] T. Molla and H. Lund, "Modeling Macroscopic Shape Distortions during Sintering of Multilayers," Technical University of Denmark, 2014.
- [38] C. Hsueh, C. R. Luttrell, and T. Cui, "Thermal stress analyses of multilayered films on substrates and cantilever beams for micro sensors and actuators," no. May, 2014.
- [39] Meggit Sensing Systems, "Pz26 (Navy I) Hard relaxor type PZT," Pz26 (Navy I) Ferroperm. [Online]. Available: /www.meggittferroperm.com.
- [40] A. Box, "standard on piezoelectric crystals," *IEEE Int. Symp. Appl. Ferroelectr.*, 1961.
- [41] B. Jaffe, W. R. Cook, and H. Jaffe, "Interpretation of some experimental results," in *Piezoelectric Ceramics*, Academic Press, 1971, pp. 237–251.
- [42] O. Santawiteea, S. Grall, C. Chayasombath, Bralee; Thanachayanontb, X. Hochartc, J. Bernardd, and H. Debédaa, "Electrode materials effect on processing and electromechanical properties of printed PZT-based microdisks," To Appear *Electrocera*mics, 2019.
- [43] S. C. Lin and W. J. Wu, "Piezoelectric micro energy harvesters based on stainless-steel substrates," *Smart Mater. Struct.*, vol. 22, no. 4, 2013.
- [44] A. Badel and E. Lefeuvre, "Nonlinear Conditioning Circuits for Piezoelectric Energy Harvesters," in *Nonlinearity in Energy Harvesting Systems*, Springer International Publishing, 2016, pp. 321–359.
- [45] E. Arroyo, A. Badel, F. Formosa, Y. Wu, and J. Qiu, "Comparison of electromagnetic and piezoelectric vibration energy harvesters: Model and experiments," *Sensors Actuators, A Phys.*, vol. 183, pp. 148–156, 2012.
- [46] R. Xu et al., "Screen printed PZT/PZT thick film bimorph MEMS cantilever device for vibration energy harvesting," in *Sensors and Actuators, A: Physical*, 2012, vol. 188, pp. 383–388.
- [47] D. Shen, J. H. Park, J. Ajitsaria, S. Y. Choe, H. C. Wickle, and D. J. Kim, "The design, fabrication and evaluation of a MEMS PZT cantilever with an integrated Si proof mass for vibration energy harvesting," *J. Micromechanics Microengineering*, vol. 18, no. 5, May 2008.
- [48] D. Zhu, S. P. Beeby, M. J. Tudor, and N. R. Harris, "A credit card sized self powered smart sensor node," *Sensors Actuators A Phys.*, vol. 169, no. 2, pp. 317–325, 2011.
- [49] Y. Tsujiura, E. Suwa, H. Hida, K. Suenaga, K. Shibata, and I. Kanno, "Lead-free piezoelectric MEMS energy harvesters of stainless steel cantilevers," 2013 *Transducers Eurosensors XXVII 17th Int. Conf. Solid-State Sensors, Actuators Microsystems, Transducers Eurosensors 2013*, no. June, pp. 474–477, 2013.
- [50] W. Chen, Y. Cao, and J. Xie, "Piezoelectric and electromagnetic hybrid energy harvester for powering wireless sensor nodes in smart grid," *J. Mech. Sci. Technol.*, vol. 29, no. 10, pp. 4313–4318, Oct. 2015.
- [51] I. Paprotny, R. White, and P. Wright, "Modeling, Design and Fabrication of (10 × 10 × 4 mm³) MEMS AC energy scavenger for smart grid applications," *PowerMEMS (2010)*, no. iii, pp. 1–4.
- [52] O. Z. Olszewski, R. Houlihan, A. Mathewson, and N. Jackson, "A low frequency MEMS energy harvester scavenging energy from magnetic field surrounding an AC current-carrying wire," in *Journal of Physics: Conference Series*, 2016, vol. 757, no. 1.
- [53] I. Paprotny, Q. Xu, W. W. Chan, R. M. White, and P. K. Wright, "Electromechanical energy scavenging from current-carrying conductors," *IEEE Sens. J.*, vol. 13, no. 1, pp. 190–201, 2013.

- [54] W. He, P. Li, Y. Wen, J. Zhang, C. Lu, and A. Yang, "Energy harvesting from electric power lines employing the Halbach arrays," *Rev. Sci. Instrum.*, vol. 84, no. 10, Oct. 2013.
- [55] G. K. Ottman, H. F. Hofmann, A. C. Bhatt, and G. A. Lesieutre, "Adaptive piezoelectric energy harvesting circuit for wireless remote power supply," *IEEE Trans. Power Electron.*, vol. 17, no. 5, pp. 669–676, Sep. 2002.
- [56] Z. Yang et al., "A Simple Wireless Sensor Node System for Electricity Monitoring Applications: Design, Integration, and Testing with Different Piezoelectric Energy Harvesters," *Sensors*, vol. 18, no. 11, p. 3733, 2018.

Chapter V

Towards SPS sintering route

Content

INTRODUCTION	166
1 STATE OF THE ART ON SPS SINTERING	167
1.1 PIEZOELECTRIC CERAMICS	167
2 OPTIMIZATION OF THE SINTERING CONDITIONS FOR PZT CERAMICS	170
2.1 SINTERING OF PZT WITHOUT SINTERING AID	170
2.1.1 Sintering temperature optimization	170
2.1.2 Approach towards one-step sintering of PZT by SPS	178
2.2 INFLUENCE OF SINTERING AID	184
2.3 SUMMARY	186
3 TRANSFER TOWARDS MULTILAYER PRINTED STRUCTURES	188
3.1 INTERFACES IN MULTILAYERS BY SPS: METAL/CERAMIC INTERFACES	188
3.2 APPROACH	189
3.3 OPTIMIZATION OF SPS SET-UP CONFIGURATION	191
3.3.1 Starting configuration (Configuration 0)	192
3.3.2 Configuration 1	193
3.3.3 Configuration 2	194
3.3.4 Configuration 3	194
3.3.5 Configuration 4	195
3.3.6 Configuration 5	195
3.4 OPTIMIZATION OF SINTERING CONDITIONS FOR THE MULTILAYER EH STRUCTURE	196
3.5 STRATEGIC LINES FOCUSED ON INTERFACE ISSUES	198
3.5.1 Nature of protective layer	201
3.5.2 Substrate thickness	203
3.5.3 Nature of electrodes	205
3.5.4 Electrical tests	206
4 CONCLUSION	207

The exploration of new densification route for printed multilayer structure is the focus of this chapter. Our approach based on the use of Spark Plasma Sintering is here presented with all the steps and investigations necessary for the optimization of multilayer sintering. Our approach includes adaptations not only of the material but also of the configuration of the SPS device. This part devoted to SPS investigations has been done in close collaboration with Dr U-Chan CHUNG, research engineer at ICMCB Laboratory (responsible of the Sintering SPS platform).

Introduction

PZT based energy harvester is a complex multi-material structure whose fabrication raises multiple issues related to (i) the control of the chemistry and microstructure (non-stoichiometry and volatility of elements, grain size) and (ii) the control of interfaces (interdiffusion, thermal expansion mismatch between ceramic and metals leading to delamination and bending). These features strongly affect properties such as electrical breakdown strength, electrical conductivity, piezoelectric strain and ferroelectric switching. Thanks to various sintering aids such as $\text{Li}_2\text{CO}_3\text{Bi}_2\text{O}_3\text{CuO}$ (LBCu) [1], $\text{LiBiO}_2 + \text{CuO}$ [2][3] or $\text{Li}_2\text{CO}_3 + \text{PbO}$ [4] the sintering temperature of thick films and PZT based ceramics was efficiently lowered ($\sim 900^\circ\text{C}$) compared to conventionally sintered commercial PZT ceramics ($T > 1200^\circ\text{C}$). However, the chemistry remains hardly controlled and the densification not always optimized. Indeed, conventional sintering performed at high temperature and during long duration can generate PZT composition fluctuations. In particular, the loss of PbO is a major drawback leading to change in chemistry and degradation of electrical properties.

Over the last few decades, electric current activated/assisted sintering (ECAS) methods, such as spark plasma sintering (SPS), have been considered as high-efficient techniques for the densification of ceramics [5]–[8]. In this context, the use of advanced sintering process such as Spark Plasma Sintering appears as a relevant approach given its specificities: fast kinetics, lower temperatures and short sintering times. Optimization of the sintering while decreasing sintering temperature and limiting the number of thermal treatments is consistent with the trend towards lower energy consumption while maintaining optimum reliability. Such an optimization is particularly critical when processing complex devices such as printed PZT thick films integrated in MEMS, for which the co-sintering with metals remains challenging.

After a survey of the literature focused on piezoelectric ceramics sintered by SPS, a first part of this chapter is devoted to SPS investigations performed using the same commercial PZT powder as for conventional process (section 2). Optimization of the sintering conditions, microstructural and electrical investigations of the PZT ceramics obtained by SPS are presented. In particular, our strategy to use a protective powder layer to target one-step sintering is highlighted. The impact of sintering aid addition is addressed. Then, the SPS ceramics performances are compared with conventional PZT ceramics and screen-printed thick films. The second part of this chapter is devoted to the transfer and further optimization of SPS conditions towards the co-sintering of the printed PZT based EH multilayer structure.

1 State of the art on SPS sintering

1.1 Piezoelectric ceramics

A review of literature shows that sintering of PZT and related solid solutions by SPS are performed under low oxygen partial pressure at temperatures that usually remain higher than 900 °C (Table V-1)). The various reported studies underline the influence of composition, additives (La_2O_3 , PbO excess, etc...) and microstructure (grain size effect) on the electrical and optical properties of PZT ceramics obtained by SPS [3], [7], [9]–[23]. The SPS route was also recently investigated for the sintering of lead-free piezoceramics, in particular for $(\text{K},\text{Na})\text{NbO}_3$ (KNN). KNN shares with PZT the tendency for volatility of the A-site cations in the perovskite ABO_3 structure and is a challenging lead-free ceramic that could be of real interest for some applications where PZT dominates [24], [25].

Three remarks arise from this brief survey of literature:

- i) The efficiency of SPS compared to conventional sintering can hardly be properly evaluated as the dielectric and piezoelectric properties are not systematically reported and when provided they relate to different initial compositions and various microstructures in terms of grain size. However, it is worth noting that most of the studies use SPS at lower or similar temperatures as the ones used for conventional sintering of screen-printed thick films. The dwell time ($\sim 5'$) is also drastically reduced compared to conventional approaches for which several hours are required to achieve high density.
- ii) Sintering aids are only rarely used whereas in conventional sintering they are required to reduce the sintering temperature, in particular to limit the loss of PbO.
- iii) A post-annealing is most of the time performed at temperatures similar or even higher than the sintering temperature and under air in order to eliminate oxygen vacancies and recover insulating properties. The control of oxygen vacancies is critical as they may play an important role in the fatigue process under electric field [26]. This post-sintering thermal treatment, performed in the range 700 – 1100 °C, is a key step to control charged defects and, more generally defect chemistry [27]. In particular, space charge accumulation at the grain boundaries can significantly alter the polarization process (reorientation of domains) and contribute to the conductivity and dielectric losses. Such post-sintering annealing represents also a drawback because it weighs on the global thermal budget limiting thus the gain of energy efficiency provided by fast sintering at low temperature.

In this context, we focus on the investigation of SPS with as a main goal to avoid the post sintering annealing step. Our objective is also to reduce the sintering temperature without using sintering aids. Our strategy is built on the use of a protective powder layer directly deposited on the top of the PZT bed powder. The use of insulating disks or thermal buffers during SPS was already reported in literature. These thermal and electrical barriers allow to reduce the heat

conduction and to control current distribution across punch/die/powder assembly (limited current leakage). They can be located either directly at the contact of the powder or between the rams and punches [28]. Alumina powders were also used to prevent ferroelectric ceramics from chemical reduction during SPS sintering [29] and to prevent the pistons from deforming copper spiral extremities in SPS co-sintering of transformers for power electronics [30]. No reaction occurs between the alumina and the powder to sinter.

In the context of this thesis, considering our goal to optimize the SPS sintering not only for PZT ceramics but also for the multilayer (Au/PZT/Au/stainless steel), our specifications for the protective layer must meet multiple criteria:

- To protect PZT from the chemical reduction without hindering densification.
- To be inert at the selected sintering temperature in order not to interact chemically with PZT but also with the metallic electrode in the case of the multilayer.
- To be removed easily by polishing or etching without altering the material in contact.

We have first selected the strontium carbonate SrCO_3 which meets all expectations, and has also proved to be very effective as a sacrificial layer in the fabrication of the released screen-printed PZT, metals or vitro-ceramic thick films [31][32]. Another carbonate has been also tested showing promising results.

Table V-1: Some properties and process conditions of PZT based ceramics densified by SPS

Material (Grain size)	Sintering temperature (heating rate)	Holding time (min)	Pressure (MPa)	Post thermal treatment	Density (g/cm ³)	Electrical Properties	Reference
PbZrO₃-PbTiO₃/ Pb(Zn_{1/3}Nb_{2/3})O₃ (Not reported)	900 °C (100 °C/min- 800 °C + 33 °C/min -900 °C)	10	29	1h at 900 °C In a PbO-rich atmosphere	7.95	Not reported	[9]
Pb(Zr_{0.53}Ti_{0.47})O₃-1%Nb (Not reported)	1000 °C (100 °C/min)	0, 1, 2, and 4	50	3h at 1000 °C	7.95	Not reported	[10]
Pb(Zr_{0.3}Ti_{0.7})O₃ (Not reported)	900 °C (100 °C/min- 800 °C + 33 °C/min -900 °C)	5	29	1h at 1100 °C	7.80	ε<500 (25 °C)	[16]
Pb(Zr_{0.52}Ti_{0.42}Sn_{0.02}Nb_{0.04})O₃ (Grain size < 500 nm)	1050 °C (100 °C/min)	5	50	4h at 700 °C under air + 6h at 1000 °C	7.64	d ₃₃ ~350 pC/N (25 °C)	[11]
Pb(Zr_{0.53}Ti_{0.47})O₃- 1%Nb₂O₅ (Grain size 330 nm)	1000 °C (120 °C/min)	1	50	Not reported	Not reported	ε ~920 (25 °C) d ₃₃ ~180 pC/N	[12]
PMN-PZT (Grain size 1 μm)	980 °C (100 °C/min)	5	50	12h at 850 °C	Not reported	ε ~6000 (25 °C) d ₃₃ ~400 pC/N	[13]
PZT-PMnN	900-1000 °C (100 °C/min)	5	50	4h at 700 °C, + 6 h at 1000 °C	7.89	d ₃₃ ~412 pC/N	[14]
PZT (SPS + Energy ball milling) (Grain size <300 nm)	750 - 900 °C (200 °C/min)	5	48	2h at 700 - 850 °C	7.92 - 8.3	ε: 700 - 1800 (25 °C) d ₃₃ : 374 - 422 pC/N	[15]
Reference: PZ26 conventional sintering Ferroperm	1200 °C	Not reported	Not reported	Not reported	7.7 (Relative density 98%)	ε ~6000 d ₃₃ ~290 pC/N	[33]

2 Optimization of the sintering conditions for PZT ceramics

Sintering conditions are first optimized using the raw powder PZT (PZ26 from Ferroperm, www.meggittferroperm.com) without sintering aid or protective layer. Then, the efficiency of the protective layer during SPS to avoid post-annealing step is tested. SPS experiments are finally performed starting from the same formulation used for the conventional approach by adding to the raw powder 3wt% of LBCu sintering aid (Chapter 4).

2.1 Sintering of PZT without sintering aid

2.1.1 Sintering temperature optimization

Spark plasma sintering is performed using an SPS apparatus Syntex Inc., SPS-515S (section 2.2 Chapter 2). PZT powder without sintering aid is loaded in a cylindrical graphite die with an inner diameter of 10 mm and heated under low oxygen partial pressure. The temperature is raised at 50 °C/min and kept at a constant value in between 800 and 875 °C for 5 min. A maximum pressure of 100 MPa is applied along the Z-axis of the graphite die during the whole sintering process. Note that these values of sintering time and pressure have been selected after investigations performed also with a pressure of 50 MPa and dwell time of 30 minutes for which lower density values have been obtained. Afterwards, the samples are annealed in air at 800 °C for 10 h in order to remove surface carbon contamination and to limit oxygen vacancies caused by the reducing conditions.

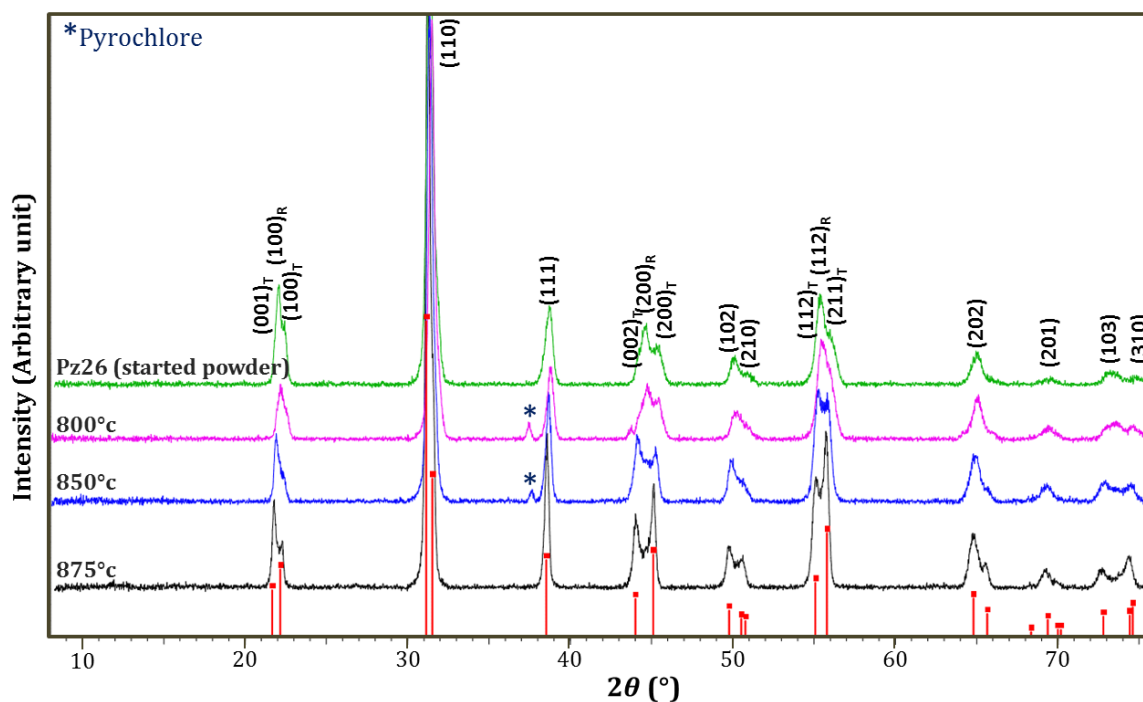
2.1.1.1 Structural and microstructural characterizations of PZT ceramics obtained by SPS

a) XRD investigations

As described in Chapter 4, the initial commercial powder PZ26 ($\text{PbZr}_x\text{Ti}_{1-x}\text{O}_3$ with $0.44 < x < 0.53$) exhibits a perovskite type structure with a coexistence of tetragonal and rhombohedral phases at room temperature. Room temperature XRD patterns of the SPS ceramics are indexed in the tetragonal and rhombohedral symmetries (Figure V-1 (a)). Extra peaks attributed to pyrochlore phase occur when the sintering temperature is below 875 °C. The diffraction peak at 44.5° observed in the patterns of both the initial powder and the powder sintered at 800 °C corresponds to the rhombohedral singlet (200). This peak is slightly shifted towards lower angle when increasing sintering temperature (Figure V-1 (b)). A better crystallinity is also observed for the ceramic sintered at temperature higher than 850 °C with in particular a pronounced splitting of tetragonal (002)/(200) peaks for a sintering temperature of 875 °C. The other rhombohedral reflections located at 22° (100) and 55.4° (112) are also shifted towards lower angles (21.5 and 55° respectively) for the patterns corresponding to 850 and 875 °C. Although the global composition of the powder does not change when the sintering temperature increases, the recorded XRD patterns reveal a change in phase structure. Wagner *et al.* already reported such a transition from rhombohedral to tetragonal structure induced by increasing the sintering temperature in the relaxor-ferroelectric system PNN-PZT [34]. In this paper, an increase of the tetragonal content from 45 to 82% is reported when grain size increases from 0.

5 to 3.7 μm . This effect, ascribed to grain growth, was correlated to stress relaxation. A higher content of tetragonal phase evidenced by the ratio $I(002)/I(200)$ was also reported in PZT-PMnN sintered by SPS compared to conventional sintering [14]. A surface effect due to the pressure applied during SPS cannot be discarded to explain the changes observed on the XRD patterns. However, extreme caution should be taken when interpreting changes in the $(002)/(200)$ ratio intensity or broadening, as polishing or grinding steps also result in significant modifications [35][36] [37]. This is well illustrated when comparing the XRD patterns of the ceramic after SPS (sintering 850°C), after polishing at the heart, and after complete grinding (powder) (Figure V-2)

(a)



(b)

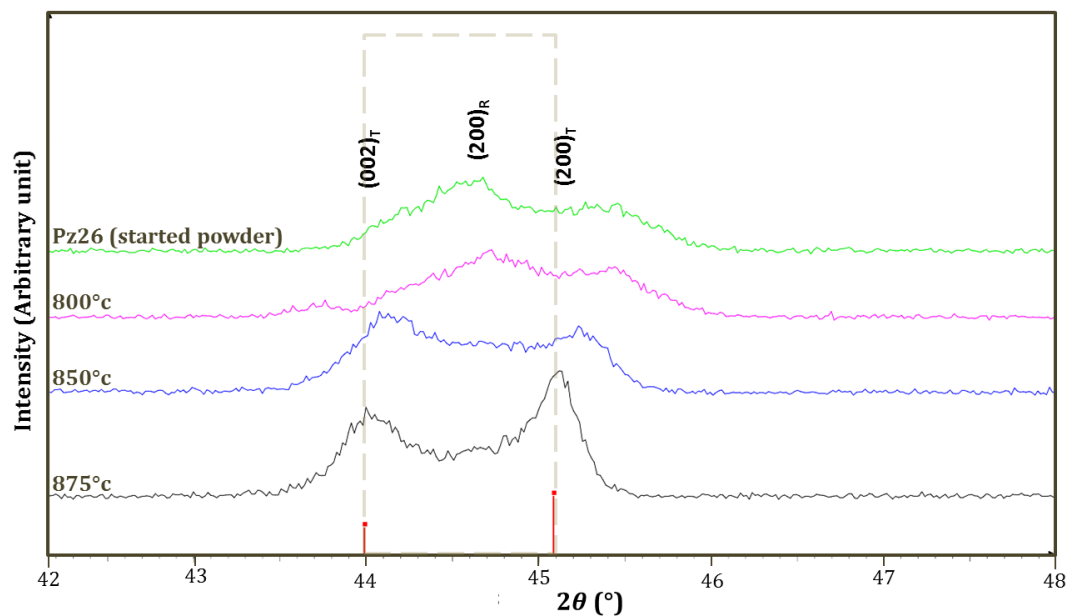


Figure V-1: (a) XRD patterns of PZT ceramics sintered by SPS at different temperatures (800 °C, 850 °C, and 875 °C) and pattern of started powder (PZ26 from Ferroperm). Sub-indices T and R correspond to tetragonal and rhombohedral respectively. $P4mm$ Bragg positions for $\text{Pb}(\text{Zr}_{0.44}\text{Ti}_{0.56})\text{O}_3$ are presented in red below the diffractograms. (b) Zoom of the XRD patterns at $2\theta = 42^\circ\text{--}48^\circ$ of PZT ceramics sintered by SPS at different temperature (800 °C, 850 °C, and 875 °C) and pattern of started powder (PZ26 from Ferroperm). Sub-indices T and R correspond to tetragonal and rhombohedral respectively. $P4mm$ Bragg positions for $\text{Pb}(\text{Zr}_{0.44}\text{Ti}_{0.56})\text{O}_3$ are presented in red below the diffractograms.

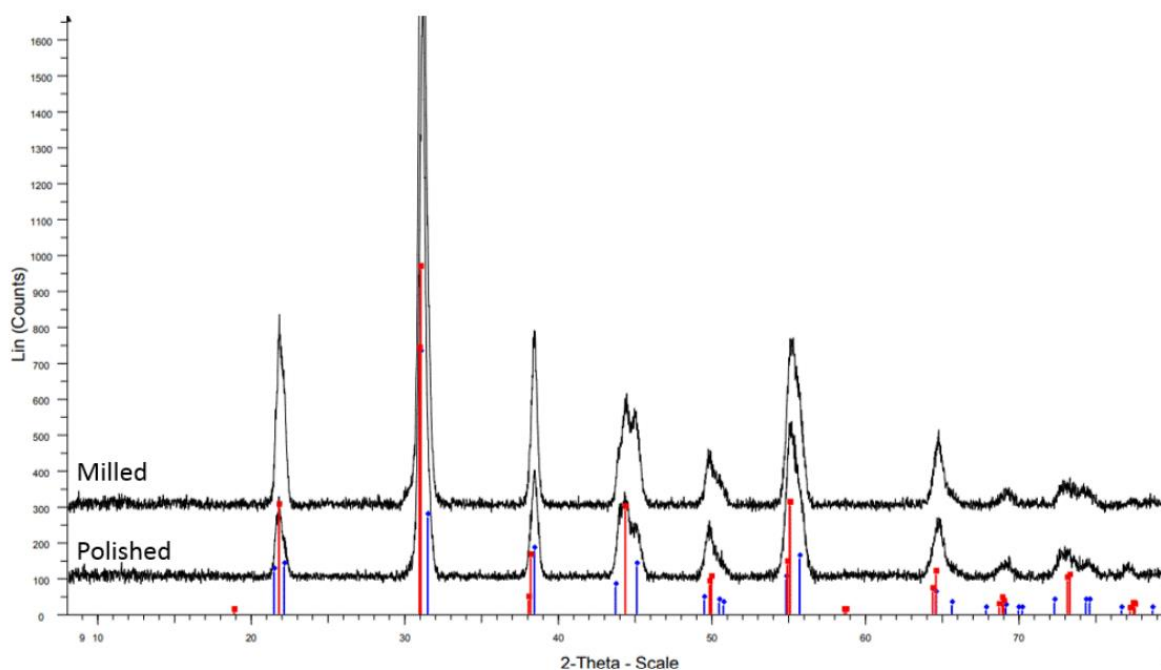


Figure V-2: XRD patterns of the ceramic sintered by SPS at 850 °C after polishing and after grinding

b) Microstructural characterizations

Figure V-3 shows SEM images of the microstructure of SPS ceramics obtained at different temperatures. The ceramic fabricated at the lowest sintering temperature displays a microstructure with a high level of porosity reflecting a poor densification with a relative density estimated close to 68% (Figure V-3 (a)). An increase of the sintering temperature of only 50 °C (i. e. 850 °C) allows a significant improvement in densification, with a relative density reaching ~94 %. Open porosities are nevertheless observed and the grain size increases from the range 500 nm–1 µm to 1-2 µm. Quite homogeneous microstructure is revealed with no evidence of differential sintering caused by the presence of agglomerates in the initial powder. Note that the grinding of the powder before SPS has been also studied and has been shown to have no effect on the improvement of sintering. The 100MPa pressure applied during sintering is thus appropriate for an efficient break-up of agglomerates in the first stage of sintering.

The optimal density is finally obtained at a sintering temperature of 875 °C with ~98% of relative density. Larger average grain size in the range ~2-4 µm is observed (Figure V-3 (c)). Referring to the work of Wagner *et al* [34], when the sintering temperature increases up to 875 °C a change in phase structure is observed by XRD, and a change in grain size from 0.5 µm to about 4 µm is generated.

It is worth noting that SPS allows to efficiently densify PZT at temperature lower than 900 °C without any additives. Density and microstructure of the SPS ceramics are comparable to those of conventionally sintered commercial ceramics at 1200 °C ([www. meggittferroperm. com](http://www.meggittferroperm.com)). Referring to the SPS studies reported in Table V-1, although the sintering temperature of 875 °C is slightly lower, density remains comparable.

Figure V-4 summarizes the obtained microstructure analysis. The evolution of average grain size and relative density are reported as a function of the sintering temperature and applied pressure. Error bars are estimated from the values obtained on three different samples sintered in similar conditions.

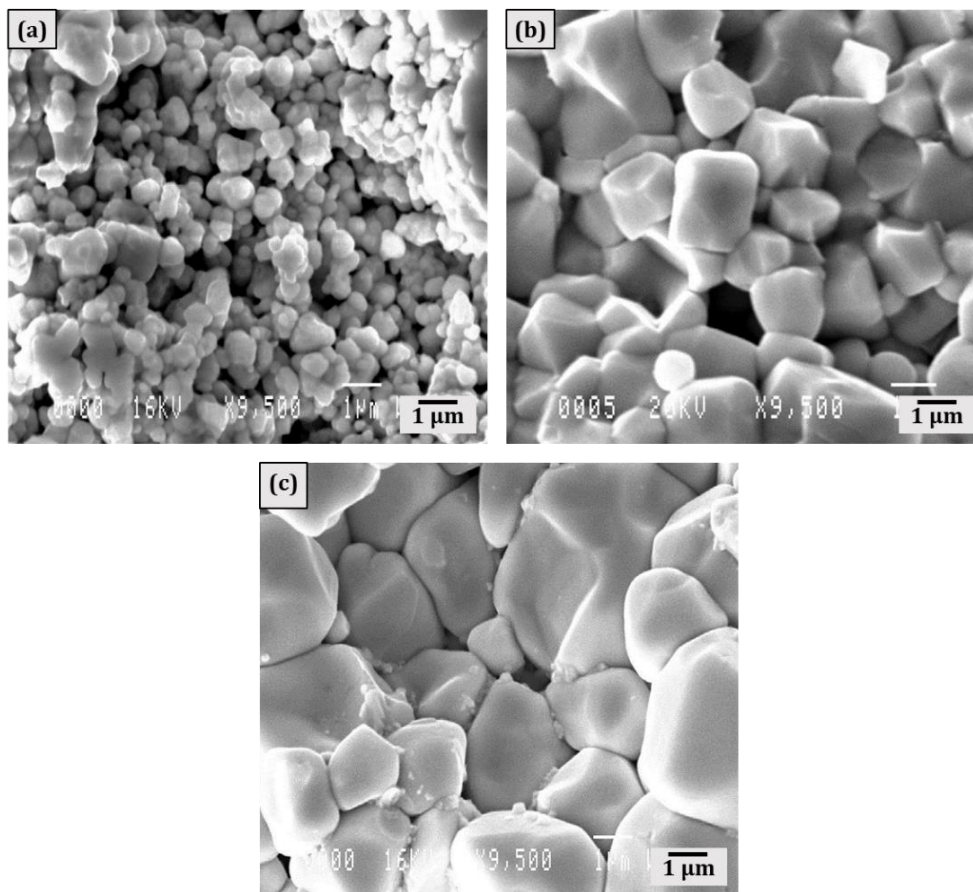


Figure V-3: SEM images of PZT ceramics densified by SPS at 800 °C (a), 850 °C (b), 875 °C (c), during 5 min under a uniaxial pressure of 100MPa.

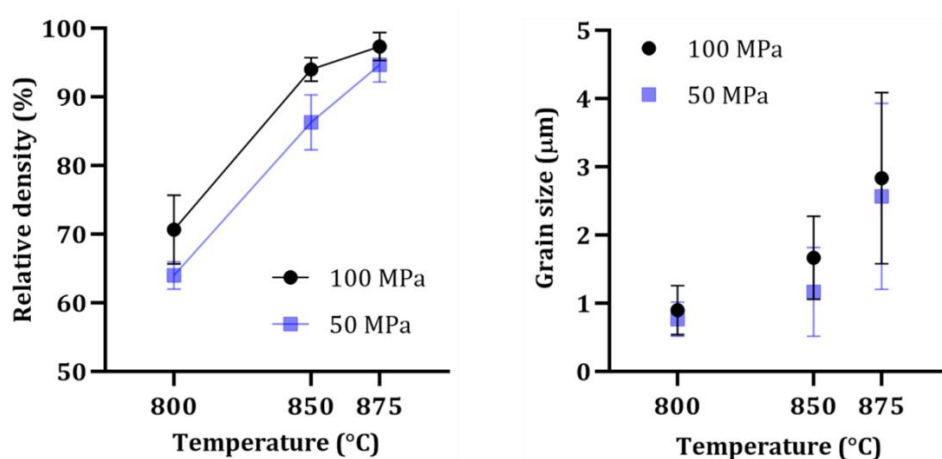


Figure V-4: Variation of grain size and relative density with sintering temperature and applied pressure.

2.1.1.2 Electromechanical characterizations of PZT ceramics obtained by SPS:

a) Electrodes and polarization step

Prior to electrical measurements, electrodes are deposited on the SPS ceramic disks before the polarization step. Here, electrodes of different nature are tested and compared in order to establish a standard protocol for samples preparation, targeting improved electrical characterizations. For this purpose two different types of electrodes are tested on ceramics sintered at 850 °C (50 MPa) and post-annealed 10 hours at 800 °C. Thin gold electrodes (≈ 100 nm) are sputtered whereas thicker Ag based electrodes (≈ 10 μ m) are screen-printed and dried at 120 °C during 20 min. The paste Ag-Epoxy ESL Ag-1901-S is used (see Annex 1 chapter 2). The choice for the screen-printed electrodes of the Ag-epoxy paste 1901-S instead of the Au paste ESL8836 used in the conventional process is justified by the low temperature process i. e. 120 °C instead of 850 °C. It will hence not modify the intrinsic properties of the PZT. Also, because the surface sample after SPS presents high rugosity, the influence of surface polishing is investigated for the thin Au sputtered electrodes (Figure V-5).

Once the electrodes have been deposited, polarization of the samples is led following the protocol described in Chapter 3. Then, for the planar vibration mode, conductance measurements are carried out to check the efficiency of the sample polarization. Characteristics of the samples are summarized in Table V-2 whereas conductance measurements are shown in Figure V-6.

On the conductance graphic, the resonance frequencies are different because of different diameters of the disks. The highest conductance peak and mechanical quality factor are observed for the Au electrodes deposited on a polished surface, whereas the sputtering of Au on a rough surface lead to deteriorated piezoelectric properties. This result is mainly attributed to the highest applied field during the polarization. Polarization with the rough electrodes can presents discontinuities and as a result the applied field could not be as high as required for a good alignment of the dipoles. The polished surface improves the interface and as a result, higher field can be applied.

A polished sample with screen-printed Ag-epoxy is also compared. The properties are improved compared to the sample with Au on a non-polished surface, but it is nevertheless not as good as for the sputtered Au. This is attributed to the quality of the electrical interface with the epoxy. Au Electrodes deposited on a polished surface of the SPS ceramic are then selected prior to electrical measurements.

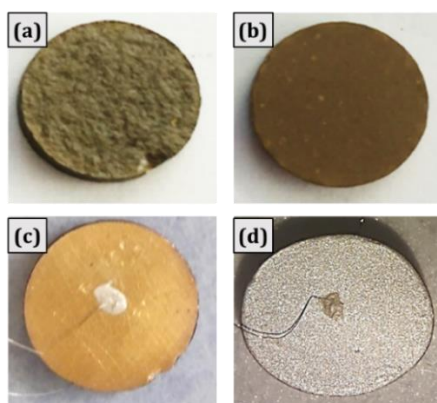


Figure V-5: Pictures of PZT disks (a) after SPS and post annealing 10 hours at 800 °C (b), after polishing with (c) Au sputtered electrode on the polished face with (d) screen-printed Ag-epoxy electrode on the polished face.

Table V-2: Summary of polarization conditions and conductance resonance peak characteristics for different type of electrodes.

Electrode	Diameter/ thickness (mm)	Applied Electric field during polarization (kV/mm)	Maximum of conductance peak G (S)	Mechanical quality factor Q_M
Screen-printed Ag-epoxy $\approx 10 \mu\text{m}$ (polished)	10.21/2.86	0.386	6.05E-04	204
Sputtered Au $\approx 100 \text{ nm}$ (non-polished)	10.21/2.91	0.233	2.05E-04	95
Sputtered Au $\approx 100 \text{ nm}$ (polished)	10.08/2.15	0.465	1.06E-03	657

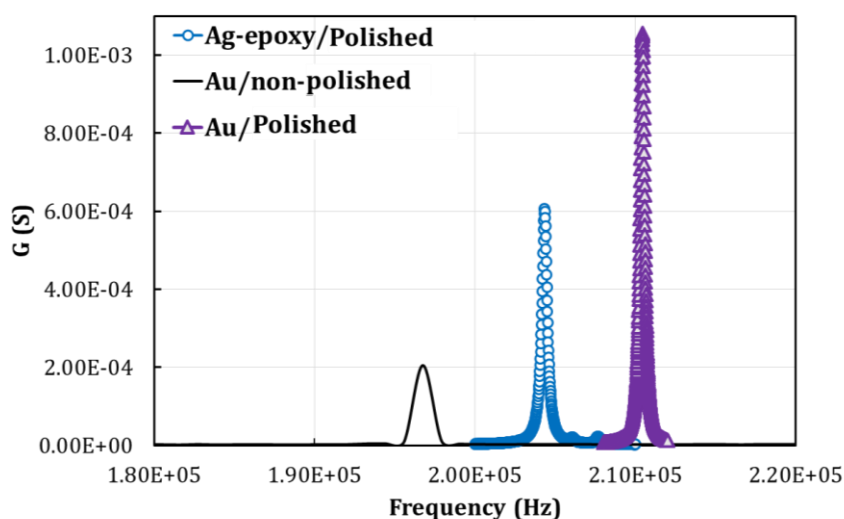


Figure V-6: Conductance response for different types of electrodes and surface quality.

b) Impedance analysis

Impedance modulus and phase as a function of the frequency are reported for the planar vibration mode of the electroded disks (Figure V-7). The results obtained for SPS ceramics sintered at 800 °C are not displayed due to their too low electromechanical response. On the reported curves, resonance and anti-resonance frequencies appear to be in the interval 210-240 kHz. Differences of few tens of kHz can be attributed to slight change in diameter between samples (± 2 mm), induced during polishing. The best electromechanical properties are clearly observed for ceramic sintered at 875 °C with in particular impedance phase angle reaching nearly 90° , this result is also confirmed with the $B(G)$ admittance circle (Figure V-8), where higher diameter of $B(G)$ circle for 875 °C is observed, supporting a better electromechanical response for this temperature. The effective coupling factor k_{eff} is evaluated close to 36%, whereas it hardly reaches 20% for the ceramic sintered at 850 °C. Such results confirm that maximum density is beneficial for piezoelectric properties. In case of free-standing thick film disk fabricated by conventional process, the value of k_{eff} is lower (26.5%), mainly due to porosity and electrode effects [38].

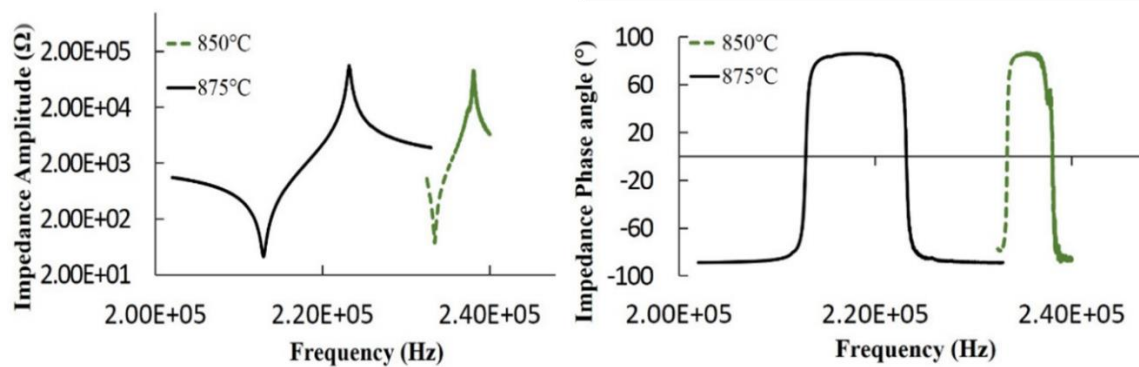


Figure V-7: Impedance amplitude and phase measured for ceramics sintered by SPS at 850 and 875 °C.

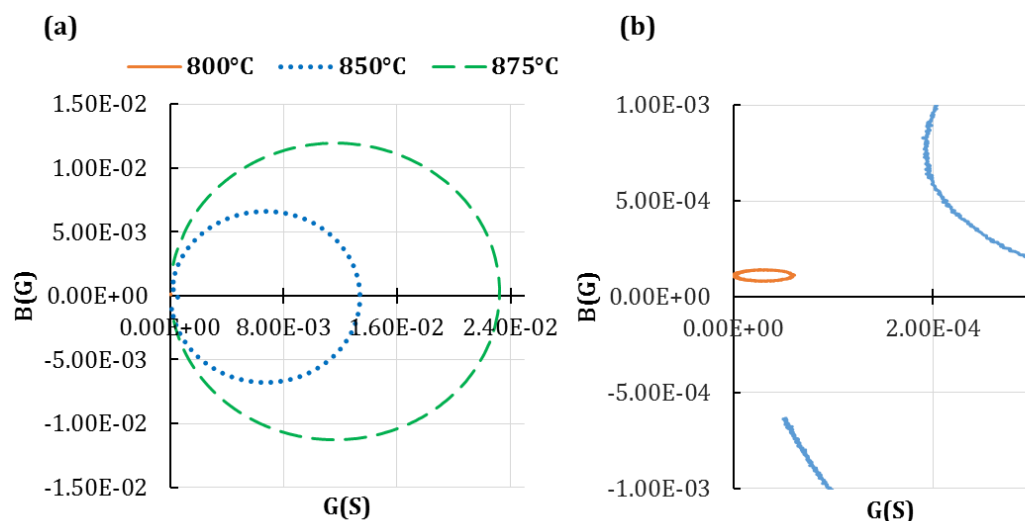


Figure V-8: (a) Admittance $B(G)$ circle of PZT ceramics sintered by SPS at different temperatures (800, 850 and 875°C), and (b) zoom close to the graphic axes origin in order to be able to observe the response of the ceramic sintered at 800°C .

The optimum sintering temperature regarding densification and properties corresponds to 875°C and is thus selected for further SPS experiments.

2.1.2 Approach towards one-step sintering of PZT by SPS

2.1.2.1 Protective layer strategy

As mentioned in the previous section, ceramics obtained by SPS need to be annealed in air at 800°C for 10 h, in order to remove surface carbon contamination and to limit oxygen vacancies caused by the reducing sintering conditions. Here we focus upon an affordable solution for one-step sintering of PZT by SPS using a protective layer. As drawn schematically on Figure V-9, a bed of protective powder is introduced into the system in between the PZT powder and two pieces of graphite foils.

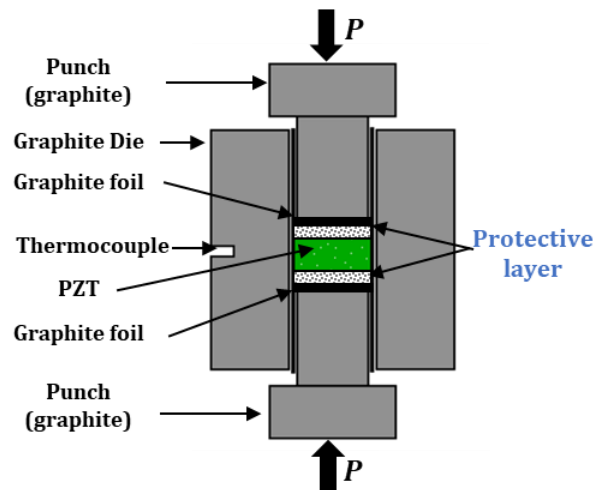


Figure V-9: Scheme of set-up configuration for sintering with a protective layer.

The strategy relies on the use of carbonates whose decomposition temperature depends on the nature of the alkaline cation (Table V-3). Strontium carbonate SrCO_3 already used at IMS as sacrificial layer for printed MEMS is first selected since its decomposition temperature is well above the optimized SPS sintering temperature (i. e. 875°C). In addition, the decomposition temperature of SrCO_3 in SrO can be further increased in controlled firing atmosphere (firing under CO_2) [32]. Here, SrCO_3 is used for the first time to prevent chemical reduction of the active piezoelectric material during SPS under low oxygen partial pressure. Tests performed using BaCO_3 which have a higher decomposition temperature than SrCO_3 are also performed. The removal of this protective layer after SPS is ensured by either polishing or chemical etching in diluted phosphoric acid prior to microstructural and electrical characterizations.

Table V-3: Decomposition temperature of principal carbonates.

Carbonate	Decomposition temperature ($^\circ\text{C}$) [32]
MgCO_3	350
CaCO_3	850
SrCO_3	1100
BaCO_3	1740

2.1.2.2 Structural and microstructural characterizations

XRD patterns at room temperature of the ceramic with and without the use of SrCO_3 are similar except the intensity ratio $I(002)/I(200)$. As already mentioned, mechanical treatments such as polishing and etching process affect the surface of the sample and can generate residual stresses. As a result, a change in intensity ratio $I(002)/I(200)$ is observed reflecting domain preferential orientation modification in the surface layer compared to the bulk [35][36] [37].

Evaluation of the relative density and SEM images of the ceramic microstructure after removal of SrCO_3 are in agreement with a highly densified ceramic ($\sim 98\%$) (Figure V-10). The average

grain size (2-4 μm) is similar to the one of PZT sintered by SPS without SrCO_3 . As a result, the protective layer does not affect the densification.

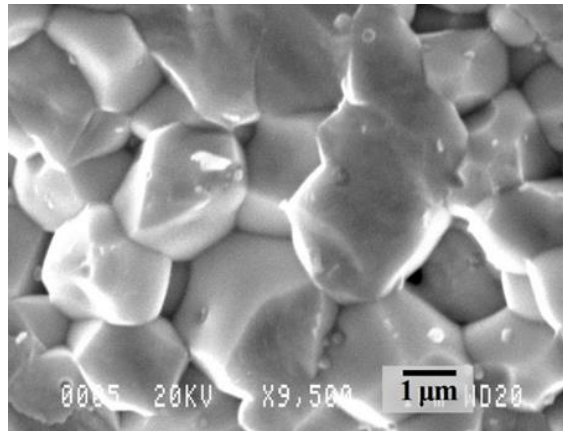


Figure V-10: SEM image of PZT sintered by SPS using a SrCO_3 protective layer.

2.1.2.3 Electrical characterizations

a) Dielectric characterizations

In order to prove the efficiency of the protective layer against reduction, electrical measurements have been led directly after sintering and etching of SrCO_3 . Dielectric characterizations performed as a function of temperature and in the frequency range 100 Hz – 100 kHz are shown on Figure V-11. The Curie temperature (T_c) corresponding to the maximum of permittivity is located at 330 °C as expected for the PZ26 composition (www.meggittferroperm.com). The room temperature permittivity reaches 1500, a value higher than the one reported for this commercial powder ($\epsilon \approx 1300$ – sintering at 1200 °C) and much higher than the one reported by Wu et al. ($\epsilon < 500$, sintering at 900 °C with an annealing 1h at 1100 °C). A slight frequency dispersion of the permittivity can be observed in the vicinity of the Curie temperature but there is no signature of conductivity (increase in permittivity) at high temperature ($T > 400$ °C). The permittivity at T_c and at 1 kHz reaches a value as high as 19800 reflecting the high quality of the ceramic. The room temperature dielectric loss ($\tan\delta$) is lower than 1% and remains stable as a function of temperature up to 350 °C (insert Figure V-11). The observed increase of $\tan\delta$ from 380 °C at the lowest frequencies (<1 kHz) nevertheless reflects the existence of residual space charges. However, the obtained dielectric characteristics, comparable or even better than those of commercial ceramics, attest to the quality of the grain boundaries and confirm the efficient role of the protective layer. In such conditions, SPS without subsequent annealing allows to obtain in one-step high quality piezoelectric ceramics exhibiting effective properties.

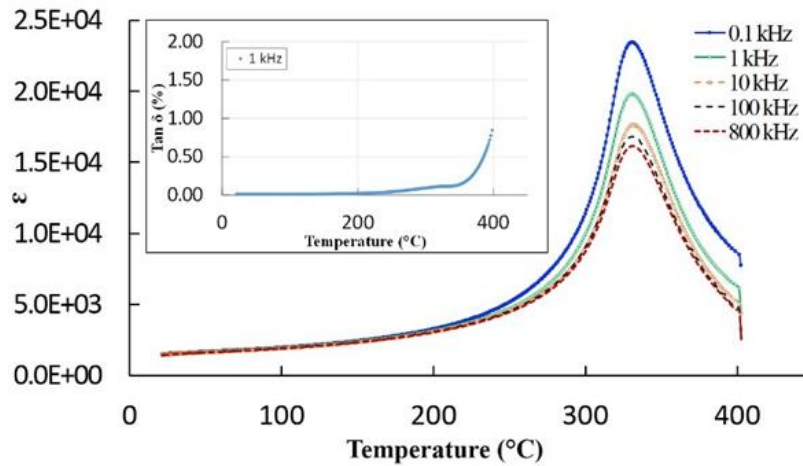


Figure V-11: Thermal variation of the permittivity at different frequencies for PZT/SrCO₃ sintered by SPS (no reoxidation) – Insert: Dielectric losses as a function of temperature at 1 kHz.

b) Electromechanical characterizations

An additional proof that the annealing is not required here, is the effective polarization of the ceramic directly after SPS. The polarization process failed when PZT is densified without a protective layer due to the charges and associated leakage current, making the annealing prior polarization process mandatory in this case. When using the SrCO₃ protective layer, Au electroded PZT ceramics can be directly polarized before electromechanical characterization. The measured admittance $B(G)$ circle of diameter $1/R_m$ (R_m is the resistance of the motional branch, as defined in chapter 3) is clearly a proof of the piezoelectric effect (see Figure V-12 (a)). Higher diameter of $B(G)$ circles reveals a better electromechanical coupling i. e. lower mechanical energy losses by viscous damping effect. The sample sintered at 875 °C using SrCO₃ clearly exhibits the best properties: larger diameter of $B(G)$ disk and highest k_{eff} reaching 40% instead of 36% without SrCO₃ protective layer (Figure V-12 (b-c)). Moreover, for this sample, the modeled curve obtained for an equivalent electric circuit without dielectric loss R_0 fits very well with the experimental curve (Figure V-13). These results clearly highlight the efficiency of the SPS sintering associated with the use of SrCO₃.

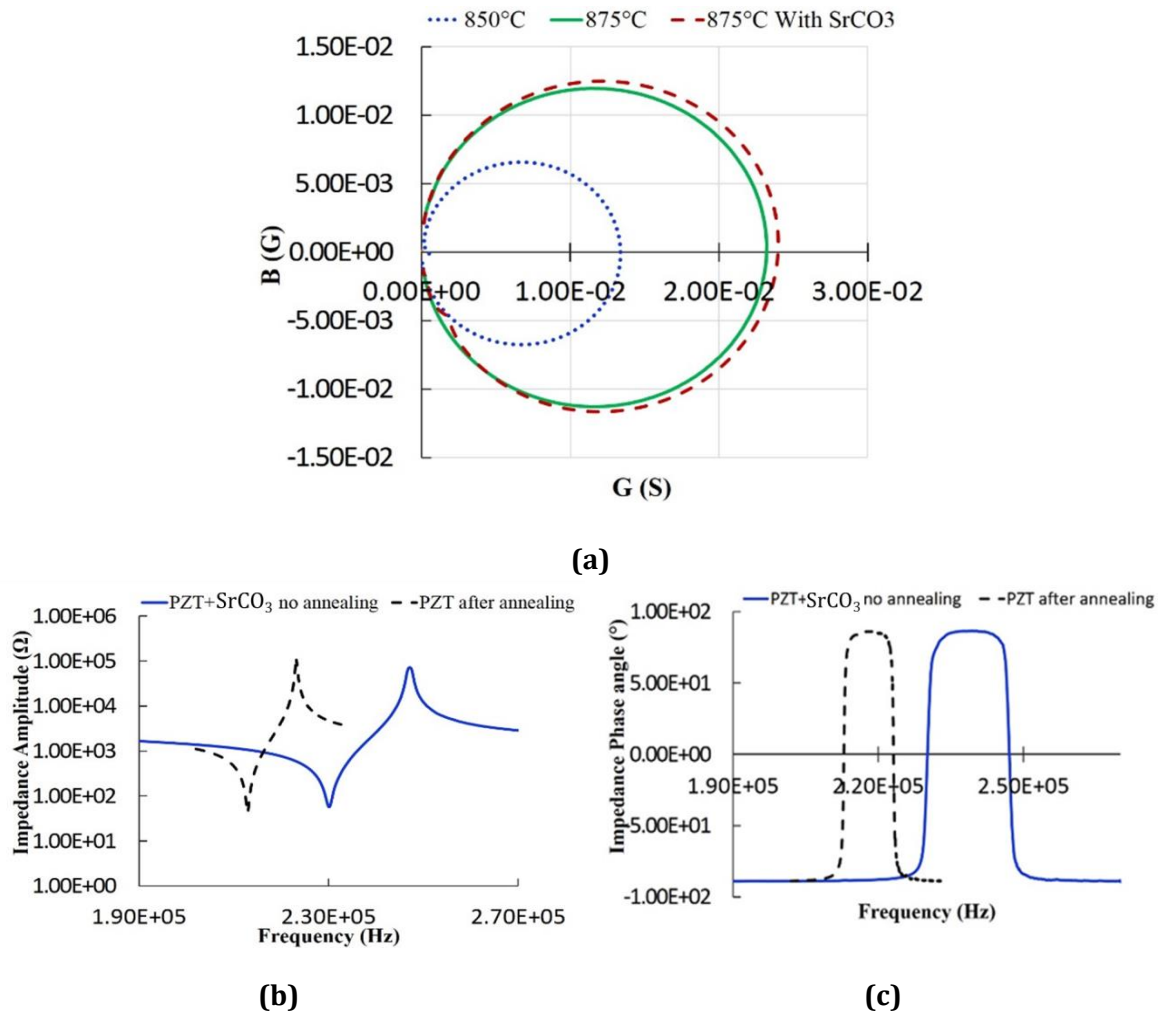


Figure V-12: Electromechanical measurements for PZT + SrCO₃ sintered by SPS (no reoxidation) in contrast with samples with no protective layer and annealing post-treatment (800 °C 10 h) (a) admittance $B(G)$ circle, impedance amplitude (b) and phase (c) for PZT/SrCO₃ (no reoxidation) and PZT(after annealing), both sintered by SPS at 875 °C.

In order to anticipate the transfer towards spark plasma sintering of EH multilayers, which will necessarily require adaptation of sintering conditions due to the reactivity between the different layers (carbonate and PZT, PZT and gold electrodes), other carbonates such as BaCO₃ have been tested. Ceramics are performed using same SPS conditions as for SrCO₃ (875 °C – 5 min – 100 MPa). The density of the obtained ceramics is close to 97.8%, a value similar to the one obtained with SrCO₃. Electromechanical measurements performed directly after SPS without annealing step are shown in Figure V-14. Results are compared to those obtained with SrCO₃ as a protective layer. Slightly lower but comparable k_{eff} is observed for samples with BaCO₃ protective layer, with a value of 38%, whereas for SrCO₃ k_{eff} =40%.

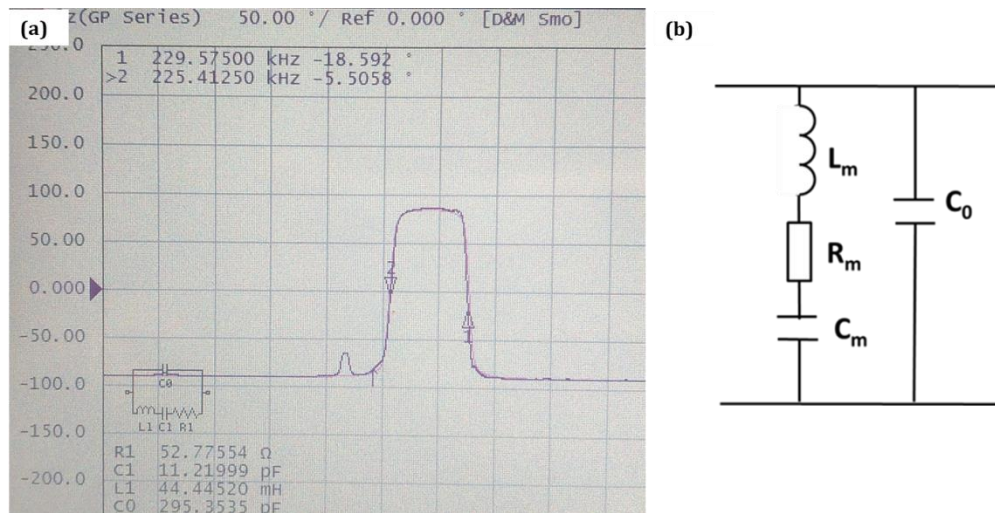


Figure V-13: (a) Experimental and fitted impedance phase angle for the PZT/SrCO₃ sample sintered at 875°C with equivalent circuit resulting response. (b) Equivalent circuit considered.

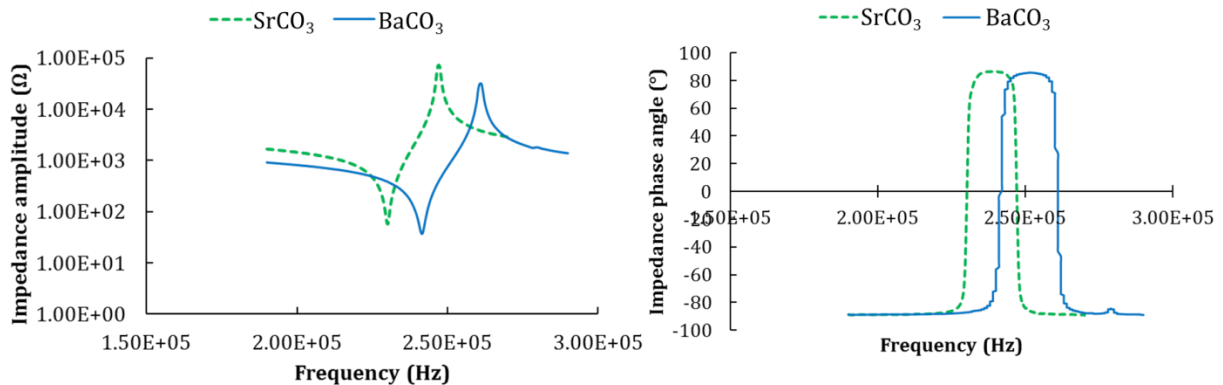


Figure V-14: (a) Impedance amplitude, and (b) phase for PZT sintered with SrCO₃ and BaCO₃ protective layer (no reoxidation), both sintered by SPS at 875 °C.

The room temperature dielectric permittivity at 1 kHz for PZT sintered with BaCO₃ reaches 950, a value lower than the one obtained using SrCO₃. Relative densities are similar whatever the nature of protective layer, a microstructural effect can be discarded to explain such a difference. Higher electric field can be applied to PZT sintered with BaCO₃ compared to PZT sintered with SrCO₃, this could explain the lower permittivity values when using BaCO₃. This could also reflect that BaCO₃ acts as a more efficient thermal barrier against diffusion and chemical reduction with as a result a lower level of charged defects within the PZT. However, if the room temperature dielectric losses at 1 kHz remain below 1%, losses start to increase at lower temperature (from 150 °C instead of 350 °C in the case of SrCO₃). Other effects such as electrodes effects should be thus considered.

2.2 Influence of sintering aid

For sake of comparison with conventional sintering of PZT and in order to study the densification of PZT based EH multilayer by SPS, specific investigations focused on the role of sintering aid on both densification, microstructure and electrical properties have been conducted. Spark plasma sintering is performed using the PZT powder mixed with 3wt% of LBCu loaded in a cylindrical graphite die with an inner diameter of 10 mm and heated under low oxygen partial pressure. The same SPS conditions (100 MPa, 50 °C/min, 5 min.) as for PZT without LBCu are considered. According to the sintering temperature, here between 700 and 875 °C, the samples are annealed in air either at 650 °C (for sintering at 700 °C and 800 °C) or 800 °C (for sintering temperature 875 °C) for 10 h.

Table V-4: Microstructural features of PZT + 3wt% LBCu sintered by SPS at different temperatures.




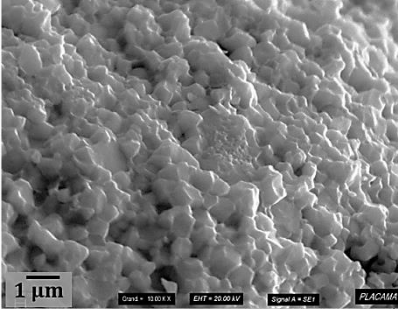
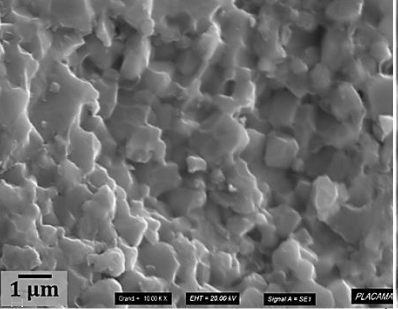
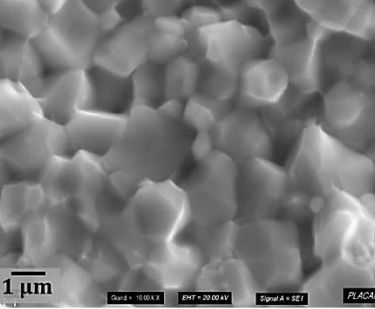
T°C	700°C	750°C	875°C
Sample			
Density	~7.8 (g/cm ³)	~7.8 (g/cm ³)	~7.8 (g/cm ³)
SEM (10kx)			
Grain size	~0.6 - 1.9 µm	~0.7 - 1.8 µm	~0.7 - 2 µm

Table V-4 summarizes the results. It is observed that whatever the sintering temperature, ceramics display very high densification with a density close to the theoretical one. The addition of sintering aid clearly allows for a decrease of sintering temperature while keeping high density value. When using LBCu, the onset of densification by SPS is estimated close to 500 °C. The densification is favored by the melting of additives leading to a liquid phase and promoting particles rearrangement. One point is to rule if liquid phase sintering aids either enter in the PZT lattice or remain as a second phase at the grain boundaries [39]. Both microstructural (EDS analysis) and structural investigations are required. The work reported by X. X. Wang [3] on PZT + LBCu ceramics obtained by conventional sintering highlights that the addition of LBCu enhances both densification and grain growth and confirms the presence of additives at the grain boundaries by XPS analysis. However, structural analysis is not provided.

XRD analysis shows no deviation of the peak positions indicating that the sintering aid does not cause significant modification of the lattice cell parameters (Figure V-15). The most remarkable feature in the XRD patterns of the ceramics sintered with LBCu is the broadening of the tetragonal splitting (002)/(200) (observed also for the others double peaks (001)/(100), (112)/(211) and (103)/(310)). However, EDS analysis (Figure V-16) has not provided additional insight to conclude on a possible correlation between chemical inhomogeneity and the observed peak broadening. EDS analysis has not allowed detecting and localizing Cu and Bi possibly due to quantities close to undetectable levels and absence of segregation.

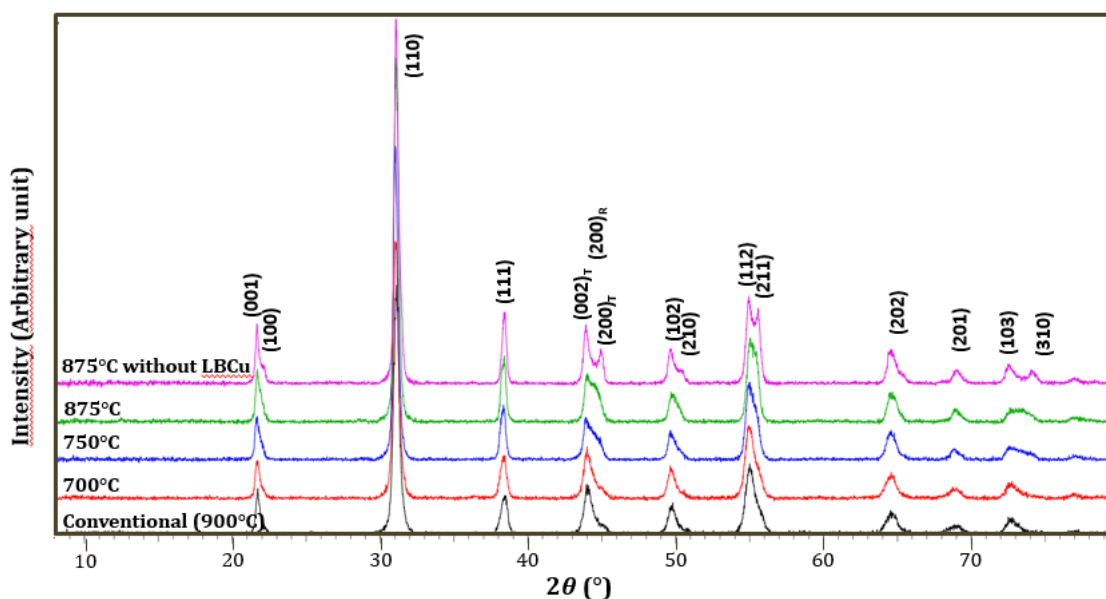


Figure V-15: XRD patterns for ceramics PZT + 3wt% LBCu sintered par SPS at different temperatures (700, 750 and 875 °C), and for PZT (without LBCu) ceramic by SPS at 875 °C and conventional ceramics sintered at 900 °C.

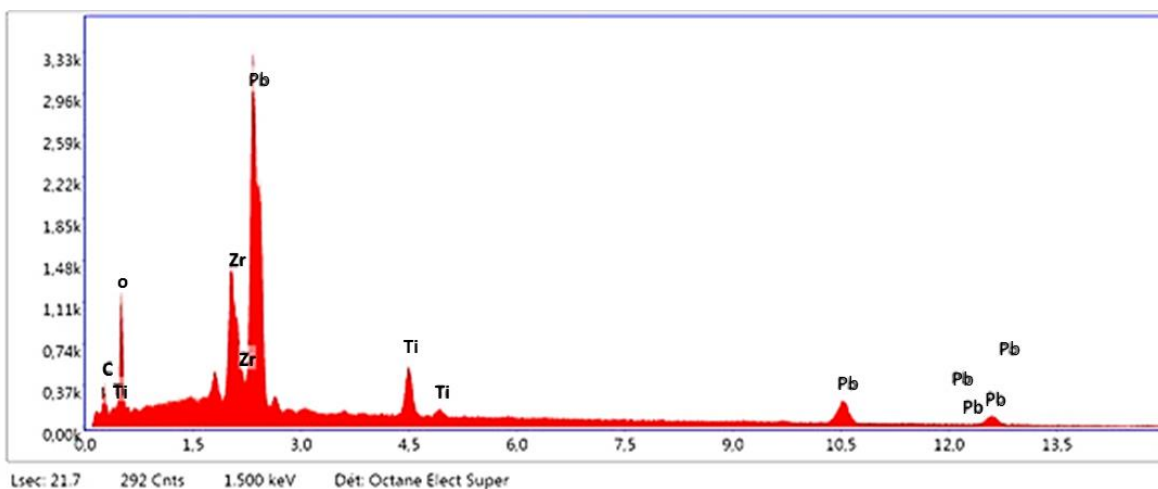


Figure V-16: EDX of PZT + 3wt% LBCu ceramics sintered by SPS at 700 °C (very similar results are obtained for 750 °C and 850 °C).

Nevertheless, preliminary electromechanical tests are performed. First, after polishing and deposition of gold electrodes, polarization is carried out at a maximum of 0.63, 0.53, and 0.50 kV/mm, respectively for 700, 750 and 875 °C. Electromechanical characterizations show, in general, a weak response, but the best result is obtained for the ceramic sintered at 750 °C (Figure V-17 (a)). The effective coupling factors k_{eff} are of 18% and 5% for ceramics sintered at 750 and 875 °C respectively. Ceramics sintered at 700 °C show very weak, nearly inexistent response. It clearly appears that, in comparison with PZT ceramics sintered without sintering aid (Figure V-17 (b)), the electromechanical response of the sintered PZT samples with LBCu is from far weaker, suggesting that the use of LBCu leads to an alteration of the piezoelectric properties when sintered by SPS. However, more in-depth microstructural analyses (especially at grain boundaries) are required at this stage to conclude on the role of LBCu on SPS ceramics and its influence of chemical inhomogeneity on the piezoelectric response.

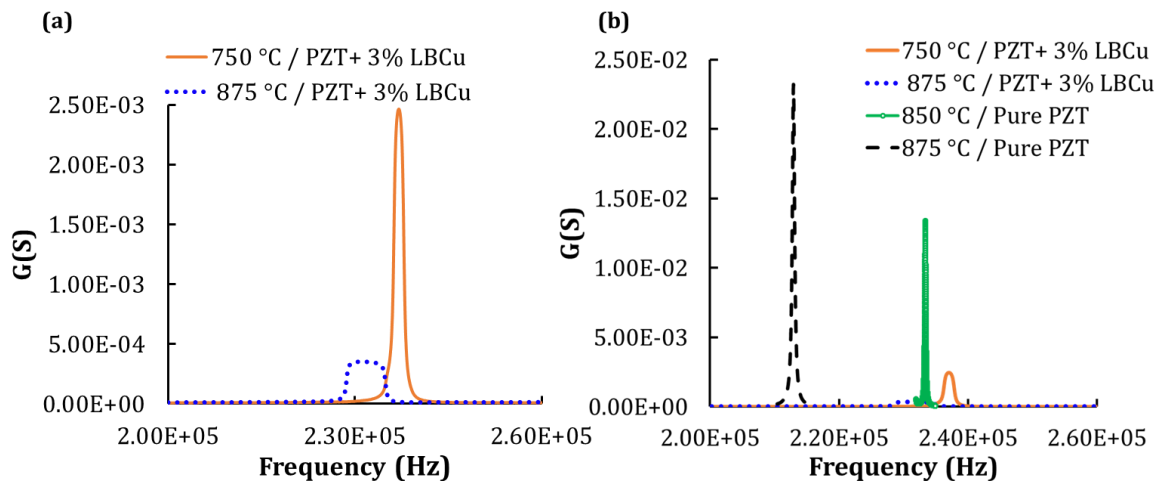


Figure V-17: Electromechanical response of PZT + 3%LBCu ceramics sintered by SPS (a) Conductance (G) response of samples at 750°C and 875°C (samples at 700°C show little nor comparable response), and (b) comparison with pure PZT ceramics sintered at 850°C and 875°C.

2.3 Summary

In order to evaluate the potentiality of SPS to sinter PZT ceramics without sintering aid and in one-step (without post annealing), the microstructural and electromechanical properties of the screen-printed thick film, the commercial PZ26 ceramic and the SPS ceramics are compared (Table V-5). These results show that for the SPS ceramic despite a lower sintering temperature, 875 °C instead of 900 °C (screen-printed thick films) and 1200 °C (commercial ceramics), and the absence of additives, the electromechanical coupling factor reaches a good value of 40%. Nevertheless, such a value is still lower than that corresponding to the commercial ceramic (50%) possibly because of non-optimized polarization conditions. The comparison clearly highlights and demonstrates the potential of the SPS process for an efficient densification in one step thanks to the use of a carbonate protective layer (SrCO_3 and BaCO_3). It was also shown that the sintering temperature can be lowered (700 °C) using sintering aid (3 %LBCu). However,

even if the density remains high, the electromechanical properties are deteriorated. Work is in progress to correlate the chemical homogeneity (arising from the introduction of LBCu) to the lower electromechanical performance observed.

Table V-5: Comparison of the properties of the PZ26 ceramics sintered by different methods

	Temperature Holding time Heating rate	Pressure (MPa)	Annealing	Grain size (μm)	Relative density (%)	k_{eff} (%)	ϵ
Screen-printed thick film (sintering aid)	900 °C 2h 40 °C/min	40	No	1-4	94	26	600
SPS ceramic	875 °C 5min 50 °C /min	100	Post annealing 8h, 800 °C	2.5-4	97.4	36	1200
SPS ceramic + protective layer (SrCO₃)	875 °C 5 min 50 °C /min	100	No	2.5-5	98.2	40	1500
SPS ceramic + protective layer (BaCO₃)	875 °C 5 min 50 °C /min	100	No	-	97.8	38	950
SPS ceramic + LBCu + SrCO₃	700 °C-875 °C 5 min 50 °C /min	100	No	0.6-2	98.0	18 (750°C) 5 (875°C)	1100
Conventional commercial sintering (Ferroperm)	1200 °C	-	Yes	2-5	98.7	50	1300

3 Transfer towards multilayer printed structures

The EH structure considered in this part is the cantilever made of a PZT layer in sandwich between two Au electrodes printed on a stainless substrate (SS/Au/PZT/Au) (Figure V-18). Multilayers are fabricated using the same screen-printed based process detailed in chapter 4, letting out the densification that includes a pressure step and conventional sintering at 900 °C during 2h.

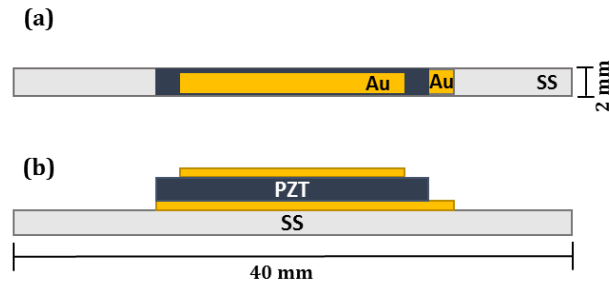


Figure V-18: Configuration of the multilayer structure (SS/Au/PZT/Au) for SPS sintering.

The main challenge in aiming at the transfer towards SPS sintering of multilayers lies in the control of interfaces. The reduction of the number of steps in the EH fabrication process by targeting one-step SPS sintering is also an ambitious objective.

3.1 Interfaces in multilayers by SPS: Metal/Ceramic interfaces

SPS is widely used for the assembly of materials and is recognized as an efficient sintering process for co-sintering or bonding. The control of chemistry and defects at interfaces is a key issue. If temperature and pressure contribute to mass transport enhancement, the influence of current through electromigration or defects concentration and mobility has also to be considered [40]. The current and/or temperature effects on the formation of interphases were mainly studied for multilayers intermetallic systems [41][42]. The studies reported in literature dealing with ceramic/metal or metal/polymer multilayers assemblies concern to a large extent Functionally Graded Materials (FGM) [43]. Composites made of biocompatible ceramic and metal ($\text{Al}_2\text{O}_3/\text{Ti}$) were investigated by SPS in order to optimize the mechanical properties [44]. It was shown through bending tests that fracture occurs within a reaction layer formed at the interface. Hardness and bending strength of the alumina–titanium composites were compared to those of FGM samples [45]. The reactivity of titanium with alumina and the presence of microcracks for SPS sintered $\text{Al}_2\text{O}_3/\text{Ti}$ functionally graded materials were also reported by Madec C. *et al* 2018 [46]. Focusing on materials designed by SPS for electronic devices applied to energy harvesting, only few studies were reported. Issindou *et al* [47][47] worked on simple SPS magnetostrictive ceramics optimized by SPS, but no multilayers were studied. Cu/PZT functionally graded materials were fabricated by SPS targeting actuators applications [48]. The impact of copper particles addition into PZT matrix on the dielectric properties and the electrical conductivity was investigated. Piezoelectric properties were not reported. In the case of multilayers stacking, monolithic transformers for power applications were co-sintered by

Spark Plasma Sintering [30]. The reported transformer is made of two spiral copper coils, a dielectric layer and a spinel ferrite magnetic circuit. The advantages of SPS lies here on the reduced sintering temperature that allows to co-sinter copper with the ferrite powder and on the possibility to obtain a monolithic structure that eases the heat transfer from the coils. Deformation and leakage inductance issues were identified and were solved by adapting dimensions and sintering conditions (sintering aid). However the argon atmosphere during SPS was revealed as detrimental regarding to the ferrite resistivity. This study illustrates well several issues that must be tackled when using SPS to co-sinter complex structures.

The overall approach envisaged for the optimization of EH cantilever sintering and the methodology are explained in the next section. The different steps that constitute this approach are critically discussed. Finally, some perspectives of improvement are proposed.

3.2 Approach

The SPS sintering conditions optimized for PZT ceramics and discussed in the previous section of this chapter cannot be fully transposed towards the sintering of the multilayer EH structure, due to:

- The shaping of the multilayer structure is done before sintering, while ceramics are shaped from their powder form into pellets during SPS sintering through an applied uniaxial pressure. Shaping of the multilayer structure is made by screen-printing. Therefore pressure parameter cannot be transposed from ceramic to multilayer.
- As previously discussed, the presence of the substrate and the printed electrodes brings to the structure additional stresses. This additional contribution is thus to be considered during the densification step. By consequence, even if the obtained SPS ceramics are highly densified (~98%), similar level of densification cannot be expected for multilayer structure. Nonetheless, higher densification than conventional one is aimed (relative densification >82%)

The approach dedicated to the sintering of the multilayer structure by SPS includes:

- A focus on the critical parameters related to multiple interfaces: bending, delamination, interdiffusion
- Optimization of the SPS set-up configuration
- Optimization of other key parameters of the assembly: nature of protective layer, specificities of each material of the multilayer structure in terms of nature and thickness.

For this, several experiments are performed, starting from the results obtained for SPS sintering of PZT ceramics and conventional sintering of multilayer structures. The first assumptions are:

- When considering the multiple interfaces within the multilayer (top Au/PZT/bottom Au/SS), the optimal sintering temperature defined for ceramics (875 °C for pure PZT)

should be slightly decreased in order to prevent interfaces related issues (in particular interdiffusion from the glass frit contained in the gold paste). However, it must be maintained sufficiently high to guarantee satisfactory densification.

- A uniaxial pressure as high as the one used for ceramics (50-100MPa) cannot be applied to the multilayer structure; this one can lead to complete damage of the sample. Therefore a minimum uniaxial pressure is used, the pressure equivalent to the SPS contact force (3kN).

Delamination and bending are the critical parameters encountered. Transient thermal gradients can induce stress gradients through the multilayer resulting in delamination issues. The most challenging aspect here identified is to avoid the delamination between the active piezoelectric layer and the electrodes (bottom and/or top electrodes). This is mandatory to guaranty not only a viable process but also to ensure the polarization of the multilayer and the reproducibility of the process. Sintering parameters as well as the features of the complete assembly such as the nature and thicknesses of multilayer structure constituents and protective layer are to be optimized.

A total of 150 experiments have been carried out during this experimental approach, in order to validate the strategic lines used for improved densification of the multilayer by SPS. They are explained through illustrations in the next section. Figure V-19 summarizes the general experimental approach used.

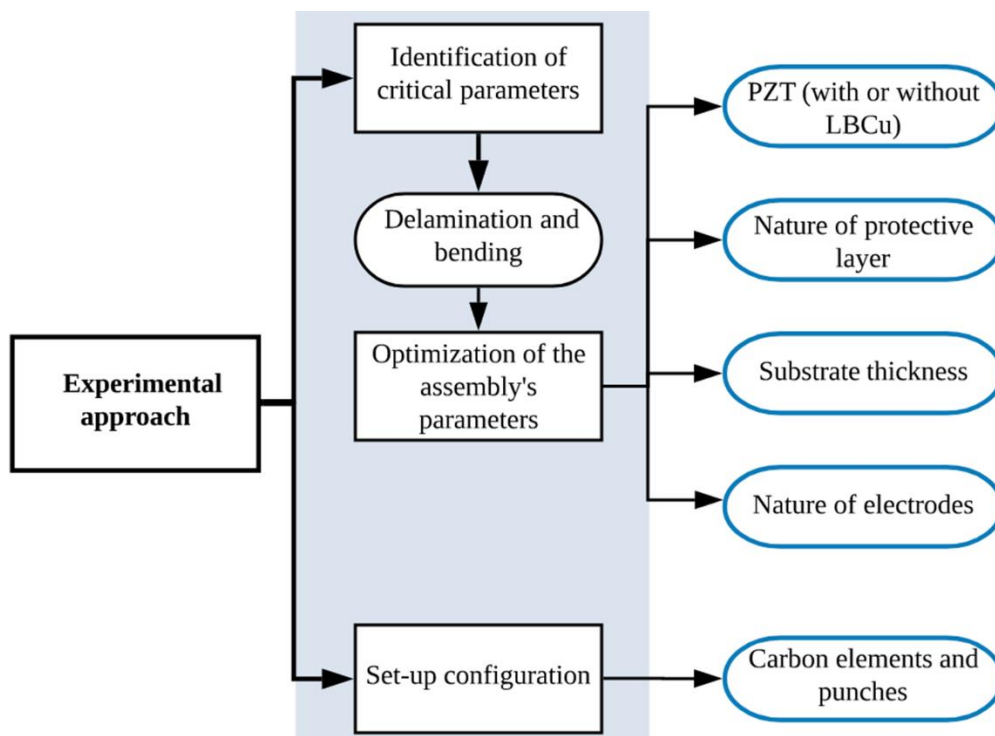


Figure V-19: Summary diagram of experimental approach towards SPS sintering of multilayer structures.

3.3 Optimization of SPS set-up configuration

Besides the sintering temperature, the pressure is another determining parameter. For screen-printed films, an isostatic pressure of 40MPa (5 min at 65 °C) is applied prior sintering; this favors PZT densification and allows to reach a relative density of ~80 %. For SPS ceramics densification, samples are compacted by uniaxial pressing during sintering using standard molds (Figure V-20) that allows a homogeneous distribution of both heat and pressure on the sample. In the case of PZT ceramic, the applied pressure of 100 MPa during SPS enhances the densification. High-applied pressure could potentially damage the stack, thus lower but uniform pressure need to be ensured.

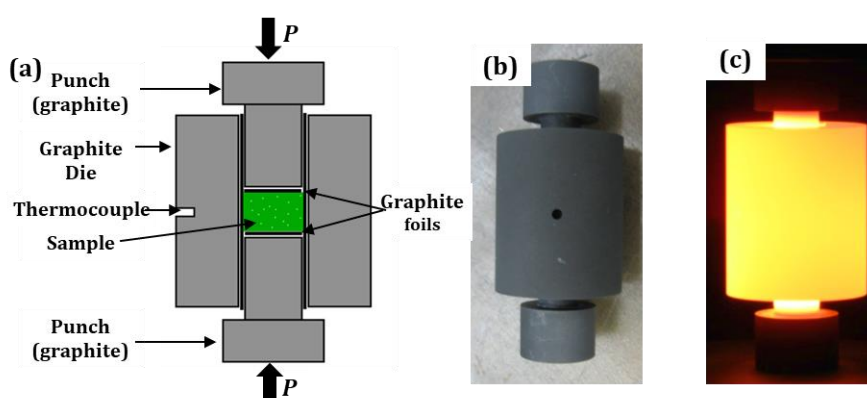


Figure V-20: Standard set-up configuration for ceramics SPS densification (a), picture of graphite mold and punches (b) and mold during densification (thermal radiation is observed at $T^{\circ} > 700$ °C (c))

Taking into account these considerations and considering the geometry of the multilayer, the standard mold based configuration is not suitable. Modification of the SPS tooling set-up through the design of specific mold is a strategy already reported in literature to adapt the process to specific materials and to target widespread applications. Many examples can be mentioned, among them adapted tools for Functionally Graded Materials [49], porous ceramics [50][51], and nanostructured materials with specific high pressure dies [52]. Tooling optimization is also mandatory to control radial thermal gradients that can generate microstructural non uniformities in sintered specimens, and which tend to become more critical in case of scale-up or when aiming complex shapes (Figure V-21) [53].

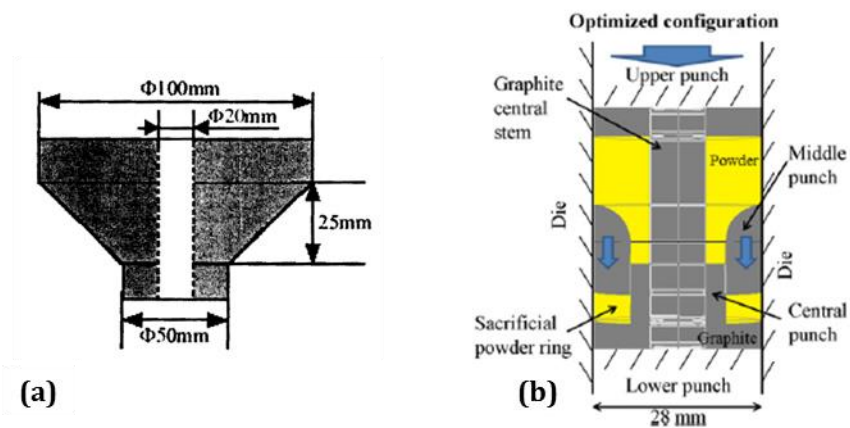


Figure V-21: Illustrations of SPS optimized tools configuration (a) Schematic view of the gradient die dedicated to FGM (from [49]), and (b) optimized configuration with a sacrificial powder ring dedicated to samples with complex shapes (from [53]).

In the framework of this thesis, several configurations (punches + carbon elements) have been developed and tested to obtain optimal conditions regarding the incorporation of the multilayer (including the protective layer) and the uniformity of the applied pressure. A total of 10 set-ups have been tested. The main steps towards their optimization are explained.

3.3.1 Starting configuration (Configuration 0)

Starting from simplified configuration made of only the two non-hollowed punches (flat surfaces) of 30 mm ϕ (configuration 0), three strategies are considered: modification of the internal set-up by adapting graphite foils (configurations 1 and 2), modification of the graphite punches (configurations 3 and 4) and finally a combination of graphite foils and punches modifications (configuration 5). This is illustrated in Figure V-22.

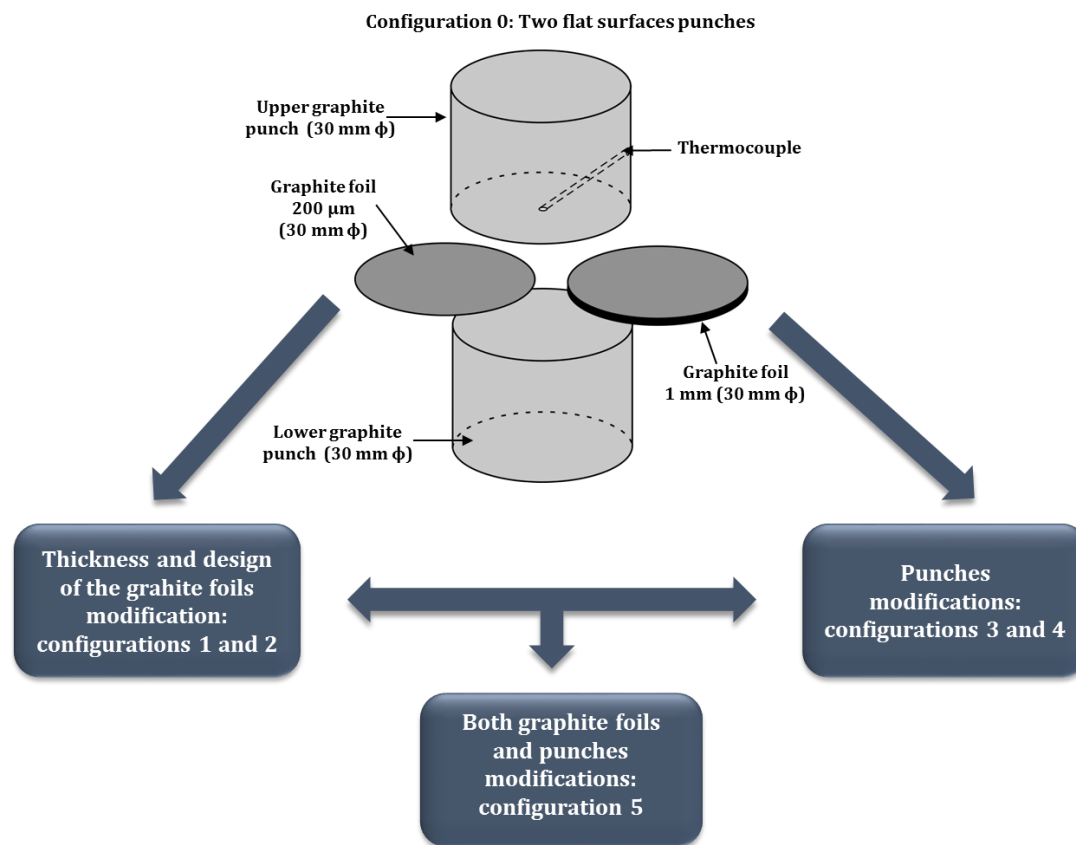


Figure V-22: Flowchart of the different steps towards the optimization of the SPS set-up configurations dedicated to the sintering of multilayer.

For all the studied configurations, graphite foils (200 μm ϕ and/or 1 mm ϕ) are placed directly in between the punches in order to hold the sample fixed and to ensure a homogeneous distribution of heat and pressure all along the surface (Figure V-22). Their design depends also on the form of the protective layer (printed layer deposited on the multilayer or bed of powder). The location of the thermocouple allows to measure the temperature very close to the sample (Figure V-22).

3.3.2 Configuration 1

In the configuration 1, the sample is placed in between the punches and graphite foils (Figure V-23). A 1 mm thick perforated graphite foil (ring-like design) is used to hold in place the protective layer. This configuration is tested either with the sample face-up (Figure V-23(a)) or face-down (Figure V-23(b)). However, all experiments (conducted 3 times) result in samples completely destroyed after sintering (Figure V-23 (c-d)).

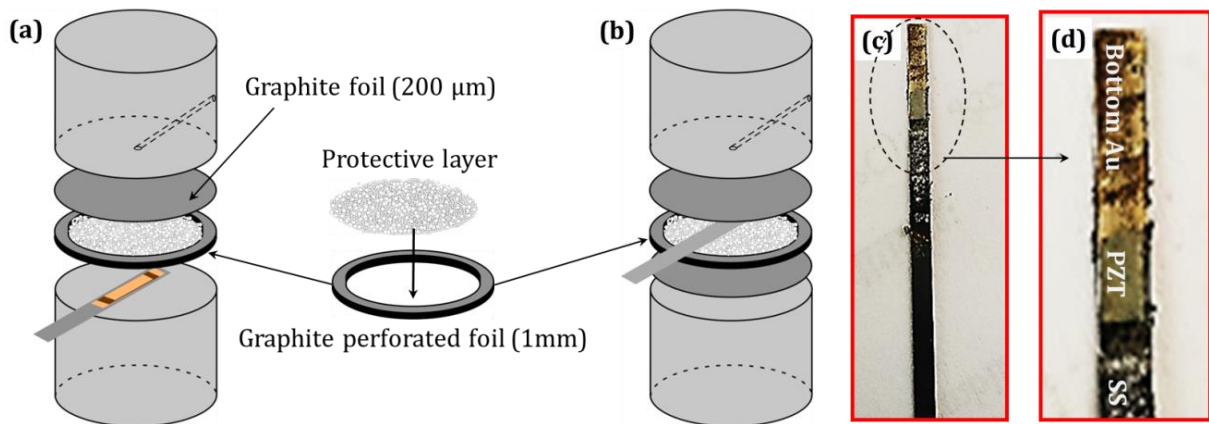


Figure V-23: Scheme of configuration 1 with the powder protective layer incorporated in a ring-like graphite foil, to place the protective layer. (a) sample facing up and (b) sample facing down. (c) Resulting samples (all layers are completely damaged) and (d) picture zoom.

3.3.3 Configuration 2

In configuration 2, instead of a circular perforated graphite foil, a rectangular shaped matching the area of the multilayer stack is cut within the graphite foil to incorporate the protective layer (Figure V-24 (a) and (b)). A more homogeneous distribution of the mechanical stress is thus expected. Nevertheless, this configuration also results in samples with peel-off of layers (Figure V-24 (c)).

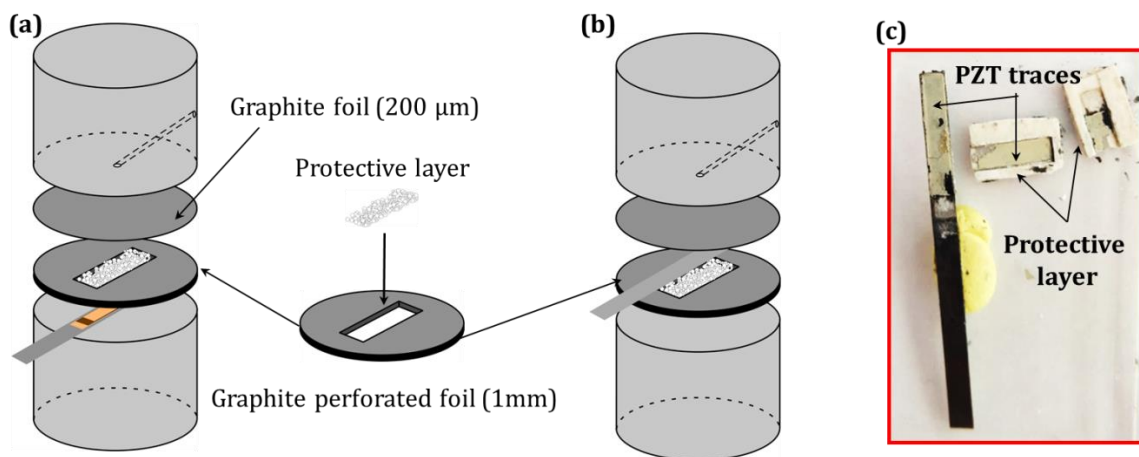


Figure V-24: Scheme of configuration 2 with protective layer incorporated in a modified rectangular shaped graphite foil, (a) sample facing up and (b) sample facing down configuration. (c) Picture of an example of obtained samples (all layers are completely destroyed).

3.3.4 Configuration 3

For configuration 3, graphite punches modification is experimented. The bottom graphite punch is perforated in a circular shape with 1 mm depth. The protective powder is then introduced in it and the sample is placed face-down on top of it (Figure V-25(a)). Samples seem to not be destroyed right after sintering process, but once the protective layer is chemically removed, the active PZT layer shows to be peel-off.

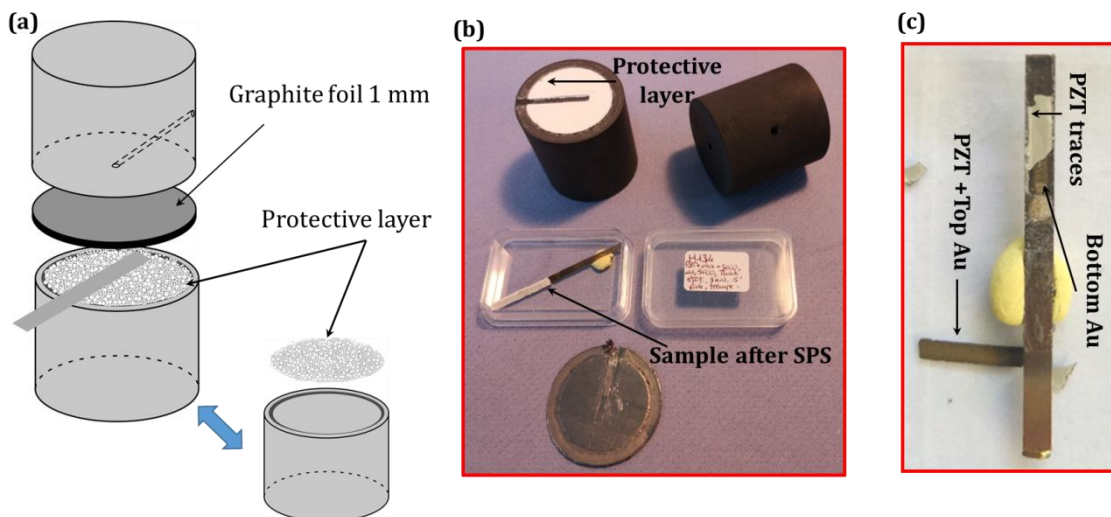


Figure V-25: Scheme of configuration 3 with the protective layer introduced in the bottom graphite punch perforated in a circular shape of 1mm depth. (b) Samples right after SPS (layers seemingly well adhered) and (c) layers are peeled-off after chemical removal of protective layer.

3.3.5 Configuration 4

Configuration 4 corresponds also to a punch modification, but here a notch corresponding exactly to the rectangular shape of the multilayer is cut in the punch (Figure V-26 (a-c)). Nevertheless this configuration does not provide satisfactory results. Layers are peeled off either when the sample is removed after sintering or during chemical attack used to remove the protective layer (Figure V-26 (d)).

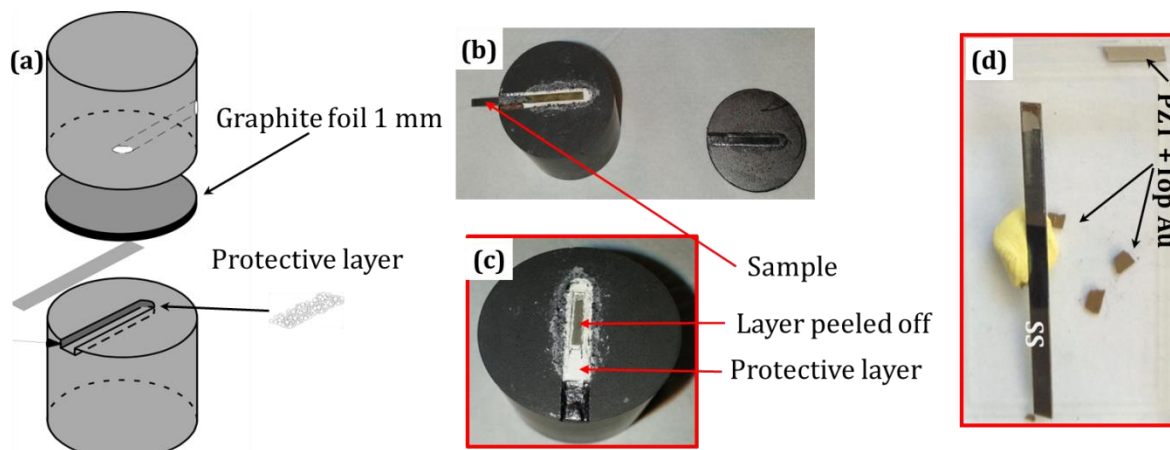


Figure V-26: Scheme of configuration 4 with a rectangular shape notch within the punch of 1mm depth. (b) Set-up right after SPS, (c) peeling-off of layer when moving out the sample and (d) peeling of layers after chemical attack

3.3.6 Configuration 5

Configuration number 5 consists of the same previous graphite punch modification (set-up 4), but this time the placement of protective layer and sample are inverted. Additionally, a carbon felt is introduced on the top of the assembly (sample + protective layer) to improve mechanical stresses distribution as well as to add slightly more pressure on the sample (Figure

V-27 (a)). This element is introduced in the rectangular notch of the punch. The resulting sintered samples meet quite satisfactory expectations : there is no systematically a peel off of layers not only after SPS but also after chemical removal of the protective layer (Figure V-27 (b-c)). These results are consistent throughout several experiences. Therefore configuration 5 combining punches and internal set-up (graphite elements) modifications is selected as the final optimized SPS set-up configuration.

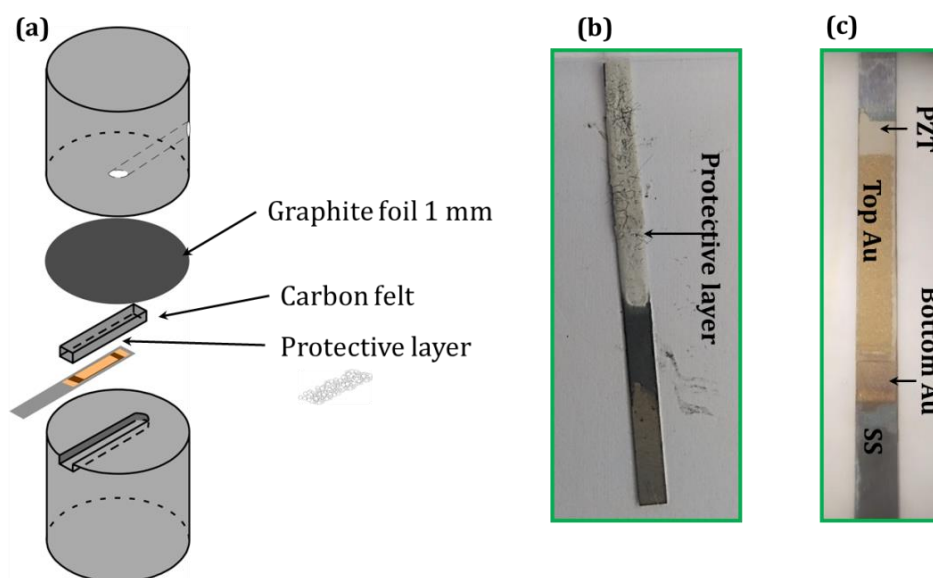


Figure V-27: Scheme of configuration 5 using an additional carbon felt element for an extra pressure applied to the sample. (b) Sample after SPS process without any damage and (c) sample after removal of protective later with still a good adhesion maintained between layers.

3.4 Optimization of sintering conditions for the multilayer EH structure

Table V-6 reports illustrations of the tests performed using the different set-up configurations. These experiments are conducted on the multilayer stack with the following characteristics: SS: 250 μm , Bottom Au: 12 μm , PZT: 55 μm and Top Au: 8 μm . The formulation of inks (Commercial Au, PZT without 3%wt LBCu) described in chapter 4 is used. Concerning the protective layer, SrCO_3 is used with two options: (i) a protective layer of SrCO_3 made of Epoxy CV59 (Annex 1) mixed with SrCO_3 powder, is printed on the top Au electrode without any preliminary firing, debinding or pressure steps. (ii) a bed of SrCO_3 powder is deposited. The selected examples reported in Table V-6 have been performed under vacuum at sintering temperature of 850 $^\circ\text{C}$. Different sintering times, cooling and heating rates are tested.

Table V-6: Summary of first experience for identification of sintering conditions and critical parameters.

Sample (PZT)	Sample Ref	Set-up	Protective layer (SrCO ₃)	Heating rate (°C/min)	Sintering Time (min)	Cooling rate (°C/min)	Forced applied (kN)	Debinding	Results		
									Delamination		No delamination
									Before ca	After ca	
1	H006	1	Printed	50	5	Natural	3	No	Delamination before ca		
2	H007	1	Printed	50	5	Natural	3	No		Delamination after ca	
3	H008	1	Printed	50	5	Natural	3.1	No		Delamination after ca	
4	H011	1	Powder	50	5	Natural	3.9	No			No delamination
5	H020	2	Powder	50	5	Natural	3.9	350°C/ 3min	Delamination before ca		
6	H022	2	Powder	25	5	Natural	3.9	No	Delamination before ca		
7	H024	3	Powder	50	5	Natural	3.1	No	Delamination before ca		
8	H039	3	Powder	50	5	50	3.1	No	Delamination before ca		
9	H040	3	Powder	25	5	25	3.1	No	Delamination before ca		
10	H044	4	Powder	25	10	25	3.1	No	Delamination before ca		
11	H063	3	Power	50	5	40	3.1	200-400 (10 °C/min) 400°C for 10 min	Delamination before ca		
12	H064	3	Powder	50	5	40	3	200-400 (10 °C/min) 400°C for 10 min		Delamination after ca	
13	H065	4	Powder	50	5	40	3	200-400 (10 °C/min) 400°C for 10 min		Delamination after ca	
14	H066	4	Powder	50	5	40	3	200-400 (10 °C/min) 400°C for 10 min	Delamination before ca		
15	H070	4	Powder	50	5	50	3.1	No	Delamination before ca		
16	H077	4	Powder	50	30	Natural	3.1	No			No delamination
17	H078	5	Powder	50	5	Natural	3.1	No			No delamination

- ca: Chemical attack
- Sintering Temperature for all cases: 850°C

■ Delamination before ca
 ■ Delamination after ca
 ■ No delamination

The whole set of tests show that changing the heating rate or adding a debinding step does not provide improvement. Concerning the cooling rate that can affect the driving force for delamination due to constraints, the different attempts do not show any significant differences. No significant improvement obtained either by increasing the sintering time from 5 to 30 minutes. Therefore, sintering conditions are settled on a heating rate of 50 °C/min without debinding step, a sintering time of 5 minutes and natural cooling.

The selected sintering temperature of 850 °C is slightly lower than that optimized for PZT ceramics by SPS (without LBCu) for two reasons: to limit interdiffusion problems as already explained and also because the position of the thermocouple in the configuration 5 used is closer to the sample than when a conventional mold is used.

The form and the nature of protective layer appears as critical parameters that can compromise the integrity of the multilayer after SPS due either to the interaction with PZT or due to the removal process by acid attack. This aspect constitutes one of the strategic lines of optimization and is discussed in detail in the next section.

Even if the optimization of the set-up configuration is essential, this aspect alone is far from sufficient to reach optimized densification of the multilayers. The various tests have clearly shown that the weakest part of the assembly is the interfaces between the PZT and the electrodes (bottom and/or top electrodes) leading to delamination issues. Interdiffusion between the different layers is also a critical parameter highly dependent on the sintering temperature. The close link between temperature, mechanical constraints and chemical reactivity, all related to the nature and thickness of the different components, leads us to explore different ways to further improve the process by SPS through a better control of interfaces.

These strategic lines are described in the next section. For each one, a summary of the most relevant experiments is given. Note that each experiment is repeated at least three times in order to confirm its reproducibility. They are all performed with the set-up configuration 5.

3.5 Strategic lines focused on interface issues

3.5.1. Role of sintering aid: PZT + LBCu as active layer

Experiments with the same multilayers structure as for conventional approach are carried out (SS/Au/PZT+3%wtLBCu/Au), in order to have a system as close as possible to the structure already fabricated in chapter 4 and to test the benefit of the sintering aid LBCu in terms of reduction in sintering temperature. Several samples are densified within a range of sintering temperatures between 700 °C and 800 °C. As previously mentioned (section 2.2), PZT+LBCu ceramics sintered by SPS show high densification within this range of temperature. However, gold electrodes ink are recommended to be fired in the range 850-930 °C with an optimal firing at 850 °C (recommended by the supplier). Considering SPS and ink specifications, a compromise is to settle the sintering temperature at 775 °C. After SPS, the microstructure of the fracture reveals different features (Figure V-28):

- There is an adhesion between the top gold electrode and the PZT layer but the interface is not continuous and some air gaps are clearly visible (Figure V-28 (a)). The presence of LBCu in the active PZT layer seems to improve the adherence between the substrate, the bottom gold electrode and the PZT. Nevertheless, because of different constraint

distribution within the active layer, this seems to cause a weakening of the interface between the PZT and the top electrode

- The PZT layer exhibits a quite homogeneous microstructure in terms of grain size with no evidence of specific grain growth due to the presence of the sintering aid. A gradient of density is observed with in particular the region located close to the electrode interface that seems to be denser. This can be due to a more constrained sintering near the interface (Figure V-28 (a-b)).
- The distribution of the sintering aid is not homogeneous since several Cu-rich grains are dispersed through the active PZT layer (Figure V-28 (b-c)). Note that Cu segregation has not been observed for PZT + LBCu ceramics sintered by SPS.

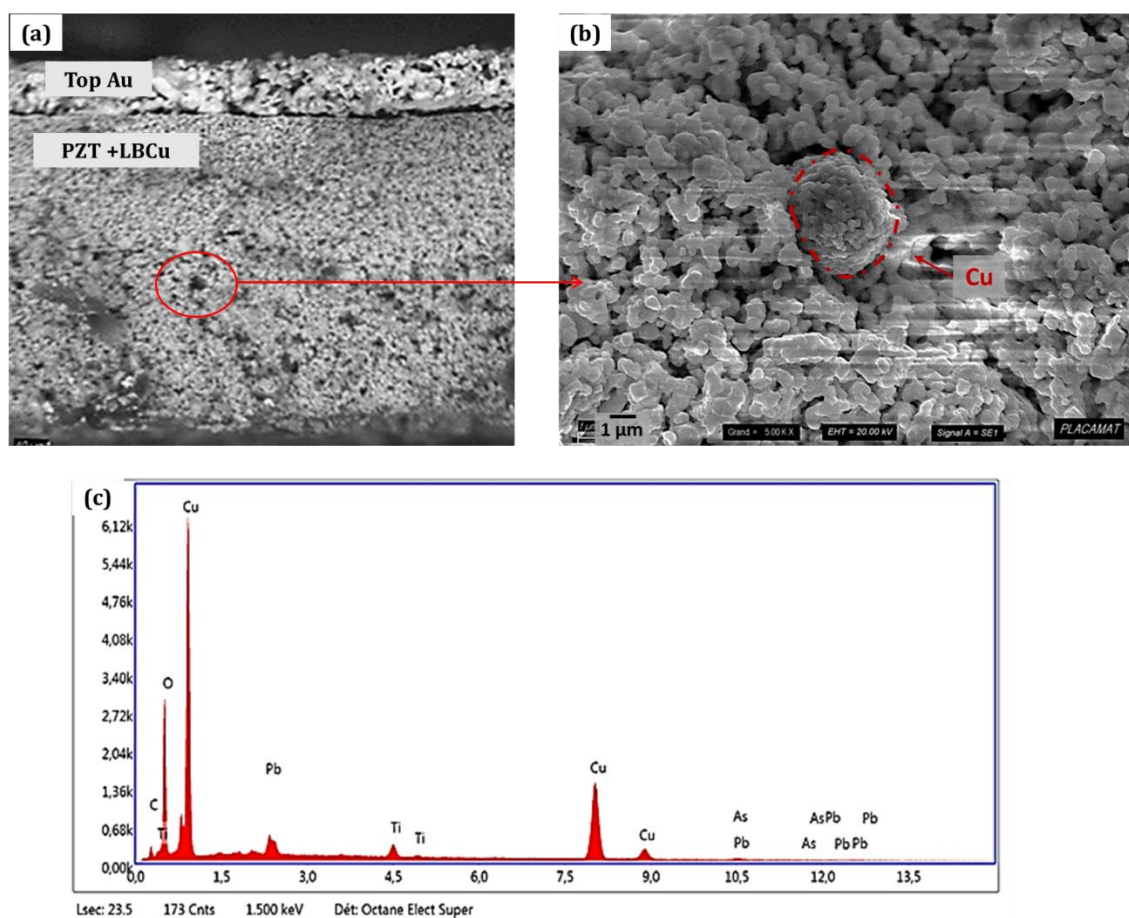


Figure V-28: Microstructure SEM image of PZT + 3%LBCu sintered by SPS at 775 °C. (a) Interface between gold electrode and PZT + 3%wtLBCu, (b) Cu-rich grains and (c) EDX analysis of Cu-rich grains.

The observed discontinuities between gold electrode and PZT and the non-homogeneous distribution of the LBCu (presence of Cu-rich grains) can be detrimental for piezoelectric properties. The weight percentage of sintering aid used (3wt%) has not been optimized for conventional sintering so it is possible that such a value is excessive for SPS resulting in additive segregation detrimental for piezoelectric response. However, Cu segregation is also observed for printed disks conventionally sintered at 900 °C [54]. As shown in literature, the use of lower

content of sintering aid (<1-2 wt.%) leads to PZT grain growth whereas an excessive content of additives inhibits grain growth due to impurities segregation [55]. In addition, the existence of an eutectic with a melting point at 690 °C for the system $\text{Cu}_2\text{O} - \text{PbO}$ [39] could lead to a deviation from PZT stoichiometry if additional PbO is not initially added.

In light of these results, two approaches can be considered to improve the densification and properties of the multilayer, either by decreasing the amount of sintering aid for SPS densification of multilayer or without using LBCu. Considering that PZT ceramics sintered by SPS without sintering aid display excellent properties, the second option has been chosen.

The microstructure of a fracture of the PZT within the multilayer is characterized and compared to the one of the screen-printed PZT thick film conventionally sintered (Figure V-29). Very similar microstructures are obtained. Grain size (with wide size distribution) are comparable ($\sim 1 - 4 \mu\text{m}$) and the level of porosity is in the same range (15-20%) although in the case of SPS, the sintering temperature is slightly lower (850 °C versus 900 °C), and the sintering dwell time significantly shorter (5' instead of 2h). In addition SPS is performed without sintering aid and without preliminary pressure step. Compared to PZT ceramic sintered by SPS, the increase of porosity within the stack can be explained perhaps by a slightly lower sintering temperature but principally by the absence of pressure during SPS sintering of the multilayer.

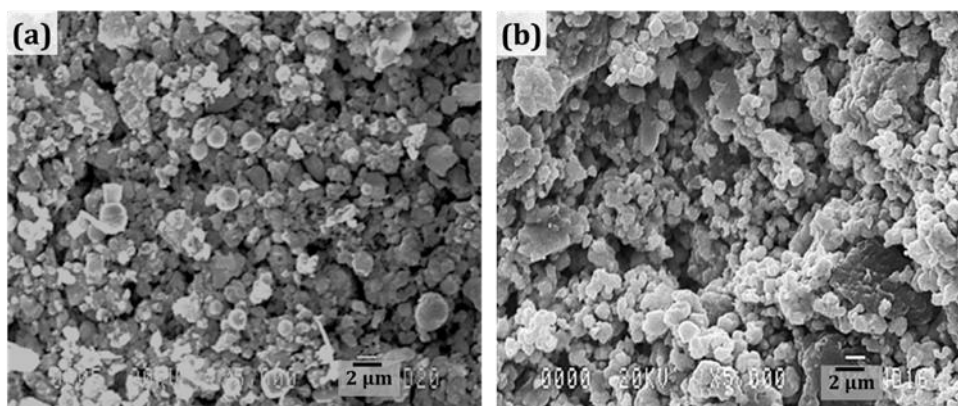


Figure V-29: (a) SEM image of the active PZT layer within the Au/PZT/Au/SS sintered by SPS at 850 °C without sintering aid and, (b) SEM image of screen-printed PZT thick film (900 °C, 2h, sintering aid).

However, even if over all the tests (Table V-6 and additional tests), configuration 5 associated with a sintering temperature of 850 °C appears to be optimal (samples globally appear not damaged), discontinuities (or even delaminations) between the PZT and the top gold electrode can still be observed when the samples are probed at the microscale (Figure V-30). This interface therefore remains a point of fragility.

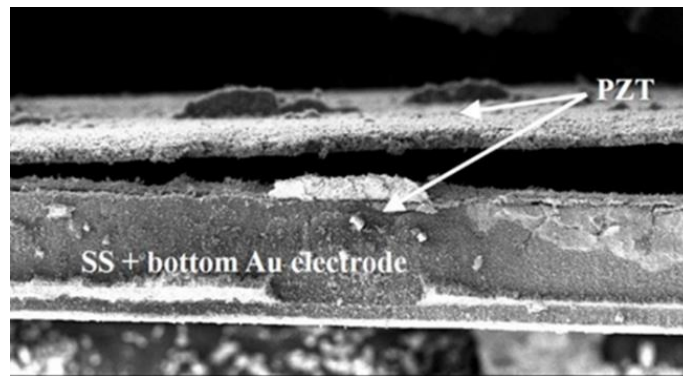


Figure V-30: SEM image showing discontinuities between PZT and top gold electrode after SPS performed at 850 °C.

An additional aspect that can affect the quality of the top gold electrode is the use of the protective layer (directly in contact with the top gold electrode) during sintering and its removal after SPS. This contribution in the optimization of the sintered multilayer is discussed in the next section.

3.5.1 Nature of protective layer

An important characteristic of the approach is the use of a protective layer to avoid post-reoxidation of the PZT based multilayer. It has been previously proved that high densified ceramics with excellent properties can be obtained without an annealing post-SPS step by using SrCO_3 or BaCO_3 as protective layer. For multilayer structures, the selection of the best form of the protective layer (printed layer or powder bed) and its nature (SrCO_3 or BaCO_3) has to be clarified.

As already mentioned, printed protective layer ink is prepared by mixing the powder with the epoxy resin ESL-CV59 as organic binder [32] (Annex 1 (formulation composition)). The advantage is that the epoxy resin is eliminated during sintering (450 °C from TGA analysis) while the remaining mineral part can be removed after SPS by chemical etching with a solution of phosphoric acid (H_3PO_4 10%vol.) following the reaction:



Where M represents either Sr or Ba. This printed layer (thickness approximatively of 30 μm) is deposited all along the multilayer stack covering the whole area. In contrast, powder bed is directly introduced into the system (modified set-up configuration) ensuring the complete coverage of all the multilayer stack.

The ease of removing the protective layer and therefore the quality of the surface of the multilayer depends on its initial form and nature. The following observations can be reported:

- Whatever its nature, protective layer is more difficult to eliminate after sintering when initially printed;

- SrCO_3 is more difficult to remove than BaCO_3 .

Higher reactivity (more intimate contact surface) between the layers of the structures and the carbonate is expected when the carbonate is printed. This effect is observed to be enhanced when LBCu is added to PZT. Contamination is observed on the surface of the sample after chemical attack in particular when using SrCO_3 (Figure V-31 (a, b)). EDX analysis (Figure V-32 (a)) reveals a carbon-rich surface. Therefore reaction with the organic binder of the ink or the carbon felt is not excluded. One difficulty compared to ceramics sintered by SPS using also SrCO_3 is that no polishing of the multilayer surface (to remove surface contamination) is possible without irreversible damages on the top gold electrode. A thermal post-treatment at $650\text{ }^\circ\text{C}$ during 2h is tested to remove contamination, but EDX analysis shows Sr content on the surface of samples (Figure V-32 (b)). This analysis reflects the reactivity of SrCO_3 with the Au electrode (even if SrCO_3 is not expected to decompose below $1100\text{ }^\circ\text{C}$) and is consistent with previous results reporting the presence of strontium in the gold electrode of printed disks sintered with a printed SrCO_3 sacrificial layer [56].

When SrCO_3 protective layer powder is used, surface contamination is lower but whitening is observed on top Au electrode as in previous work [2] (Figure V-31 (d)). When using BaCO_3 protective layer powder, the surface of the sample is not contaminated and the carbonate layer is much more easily removed compared to SrCO_3 (Figure V-31 (e)).

At this stage, the use of BaCO_3 , possibly because of a higher decomposition temperature ($1350\text{ }^\circ\text{C}$) compared to that of SrCO_3 and thus a higher stability in the used SPS conditions, represents the best option to protect the active layer of PZT from chemical reduction and avoid post-thermal treatment (including to remove surface contamination).

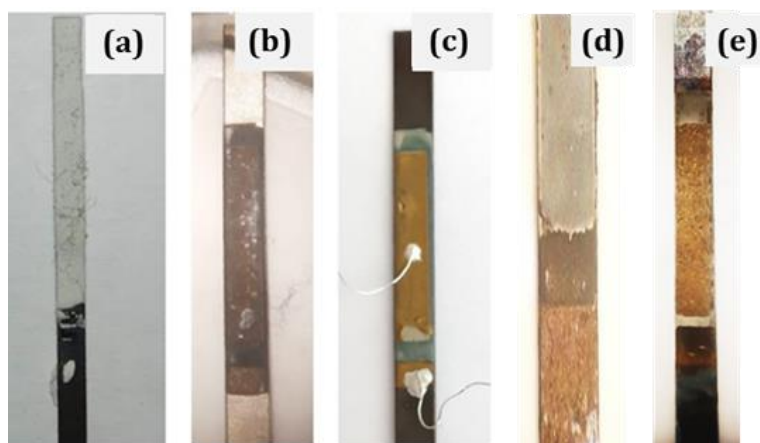


Figure V-31: Comparison of multilayers after SPS using different form and nature of protective layers. (a) Sample with printed SrCO_3 after SPS, (b) after chemical attack with H_3PO_4 showing the appearance of a dark conductive surface, (c), and after post-annealing treatment at $650\text{ }^\circ\text{C}$ during 2h. (d) Powder SrCO_3 protective layer form after chemical attack (whitening on top Au electrode). (e) BaCO_3 in powder form after chemical removal.

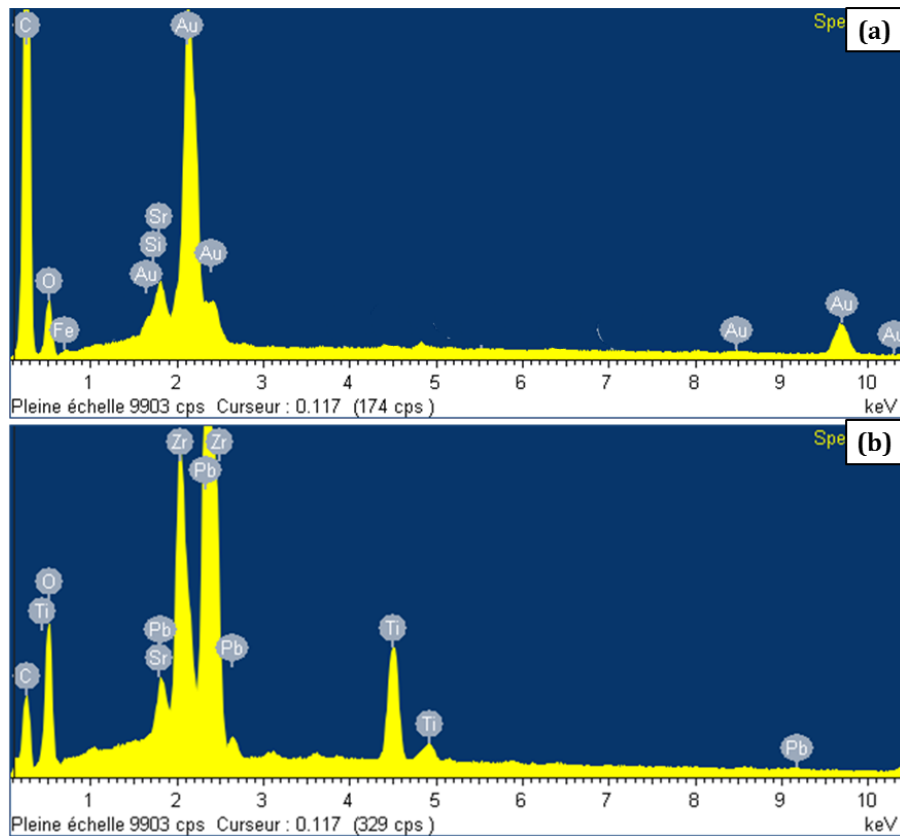


Figure V-32: EDX analysis of samples sintered with printed SrCO_3 protective layer, (a) of Au top gold electrode surface after chemical attack and before post-annealing step, showing a carbon-rich surface and (b) on PZT surface layer after post-annealing step at 650 °C during 2h showing evidence of Sr content afterwards.

Note that SEM observations of the interfaces using the same protocol as in chapter 4 (Cross-polishing) proved unsuitable for these still fragile multilayers. Therefore a detailed analysis of the interfaces to probe in particular the interdiffusion zone between the substrate and the bottom gold electrode has not been possible. Optimization of sample preparation for SEM observations should be implemented.

3.5.2 Substrate thickness

Another option to limit interface issues is to adapt the thicknesses of multilayers constituents. As already proved in chapter 4, high thermal stresses during sintering are the cause of bending and delamination problems in the multilayer structure, arising mainly from the mismatch between thermal expansion coefficients. In chapter 4 this thermal stress has been compensated by reducing the PZT thickness ($\sim 55\mu\text{m}$), but reducing even more this one will directly reduce the performance of the EH. Therefore we choose to modify the substrate thickness not only to limit delamination issues by reducing thermal stresses, but also to target higher deformation during performance of the device. Two different SS301 substrate thicknesses are used: $25\mu\text{m}$ and $100\mu\text{m}$. Samples are fabricated using the same process described in chapter 4 for thick films. The different multilayer structures fabricated are given in Table V-7:

Table V-7: Multilayer configuration fabricated for experiments with lower substrate thickness

Multilayer structure/ Thicknesses	A	B	B'	Original
PZT (μm)	≈ 25	< 50	< 50	≈ 55
Au thickness (Top/Bottom) (μm)	$\approx 3/5$	$\approx 6/10$	$\approx 8/10$	$\approx 8/12$
SS substrate (μm)	25	100	100	250

As observed in Table V-7, PZT thickness is reduced when using thinnest substrates. Gold electrodes thicknesses are also decreased and are non-symmetric as for the original multilayer structure. Indeed, for these first experiments with thinner SS substrates, the screen-printing process settings, especially the substrate holder thickness and the off-contact distance could not be correctly adapted.

Samples are then sintered using a protective layer of BaCO_3 powder. The chemical removal is made without problem or damage of the samples (Figure V-33). A good adhesion of pure PZT layer is observed whatever the thickness of the substrate. In particular the complete multilayer structure (SS/Au/PZT/Au) seems to be intact for multilayer structure A (SS: $25 \mu\text{m}$) (Figure V-33 (a)).

On the other hand, the multilayer corresponding to structure B (SS: $100 \mu\text{m}$), presents more or less damage on the top Au electrode (Figure V-33 (b)). For configuration B' obtained by printing two layers of top Au electrode, damage of the top electrode is still observed (Figure V-33 (c)). These damages of the gold top electrode are attributed to the lack of optimizations of the printing settings with reduced SS substrates (substrate holder height not adequate). As a result the squeegee cannot apply homogeneous pressure during printing and deteriorate the humid layer. However, the obtained results are already promising and demonstrate that by reducing the thickness of the substrate, adhesion problems of pure PZT could be solved.

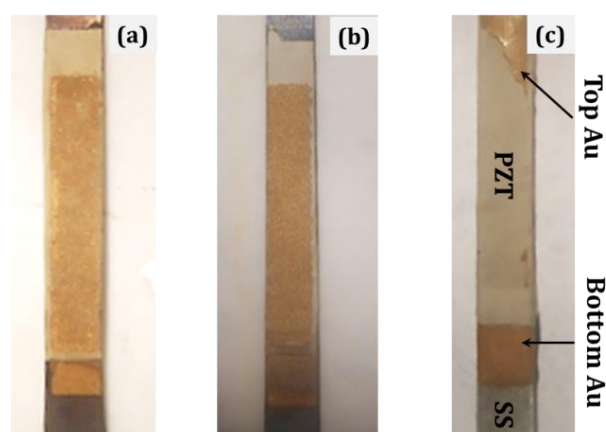


Figure V-33: Results obtained for samples with lower SS substrate thickness. (a) Structure A (SS: $25 \mu\text{m}$), (b) structure B (SS: $100 \mu\text{m}$), and (c) structure B': sample with Au top electrode printed twice.

3.5.3 Nature of electrodes

The last strategic line probed concerns the nature of electrodes. Au electrodes present good chemical compatibility with PZT, but Ag or Ag alloys are more favorable at industrial level (reduced cost). Ag has a great conductivity, but is likely to migrate and this can contribute to a failure of electric properties in PZT films. However the presence of Pd, glass or oxides additives [54] can minimize this effect and can act as sintering aids for PZT inducing a rise in densification and electrical properties at low co-firing temperature. A conductive silver-palladium based ink (AgPd) supplied by Exxelia-Temex company (Pessac, France) has been tested as an alternative to gold ink. This ink has a low proportion of Pd present (10 wt.%) (Table V-8). The mineral additive is an oxide (MgTiO_3) with low permittivity, used in the manufacture of capacitors by Exxelia-Temex. The ink is printed with the same screen as for gold (325 mesh + 15 μm emulsion). First, a single layer is screen printed for the top and bottom electrodes. The layers are thinner than those printed with gold under the same conditions due to the higher proportion of solvent. A double printing of the two electrodes solves the problem, thickness of around 10 μm each are obtained for multilayer structure using 250 μm and 100 μm SS substrates.

Table V-8: Composition of AgPd ink from Exxelia-Temex used.

Metal part	Solvent/ binder	Mineral part
Ag (90 wt.)/Pd (10 wt.)	Aliphatic solvent + cellulosic binder	MgTiO_3
54 wt.%	44 wt.%	2 wt.%

However, experiments performed with 250 μm substrate thickness do not show improvement in adhesion (Figure V-34). Conversely and as expected, samples with 100 μm show good adhesion within the multilayer.

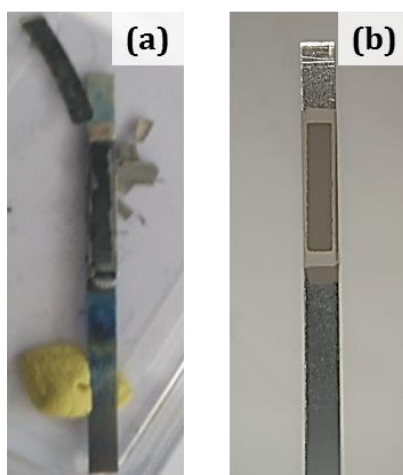


Figure V-34: Samples obtained after SPS using Ag/Pd electrodes (a) on 250 μm substrate thickness, resulting in destroyed samples, and (b) on 100 μm substrate thickness, resulting in samples with good adhesion

3.5.4 Electrical tests

Undamaged samples with seemingly good adhesion between layers are further electrically characterized, when it is possible. Basic tests with a multimeter are first led to ensure (i) the absence of short-circuits between top and gold electrodes and (ii) electrical continuity of the top electrode. Then, when these preliminary tests are positive, a voltage is applied for the polarization step. Table V-9 summarizes these results.

In general the most challenging aspect among samples sintered without sintering aid LBCu (samples from 3 to 6) is the degradation of the top electrode mainly when this layer is too thin. On the other hand, samples sintered with LBCu (samples 1 and 2) do not present any damage of the constituent's layers. Nevertheless, electrical test performed on one of this sample shows that it is a bad dielectric (high leakage current impeding the application of a high voltage), whereas a second similar sample, even after a successful polarization step, doesn't show any visible piezoelectric properties. Therefore, the same conclusion that in the case of ceramics densified by SPS can be made, the presence of sintering aid can be critical for the piezoelectric properties of the multilayer containing PZT+LBCu and sintered by SPS.

Table V-9: Summary of successful samples.

Sample	Nature of PZT and protective layer	Electrode's nature and top thickness	SS substrate's thickness	PZT thickness	Sintering temperature	Short-circuit between top and bottom electrodes	Applied voltage at 280°C, 10min
1	PZT+ 3%wt LBCu /SrCO ₃	Au / 8μm ± 2 μm	250μm	55	775 °C	No	Not possible (high leakage current)
2	PZT + 3%wt LBCu /BaCO ₃	Au /8μm ± 2 μm	250μm	55	775 °C	No	1 kV, 10min, 280 C, under N atmosphere.
3	PZT /BaCO ₃	Au / 3μm ± 1 μm	25μm	25	850 °C	Yes	No
4	PZT /BaCO ₃	Au /6μm ± 2 μm	100μm	50	850 °C	No	No
5	PZT /BaCO ₃	Au /(x 2 prints top electrode) /8μm ± 2 μm	100μm	50	850 °C	No	No
6	PZT/ BaCO ₃	AgPd (x 2 prints) /6 μm ± 2 μm	100μm	50	850°C	No	No

4 Conclusion

Spark Plasma Sintering has been successfully used for the densification of PZT ceramics. A relative density as high as 98% has been obtained at a sintering temperature of 875°C without the use of sintering aid. Compared to conventional process, the sintering temperature is thus decreased by 300-400°C while reaching similar density. Furthermore, the post-annealing step usually performed after SPS to ensure re-oxidation of the sample has been avoided thanks to the use of a carbonate protective layer during SPS. Our first goal to efficiently densify PZT in one step while controlling microstructure and chemistry was thus achieved. As a proof, the corresponding overall dielectric and electromechanical properties (a relative permittivity of 1100 at room temperature and a coupling factor k_{eff} of 36%) have been shown to be comparable to commercial PZT ceramics. These results highlight the benefit of SPS as a low time and energy consuming process.

The impact of sintering aid addition during SPS has also been addressed. If a further decrease of sintering temperature was proved (98% relative density at 750°C), the poor piezoelectric properties obtained using 3%wt LBCu raise possible chemical homogeneity issues. However, in-depth analyses, in particular chemical analysis at the grain boundaries, are necessary to decipher the influence of the LBCu on the microstructure and the related impact on piezoelectric properties.

The second part of this chapter was focused on the transfer and further optimization of SPS conditions towards the co-sintering of the printed PZT based multilayer EH structure.

The challenge was to face the most critical parameters identified in chapter 4, bending and delamination of the different layers. Indeed, the interface metal electrode/active PZT ceramic was shown to withstand high thermo-mechanic stresses that were expected to be enhanced in SPS conditions. The first step of our approach was to adapt the SPS set – up configuration. Both the graphite elements and punches were specifically designed to ensure in particular a uniform application of minimal pressure. Additional lines of optimization were focused on the nature of electrodes, substrate thickness and nature of the protective layer. Even if bending and delamination issues were significantly limited, the integrity of the gold electrode remains critical. The damage of the top electrode led to reduced conductivity and/or short circuits detrimental for piezoelectric properties. The key parameters to solve the problem do not concern only SPS but also the screen-printing process whose optimization could allow to improve the deposition of the electrodes. Finally, the complete approach investigated in this chapter and dedicated to the SPS sintering of EH multilayers is summarized in Figure V-35. This approach, combining both material and processes optimizations, has not only allowed to cope with several issues specific to multilayers but has also demonstrated the potential of Spark Plasma Sintering towards one step elaboration of printed multilayer EH structures.

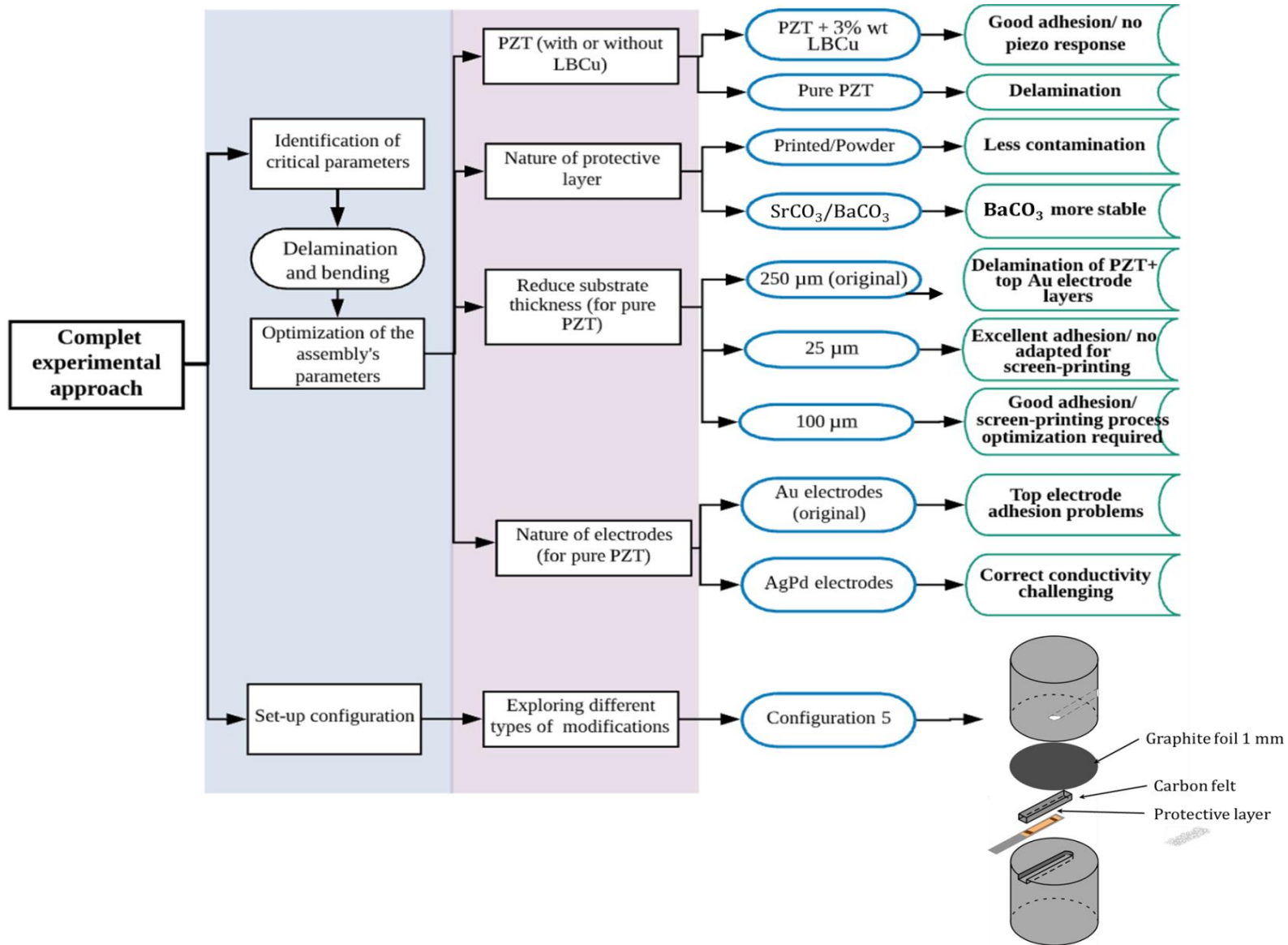


Figure V-35: Complete experimental approach used towards sintering of printed multilayer EH structure

References

- [1] A. Medesi et al. , “Low Temperature Sintering of PZT,” *Artic. J. Phys. Conf. Ser.* , 2014.
- [2] R. Lakhmi, H. Debeda, I. Dufour, C. Lucat, and M. Maglione, “Study of screen-printed PZT cantilevers both self-actuated and self-read-out,” *Int. J. Appl. Ceram. Technol.* , vol. 11, no. 2, pp. 311–320, 2014.
- [3] X. X. Wang, K. Murakami, O. Sugiyama, and S. Kaneko, “Piezoelectric properties, densification behavior and microstructural evolution of low temperature sintered PZT ceramics with sintering aids,” *J. Eur. Ceram. Soc.* , vol. 21, no. 10–11, pp. 1367–1370, 2001.
- [4] N. J. Donnelly, T. R. Shrout, and C. A. Randall, “The role of Li₂CO₃ and PbO in the low-temperature sintering of Sr, K, Nb (SKN)-doped PZT,” *J. Am. Ceram. Soc.* , vol. 92, no. 6, pp. 1203–1207, 2009.
- [5] V. R. Mudinepalli, S. Song, J. Li, and B. S. Murty, “A comparative study of structural and electrical properties of Ba_{0.8}Pb_{0.2}TiO₃ nanocrystalline ceramics prepared by microwave and spark plasma sintering,” *Mater. Chem. Phys.* , vol. 142, no. 2–3, pp. 686–691, 2013.
- [6] V. R. Mudinepalli, S. Song, J. Li, and B. S. Murty, “Effect of grain size on the electrical properties of high dense BPT nanocrystalline ferroelectric ceramics,” *Ceram. Int.* , vol. 40, no. 1 PART B, pp. 1781–1788, 2014.
- [7] S. Song, Q. Song, J. Li, V. R. Mudinepalli, and Z. Zhang, “Characterization of submicrometer-sized NiZn ferrite prepared by spark plasma sintering,” *Ceram. Int.* , vol. 40, no. 5, pp. 6473–6479, 2014.
- [8] S. H. Song, Q. S. Zhu, L. Q. Weng, and V. R. Mudinepalli, “A comparative study of dielectric, ferroelectric and magnetic properties of BiFeO₃ multiferroic ceramics synthesized by conventional and spark plasma sintering techniques,” *J. Eur. Ceram. Soc.* , vol. 35, no. 1, pp. 131–138, 2015.
- [9] Y. J. Wu, R. Kimura, N. Uekawa, K. Kakegawa, and Y. Sasaki, “Spark Plasma Sintering of Transparent PbZrO₃-PbTiO₃-Pb(Zn_{1/3}Nb_{2/3})O₃ Ceramics,” *Jpn. J. Appl. Phys.* , vol. 41, no. Part 2, No. 2B, pp. L219–L221, 2002.
- [10] F. K. Chinen and I. F. Machado, “PZT consolidation by Spark Plasma Sintering (SPS).” , 21st Int. Congr. Mech. Eng. , vol. 1050, 2011.
- [11] B. Han et al. , “Temperature-Insensitive Piezoelectric Performance in Pb(Zr_{0.52}Ti_{0.42}Sn_{0.02}Nb_{0.04})O₃ Ceramics Prepared by Spark Plasma Sintering,” *ACS Appl. Mater. Interfaces*, vol. 9, no. 39, pp. 34078–34084, Oct. 2017.
- [12] D. A. Ochoa, F. Suñol, F. Rubio-Marcos, and J. E. García, “Enhancement of piezoelectric properties stability of submicron-structured piezoceramics obtained by spark plasma sintering,” *J. Eur. Ceram. Soc.* , vol. 38, no. 14, pp. 4659–4663, 2018.
- [13] C. Chen, R. Liang, Z. Zhou, W. Zhang, and X. Dong, “Enhanced bipolar fatigue resistance in PMN-PZT ceramics prepared by spark plasma sintering,” *Ceram. Int.* , vol. 44, no. 4, pp. 3563–3570, 2018.
- [14] L. -Q. Cheng et al. , “Significantly improved piezoelectric performance of PZT-PMnN ceramics prepared by spark plasma sintering,” *RSC Adv.* , vol. 8, no. 62, pp. 35594–35599, 2018.
- [15] R. V. Mudinepalli and F. Leng, “Dielectric and Ferroelectric Studies on High Dense Pb(Zr_{0.52}Ti_{0.48})O₃ Nanocrystalline Ceramics by High Energy Ball Milling and Spark Plasma Sintering,” *Ceramics* , vol. 2, no. 1. 2019.

- [16] Y. J. Wu, N. Uekawa, K. Kakegawa, and Y. Sasaki, "Compositional fluctuation and dielectric properties of $\text{Pb}(\text{Zr}_{0.3}\text{Ti}_{0.7})\text{O}_3$ ceramics prepared by spark plasma sintering," *Mater. Lett.*, vol. 57, no. 3, pp. 771–775, 2002.
- [17] Y. J. Wu, J. Li, X. M. Chen, R. Kimura, and K. Kakegawa, "Effects of La_2O_3 addition and PbO excess on the transmittance of $\text{PbZrO}_3\text{-PbTiO}_3\text{-Pb}(\text{Zn}_{1/3}\text{Nb}_{2/3})\text{O}_3$ ceramics by spark plasma sintering," *J. Am. Ceram. Soc.*, vol. 91, no. 1, pp. 13–16, 2008.
- [18] Y. J. Wu, J. Li, R. Kimura, N. Uekawa, and K. Kakegawa, "Effects of preparation conditions on the structural and optical properties of spark plasma-sintered PLZT (8/65/35) ceramics," *J. Am. Ceram. Soc.*, vol. 88, no. 12, pp. 3327–3331, 2005.
- [19] K. Chen, C. Li, X. Zhang, and Y. Huang, "Microstructure and electrical properties of $0.7\text{Pb}(\text{Mg}_{1/3}\text{Nb}_{2/3})\text{O}_3\text{-}0.3\text{PbTiO}_3$ ceramics by spark plasma sintering," *Mater. Lett.*, vol. 57, no. 1, pp. 20–23, 2002.
- [20] J. -K. Park, U. -J. Chung, N. M. Hwang, and D. Kim, "Preparation of Dense Lead Magnesium Niobate–Lead Titanate ($\text{Pb}(\text{Mg}_{1/3}\text{Nb}_{2/3})\text{O}_3\text{-PbTiO}_3$) Ceramics by Spark Plasma Sintering," *Society*, vol. 59, pp. 3057–3059, 2001.
- [21] L. Zhou, Z. Zhao, A. Zimmermann, F. Aldinger, and M. Nygren, "Preparation and properties of lead zirconate stannate titanate sintered by spark plasma sintering," *J. Am. Ceram. Soc.*, vol. 87, no. 4, pp. 606–611, 2004.
- [22] L. Zhou, G. Rixecker, F. Aldinger, R. Zuo, and Z. Zhao, "Electric fatigue in ferroelectric lead zirconate stannate titanate ceramics prepared by spark plasma sintering," *J. Am. Ceram. Soc.*, vol. 89, no. 12, pp. 3868–3870, 2006.
- [23] T. Takeuchi, M. Tabuchi, I. Kondoh, N. Tamari, and H. Kageyama, "Synthesis of Dense Lead Titanate Ceramics with Submicrometer Grains by Spark Plasma Sintering," *J. Am. Ceram. Soc.*, vol. 83, no. 3, pp. 541–544, 2004.
- [24] J. Rödel, K. G. Webber, R. Dittmer, W. Jo, M. Kimura, and D. Damjanovic, "Transferring lead-free piezoelectric ceramics into application," *J. Eur. Ceram. Soc.*, vol. 35, no. 6, pp. 1659–1681, 2015.
- [25] J. Koruza, A. J. Bell, T. Frömling, K. G. Webber, K. Wang, and J. Rödel, "Requirements for the transfer of lead-free piezoceramics into application," *J. Mater.*, vol. 4, no. 1, pp. 13–26, 2018.
- [26] D. Damjanovic, "Ferroelectric, dielectric and piezoelectric properties of ferroelectric thin films and ceramics," *Reports Prog. Phys.*, vol. 61, no. 9, pp. 1267–1324, 1998.
- [27] M. Legallais, "Conception , étude et modélisation d ' une nouvelle génération de transistors à nanofils de silicium pour applications biocapteurs To cite this version : HAL Id: tel-01745520 Conception , étude et modélisation d ' une nouvelle génération de transistors à," 2018.
- [28] S. Grasso, Y. Sakka, and G. Maizza, "Electric current activated/assisted sintering (ECAS): a review of patents 1906-2008," *Sci. Technol. Adv. Mater.*, vol. 10, no. 5, p. 53001, Nov. 2009.
- [29] C. Elissalde et al. , "Innovative architectures in ferroelectric multi-materials: Chemistry, interfaces and strain," *J. Adv. Dielectr.*, vol. 05, no. 02, p. 1530001, Jun. 2015.
- [30] A. Mercier, "Contribution à l'étude et à la réalisation de composants magnétiques monolithiques réalisés par PECS/SPS et à leurs applications en électronique de puissance," 2016.
- [31] H. Debéda, P. Clément, E. Llobet, and C. Lucat, "One-step firing for electroded PZT thick films applied to MEMS," *Smart Mater. Struct.*, vol. 24, no. 2, 2015.
- [32] P. GINET, "Conception et élaboration de microstructures en technologie hybride couche

- épaisse pour des applications MEMS," 2013.
- [33] Meggit Sensing Systems, "Pz26 (Navy I) Hard relaxor type PZT," Pz26 (Navy I) Ferroperm. [Online]. Available: /www.meggitferroperm.com.
- [34] S. Wagner et al. , "Effect of temperature on grain size, phase composition, and electrical properties in the relaxor-ferroelectric-system $\text{Pb}(\text{Ni}_{1/3}\text{Nb}_{2/3})\text{O}_{3-\text{Pb}}(\text{Zr,Ti})\text{O}_3$," *J. Appl. Phys.* , vol. 98, no. 2, 2005.
- [35] S. Cheng, I. K. Lloyd, and M. Kahn, "Modification of Surface Texture by Grinding and Polishing Lead Zirconate Titanate Ceramics," *J. Am. Ceram. Soc.* , vol. 75, no. 8, pp. 2293–2296, 1992.
- [36] E. V. Barabanova, O. V. Malyshkina, and G. M. Akbaeva, "Structural features of ceramics based on PZT," *Ferroelectrics*, vol. 513, no. 1, pp. 22–26, Jun. 2017.
- [37] X. P. Li, W. Y. Shih, J. S. Vartuli, D. L. Milius, I. A. Aksay, and W. H. Shih, "Effect of a transverse tensile stress on the electric-field-induced domain reorientation in soft PZT: In situ XRD study," *J. Am. Ceram. Soc.* , vol. 85, pp. 844–850, Apr. 2002.
- [38] T. Molla and H. Lund, "Modeling Macroscopic Shape Distortions during Sintering of Multilayers," Technical University of Denmark, 2014.
- [39] D. L. Corker, R. W. Whatmore, E. Ringgaard, and W. W. Wolny, "Liquid-Phase Sintering of PZT Ceramics," *J. Eur. Ceram. Soc.* , vol. 20, pp. 2039–2045, Nov. 2000.
- [40] Z. A. Munir, U. Anselmi-Tamburini, and M. Ohyanagi, "The effect of electric field and pressure on the synthesis and consolidation of materials: A review of the spark plasma sintering method," *Journal of Materials Science*, vol. 41, no. 3, pp. 763–777, Feb-2006.
- [41] J. E. Garay, U. Anselmi-Tamburini, and Z. A. Munir, "Enhanced growth of intermetallic phases in the Ni-Ti system by current effects," *Acta Mater.* , vol. 51, no. 15, pp. 4487–4495, Sep. 2003.
- [42] W. Chen, U. Anselmi-Tamburini, J. E. Garay, J. R. Groza, and Z. A. Munir, "Fundamental investigations on the spark plasma sintering/synthesis process: I. Effect of dc pulsing on reactivity," *Mater. Sci. Eng. A*, vol. 394, no. 1–2, pp. 132–138, Mar. 2005.
- [43] M. Tokita, "Development of Large-Size Ceramic/Metal Bulk FGM Fabricated by Spark Plasma Sintering," *Mater. Sci. Forum*, vol. 308–311, pp. 83–88, May 1999.
- [44] T. Fujii, K. Tohgo, M. Iwao, and Y. Shimamura, "Fabrication of alumina-titanium composites by spark plasma sintering and their mechanical properties," *J. Alloys Compd.* , vol. 744, pp. 759–768, May 2018.
- [45] M. Bahraminasab, S. Ghaffari, and H. Eslami-Shahed, "Al₂O₃-Ti functionally graded material prepared by spark plasma sintering for orthopaedic applications. ," *J. Mech. Behav. Biomed. Mater.* , vol. 72, pp. 82–89, 2017.
- [46] C. Madec, S. Le Gallet, B. Salesse, N. Geoffroy, and F. Bernard, "Alumina-titanium functionally graded composites produced by spark plasma sintering," *J. Mater. Process. Technol.* , vol. 254, pp. 277–282, Apr. 2018.
- [47] V. Issindou, B. Viala, L. Gimeno, O. Cugat, C. Rado, and S. Bouat, "Fabrication methods for high-performance miniature disks of Terfenol-D for energy harvesting," *Sensors Actuators, A Phys.* , vol. 284, pp. 1–5, Dec. 2018.
- [48] F. MH, W. P, W. RG, C. ZZ, J. C, and L. H, "Fabrication of Cu/PZT functionally graded actuators by spark plasma sintering," *Mater. Sci. Forum*, vol. 423–4, pp. 423–426, 2003.
- [49] M. H. Fang, W. Pan, R. G. Wang, Z. Z. Cao, J. Chen, and L. K. Hou, "Fabrication of Cu/PZT Functionally Graded Actuators by Spark Plasma Sintering," *Mater. Sci. Forum*, vol. 423–425, pp. 423–426, May 2003.
- [50] D. Giuntini, X. Wei, A. L. Maximenko, L. Wei, A. M. Ilyina, and E. A. Olevsky, "Initial stage of

- Free Pressureless Spark-Plasma Sintering of vanadium carbide: Determination of surface diffusion parameters," *Int. J. Refract. Met. Hard Mater.* , vol. 41, pp. 501–506, Nov. 2013.
- [51] D. V. Dudina, B. B. Bokhonov, and E. A. Olevsky, "Fabrication of porous materials by spark plasma sintering: A review," *Materials*, vol. 12, no. 3. MDPI AG, 12-Feb-2019.
- [52] U. Anselmi-Tamburini, J. E. Garay, and Z. A. Munir, "Fast low-temperature consolidation of bulk nanometric ceramic materials," *Scr. Mater.* , vol. 54, no. 5, pp. 823–828, Mar. 2006.
- [53] C. Manière, L. Durand, A. Weibel, G. Chevallier, and C. Estournès, "A sacrificial material approach for spark plasma sintering of complex shapes," *Scr. Mater.* , vol. 124, pp. 126–128, Nov. 2016.
- [54] O. Santawiteea, S. Grall, C. Chayasombath, Bralee; Thanachayanontb, X. Hochartc, J. Bernardd, and H. Debédaa, "Electrode materials effect on processing and electromechanical properties of printed PZT-based microdisks," to Appear *Electroceramics*, 2019.
- [55] K. H. Chung et al. , Effects of Li_2CO_3 and Bi_2O_3 additives on sintering temperature and piezoelectric properties of PNIN-PCW-PZT ceramics for multilayer piezoelectric transformer, vol. 14. 2004.
- [56] H. Debéda, C. Lucat, M. Maglione, V. Pommier-Budinger, X. Hochart, and W. Sourbe, "Feasibility of Screen-Printed PZT Microceramics for Structural Health Monitoring Applications," *Int. J. Appl. Ceram. Technol.* , vol. 11, no. 3, pp. 413–421, May 2014.

General conclusion

Energy harvesting offers significant advantages and opportunities for the development of a wide range of smart applications (smart cities, smart homes, smart health, smart agriculture, intelligent transportation, industry, security, marine, etc). Indeed, the increasing use of autonomous electronic devices faces the issue of energy autonomy. Among the possible options, the recovery of vibratory mechanical energy using piezoelectric transducers is one of the most promising alternatives because of the availability of mechanical vibrations and the simplicity of electromechanical piezoelectric conversion.

In this context, this thesis work was dedicated to the study and fabrication of piezoelectric Micro Electro-Mechanical Systems (MEMS), aiming a resonant mechanical energy harvester (frequency < 100 Hz) for the supply of autonomous systems.

A literature survey of the various types of energy harvester configurations, related piezoelectric materials and fabrication techniques, has highlighted some of the challenging issues relative to the enhancement of the power output and broadening of the working frequency bandwidth. Our approach to address these challenges was based on the optimization of the EH design and the improvement of the active piezoelectric material properties.

The fabrication of the piezoelectric MEMS by screen-printing has been described in detail to highlight all the experimental parameters whose optimization is required to target efficient final device. Two different structures, a simple cantilever and a modified zig-zag geometry, have been successfully fabricated by screen-printing and co-firing of multilayers made of $\text{Pb}(\text{ZrTi})\text{O}_3$ (PZT) as the active piezoelectric material, sandwiched between two gold electrodes and deposited on a stainless steel (SS) substrate. This confirms the capabilities and the potential of the thick film screen printing technique to design complex geometries.

The densification by conventional sintering has been achieved at 900°C with the use of the LBCu sintering aid. Compared to bulk ceramics, the main limiting features of the multilayer EH structures are the interfaces and the bending issues. The SS passive substrate generates constrained sintering that hinders an optimal densification (about 20% of residual porosity). The bending of the structure arises from high thermal stresses during sintering due to TEC mismatch between the different constituents. Nevertheless, both modeling and experimental approaches have demonstrated and confirmed that decreasing the PZT layer or SS is as an efficient way to reduce these thermal stresses. A suitable substrate/PZT thickness ratio must be carefully selected to ensure low thermal stresses by maintaining a right output power. At the microscale, the microstructural analysis of the interfaces within the cantilever has shown the formation of an interphase layer that ensures the cohesion between the electrode and the substrate but that could also limit the dynamics of the structure.

The simple cantilever structure exhibits a maximum power output of $1.3\mu\text{W}$ (load resistance $2.64\text{ M}\Omega$) at 129 Hz and a normalized power density of $0.86\ \mu\text{W}/\text{g}^2\cdot\text{mm}^3$, which is too low for any application implementation. Some perspectives for performance improvement, such as thickness optimization, tip mass use, and bimorph cantilever structure type, are several options for future investigations.

The zig-zag geometry developed in collaboration with the University of Waterloo in Canada and dedicated to smart grid technologies has also been tested. It operates on the basis of a coupling between piezoelectric and electromagnetic effects, with the integration of a magnet and the interaction of an electromagnetic field around an alternating current (AC) carrier wire. For a magnet placed at the end of the structure, a current of 7 A and a wire-magnet distance of 6.5 mm,

a resonance frequency of 60Hz has been obtained with an output power of 9 μ W (load resistance 1 M Ω). Compared to other piezoelectromagnetic devices in the MEMS-based literature, the normalized power density is significantly improved. Electronics associated with this device has also valorized this microsystem (developed at UW).

Although the performance of the EH has been validated, the identified weak points are the non-optimal densification of the active layer of PZT (density \approx 82%) and the control of interfaces within the multilayer. The limitation of the number of steps in the fabrication is also a concern that is added to the specifications towards the optimization of the whole process.

Thus, in order to be able to achieve all or some of these objectives, the second part of this thesis work was focused on the SPS process. The implementation of SPS has been made in a two-step approach. First, an optimization of the various SPS parameters (temperature, pressure, duration and heating rate) has been carried out for the densification of commercial PZT powders. Optimal SPS conditions have been determined and ceramics with relative density as high as 98% have been obtained at temperatures as low as 875°C, without sintering aid. Compared to conventional sintering of PZT, this represents a decrease of sintering temperature of more than 300°C. In addition, the original use of a protective carbonate layer to prevent the PZT from chemical reduction during sintering has allowed to avoid a post-SPS heat treatment. The electromechanical properties close to those of PZT's commercial ceramics attest to the effectiveness of SPS and the relevance of our approach. Successful one-step SPS sintering with a short cycle represents a significant energy saving.

A further decrease of the SPS sintering temperature has been reached when using LBCu sintering aid but at the expense of piezoelectric performances of the ceramics. Compared to conventional sintering, the fast kinetics of SPS seems to not guaranty the chemical homogeneity required for properties improvement. However in-depth microstructural analyses are required to clearly understand this point.

The second step was dedicated to the most challenging aspect i.e the implementation of SPS for Au/PZT/Au/SS screen-printed multilayer structures. The main locks identified are the porosity of the active PZT layer, interface issues leading to interdiffusion between layers, delamination or curvature of the cantilever. To address these issues, both the design of the SPS set-up and the features (thickness, nature, protective layer) of each material constituting the multilayer have been optimized. Various tests have led to an optimized SPS set-up configuration with specifically designed punches and graphite elements. The selected configuration ensures a uniform application of minimal pressure to avoid damages of the samples. From the material point of view, the most promising optimization lines were shown to be the reduction of the substrate thickness and the use of BaCO₃ instead of SrCO₃ as a protective layer. Once again, the benefit of sintering aid regarding the decrease of sintering temperature (and thus reduced thermal constraints) was shown to be at the expense of the chemical homogeneity of the PZT layer. In particular copper segregation arising from the LBCu sintering aid was evidenced.

Thanks to the different optimizations, it appears that bending and delamination issues can be significantly reduced and robust multilayers can be obtained even after removal of the protective layer. However, the integrity of the gold electrode remains critical. The damage of the top electrode led to reduced conductivity detrimental for piezoelectric polarization. The key parameters to solve the problem do not concern only SPS but also the screen-printing process

whose optimization could allow to improve the quality of the top electrode deposit. As a result, dielectric and electromechanical performances would be properly evaluated.

Finally, the complete investigated approach, combining both material and process optimizations, has not only allowed to cope with several issues specific to multilayers but has also demonstrated the potential of Spark Plasma Sintering towards one step elaboration of printed multilayer EH structures.

Some perspectives of this thesis work are:

- Optimization of the content of sintering aid (decrease the wt% LBCu) for densification of PZT or PZT based structure by SPS sintering could solve issues related to chemical homogeneity. Thus, the decrease in temperature thanks to the sintering aid would reduce thermal constraints and thus solve some delamination problems.
- Optimization of screen-printing parameters for the deposit of specific thickness of electrodes when using thin stainless substrates. A more robust top electrode would be expected.
- Further optimization of the SPS set-up to implement slighter higher applied pressure on the multilayer to improve adhesion between the layers
- The use of bimorph structure to improve power density while equilibrating thermal stresses.

Annexes

Annexes Chapter II

1. Polymer silver conductor ESL1901 used for screen fiducials



ESL ELECTRO-SCIENCE

CERAMIC TAPES &
THICK-FILM MATERIALS

416 EAST CHURCH ROAD
KING OF PRUSSIA, PA 19406-2625 USA

T: 610.272.8000
F: 610.272.6759

www.electroscience.com

POLYMER SILVER CONDUCTOR

19101

RoHS Compliant* High Temperature Conductor

ESL 19101 is a high-temperature, low-resistivity silver polymer conductor, that provides very good adhesion and thermal stability. It is designed for use as conductor traces and resistor terminations. This paste can be blended with ESL 15501 Resistor Paste to achieve intermediate resistance values on glass, ceramic and polyimide film substrates. ESL 19101 can also be used on ESL 14401 and 14402-A and 14404 polymer dielectric on metal substrates.

Please review the Application Note: Polyimide Thick Film Materials before using this product.

PASTE DATA

RHEOLOGY:	Thixotropic, screen-printable paste
VISCOSITY: (Brookfield RVT, ABZ spindle, 10 rpm, 25.5°C ± 0.5°C)	100 ± 10 Pa·s
SHELF LIFE: (at 0°C)	3 months
(at -18°C)	12 months

PROCESSING

SCREEN MESH / EMULSION:	200 / 20-30 μm
LEVELING TIME: (25°C)	5-10 minutes
DRYING at 125°C:	10-15 minutes
CURING CYCLE:	320°C / 150 minutes (10-15°C/min. rise)
SUBSTRATE OF CALIBRATION:	glass
THINNER	ESL 455

19101 1401-B

ESL Affiliates

ESL China • Room#2712 • Far East International Plaza • No.317 Xianxia Road, • Changning District • Shanghai, China 200051 • Tel: +86-21-6237-0336 • Fax: +86-21-6237-0338 • eslchina@eslshanghai.net

ESL Europe • 8 Commercial Road • Reading, Berkshire, England RG2 0QZ • Tel: +44-118-918-2400 • Fax: +44-118-986-7331 • sales@esleurope.co.uk

ESL in Korea • AMT • South Korea • Tel: +82-31-466-0651 • Fax: +82-31-466-0658 • yunikim@esl-amt.co.kr

ESL-Nippon • Sukeyama Bldg 6th floor • 1-3-4 Yanagibashi • Taito-ku • Tokyo, Japan 111-0052 • Tel: +81-3-3864-8521 • Fax: +81-3-3864-9270 • sales@esl-nippon.co.jp

ESL Taiwan • 14F, No. 168, Dunhua N. Road • Sungshan District • Taipei 105, Taiwan • Tel: +886-975-553-612 • dshih@esl-taipei.com

See Caution and Disclaimer on other side.

2. Dielectric ink ESL4924 used for substrate holder fiducials



ESL ELECTRO-SCIENCE

CERAMIC TAPES &
THICK-FILM MATERIALS

416 EAST CHURCH ROAD
KING OF PRUSSIA, PA 19406-2625 USA

T: 610.272.8000
F: 610.272.6759

www.electroscience.com

INSULATING COMPOSITION

4924

HOS Heaters on Steel® • COS Circuits on Steel® • TFOS Thick Film on Steel®

Cadmium, Lead, Nickel and Barium-Free*

ESL 4924 is a dielectric composition designed to insulate unabraded, unoxidized, ferritic steels. The 4924 is non-porous and its TCE closely matches that of BS970/1449 Type 430-S17 or AISI Type 430 stainless steel. Three separately fired layers of 4924, having a total minimum thickness of 80 micrometers, provide excellent breakdown voltage between top conductive prints and the stainless steel base. It is essential that the stainless steel is only handled using protective gloves and that all printing is carried out in clean room conditions. With ESL 9695 or 9501-CH terminations and 29XXX Series resistors used as heating elements 4924 is recommended as an 850°C firing overglaze. These materials are also useful in other TFOS (Thick Film on Steel)® applications.

PASTE DATA

RHEOLOGY:	Thixotropic, screen printable paste
VISCOSITY: (Brookfield RVT, ABZ Spindle, 10 rpm, 25.5°C ± 0.5°C)	120 ± 20 Pa·s
COLOR:	Dark blue
SHELF LIFE: (25 °C)	6 months

PROCESSING

SCREEN MESH/EMULSION:	165 S/S, 0.0 µm
LEVELING TIME:	5-10 minutes
DRYING AT 125 °C: (Depending upon substrate volume)	> 15 minutes
FIRING TEMPERATURE:	850 °C to 930 °C
OPTIMUM:	850 °C
TIME AT PEAK:	10 minutes

4924 0412-C

ESL Affiliates

ESL China • Rm#1707, Tower A • City Center of Shanghai • 100 Zunyi Road • Shanghai, China 200051 Tel: (011-86)-21-62370336 • Fax: (011-86)-21-62370338 • eslchina@guomai.sh.cn

ESL Europe • 8 Commercial Road • Reading, Berkshire, England RG2 0QZ • Tel: (011-44)-118-918-2400 • Fax: (011-44)-118-986-7331 • Sales@ESLEurope.co.uk

ESL Nippon • Sukegawa Bldg • 6th floor • 3-4 Yanagibashi 1-chome • Taiho-ku • Tokyo 111, Japan • Tel: (011-81)-3-3864-8521 • Fax: (011-81)-3-3864-9270 • Sales@ESL-Nippon.co.jp

See Caution and Disclaimer on other side.

SUBSTRATE FOR CALIBRATION: Unabraded, unoxidized 430 S17 stainless steel
122.5 mm diameter x 1.2 mm

THINNER: ESL 401

TYPICAL PROPERTIES

FIRED THICKNESS:
(At least 3 layers between 9695 and 430 S 17 stainless steel, measured using an Elcometer 345 thickness gauge) > 80 μm

BREAKDOWN VOLTAGE:
(Measured on an 88 mm diameter 9695 print on a 108 mm diameter area of dielectric at 25 °C in air, using a standard Clare Flash Tester) >1800 VAC

APPROXIMATE COVERAGE: (80 μm thickness) 40 cm²/g

INSULATION RESISTANCE:
(Measured on an 88 mm diameter 9695 print on a 108 mm diameter area of dielectric using 500 VDC at 25 °C in air)

After storage at 93 % ± 2 % RH, 25 °C ± 2 °C for 48 hours > 10⁹ Ω

At 300 °C > 10⁹ Ω

A wide range of ESL materials are compatible with 4924 permitting the fabrication of other COS (Circuits on Steel)[®].

Annexes Chapter III

1. Estimation of the values of the equivalent circuit elements

Based on the proposed equivalent circuit for a piezoelectric resonator, the behavior of the conductance G and the susceptance B can be determined as a function of frequency. Indeed, complex admittance Y (inverse of impedance) can be described as following:

$$Y = G + jB = \frac{1}{R_0} + jC_0\omega + \frac{1}{R_m + jL_m\omega + \frac{1}{jC_m\omega}}$$

$$= \frac{1}{R_0} + jC_0\omega + \frac{R_m - j\left(L_m\omega - \frac{1}{C_m\omega}\right)}{R_m^2 + \left(L_m\omega - \frac{1}{C_m\omega}\right)^2} \quad (\text{Eq. A-1.1})$$

If $a = L_m\omega - \frac{1}{C_m\omega}$, then:

$$Y = \frac{1}{R_0} + \frac{R_m}{R_m^2 + a^2} + j\left(C_0\omega - \frac{a}{R_m^2 + a^2}\right) \quad (\text{Eq. A-1.2})$$

The conductance G and the susceptance B can be then be identified from Eq. 3.12, obtaining:

$$G = \frac{1}{R_0} + \frac{R_m}{R_m^2 + a^2} \quad (\text{Eq. A-1.3})$$

$$B = C_0\omega - \frac{a}{R_m^2 + a^2} \quad (\text{Eq. A-1.4})$$

With $\omega = 2\pi f$ and considering the behavior in function of the frequency, $G(f)$ can be described as:

When $f \rightarrow 0_+$

$$\lim(a) = \frac{-1}{2\pi f C_m} \text{ and } \lim(G) = \frac{1}{R_0} + 4\pi^2 R_m C_m^2 f^2 = \frac{1}{R_0} + 0_+ \quad (\text{Eq. A-1.5})$$

When $f \rightarrow +\infty$

$$\lim(a) = 2\pi L_m f \text{ and } \lim(G) = \frac{1}{R_0} + \frac{R_m}{4\pi^2 L_m^2 f^2} = \frac{1}{R_0} + 0_+ \quad (\text{Eq. A-1.6})$$

Hence $G(f)$ presents vertical asymptotes at $G= 1/R_0$, and a maximum when $a=0$,t then becomes:

$$2\pi L_m f_r = \frac{1}{2\pi C_m f_r} \rightarrow f_r^2 = \frac{1}{4\pi^2 L_m C_m} \quad (\text{Eq. A-1.7})$$

The solution to Eq. A-1.7 results in:

$$f_r = \frac{1}{2\pi\sqrt{L_m C_m}} \quad (\text{Eq. A-1.8})$$

At the resonance frequency G and B take the following values:

$$G = G_{max}(f_r) = \frac{1}{R_0} + \frac{1}{R_m} \quad (\text{Eq. A-1.9})$$

$$B = B(f_r) = \frac{C_0}{\sqrt{LC}} \quad (\text{Eq. A-1.0})$$

In the same way from Eq. 3.14 $B(f)$ can be described as:

When $f \rightarrow 0_+$

$$\lim(B) = 2\pi C_0 f + \frac{\frac{1}{2\pi C_m f}}{R_m^2 + \frac{1}{4\pi^2 C_m^2 f^2}} = 0_+ \quad (\text{Eq. A-1.11})$$

When $f \rightarrow +\infty$

$$\lim(B) = 2\pi C_0 f - \frac{2\pi L_m f}{R_m^2 + 4\pi^2 L_m^2 f^2} = 2\pi C_0 f \quad (\text{Eq.A-1.12})$$

When the frequency tends to ∞ , B and G values diminish which represents the behavior of a capacitor without piezoelectric effect (Figure III-1-A).

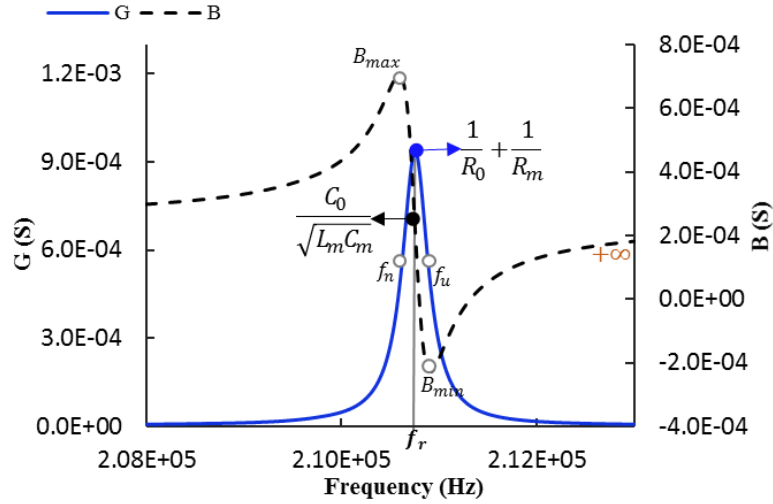


Figure III-A- 1: Conductance G and susceptance B as function of the frequency. Special points (G_{max} , B_{max} , B_{min} , f_n and f_u) are represented, allowing extraction of R_m , C_m and L_m . The frequencies f_n and f_u are defined at $G = G_{max}/2$ and correspond to the bandwidth at -3dB or $|Y| = |Y|_{max}/\sqrt{2}$

G and B represent also an admittance circle $B = f(G)$ (Figure III-A-2). If we consider an angle θ as the intersection of any extremity of a ratio line of the circle with the horizontal axis, then the coordinate's notation is:

$B = B_0 + r \sin \theta$, with $\theta = \pm \arccos(G - G_0)/r$, r the ratio of the admittance circle equal to $(1/2R_m)$, B_0 the coordinate of the circle center and G_0 its abscissa equal to $(1/R_0 + 1/R_m)$. Assuming a variable change: $u = G - (1/R_0)$, with $u = 1/2R_m$ then G :

$$\frac{1}{2R_m} = \frac{R_m}{R_m^2 + a^2} \rightarrow R_m^2 = a^2 \rightarrow a = \pm R_m \rightarrow L_m \omega - \frac{1}{C_m \omega} = \pm R_m \quad (\text{Eq. A-1.13})$$

The possible solutions of Eq. A-1.13 are:

$$\omega^+ = \frac{R_m}{2L_m} + \sqrt{\frac{R_m^2}{4L_m^2} + \frac{1}{L_m C_m}} \text{ and } \omega^- = -\frac{R_m}{2L_m} + \sqrt{\frac{R_m^2}{4L_m^2} + \frac{1}{L_m C_m}} \quad (\text{Eq.A-1.14})$$

ω^+ and ω^- represent the squares roots obtained for $+R_m$ and $-R_m$ and correspond respectively to a minimum and a maximum of B in the vicinity of the resonance frequency. Assuming $\omega^+ = 2\pi f_n$ and $\omega^- = 2\pi f_u$, the equivalent circuit elements can be deduced by the following relationships:

$$R_m = \frac{1}{G_{max}}, L_m = \frac{R_m}{2\pi(f_n - f_u)} \text{ and } C_m = \frac{1}{4\pi^2 L_m f_r^2} \quad (\text{Eq.A-1.15})$$

The values of f_n , f_u and f_r can be deduced from experimental measurements of $G(f)$ and $B(f)$ (Figure III-A-2).

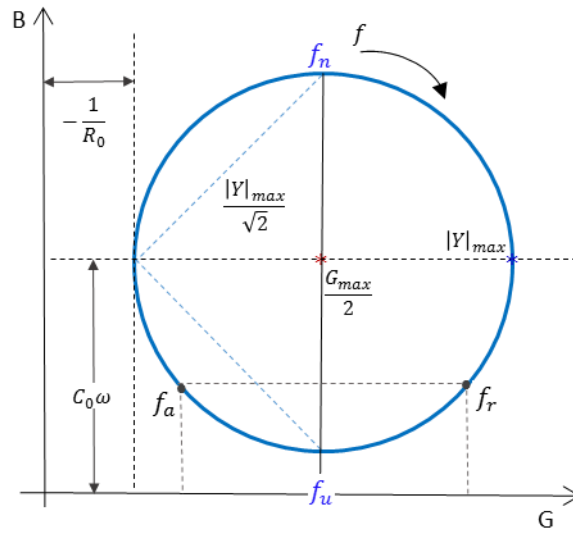


Figure III-A- 2: Characteristic $G(f)$ admittance circle.

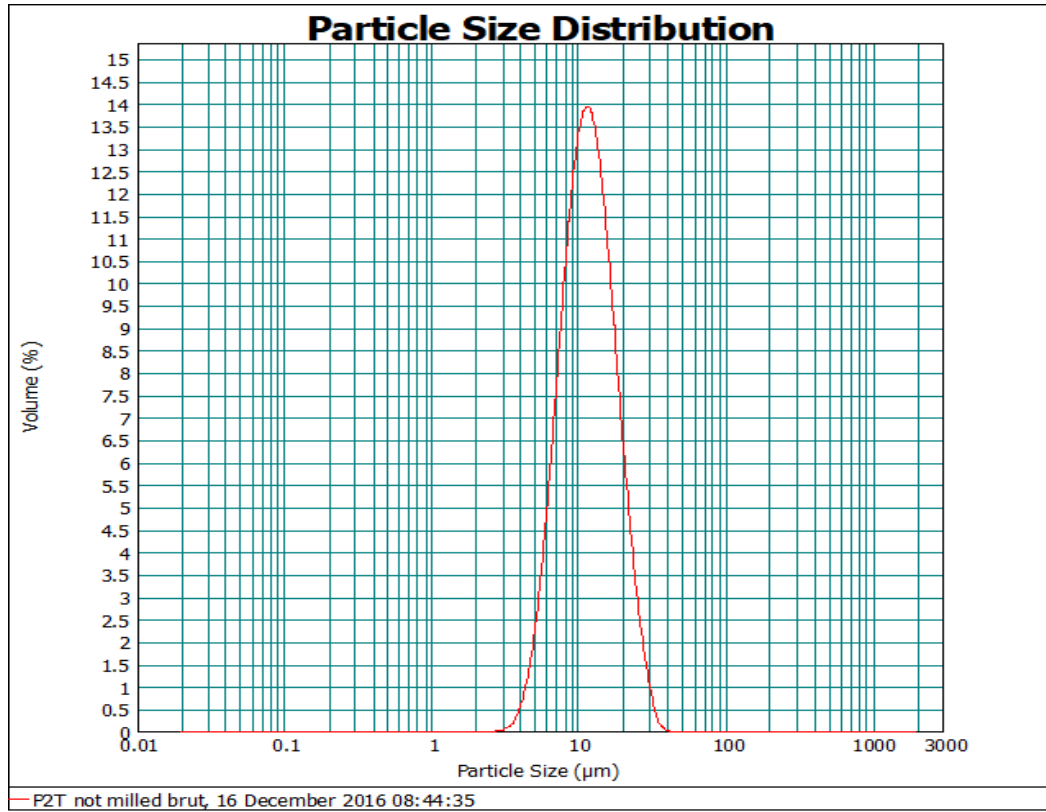
The value of the leakage resistance R_0 is determined using the equation of the admittance circle $B = f(G)$ with the characteristics described previously, subsequently:

$$B = B_0 + \left(\pm \frac{1}{2R_m} \right) \sin \left(\arccos 2R_m \left(G - \frac{1}{R_0} - \frac{1}{2R_m} \right) \right) \quad (\text{Eq. A-1.16})$$

Approximate values of B_0 , and R_0 can be inferred from the experimental values points and then refined by the least squares method. For the calculations to be accurate, it is necessary to take the maximum points in frequency around the vicinity of the resonance frequency corresponding to the maximum value of G .

Annexes Chapter IV

1. Particle size distribution of PZT powder analysis



2. Commercial Au paste ESL8836



Electro-Science Laboratories, Inc.

416 East Church Road • King of Prussia, PA 19406-2625, U.S.A
610-272-8000 • Fax: 610-272-6759 • www.ElectroScience.com • Sales@ElectroScience.com

CERMET GOLD CONDUCTOR

8836
8836-A

ESL 8836 and 8836-A mixed bonded thick film gold pastes are specially designed for thin printing. They produce a very smooth, dense film of 6 to 9 micrometers fired thickness. ESL 8836 is particularly well suited for automatic thermosonic wirebonding. While they have a wide firing range, a peak firing temperature of 850°C gives the best properties.

ESL 8836-A is an alloyed version of 8836. Its properties are similar to 8836, but it is designed for ultrasonic wire bonding using 25 micrometers diameter aluminum wire.

PASTE DATA

RHEOLOGY:	Thixotropic, screen printable paste
VISCOSITY: (Brookfield RVT, ABZ Spindle, 10 rpm, 25.5°C±0.5°C)	250±25 Pa·s
BONDING MECHANISM:	Mixed
SHELF LIFE: (25°C)	6 months

PROCESSING

SCREEN MESH/EMULSION:	325/25 µm
LEVELING TIME: (25°C)	5-10 minutes
DRYING AT 125°C:	10-15 minutes
FIRING TEMPERATURE RANGE:	850°C-930°C
OPTIMUM:	850°C
TIME AT PEAK:	10-12 minutes
RATE OF ASCENT/DESCENT:	60°C-100°C/minute
SUBSTRATE OF CALIBRATION:	96% alumina
THINNER:	ESL 413

8836/A 9711-E

ESL Affiliates

Japan: ESL-Nippon Company, Ltd. • Sukeyama Bldg. • 6th floor • 3-4 Yanagibashi 1-chome • Taito-ku • Tokyo 111, Japan • Tel: (011-81)-3-3864-8521 • Fax: (011-81)-3-3864-9270
NipponSales@ESLNippon.com

China: Shanghai Agmet Electro-Science Laboratory Ltd. • Second Floor Bldg. 12A1 • #223 North Fe Te Road • Waigaoqiao Free Trade Zone • Shanghai, China
Tel: (011-86)-21-5866-0497 • Fax: (011-86)-21-5866-0497 • ShanghaiSales@ShanghaiESL.com

Europe: Agmet, Ltd. • 8 Commercial Road • Reading, Berkshire, England RG2 0QZ • Tel: (011-44)-118-987-3139 • Fax: (011-44)-118-986-7331 • Sales@ESLEurope.co.uk

3. Organic binder ESLV400 provider information

Texanol-based vehicle, general purpose for dielectrics

Additional Information

Product Features: Vehicle, Solvent, Printing Medium, Viscosity Adjustment

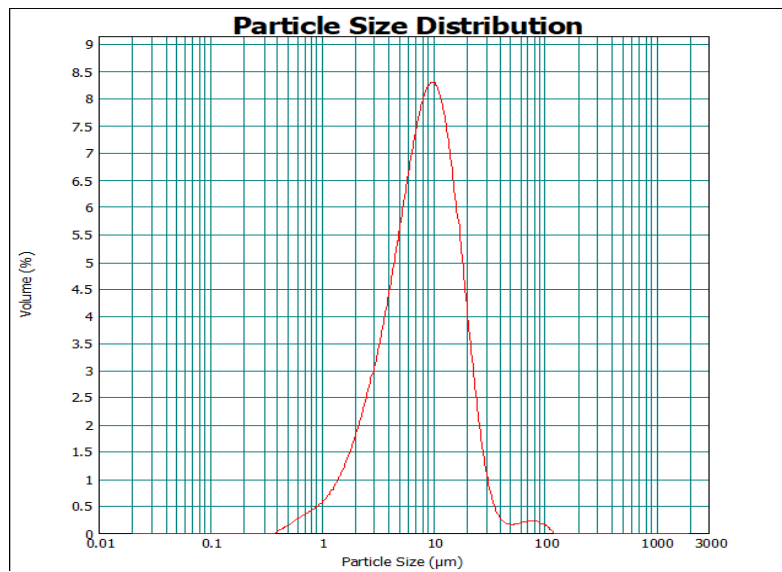
Environmental Compliance: Cadmium-Free (Cd-Free)|Lead-Free (Pb-Free)|Nickel-Free (Ni-Free)|RoHS Compliant

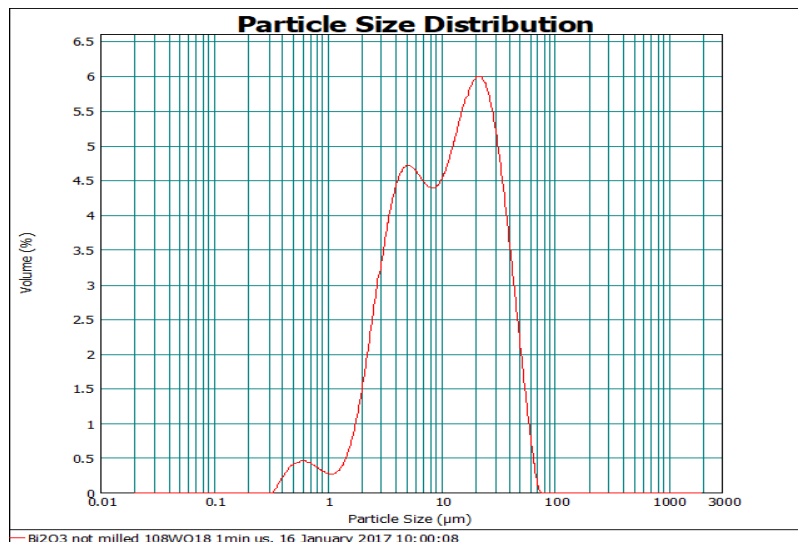
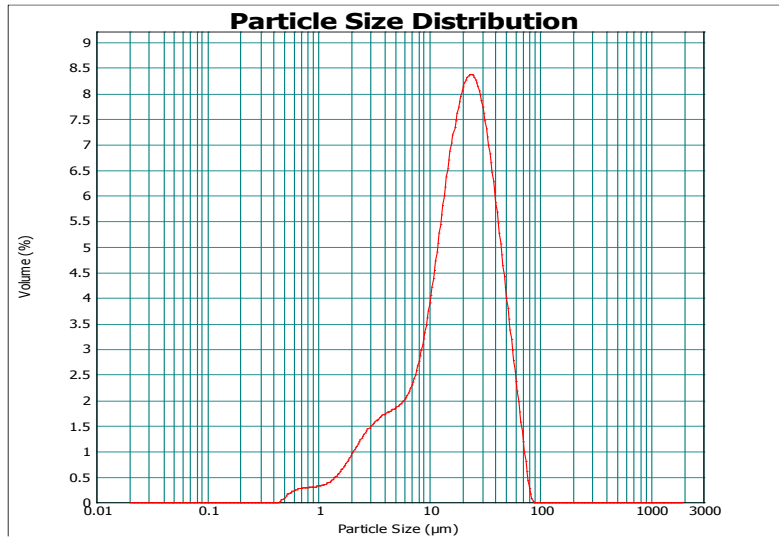
Common Uses: Paste Formulation, Ink Formulation

Technical Name: Texanol

4. Particle size distribution of LBCU sintering aid powders

CuO





5. Sacrificial layer ESL 244-T

The sacrificial layer technique allows, in a stack of layers, to partially or totally release the upper layers by removing the sacrificial layer provided for this purpose. The release mechanism could be chemical (e. g. by specific dissolution of the sacrificial layer) or physical (thermal decomposition). Printed disk are release during sintering using a sacrificial layer (ESL 244-T)



ESL ELECTROSCIENCE

CERAMIC TAPES &
THICK-FILM MATERIALS

416 EAST CHURCH ROAD
KING OF PRUSSIA, PA 19406-2625, U.S.A

T: 610-272-8000
F: 610-272-6759

www.electroscience.com

PROTECTIVE POLYMER COATING

244-T

RoHS Compliant*

ESL 244-T is a screen-printable resin coating. This coating may be used to protect silver polymer on glass substrates.

PASTE DATA

Rheology: Thixotropic, screen-printable paste

Viscosity:
(Brookfield RVT, 10 rpm
No. 7 spindle, 25.5 ± 0.5 °C) 100 ± 20 Pa.s

Shelf Life (20 - 25 °C): 6 months

PROCESSING

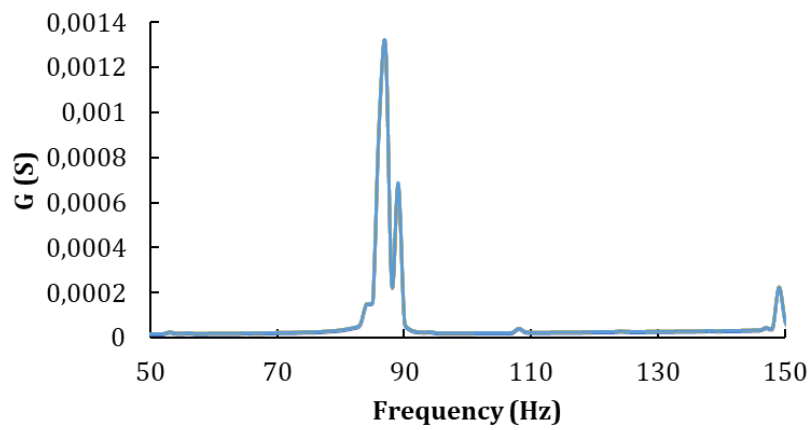
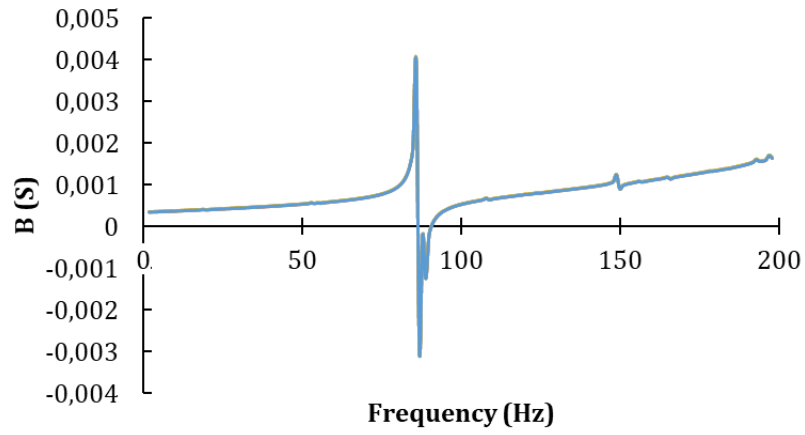
Screen Mesh, Emulsion: 200 S/S, 38 µm

Curing Schedules: 125°C / 5 - 15 min

Substrate for Calibration: Glass

Thinner: ESL 110

6. Electromechanical impedance graphics response of conventional ceramic pellet (PZT+ 3 %LBCu) sintered at 900°C during 2h



Annexes Chapter V

1. ESL CV59



ESL EUROPE
8 COMMERCIAL ROAD,
READING, ENGLAND RG2 0QZ
T: +44 (0) 118 9182400
F: +44 (0) 118 9867331
sales@esleurope.co.uk
www.electroscience.com



FICHE DE DONNÉES DE SÉCURITÉ N° 375

RÈGLEMENT: CE No. 1907/2006, Article 31
RÉVISION: 2
DATE DE REDACTION: 01.06.2015
DATE D'IMPRESSION: 02.03.2018

SECTION 1: IDENTIFICATION DE LA SUBSTANCE/DU MÉLANGE ET DE LA SOCIÉTÉ/L'ENTREPRISE

1.1 Identificateurs de produit

Liant CV59

1.2 Utilisations identifiées pertinentes de la substance ou du mélange et utilisations déconseillées

Solvant

1.3 Renseignements concernant le fournisseur de la fiche de données de sécurité

ESL Europe (Agmet Ltd)
8 Commercial Road
Reading
Berkshire
RG2 0QZ
Royaume-Uni.

Adresse e-mail: sds@esleurope.co.uk

1.4 Numéro d'appel d'urgence

UK: 0118 918 2400
International: +44 118 918 2400

Lundi - vendredi
8h00 à 16h30 (heure anglaise)
Langue anglaise

SECTION 2: IDENTIFICATION DES DANGERS

2.1 Classification de la substance ou du mélange

Classification en accord avec la réglementation (EC) No 1272/2008

Cette substance n'est pas classée comme dangereuse selon la législation de l'Union européenne.

2.2 Conteneur d'étiquette

Etiquetage en accord avec la réglementation (CE) No 1272/2008

N'est pas une substance dangereuse selon le SGH.

2.3 Autres dangers

L'évaporation des solvants durant les étapes de sérigraphie et de séchage

SECTION 3: COMPOSITION/INFORMATIONS SUR LES COMPOSANTS

Nature chimique: Résine époxy dispersée dans un solvant organique

3.1 Substance

Sans objet

3.2 Mélange

Réglementation (CE) No 1272/2008

CAS	NOM CHIMIQUE	%	CLASSIFICATION
N/D	Résine époxy	15 - 40	N/D
124-17-4	Acétate de Butyle diglycol	60 - 85	N/D

SECTION 4: PREMIERS SECOURS

4.1 Description des premiers secours

INHALATION	Déplacer la personne à l'air frais.
INGESTION	Rincer abondamment la bouche avec de l'eau. Solliciter des soins médicaux.
CONTACT AVEC LA PEAU	Laver les régions affectées avec de l'eau. Retirer les vêtements et chaussures contaminés.
CONTACT AVEC LES YEUX	Laver les régions affectées avec de l'eau. Oter les lentilles de contact. Solliciter des soins médicaux.

4.2 Principaux symptômes et effets, aigus et différés

INHALATION	Irritation des voies respiratoires.
INGESTION	Problèmes gastriques tels que vomissements, diarrhées ou douleurs abdominales.
CONTACT AVEC LA PEAU	Irritation de la peau.
CONTACT AVEC LES YEUX	Irritation des yeux.

Scientific Communications

❑ Journal articles

- Maria Isabel Rua-Taborda, Onuma Santawitee, Angkana Phongphut, Bralee Chayasombat, Chanchana Thanachayanont, et al. Printed PZT Thick Films Implemented for Functionalized Gas Sensors. *Key Engineering Materials*, Trans Tech Publications, 2018, 777, pp.158-162.
- Egon Fernandes, Maria Isabel Rua Taborda, Blake Martin, Sid Zarabi, H  l  ne Deb  da et al. *Design, Fabrication, and Testing of a Low Frequency MEMS Piezoelectromagnetic Energy Harvester*. *Smart Materials and Structures*, IOP Publishing, 2018.
- Zongxian Yang, Sid Zarabi, Egon Fernandes, Maria Isabel Rua Taborda, H  l  ne Deb  da et al. *A Simple Wireless Sensor Node System for Electricity Monitoring Applications: Design, Integration, and Testing with Different Piezoelectric Energy Harvesters*. *Sensors*, MDPI, 2018, Special Issue Low Energy Wireless Sensor Networks: Protocols, Architectures and Solutions, 18(11), 3733.

❑ Book chapter

- H. Deb  da, M.-I. Rua-Taborda, U.-C. Chung, C. Elissalde, Chapter 10 - *One step densification of printed multilayers by SPS: Towards new piezoelectric energy harvester MEMS*, Editor(s): Giacomo Cao, Claude Estourn  s, Javier Garay, Roberto Orr  , **Spark Plasma Sintering**, Elsevier, 2019.

❑ International conferences

- Maria Isabel Rua Taborda, Catherine Elissalde, U-Chan Chung-Seu, H  l  ne Deb  da. *Implementation and Optimization of SPS Sintering for a printed Piezoelectric Energy Harvester MEMS. Electroceramics XVI*, Jul 2018, Hasselt, Belgium.
- Maria Isabel Rua Taborda, Catherine Elissalde, U-Chan Chung-Seu, H  l  ne Deb  da. *New densification route of metallic supported printed multilayer for piezoelectric energy harvester*; 4th International workshop on Spark Plasma Sintering, May 2018, Cagliari, Italy.
- H  l  ne Deb  da, Maria Isabel Rua Taborda, Egon Fernandes, Sid Zarabi, David Nairn et al. Printed MEMS-based self-contained piezoelectric-based monitoring device for smart grids, *PowerMEMS 2017*, the 17th international conference on micro and nanotechnology for power generation and energy conversion applications, Nov 2017, Kanazawa, Japan.
- Sid Zarabi, Egon Fernandes, Maria Isabel Rua Taborda, Armaghan Salehian, H  l  ne Deb  da et al. Design and Development of a Self-contained and Non-Invasive Integrated System for Electricity Monitoring Applications, *IEEE 12th International Conference on ASIC (ASICON)*, Oct 2017, Guiyang, China.
- Catherine Elissalde, U-Chan Chung-Seu, Maria Isabel Rua Taborda, Mario Maglione, Graziella Goglio et al. Some strategies to (co)-sinter refractory functional oxides at low temperature by Spark Plasma Sintering.

□ National conferences

- Maria Isabel Rua Taborda, Catherine Elissalde, U-Chan Chung Seu, Alexis Brenes, Elie Lefeuvre et al. Cermet piezoelectric vibration energy harvester: SPS route for denser screen-printed PZT active layer, JNRSE 2019, May 2019, Blois, France (**Best oral presentation award**).
- Maria Isabel Rua Taborda, Egon Fernandes, Sid Zarabi, David Nairn, Lan Wei et al. Optimization of the fabrication of a low frequency energy harvester made of printed PZT layers on a meander shape stainless substrate Design DTIP'2017, May 2017, Bordeaux, France;
- Maria Isabel Rua Taborda, Egon Fernandes, Armaghan Salehian, H  l  ne Deb  da. Densification of printed PZT thick films on SS substrates used for vibration energy harvesting JNRSE 2017, May 2017, Lyon, France. 2017
- Maria Isabel Rua Taborda, H  l  ne Deb  da, Egon Fernandes, Armaghan Salehian, U-Chan Chung, et al. Multicouches Au/PZT/Au/SS imprim  s par s  rigraphie - Application MEMS pour la r  cup  ration d'  nergie. Journ  es Annuelles du Groupe Fran  ais de la C  ramique, Mar 2018, Bordeaux, France
- U-Chan Chung-Seu, Maria Isabel Rua Taborda, H  l  ne Deb  da, Emilie Perret, Jean-Marc Heintz, et al.. Moules SPS adapt  s aux Mat  riaux. Journ  es annuelles 2019 du GFC, Mar 2019, Montpellier, France